THE FATIGUE RESISTANCE OF SURFACE HARDENED STEELS

by

ABHAY SHRIPAD NADKARNI

A thesis submitted for
the degree of Doctor of Philosophy

The University of Aston in Birmingham

July 1981

CONTENTS

		PAGE
Synopsis		(i)
List of Tables		(ii)
List of Figures		(iii)
List of Plates		(iv)
Acknowledgements		(v)
1.	INTRODUCTION	1
2.	FATIGUE FAILURE	4
2.1	Introduction	4
2.2	Metallurgical aspects of fatigue	5
2.2.1	Initiation of fatigue crack and stage I crack growth	5
2.2.2	Propagation of fatigue crack (stage II)	9
2.3	Engineering aspects of fatigue	12
2.3.1	Initiation of an engineering fatigue crack	12
2.3.2	Propagation of fatigue crack (stage II)	15
2.4	Initiation and propagation of fatigue crack from notches	20
2.4.1	Initiation of an engineering fatigue crack	21
2.4.1.1	Elastic-plastic analysis of stress concentration in fatigue	21
2.4.1.2	Fracture mechanics approach	22
2.4.2	Propagation of fatigue cracks	26
2.4.3	Experimental method to determine modified K calibration constant	30

		PAGE
3.	FATIGUE PROPERTIES OF CASE HARDENED STEELS	34
3.1	Introduction	34
3.2	Carburising	36
3.3	Carbonitriding and ferritic nitro-carburising	43
3.4	Induction hardening	46
3.5	Engineering analysis of case hardened steel	47
3.6	Summary	54
4.	FATIGUE CRACK MONITORING	57
4.1	Methods of detection	57
4.1.1	Electrical potential methods	57
4.2	Problems associated with monitoring initiation and early growth of fatigue crack from notches	60
5.	EXPERIMENTAL WORK	64
5.1	The materials	64
5.2	Heat treatment	64
5.2.1	Chemico-thermal methods	64
5.2.2	Induction hardening	66
5.3	The specimens	71
5.4	Design of experimental programme	72
5.4.1	Fatigue crack initiation	72
5.4.2	Fatigue crack propagation	76
5.4.3	Fatigue crack initiation and propagation in case hardened specimens	77

		PAGE
5.5	Equipment and test methods	78
5.5.1	The equipment	78
5.5.2	Test methods	81
5.5.2.1	Specimen preparation	81
5.5.2.2	Fatigue crack initiation and propagation	84
5.5.2.3	Electrical potential calibration	85
5.6	Hardness and composition gradient	86
5.7	Metallography and fractography	88
6.	RESULTS	90
6.1	Electrical potential calibration	90
6.2	Determination of stress intensity factor coefficient	97
6.2.1	Propagation of fatigue cracks	97
6.2.2	Propagation of fatigue cracks from blunt notches	103
6.3	Fatigue crack initiation	108
6.3.1	Fatigue crack initiation in 080M15 and 080A47	108
6.3.2	Initiation of fatigue crack in case hardened 080M15	123
6.3.3	Initiation of fatigue crack in case hardened 080A47	138
6.4	Fatigue crack propagation in case hardened 080M15	146
6.5	Composition and hardness gradient	155
6.5.1	Carbon gradient	155
6.5.2	Hardness gradient	164

		PAGE
6.6	Metallographic and fractographic examination	173
6.6.1	Material microstructure	173
6.6.1.1	Untreated material	173
6.6.1.2	Carburised 080M15	175
6.6.1.3	Carbonitrided 080M15	180
6.6.1.4	Nitrocarburised 080M15 (Nitempered)	183
6.6.1.5	Induction hardened 080A47	188
6.6.2	Fracture surface examination	193
6.6.2.1	Fatigue fracture of carburised and carbonitrided shallow and sharp notches	194
6.6.2.2	Fatigue fracture of carburised and carbonitrided deep and blunt notches	201
6.6.2.3	Fatigue fracture of nitrocarburised 080M15	210
6.6.2.4	Fatigue fracture in induction hardened 080A47	210
6.6.3	Fatigue crack initiation	218
6.7	Fatigue crack initiation threshold	224
6.7.1	Effect of stress concentration or notch geometry on the threshold value of the parameters for case hardened 080M15	224
6.7.2	Effect of heat treatment and case depth on the threshold value of the parameters for case hardened 080M15	233
6.7.3	Effect of induction hardening on the threshold values of the parameters for 080A47	236

		PAGE
7.	DISCUSSION	241
7.1	Electrical potential difference calibration	241
7.2	Determination of stress intensity factor coefficient	244
7.3	Fatigue crack initiation	247
7.3.1	Stress concentration approach	247
7.3.2	Fracture mechanics parameters	249
7.3.3	Effect of case hardening on fatigue crack initiation	257
7.3.4	Fractography of fatigue crack initiation	259
7.4	Fatigue crack initiation threshold	262
7.5	Fatigue crack propagation	263
7.6	Application of results	268
8.	CONCLUSIONS	280
9.	SUGGESTIONS FOR FUTURE WORK	284
10.	APPENDIX	286
11.	REFERENCES	289

THE UNIVERSITY OF ASTON IN BIRMINGHAM

Title: THE FATIGUE RESISTANCE OF SURFACE HARDENED STEELS

Name: ABHAY SHRIPAD NADKARNI

Degree: Ph.D. 1981

SYNOPSIS

The initiation and propagation of fatigue cracks from notches in 10 mm thick sections of two engineering steels 080M15 and 080A47 has been studied in three point bending fatigue. A range of notch root radii varying from 0.13 mm to 3.17 mm provided different absolute distances within which the fatigue crack propagation is influenced by the notch stress field. The fatigue crack propagation data from the regions affected by the notch stress field were compared with that not influenced by the notch stress field, to obtain the modified stress intensity factor coefficient for cracks emanating from notches. It was found that the modified stress intensity factor coefficient does not fall to zero at the tip of a blunt notch. The effective stress intensity factor coefficient for blunt notches could be described as a function of notch geometry and microstructural features of steels, viz. grain size.

The initiation and propagation of fatigue cracks from notches in 10 mm thick sections of gas carburised, gas carbonitrided and nitrocarburised 080M15 and induction hardened 080A47 were tested in three point bending fatigue. The number of cycles to produce a detectable fatigue crack, N_i, correlated well with the effective stress intensity factor range. The microstructural feature in case hardened steel was the prior austenitic grain size. The fracture surface exmination did not indicate subsurface crack initiation generally associated with the case hardened steels subjected to fatigue. The results of fatigue crack initiation in carburised and carbonitrided notched geometries indicated that fatigue crack initiation is not affected by the case depth. The fatigue crack propagation data for cracks emanating from case hardened notches in 080M15 could be correlated to the effective stress intensity factor range.

The results provided an adequate engineering method for design against fatigue failure from a range of stress concentrations for the surface hardened steels examined.

KEY WORDS: STEELS, SURFACE HARDENING, NOTCHES, FATIGUE RESISTANCE, FRACTURE MECHANICS

LIST OF TABLES

TABLE NO.		PAGE
1	Values of crack length C_o (which indicates the extent of notch stress field) as suggested by different investigators	31
2	Rotating bending fatigue strength of case hardened steels	56
3	Material composition and mechanical properties	65
4	Specimen dimensions and stress concentration factors	73
5	Constants of equation 31 for various notch geometries	93
6	Calculated crack lengths using different methods	96
7	Fatigue crack initiation data for 080M15	110-112
8	Fatigue crack initiation data for 080A47	113-116
9a	Fatigue crack initiation data for carburised 080M15 (case depth 0.38 mm)	125-127
9b	Fatigue crack initiation data for carburised 080M15 (case depth 0.76 mm)	128
9c	Fatigue crack initiation data for carbonitrided 080M15 (case depth 0.38 mm)	129

TABLE NO		PAGE
9d	Fatigue crack initiation data for carbonitrided 080M15 (case depth 0.76 mm)	130
9e	Fatigue crack initiation data for nitrocarburised 080M15	131
10	Fatigue crack initiation data for induction hardened 080A47	139-142
11	Effective case depth for various case hardening treatments (080M15)	162
12	Fatigue crack initiation thresholds for case hardened 080M15 by different treatments and for different geometries in terms of fibre stress ΔS $MN/m^{3/2}$	225
13	Fatigue crack initiation thresholds for 080M15, case hardened by different notch geometries in terms of $K_t \Delta s$ MN/m^2	226
14	Fatigue crack initiation thresholds for 080M15, case hardened by different treatments and different notch geometries in terms of $\frac{\Delta K}{\sqrt{\rho}}$ MN/m^2	227
15	Fatigue crack initiation thresholds for 080M15, case hardened by different treatments and for different notch geometries in terms of ΔK_B $MN/m^{3/2}$	228

TABLE NO		PAGE
16	Percentage change in fatigue crack initiation threshold of O8OM15 due to case hardening in different notch geometries	234
17	Fatigue crack initiation threshold data for induction hardened O8OA47 in terms of different parameters	237
18	Comparison of fatigue crack initiation threshold values of carburised O8OM15 for different notch geometries for case depths 0.38 mm and 0.76 mm (one way analysis of variance, degrees of freedom $\nu_1 = 1$, $\nu_2 = 4$)	264
19	Comparison of fatigue crack initiation threshold values of carbonitrided O8OM15 for different notch geometries for case depths 0.38 mm and 0.76 mm (one way analysis of variance, degrees of freedom $\nu_1 = 1$, ν_2 2 4)	265
20	Comparison of fatigue crack initiation threshold values of carburised and carbonitrided O8OM15 for different notch geometries for case depths 0.38 mm and 0.76 mm (one way analysis of variance, degrees of freedom $\nu_1 = 3$, $\nu_2 = 8$)	266

TABLE NO		PAGE
21	Average threshold values for fatigue crack initiation in terms of ΔK_B $MN/m^{3/2}$ for case hardened O80M15 and O80A47	272
22	Constants of Paris law for case hardened O80M15 (case depth 5 mm, root radius 0.13 mm)	274

LIST OF FIGURES

FIGURE		PAGE
1	Schematic diagram of the three stage fatigue-failure process	6
2	Diagramatic representation of the mechanism of striation formation by a process of plastic blunting	10
3	Schematic representation of fatigue crack growth behaviour in non-aggresive environment	17
4	Schematic representation of equivalence of fatigue cracks	28
5	Schematic representation of stress patterns in the tension side of a case carburised bar in bending (88)	49
6	Schematic representation of stress-distribution in a case-carburised bar subjected to bending (58)	51
7	Stress-strength profiles for carburised bend specimens (89)	51
8	Schematic diagram of an engineering crack	61
9	Schematic diagram of induction hardening set-up	69
10	Specimen geometry of fatigue specimens	74

FIGURE		PAGE
11	Circuit diagram for electrical potential difference measurement system	80
12a	Experimental electrical potential calibration curves (notch depth 5 mm, root radii 0.13 mm, 0.36 mm and 0.76 mm, curve 1 represents theoretical calibration[97])	91
12b	Experimental electrical potential calibration curves (notch depth 10mm, root radii 1.52 mm, and 3.17 mm, curve 1 and 2 represent theoretical calibrations for 1.52 mm and 3.17 mm root radius respectively)	92
13	Sensitivity of experimental electrical potential calibration curves	98
14	Fatigue crack growth data for BS970 080M15 (En32)	99
15	Fatigue crack growth data for BS970 080A47 (En43B)	100
16	Comparison between proposed equation (curve 1), Jergeus equation (curve 2,[42]) and experimental data (notch depth 5 mm and root radius 0.76 mm)	104
17	Comparison between proposed equation (curve 1), Jergeus equation (curve 2[42]) and experimental data (notch depth 10 mm and root radius 1.52 mm)	105

FIGURE		PAGE
18	Comparison between proposed equation (curve 1), Jergeus equation (curve 2 [42]) and experimental data (notch depth 10 mm and root radius 3.17 mm)	106
19	Fatigue crack initiation data for 080M15: parameter ΔK_B	117
20	Fatigue crack initiation data for 080M15: parameter $\Delta K/\sqrt{\rho}$	118
21	Fatigue crack initiation data for 080M15: parameter $K_t \Delta s$	119
22	Fatigue crack initiation data for 080A47: parameter ΔK_B	120
23	Fatigue crack initiation data for 080A47: parameter $\Delta K/\sqrt{\rho}$	121
24	Fatigue crack initiation data for 080A47: parameter $K_t \Delta s$	122
25	Fatigue crack initiation data for carburised and carbonitrided 080M15: parameter ΔK_B	132
26	Fatigue crack initiation data for carburised and carbonitrided 080M15: parameter $\Delta K/\sqrt{\rho}$	133
27	Fatigue crack initiation data for carburised and carbonitrided 080M15: parameter $K_t \Delta s$	134

FIGURE		PAGE
28	Fatigue crack initiation data for nitrocarburised 080M15: parameter ΔK_B	135
29	Fatigue crack initiation data for nitrocarburised 080M15: parameter $\Delta K/\sqrt{\rho}$	136
30	Fatigue crack initiation data for nitrocarburised 080M15: parameter $K_t \Delta s$	137
31	Fatigue crack initiation data for induction hardened 080A47: parameter ΔK_B	143
32	Fatigue crack initiation data for induction hardened 080A47: parameter $\Delta K/\sqrt{\rho}$	144
33	Fatigue crack initiation data for induction hardened 080A47: parameter $K_t \Delta s$	145
34	Fatigue crack propagation data of carburised 080M15: case depth 0.38 mm	147
35	Fatigue crack propagation data of carburised 080M15: case depth 0.76 mm	148
36	Fatigue crack propagation data of carbonitrided 080M15: case depth 0.38 mm	149
37	Fatigue crack propagation data of carbonitrided 080M15: case depth 0.76 mm	150
38	Fatigue crack propagation data of nitrocarburised 080M15	151

FIGURE		PAGE
39	Fatigue crack propagation data of 080M15 as a function of unmodified and modified stress intensity factor range (case depth 0.38 mm, notch depth 10 mm, root radius 1.52 mm)	152
40	Fatigue crack propagation data of carburised 080M15 as a function of crack length (notch depth 5 mm, root radii 0.13 mm and 0.76 mm)	153
41	Fatigue crack propagation data of carburised 080M15 as a function of crack length (notch depth 10 mm, root radii 1.52 mm and 3.17 mm)	154
42	A representative plot of number of counts obtained from electron microprobe analyser to determine the carbon gradient at the notch root	157
43	Carbon gradients at the notch root of carburised 080M15 specimens for different notch geometries (case depth 0.38 mm)	158
44	Carbon gradients at the notch root of carburised 080M15 specimens for different notch geometries (case depth 0.76 mm)	159

FIGURE		PAGE
45	Carbon gradients at the notch root of carbonitrided 080M15 specimen for different notch geometries (case depth 0.38 mm)	160
46	Carbon gradients at the notch root of carbonitrided 080M15 specimens for different notch geometries (case depth 0.76 mm)	161
47	Carbon gradients at the notch root of nitrocarburised 080M15 specimens for different notch geometries	165
48	Representative hardness gradient for carburised 080M15, case depth 0.38 mm	167
49	Representative hardness gradient for carburised 080M15, case depth 0.76 mm	168
50	Representative hardness gradient for carbonitrided 080M15, case depth 0.38 mm	169
51	Representative hardness gradient for carbonitrided 080M15, case depth 0.76 mm	170
52	Hardness gradient at the notch root of nitrocarburised 080M15 specimens for different notch geometries	171

FIGURE		PAGE
53	Hardness gradients at the notch root of induction hardened O8OA47 specimens for different notch geometries	172
54	Variation in fatigue crack initiation threshold with K_t: carburised, carbonitrided and nitrocarburised O8OM15: parameter Δs	229
55	Variation in fatigue crack initiation threshold with K_t, carburised, carbonitrided and nitrocarburised O8OM15: parameter ΔK_B	230
56	Variation in fatigue crack initiation threshold with K_t, carburised, carbonitrided and nitrocarburised O8OM15: parameter $\Delta K/\sqrt{\rho}$	231
57	Variation in fatigue crack initiation threshold with K_t, carburised, carbonitrided and nitrocarburised O8OM15: parameter $K_t \Delta s$	232
58	Variation in fatigue crack initiation threshold, in terms of ΔK_B, with the case depth for carburised and carbonitrided O8OM15	235

FIGURE		PAGE
59	Variation in fatigue crack initiation threshold with K_t, induction hardened 080A47: parameter ΔK_B	238
60	Variation in fatigue crack initiation threshold with K_t, induction hardened 080A47: parameter $\Delta K/\sqrt{\rho}$	239
61	Variation in fatigue crack initiation threshold with K_t, induction hardened 080A47: parameter $K_t \Delta s$	240
62a	Fatigue crack initiation data for BS1458A[35]: parameter ΔK_B	253
62b	Fatigue crack initiation data for BS1458A [35]: parameter $\Delta K/\sqrt{\rho}$	254
63a	Fatigue crack initiation data for BS1456 grade A [35]: parameter ΔK_B	255
63b	Fatigue crack initiation data for BS1456 grade A [35]: parameter $\Delta K/\sqrt{\rho}$	256
64	Modification function Y_s/Y_1 as a function of crack length, carburised 080M15, case depth 0.38 mm (curve represents equation 34)	275
65	Modification function Y_s/Y_1 as a function of crack length, carburised 080M15, case depth 0.76 mm (curve represents equation 34)	276

FIGURE		PAGE
66	Modification function Y_s/Y_1 as a function of crack length, carbonitrided 080M15, case depth 0.38 mm (curve represents equation 34)	277
67	Modification function Y_s/Y_1 as a function of crack length, carbonitrided 080M15, case depth 0.76 mm (curve represents equation 34)	278
68	Modification function Y_s/Y_1 as a function of crack length, nitrocarburised 080M15 (curve represents equation 34)	279

LIST OF PLATES

PLATE NO.		PAGE
1	Copper coil used for induction hardening	68
2	General view of the fatigue machine and other equipment	82
3	Closer view of 3 point bend rig and the specimen	83
4	Fatigue crack shape at initiation in 080A47 specimen (magnification x24)	94
5	Fatigue crack shape at initiation in 080A47 specimen (magnification x24)	94
6	Microstructure of untreated 080M15 (magnification x200)	174
7	Microstructure of untreated 080A47 (magnification x200)	174
8	Microstructure of case carburised 080M15, case depth 0.38 mm (magnification x 250)	176
9	Microstructure of case carburised 080M15, case depth 0.76 mm (magnification x250)	177
10	Microstructure at the notch root, carburised 080M15, root radius 0.76 mm, showing non-martensitic transformation products (case depth 0.38 mm) (magnification x450)	178

PLATE NO		PAGE
11	Microstructure at the notch root, carburised 080M15, root radius 3.17 mm (case depth 0.38 mm) (magnification x450)	178
12	Microstructure at the notch root, carburised 080M15, root radius 0.76 mm, midsection (case depth 0.76 mm) (magnification x450)	179
13	Microstructure at the notch root, carburised 080M15, root radius 3.17 mm, midsection (case depth 0.76 mm) (magnification x450)	179
14	Microstructure of case carbonitrided 080M15, case depth 0.38 mm (magnification x 250)	181
15	Microstructure of case carbonitrided 080M15, case depth 0.76 mm (magnification x 250)	182
16	Microstructure at the notch root, carbonitrided 080M15, root radius 0.13 mm, (case depth 0.38 mm) (magnification x450)	184
17	Microstructure at the notch root carbonitrided 080M15, root radius 3.17 mm, (case depth 0.38 mm) (magnification x450)	184

PLATE NO		PAGE
18	Microstructure at the notch root, carbonitrided O8OM15 showing non-martensitic transformation product, root radius 0.13 mm, (case depth 0.76 mm) (magnification x450)	185
19	Microstructure of carbonitrided O8OM15 root radius 0.76 mm (case depth 0.76 mm) (magnification x450)	186
20	Microstructure of carbonitrided O8OM15 root radius 3.17 mm (case depth 0.76 mm) (magnification x450)	186
21	Microstructure at the notch root of nitrocarburised O8OM15 specimen showing compound layer, root radius 0.13. mm, (magnification x450)	187
22	Microstructure of nitrocarburised O8OM15 specimen, midsection, at the notch root, root radius 3.17 mm (magnification x450)	187
23	Microstructure of induction hardened O8OA47, at the notch root, root radius 3.17 mm, (magnification x450)	189
24	Microstructure of induction hardened O8OA47, at the notch root and mid-section, root radius 3.17 mm, (magnification x450)	189

PLATE NO		PAGE
25	Microstructure in the core of induction hardened 080A47, root radius 3.17 mm (magnification x450)	190
26	Microstructure of induction hardened 080A47, at the notch root, root radius 0.36 mm (magnification x450)	190
27	Microstructure at the notch root in induction hardened 080A47, showing non-martensitic transformation product, root radius 0.36 mm, midsection (magnification x450)	191
28	Microstructure in core of induction hardened 080A47 specimen (magnification x450)	192
29	Microstructure in core of induction hardened 080A47 specimen (magnification x450)	192
30	Fatigue fracture of carburised case below the notch root, case depth 0.38 mm, root radius 0.13 mm, N_i = 429,940	195
31	Fatigue fracture of carburised case at the notch root, case depth 0.38 mm, root radius 0.13 mm, N_i = 209,550	195
32	Fatigue fracture of carburised case at the notch root, case depth 0.38 mm, root radius 0.13 mm, N_i = 90,630	196

PLATE NO		PAGE
33	Fatigue fracture of carburised case at the notch root, case depth 0.76 mm, root radius 0.76 mm, N_i = 231,000	196
34	Fatigue fracture of carburised case at the notch root, case depth 0.76 mm, root radius 0.13 mm, N_i = 295,800	197
35	Fatigue fracture of carburised case at the notch root, case depth 0.76 mm, root radius 0.76 mm, N_i = 229,000	197
36	Fatigue fracture in carbonitrided case at the notch root, case depth 0.38 mm, root radius 0.13 mm, N_i = 459,120	198
37	Fatigue fracture in carbonitrided case at the notch root, case depth 0.38 mm, root radius 0.76 mm, N_i = 363,240	198
38	Fatigue fracture of carbonitrided case at the notch root, case depth 0.76 mm, root radius 0.13 mm, N_i = 168,770	199
39	Fatigue fracture of carbonitrided case at the notch root, case depth 0.76 mm, root radius 0.76 mm, N_i = 173,780	199
40	Fatigue fracture in carbonitrided case below the notch root, showing sub-surface porosity, case depth 0.76 mm, root radius 0.13 mm, N_i = 168,770	200

PLATE NO		PAGE
41	Fatigue fracture in carbonitrided case below the notch root, showing sub-surface porosity, case depth 0.76 mm, root radius 0.76 mm, N_i = 173,780	200
42	Fatigue fracture of carburised case at the notch root, case depth 0.38 mm, root radius 1.52 mm, N_i = 62,050	202
43	Fatigue fracture of carburised case at the notch root, case depth 0.38 mm, root radius 1.52 mm, N_i = 118,470	202
44	Fatigue fracture of carburised case at the notch root, case depth 0.38 mm, root radius 1.52 mm, N_i = 20,000	203
45	Fatigue fracture of carburised case at the notch root, case depth 0.38 mm, root radius 3.17, N_i = 210,000	203
46	Fatigue fracture of carburised case at the notch root, case depth 0.76 mm, root radius 1.52 mm, N_i = 305,700	204
47	Fatigue fracture of carburised case at the notch root, case depth 0.76 mm, root radius 3.17, N_i = 51,600	204
48	Fatigue fracture in carbonitrided case below the notch root, case depth 0.38 mm, root radius 1.52 mm, N_i = 158,650	205

PLATE NO		PAGE
49	Fatigue fracture in carbonitrided case at the notch root, case depth 0.38 mm, root radius 3.17 mm, N_i = 211,200	205
50	Fatigue fracture in carbonitrided case at the notch root, case depth 0.76 mm, root radius 1.52 mm, N_i = 185,000	206
51	Fatigue fracture in carbonitrided 0.76 mm, at the notch root, case depth 0.76 mm, root radius 3.17 mm, N_i = 241,270	206
52	Fatigue fracture of core in carburised 080M15	208
53	Fatigue fracture of core in carburised 080M15	208
54	Fatigue fracture of core in carbonitrided 080M15	209
55	Fast fracture topography of carburised case	209
56	Fatigue fracture of compound layer in nitrocarburised 080M15 at the notch root, root radius 0.13 mm, (midsection), N_i = 191,000	211
57	Fatigue fracture of nitrocarburised case at the notch root (same area as that in plate 56, at a lower magnification) N_i = 191,000	211

PLATE NO		PAGE
58	Fatigue fracture in the compound layer at the notch root, showing micro-porosity, nitrocarburised 080M15, root radius 0.76 mm, N_i = 610,000	212
59	Fatigue fracture of core in nitro-carburised 080M15	212
60	Fatigue fracture in the compound layer at the notch root, showing microporosity, nitrocarburised 080M15, root radius 1.52 mm, N_i = 646,250	213
61	Fatigue fracture in the compound layer at the notch root, nitrocarburised 080M15, root radius 1.52 mm, N_i = 646,250	213
62	Fatigue fracture in nitrocarburised 080M15 at the notch root, midsection, root radius 1.52 mm, N_i = 646,250	214
63	Fatigue of compound layer at the notch root, nitrocarburised 080M15, root radius 3.17 mm, N_i = 191,000	214
64	Fatigue fracture in the nitrocarburised 080M15 below the notch root, midsection root radius 3.17 mm.	215
65	Fatigue fracture in nitrocarburised case below the notch root, midsection root radius 3.17 mm	215

PLATE NO		PAGE
66	Fatigue fracture of case in induction hardened 080A47, location: notch root, midsection, root radius 0.36 mm, N_i or N_f = 254,000	216
67	Fatigue fracture of case in induction hardened 080A47, location: notch root, midsection, root radius 0.76 mm, N_i or N_f = 377,000	216
68	Fatigue fracture in core of induction hardened 080A47	217
69	Fatigue crack shape at initiation in carburised 080M15, case depth 0.38 mm, root radius 0.13 mm (magnification x10)	219
70	Fatigue crack shape at initiation in carbonitrided 080M15, case depth 0.76 mm (magnification x10)	219
71	Fatigue fracture of case in carburised 080M15 at the notch root, showing a cusp, grown in transgranular mode. Surface topography at locations marked A and B at higher magnification is shown in plates marked A and B respectively, root radius 3.17 mm, case depth 0.38 mm, N_i = 210,000	220

PLATE NO		PAGE
72	Fatigue fracture of case in carburised 080M15 at the notch root, showing a cusp grown in transgranular mode, surrounded by an area fractured in intergranular mode, root radius 3.17 mm, case depth 0.76 mm, N_i = 51,600	221
73	Fatigue fracture of case in carburised 080M15 at the notch root, fractography of the area at location A in plate 72, at higher magnification	221
74	Fatigue fracture of case in carbonitrided 080M15 at the notch root, showing a cusp grown in transgranular mode surrounded by an area fractured in intergranular mode. Fractography of area at locations A and B is shown at higher magnification, is shown in plates marked A and B, root radius 1.52 mm, case depth 0.38 mm, N_i = 158,650	222
75	Fatigue fracture of case in carbonitrided 080M15 at the notch root, showing a cusp - grown in transgranular mode, surrounded by an area fractured in intergranular mode, case depth 0.76 mm, root radius 0.76 mm, N_i = 173,780	223

ACKNOWLEDGEMENTS

I would like to express my thanks to Professor J.T. Barnby for his guidance, invaluable suggestions and constant encouragement during the period this work was carried out. I would like to record my thanks to Joseph Lucas Research Centre and The University of Aston in Birmingham for the financial support which enabled me to carry out this research. I would like to thank the staff and technicians of the Department of Metallurgy and Materials Engineering for their help. Finally, thanks are also due to Mrs. Howell for typing the thesis.

1. INTRODUCTION

In many engineering components that require a hard wear resistant surface, it is also necessary that the piece as a whole has a high fatigue strength. One of the frequently cited examples is that of a gear. Such a part can be provided with a hardened surface layer by different treatments. The high fatigue strength resulting from these case hardening treatments stems from two conditions: the higher endurance limit of the hard case material and the residual compressive stresses produced within the case by the hardening process.

These treatments may be classified according to the type of the processes involved, viz.

1. Mechanical treatments, involving pre-straining of the surface beyond yield, e.g. shot peening of components.

2. Thermal treatments, which lead to phase changes in the surface layers only, e.g. induction and flame hardening.

3. Chemico-thermal treatments, based on the diffusion of active species in the surface layer and subsequent heat treatment, e.g. carburising, nitriding, carbonitriding.

It has long been recognised that a considerable improvement in fatigue properties results from these treatments. This effect has been conventionally represented as an upward shift of S-N curve. Such representation, however, has limitations. It does not provide sufficient information, when applied to situations where stress concentrations of increasing severity are present. The fatigue limit is seriously reduced by the introduction of a stress raiser, which is a feature of most machine parts.

The effect of stress raisers on fatigue is generally studied by testing specimens containing a notch. The effectiveness of the notch in decreasing the fatigue limit is expressed by the fatigue strength reduction factor K_f. This factor is simply a ratio of the fatigue limit of unnotched specimens to the fatigue limit of notched specimens. K_f not only depends on specimen size and shape, but also on material, state of stress and fatigue life range. An up-to-date review of the effects of stress raisers and approaches to notch sensitivity in fatigue has been made by Frost et al [1]. It shows clearly that the fatigue strength reduction factor has to be determined experimentally and a suitable analytical technique is not available. Analytical relationships developed are applicable to a particular set of conditions and none of these are effective over the whole field.

The failure to establish analytical criteria to solve the problem of fatigue failure, which incorporates at least

some of the conditions, leads investigators to consider new possibilities. Development of fracture mechanics in the last few decades opened a new avenue.

The present research programme aims at establishing inter-relationships between some of the parameters controlling fatigue lives of case hardened steels, based on fracture mechanics. To derive these relationships, initiation and propagation of fatigue cracks from notches of varying stress concentrations and the relationship between fatigue properties and microstructure of untreated steels needs to be examined. The relationships derived from this information will then be extended to assess the fatigue behaviour of case hardened steels, with varying degrees of stress concentrations.

2. FATIGUE FAILURE

2.1 Introduction

The most characteristic feature of the fatigue failure is the absence of gross plastic deformation before fracture, in most materials, generally when the part has been stressed, though repeatedly, below the macroscopic elastic limit. The traditional approach to fatigue behaviour was based on testing smooth or notched specimens at given nominal alternating stresses and establishing the number of cycles after which failure occurred. Early research was aimed at establishing fatigue crack initiation mechanisms, as initiation was thought to occupy most of the fatigue life. Recent work recognises the fact that the fatigue life is made up of three stages, initiation of crack, propagation of crack, at the end of which unstable propagation and static separation ensues. Several disciplines are involved in development of Fatigue design procedures. Materials science concerns itself with the metallurgical aspects of fatigue processes on the scale of dislocations, impurity atoms and grains. Engineering and applied mechanics are concerned with stress-strain analysis and evaluate the behaviour of a material from an engineering point of view, during three stages of fatigue.

2.2 Metallurgical Aspects of Fatigue

In a comprehensive review on metallography of fatigue, Plumbridge and Ryder [2] postulated a multistage model of fatigue (Figure 1).

a. Crack initiation: Initiation of crack in slip bands or other regions of strain localisation which is controlled by shear stress. Such fatigue damage could be eliminated by a suitable thermal anneal.

b. Slip band crack growth: Forsyth [3] termed it as 'stage I' crack growth. In this stage, growth occurs by extension of an initial crack on a slip plane or conjugate slip planes of high shear stress.

c. Crack growth on planes of high tensile stress: Growth of fatigue crack normal to the direction of maximum tensile stress. Forsyth [3] termed it as stage II crack growth.

d. Ultimate failure: When the crack reaches a sufficiently long length, failure occurs either because the remaining section can no longer support the stress or the stress intensity factor for the crack reaches a critical value (K_{IC}).

2.2.1 Initiation of Fatigue Crack and Stage I Crack Growth

Theories of fatigue crack initiation can be divided into two categories. Those based on repeated work hardening of a soft matrix inside an elastic matrix, localised strain hardening using up the plasticity of the metal so that

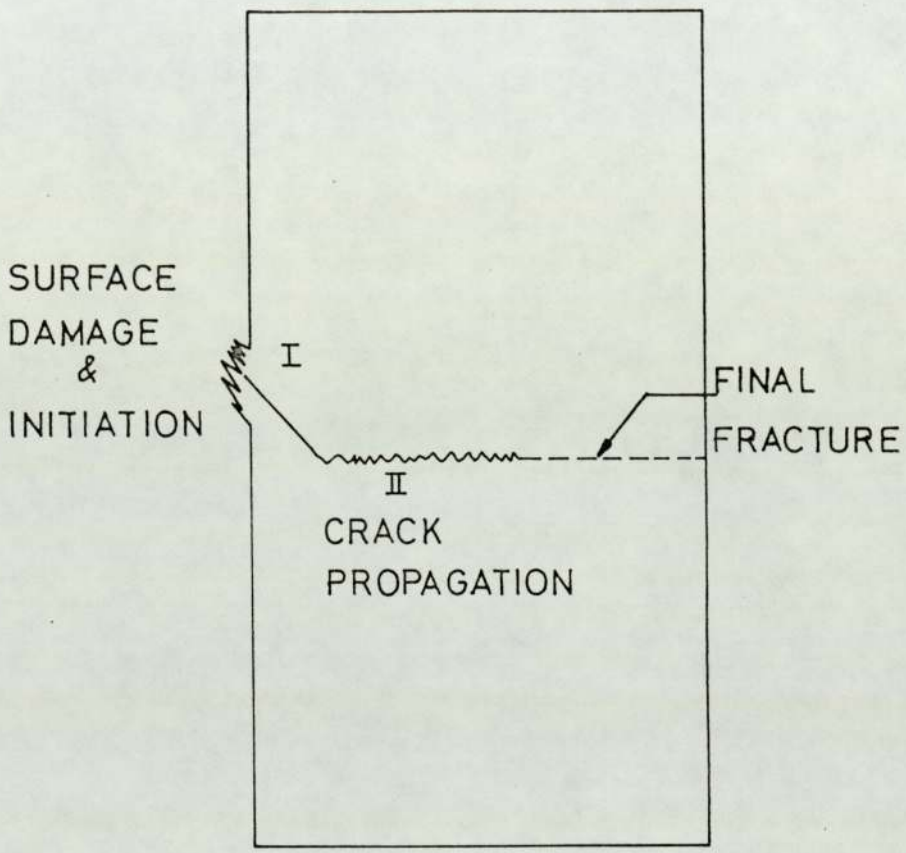

FIGURE 1 Schematic diagram of the three stage fatigue-failure process

initiation can occur [4] and those based on repeated slip leading to some form of damage on preferred planes, hence formation of a crack [5,6,7,8]. A second theory describes the mechanism of initiation which is well supported by experimental observations. Electron microscopy has shown that grooves and surface ridges called slip band intrusions and slip band extrusions are formed due to fatigue deformation. Fatigue cracks were found to initiate at the intrusions and extrusions [3]. Wood [5] has suggested a mechanism for producing slip band intrusions and extrusions. He pointed out that slip bands are a result of a systematic accumulation of fine reverse slip movements of the order of 10^{-3} μm. An intrusion acts as a notch with the notch root of atomic dimensions, where a fatigue crack forms. Though formation of a slip band is necessary prior to fatigue crack initiation, it does not follow that all slip bands will initiate a fatigue crack. It has been suggested that a free surface is a prerequisite for a fatigue crack to initiate. However, in some cases, such as case hardened steels and composites, fatigue crack initiation has been reported to occur at subsurface sites. The initiation process discussed so far referred to ductile materials. In the case of brittle materials fatigue cracks were found to initiate around inclusions or precipitates.

The criterion for stage I crack growth is a range of resolved shear stresses on the slip plane. The physical process of reverse slip, involved in initiation and stage I crack growth are similar, except that during

stage I crack growth, intrusion continues while extrusion ceases. The tip of the intrusion becomes a very active dislocation source, and growth of crack occurs by the emission of dislocations from the tip of the crack.

Forsyth [3] pointed out that by defining crack initiation as stated earlier, certain difficulties are encountered concerning the size of the crack at initiation. Such a definition requires the specification of a minimum crack size on the atomic scale. Moreover, initiation and stage I crack growth occur by similar mechanisms. Thus he postulated that the first two stages could be treated as one.

The effect of various factors on initiation of a crack and stage I crack growth was summarised by Plumbridge and Ryder [2]. The mechanism of crack initiation was elucidated and the role of variables such as environment, stacking fault energy, grain size and material was described. Frost et al [1] pointed out that the initiation and development of microcracks depends on the maximum resolved shear stress. Thus a mean stress will not have a marked effect on the initiation process. A compressive mean stress, however, will prevent it from opening and so will retard its development to a macrocrack stage.

Stage I of fatigue crack growth ends, when the slip band cracks eventually link up to form dominant cracks which then start to extend on a plane normal to the applied stress. The transition from stage I to stage II is

generally supposed to occur due to the reduction in the ratio of shear to normal stress at the crack tip.

2.2.2 Propagation of Fatigue Crack (Stage II)

Extensive research has been carried out to understand this mode of crack growth (stage II) and many laws have been proposed to describe it. This mode of crack growth generally occupies the largest area of cross-section and often shows macroscopic progression marks. Forsyth et al [9] identified two different types of striation marks.

Type A: "DUCTILE" striations lying on irregular non-crystallographic plateau.

Type B: "BRITTLE" striations lying on crystallographic facets.

It was also found that each striation is produced by a single cycle, however the converse of this was found to be valid only in some cases. It is generally accepted that striation formation involves alternate blunting and resharpening of the crack tip, but the argument regarding its precise mechanism still persists. The mechanisms of plastic blunting as proposed by Laird [10] are illustrated diagramatically in Figure 2. The double notch tip at the end of the sharp crack (Figure 2a), concentrates deformation along planes at 45^{o}, under the application of tensile load (Figure 2b). The crack widens to its maximum extension and growth occurs by plastic shearing, the crack tip

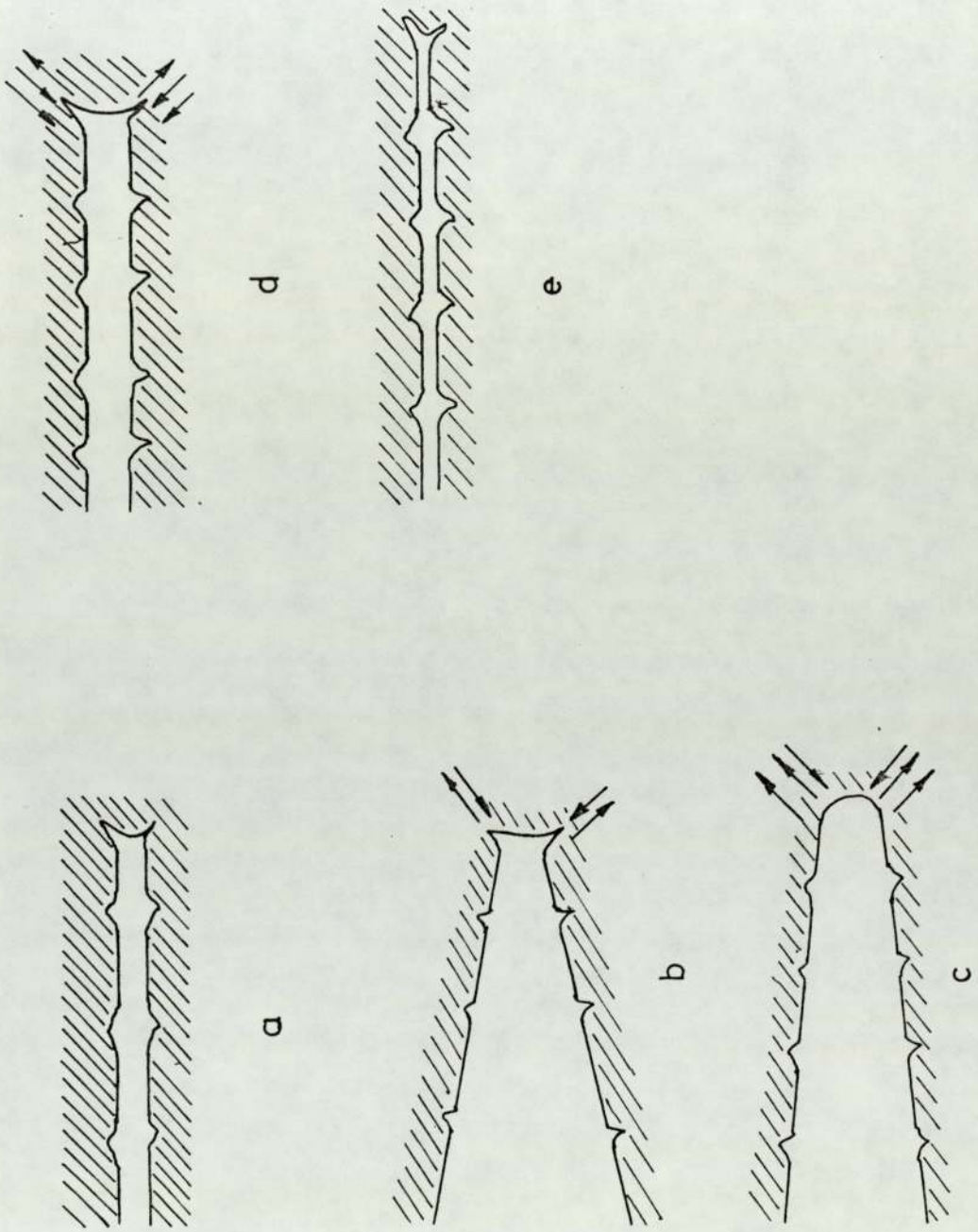

FIGURE 2 Diagramatic representation of the mechanism of striation formation by a process of plastic blunting

blunting at the same time (Figure 2c). Reversal of load reverses the slip direction in the end zone and the crack faces are crushed together. Part of the newly created surface folds, resharpening the crack in the process (Figures 2d and e). Material, temperature and environment will control whether the crack propagation proceeds by either purely "DUCTILE" or "BRITTLE" striation formation or a combination of both. At higher values of stress intensity factors nearing net section yielding, instead of striation formation, large scale steps of crack increment or static modes of crack growth, occur by microvoid coalescence in ductile materials. Such large scale crack advances are also found in embrittled steels which result from microcleavage or intergranular mechanisms.

2.3 Engineering Aspects of Fatigue

The study of mechanisms in different stages of fatigue helps to establish the criteria which govern initiation and growth of a fatigue crack. These criteria are then used to predict the behaviour of crack under a given set of conditions. This set of conditions includes history, magnitude and type of stress, environment and frequency. The prediction of crack behaviour generally involves estimation of life spent in each stage of fatigue crack growth. This information is of considerable value to a design engineer.

2.3.1 Initiation of an Engineering Fatigue Crack

To describe the initiation of a fatigue crack in an engineering component, Forsyth's [3] postulate is more important. Initiation as defined by Plumbridge and Ryder [1] will involve detecting a slip band crack. A careful surface preparation is necessary, which is not normally possible in an engineering environment. Although geometric features of such a crack have not been reported so far, it will involve detection of a crack not longer than 5 μm, which poses considerable problems. The stage I of crack propagation however extends well over a few grains diameter, which may mean that a crack is more than 150 μm long.

Generally, in engineering practice an initiated fatigue crack is one which can be detected using low power magnification, i.e. around x 25. A typical surface crack

defined in this way will be around 0.5 mm long and 0.15 mm deep [11]. It is noteworthy that initial flaw size specified in "Airplane damage tolerance design requirements" of the United States Air Force is 0.127 mm[12]. Other reports on initiation of an engineering crack also report similar crack sizes [13,14].

In metallurgical terms, such an initiated crack may have passed through initiation and stage I of crack growth. The shape of an initiated crack is normally found to be semi-circular or semi-elliptical. The behaviour of the crack front during initiation and stage I is as yet obscure.

A criterion for initiation of an engineering crack was proposed by Fuchs [15]. He used Sine's criterion for fatigue failure and reasoned that the loads required to propagate a fatigue crack must be smaller than those required to nucleate it. He states the criterion for initiation of a fatigue crack.

"A fatigue crack will initiate when the alternating octahedral shear stress plus a fraction of the sum of the mean principal stresses is equal to or greater than the value of the octahedral shear stress in a uniaxial specimen stressed to the appropriate axially reversed fatigue strength divided by the fatigue strength reduction factor."

This criterion cannot be used to estimate the life to initiation of the crack. Further, this analysis can only be used when the number of cycles to initiation exceeds 10^7. Also it is necessary that the nominal stresses and strains are elastic. Early investigations of fatigue failures were mainly concentrated on endurance cycles beyond 10^5, which is generally termed high cycle fatigue (HCF). In the HCF region, stage II crack growth occupies only 10% or so of total fatigue life. Thus initiation and final failure were treated as simultaneous events. The engineering analysis was thus based on predicting final failure and considered nominal stresses and strains. This approach is valid since during and up to the end of formation of an engineering crack from a smooth specimen, stresses and strains remain essentially the same. The nominal stress ΔS versus cycles to failure N_f curve established for smooth specimens could be thus treated as a prediction of initiation of a crack, errors in prediction increasing when N_f decreases. It can be described by following equation.

$$N_f = \left(\frac{\Delta S}{\sigma_f'}\right)^{\alpha} \qquad \text{.....(1)}$$

σ_f' = fatigue strength coefficient

α = Basquin's exponent

In the case of low cycle fatigue (LCF), i.e. when the number cycles to failure are less than 10^4, nominal stress exceeds yield stress and failure is found to depend on nominal strain in the case of smooth specimens. The fatigue is described by applied strain range $\Delta\varepsilon$

versus N_f diagram. Manson and Coffin [16] proposed a relationship to represent the above mentioned curve.

$$N_f = \left(\frac{\Delta\varepsilon}{\varepsilon_f'}\right)^{1/\alpha} \quad \ldots\ldots\ldots\ldots\ldots\ldots (2)$$

ε_f' = fatigue ductility coefficient

α = fatigue ductility exponent

In the LCF region, propagation of a crack represents a significant part of the failure process, thus it becomes necessary to establish a separate correlation to predict initiation of an engineering crack. Manson [17] established a correlation between cycles to initiation N_i and cycles to failure N_f

$$N_i = N_f - 4.0(N_f)^{0.6} \quad \ldots\ldots\ldots\ldots\ldots (3)$$

He plotted data for several materials and proved its validity in LCF region. Substituting for N_f from equation 2, the value of N_i can thus be predicted.

2.3.2 Propagation of Fatigue Crack (stage II)

The rate of crack growth depends primarily on the amplitude of stress or strain, the material characteristics, geometric configuration, environment and frequency. Since the elastic stress field at the tip of the crack can be fully described by the stress singularity (provided macroscopic plasticity does not occur), the crack growth has been examined using fracture mechanics parameters. The models for stage II propagation mentioned in section 2.2.2, suggest that the range of plastic strain range $\Delta\varepsilon_p$ will be

the controlling parameter, as the crack advances by plastic processes. Under quasi-linear elastic conditions $\Delta\varepsilon_p$ will be proportional to the crack opening displacement or square of stress intensity factor range. Many laws have been proposed based on this principle, one suggested by Paris and Erdogan [18] is generally used to describe crack growth

$$\frac{da}{dN} = C(\Delta K)^n \qquad \text{.....(4)}$$

$\frac{da}{dN}$ = rate of crack growth
mm/cycle or in/cycle

ΔK = stress intensity factor range

C,n = material constant.

Values of C and n are determined experimentally. It was pointed out by Paris and Erdogan [18] that these values should not be determined from one plot alone due to the empirical nature of the constants.

Equation (4) indicates that the double logarithmic plot of $\frac{da}{dN}$ versus ΔK should be a straight line. However later investigations into crack propagation behaviour showed that crack growth rates do not usually follow a straight line pattern, but can be divided into three regions (Figure 3). The slope of the line ie n = 4 reported in earlier investigations was found to give an average line covering all three regions. It was proposed [19] that region B should be regarded as stage II of Forsyth's model [3]. The experimental values of n in region B vary between 2 and 3 for a wide range of material. In region A, theoretical considerations based on stress and strain

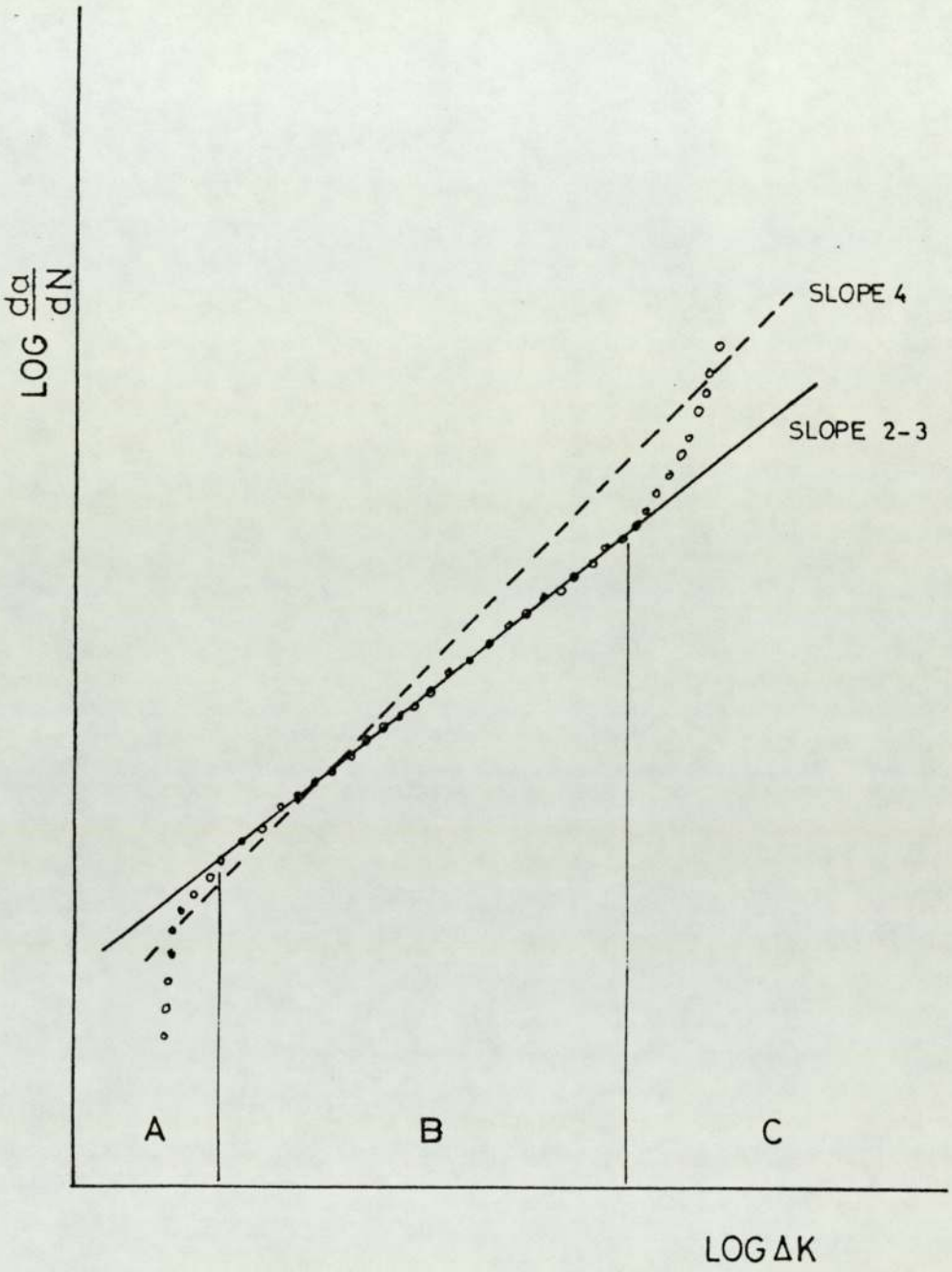

FIGURE 3 Schematic representation of fatigue crack growth behaviour in non-aggresive environment

predict a vertical line, however inhomogeneities and grain boundary effects (when the plastic zone is less than a grain diameter) decrease the value of slope and a region of steep slope is obtained. Similarly in region C, bursts of brittle cracking and/or contribution from monotonic modes of fracture result in a steep slope.

Though the Paris relationship (equation 4) is a valuable method for assessing crack growth, it does not account for important factors which affect the crack growth. Many attempts have been made to propose laws which account for mean stress, one developed by Forman et al [20] is as follows:

$$\frac{da}{dN} = C_3(\Delta K)^n/K_c(1-R)-\Delta K \quad \ldots\ldots\ldots\ldots\ldots(5)$$

C_3 and n = material constants

R = stress ratio

K_c = critical stress intensity

Irving and McCartney [21] examined a selection of continuum based theoretical crack growth laws and concluded that

1. The crack growth laws could be divided into three categories.
   a. Those based on instantaneous values of crack opening displacement,
   b. Those based on either damage or strain accumulation at the crack tip,

c. Those based on energy balance criterion and containing a concept of crack tip process zone.

2. Data, gathered in air have a minimum exponent (i.e. n) between 2 - 4.

3. Experimentally produced data agreed with the energy balance criterion, given by

$$\frac{da}{dN} = \frac{\Delta K^2 * [(\Delta K)^2 - (\Delta K_{threshold})^2] C}{\sigma_{ys}^2 * (K_{IC}^2 - K^2)} \quad \ldots\ldots\ldots (6)$$

Fatigue crack growth being dependent on so many uncontrollable variables, a large scatter has to be expected in practice. This means that any empirical expression may have some merit and a comparison of different laws representing crack growth becomes a pointless exercise. Each individual expression could be treated as valid as long as it is applied to a limited amount of data and to a few materials. Even then fracture mechanics and Paris Law remain by far the best representation of crack growth. In view of the factors affecting crack growth it is necessary to apply a large safety factor when predicting crack growth rates using the Paris Law.

2.4 Initiation and Propagation of Fatigue Crack from Notches

In previous sections there has been an implicit assumption that the geometry of the material subjected to fatigue loading was smooth. In practice a change is inevitable in the cross-section of a component. Such a change, however gradual, will introduce a notch, which will change the fatigue behaviour. The traditional approach to designing against fatigue failure from notches was based on nominal stresses and K_f. This leads to a highly conservative estimate of design stress. As described before, a new approach based on recognition of different stages in fatigue is also extended to fatigue failure from notches. To predict life spent in crack propagation, a fracture mechanics approach is generally used. In the case of initiation, however two different criteria have been proposed. It is accepted that the physical processes leading to initiation and propagation remain the same, as discussed in section 2.2. Similarly definition of an engineering crack is also assumed to be adequate. To describe initiation and propagation of a crack from a notch in terms of a measurable criterion, it becomes necessary to examine the stress-strain field in front of the notch. Most of the theories emerge from following hypothesis.

1. The initiation and propagation of a fatigue crack is determined by the stress and strain field at the notch root.

2. There is a measurable criterion which characterises the field.

3. This criterion can be related to the amplitude of the nominal load applied to the specimen.

2.4.1. Initiation of an Engineering Fatigue Crack

There are two concepts proposed to characterise the stress-strain field in front of the notch.

a. Elastic-plastic analysis of stress concentration in fatigue (local strain approach).

b. Fracture mechanics.

2.4.1.1 Elastic-plastic Analysis of Stress Concentration in Fatigue

The local strain approach assumes that a given notch surface strain always results in the same fatigue crack initiation life. This enables smooth specimen simulation of notched specimen behaviour. To correlate stress and strain in a smooth specimen to those at the notch tip, Neuber's [22] relationship is used.

$$K_\sigma * K_\varepsilon = K_t^2 \qquad \text{.....(7)}$$

where $K_\sigma = \dfrac{\text{Local stress range } \Delta\sigma}{\text{nominal stress range } \Delta s}$

$K_\varepsilon = \dfrac{\text{Local strain range } \Delta\varepsilon}{\text{nominal strain range } \Delta e}$

This formula is applicable only in the case of monotonic loading. In the case of fatigue, K_t is replaced by K_f.

$$K_f^2 = \left(\frac{\Delta\sigma * \Delta\varepsilon}{\Delta S * \Delta e}\right) \quad \ldots\ldots\ldots\ldots\ldots(8)$$

Rearranging

$$\Delta\sigma * \Delta\varepsilon = K_f^2 * (\Delta S * \Delta e) \quad \ldots\ldots\ldots(9)$$

A smooth specimen subjected to $\Delta\sigma$ and $\Delta\varepsilon$ will have the same initiation life as that of a notched specimen with the fatigue strength reduction factor K_f and subjected to Δs and Δe. The fatigue data used in this case is generally described by Manson-Coffin Law [16]. It is necessary however that such data should correspond to a specific crack size. If a significant part of the fatigue life of a smooth specimen considered as initiation is actually spent in growth, then differing strain gradients will cause error in prediction.

As the method described requires accurate determination of K_f, it requires additional experimentation since K_f must be determined experimentally for each material and geometry. To overcome this difficulty other investigators evaluated local strain range $\Delta\varepsilon$ analytically. An up-to-date review of these methods is given in (11). The value of $\Delta\varepsilon$ is then substituted in the modified Manson-Coffin Law [11] to obtain crack formation life.

2.4.1.2 Fracture Mechanics Approach

This approach is most attractive as it is almost independent of the material under investigation and also accounts for the effects of the geometry. Its main criticism stems from the fact that the stress intensity factor cannot be defined for a notch. Crack initiation and fast fracture from

blunt notches has been observed in engineering practice. Various theories and models proposed to describe the fracture event relate the critical stress intensity factor K_{IC} to the notch root radius, notch depth and yield strength [23,24,25]. Further, the stress distribution for a sharp notch of finite root radius differs from that for a sharp crack only over a very short distance ahead of the notch tip [26]. This distance was found to be a quarter of the root radius [27]. It was suggested that the stress intensity factor controls displacement at the end of this critical element and Ni, the number of cycles to initiation of an engineering crack, is controlled by these displacements rather than those at the notch root [27].

The Bilby and Heald [28] analysis of plastic relaxation at the crack tip in fatigue forms the basis of the analytical proof of this approach. The Bilby and Heald analysis obtains a cumulative displacement ϕ_c by summing plastic displacements ϕ per fatigue cycle. It is proposed that the crack starts to move when the cumulative fatigue damage described by ϕ_c reaches a critical value ϕ_c^*. It is related to Ni as follows:

$$Ni = \frac{2\phi_c^* G\sigma_{ys}}{\pi (\Delta K)^2} \qquad \text{.....(10)}$$

Rearranging

$$Ni = B(\Delta K)^m \qquad \text{.....(11)}$$

where $B = \frac{2\phi_c^* G\sigma_{ys}}{\pi}$

$m = -2$

G = Elastic shear modulus

σ_{ys} = Yield strength

Jack and Price [27] suggested that, in practice, deformation occurs randomly on several slip planes instead of on a single plane as in the Bilby and Heald analysis. Further, the critical cummulative displacement should be a summation of the squares of the individual displacements. This changes equation (11) to:

$$Ni = B(\Delta K)^{-4} \qquad \text{.....(12)}$$

Using Weiss's approximation and concept of a critical element, Jack and Price [27] developed an expression for the effective stress intensity factor ΔK_{eff} for a blunt notch.

$$\Delta K_{eff} = \Delta K\left[\frac{\rho_o}{\rho}\right]^{\frac{1}{2}} \qquad \text{.....(13)}$$

where ΔK = stress intensity factor calculated for a crack of the same length of the notch

ρ_o = Critical root radius below which notch is equivalent to a sharp crack.

ρ = root radius of the notch.

The parameter described in equation (13) was found to give excellent correlation with the N_i when considered in conjunction with equation (12). Similar results were obtained for cast steels [29], wrought steels [27,30-32], aluminium alloys [33] and titanium alloys [34]. The magnitude of the critical radius seems to be a material constant varying around 0.25 mm for mild steels [27], 0.20 mm for HY-130 [14], and 0.1 mm for titanium alloys [34]. Though magnitude of ρ_o does not seem to depend on material

properties such as σ_{ys} or K_{IC}, there seems to be a consistent dependence on the grain size. This probably means that the critical element necessary for this theory is dependent on the grain size. Similar dependence is also observed in investigations of fast fracture from blunt notches [23,24,25]. It is also noteworthy that the parameter $K_f \Delta S$ used in the traditional approach and $\Delta K\left[\frac{\rho_o}{\rho}\right]^{\frac{1}{2}}$ are of similar magnitude when applied to sharp notches but the difference becomes increasingly larger for blunt notches. This is obvious since the value of K_f becomes unity for smooth specimens, whereas ΔK must be zero. This suggests that applicability of this parameter is limited to a certain large notch root radius. Recently Haddad et al [36] proposed threshold stress intensity factor ΔK_{th} for smooth specimens.

$$\Delta K_{th} = \sigma_f \sqrt{\pi \ell_o} \qquad \ldots\ldots\ldots\ldots\ldots (14)$$

where ℓ_o is a material constant dependent on the grain size. Though equation (14) has been proposed for fatigue limit, it is possible that it could be extended for stress levels above the fatigue limit. It is, thus possible to extend the range of fracture mechanics parameters provided the limits in which the equations are valid, are defined.

The effect of thickness on Ni was investigated by Jack and Price [30] in terms of ΔK. The state of stress in thin specimens was found to be plane stress. The number of cycles to initiation in thin specimens were lower than those in thick specimen where plane strain condition was realised. A simple linear relationship was observed between Ni and R

ratio ($\Delta K_{max}/\Delta K_{min}$) in the cast steels samples tested in investigation by Holder [35].

2.4.2 Propagation of Fatigue Crack

The use of the range of the stress intensity factor ΔK to predict the stage II crack growth was described in section 2.3.2. The crack growth was, however, assumed to occur in a constant stress-strain field. The presence of a notch introduces a constantly decreasing stress-strain which is asymptotic towards the nominal stress-strain in the section. It becomes necessary, therefore, to show that crack growth rate depends on ΔK and the nature of this dependence needs to be established.

Bilby and Heald [28] analysed the rate of crack growth from an elliptical and a sharp notch in an infinite body under antiplane strain condition. Using the model of plastic relaxation at the crack tip, it was shown that the crack growth rate depends on fourth power of stress intensity factor range ΔK_{eff}. The value of ΔK_{eff} was calculated for a notch plus crack geometry, using conformal mapping technique is given by(for an elliptical notch in mode III):

$$\Delta K_{eff} = (\pi \Delta S p)^{\frac{1}{2}} \left[\frac{(a+N)\sqrt{p^2+1}}{N\sqrt{p^2+1} + ap} \right]^{\frac{1}{2}} \quad \ldots\ldots\ldots (15)$$

and

$$p = \frac{a}{a^2-N^2} \left[(a+c)^2 - (a^2-N^2) \right]^{\frac{1}{2}} - \frac{N(a+c)}{a^2-N^2}$$

a = notch depth

N = notch width

c = crack length

When the crack length c is sufficiently long ΔK_{eff} should have the same value of ΔK calculated assuming notch plus crack to be a sharp crack. Thus, equation (15) should be valid only upto a certain value of c, say Co. This value of Co was not suggested or established in the investigation.

Benthem and Koiter [37] derived an expression to account for the effect of notch on stress gradient for the geometry shown in Figure 4a, from which an approximate value of K_I can be calculated. Yamamoto et al [38] modified this expression and using a finite element technique derived expressions for stress intensity factors for different specific geometries.

Smith and Miller [39] used an alternative approach to determine K values. It is based on the principle derived from the Paris Law, which suggests that the crack growth rates for two cracks in two different geometries will be identical if the stress strain fields at the crack tips are identical. It is necessary to maintain frequency, environment and other factors affecting the crack growth under identical conditions. This means that "A fatigue crack of length ℓ growing in an unnotched specimen can be equated to a fatigue crack of length c growing from a notch when both have same instantaneous velocity under identical conditions of bulk-applied stresses." (Figure 4). Thus for an elliptical notch with depth a and root radius ρ with a crack of length c emanating from it, an equivalent crack length was experimentally determined to be:

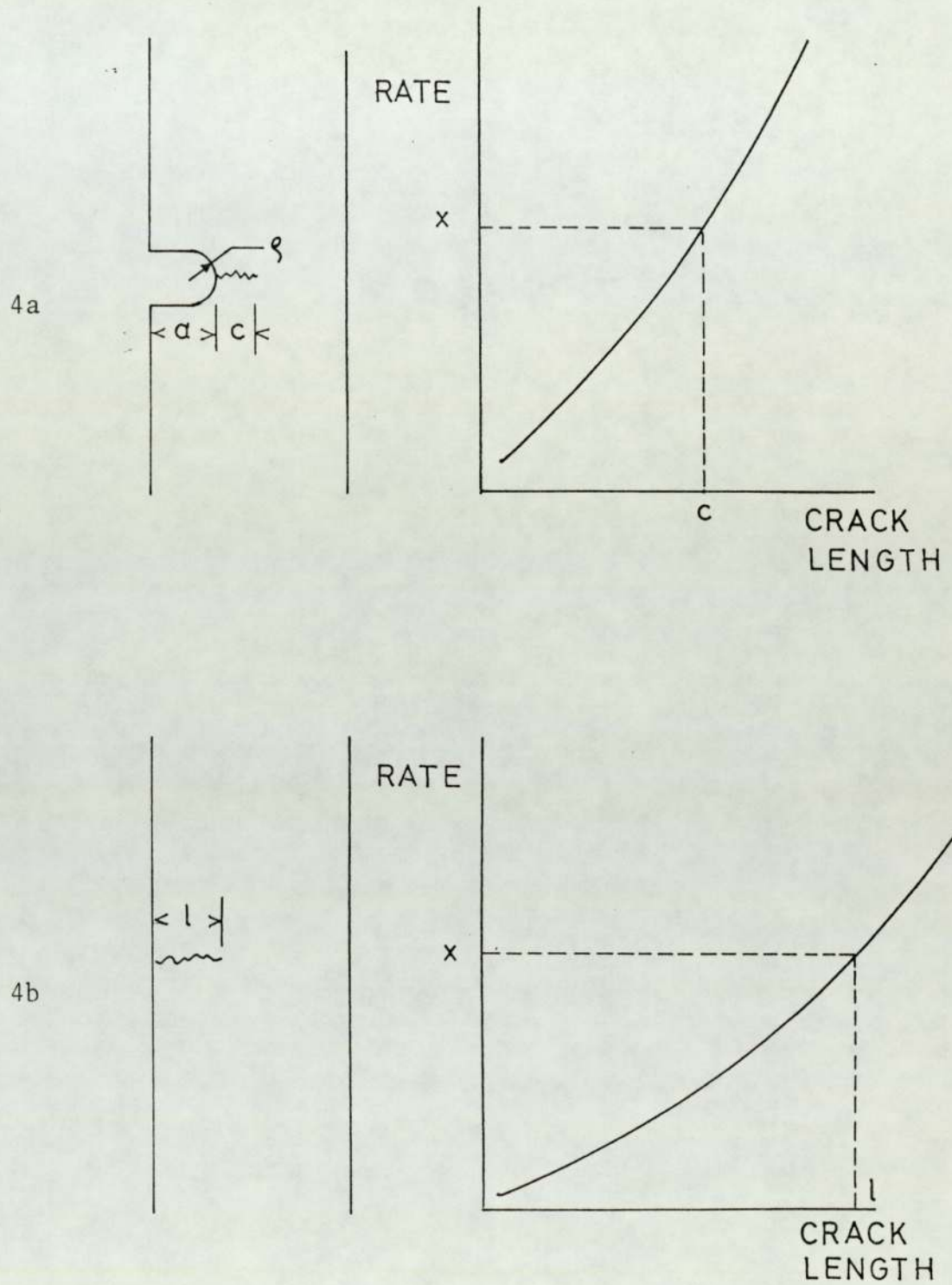

FIGURE 4 Schematic representation of equivalence of fatigue cracks

$$\ell = (1 + 7.69\sqrt{\frac{a}{\rho}}) * c \quad \text{.....(16)}$$

for $0 < c < 0.13\sqrt{a\rho}$

The effective crack length ℓ could also be written as:

$$\ell = e + c \quad \text{.....(17)}$$

Where e = contribution from notch or equivalent crack length for a notch.

For this particular case

$$e = 7.69 * \sqrt{\frac{a}{\rho}} * c \quad \text{.....(18)}$$

This suggests a linear dependence of notch contribution on crack length. Further, the notch contribution increases continuously till it reaches the value of notch depth a at $0.13\sqrt{a\rho}$ and beyond. In fact, e should asymptotically reached a as suggested by the analytical solutions of Newman [40] and Nishitani [41]. It is possible to rearrange the equations derived by the aforementioned investigators, in the form of equation (16). These rearranged equations show a much more complicated dependence on the contribution of the notch to the crack length.

Jergeus [42] showed that if the equation derived by Benthem and Koiter [37] is modifed to obtain a value of e for a specific geometry of notch it gives a relative minimum. This is implausible. He therefore suggested an empirical equation based on the finite element results,

$$e = a(1-\text{Exp}(-\frac{4(1+\sqrt{a/\rho})*c}{\sqrt{a\rho}}) \quad \text{.....(19)}$$

Each of these investigations cited before refers to a particular value of Co beyond which e is equal to a. The values suggested by different workers are summarised in table 1. The considerable difference in Co values may arise due to the differences in the approaches adopted by the investigators. The notch contribution e thus reaches the value of a depending on the degree of approximation. Smith and Miller [39] approximate the actual curve by a straight line and suggest Co to be equal to $0.13\sqrt{a\rho}$, whereas the Jergeus solution (equation 19) being closer to the analytical curve, gives Co a value of $0.5\sqrt{a\rho}$. The argument regarding Co still persists.

It is also noteworthy that all the equations noted so far predict the value of stress intensity to be zero at the notch root. This is not consistent with the theories of initiation described before. An equation for intensity factor should in fact have a specific value at the root of notch and should correlate to N_i.

2.4.3 Experimental Method to Determine Modified K Calibration Constant

The experimental method is based on the fact that the mean crack propagation rate can be expressed in terms of the stress intensity factor range, which is the 'Paris Law' [18]

$$\frac{da}{dN} = C(\Delta K)^n$$

For homogeneous materials, constants C and n could be treated as the material constants. The Paris Law provides a convenient means of determining the stress intensity

TABLE 1

VALUES OF CRACK LENGTH C_o (WHICH INDICATED THE EXTENT OF NOTCH STRESS FIELD) AS SUGGESTED BY DIFFERENT INVESTIGATORS

Reference	C_o
Smith and Miller [39]	$0.13\sqrt{a\rho}$
Dowling [43]	$0.2\sqrt{a\rho}$
Novak and Barsom [44]	$0.25\sqrt{a\rho}$
Jergeus [42]	$0.5\sqrt{a\rho}$
Newman [40], Nishitani [41]	
Yamamoto et al [38]	$\xi_o = 1-\mathrm{Exp}\left[\frac{-0.5\sqrt{a\rho}}{(W-a)}\right]$ $(W-a)\xi_o$

factors of specific geometries experimentally. First, values of C and n need to be found from the fatigue tests on crack geometries with known stress intensity factor calibrations. Further, the crack growth rates for the uncalibrated crack geometries could be measured. Substituting these values of crack growth rates in the Paris Law the values of the corresponding stress intensity factor range could be determined experimentally.

It is the compliance function which accounts for the geometry dependence of the stress intensity factor. Thus, from the method described above the value of the compliance function could be determined as the stress and the crack length are known. This procedure has been successfully used by many investigators [45-48] to find the compliance functions for uncalibrated crack geometries.

Rearranging the Paris Law

$$\Delta K_{cal} = \left(\frac{da}{dN} * \frac{1}{C}\right)^{\frac{1}{n}}$$

also $$\Delta K_s = \Delta S * Y_s * \sqrt{a+c} \quad \text{.....(21)}$$

But ΔK_{cal} is equal to ΔK_s

Thus,

$$Y_s = \frac{\left(\frac{da}{dN} * \frac{1}{c}\right)^{\frac{1}{n}}}{\Delta S * \sqrt{a+c}} \quad \text{.....(22)}$$

For a crack of length ℓ whose geometric length is equal to (a+c) the compliance function is known, which is Y_L. A modification factor B_m can be defined which accounts for the presence of a notch

$$B_m = Y_S/Y_L \qquad \text{.....(23)}$$

The value of B_m would then increase assymptotically as the crack length increases, towards the value of 1.

3. FATIGUE PROPERTIES OF CASE HARDENED STEELS

3.1 Introduction

The prediction of fatigue properties of case hardened steels has been largely dependent on empirical data, obtained from a variety of sources ranging from laboratory tests to more complex evaluations such as determining fatigue strength of a crank shaft. Earlier attempts to determine the effect of case hardening concentrated on evaluating stress levels which would ensure fatigue lives in excess of 10^7 cycles. Though it was noted that the case hardening is effective in reducing the notch effect and reduces the dependence on surface finish, earlier reports did not quantify this behaviour.

To assess the fatigue behaviour of the case hardened steels, it was suggested that summation of contributions from the case and core should be adequate [49]. It can be seen, however, that three interacting gradients exist in a case hardened steel part subjected to cyclic loading.

1. Fatigue strength gradients: The surface heat treatment gives rise to a variation of composition and/or structure in the case. Consequently, the material at the surface has a high fatigue strength. The fatigue strength of the subsequent layers is found to decrease continuously through the case till the case-core interface, the rate of decrease depending on the composition and the microstructural variation.

2. Residual stress gradient: The volume changes associated with the heat treatment lead to the development of residual stresses in the case hardened steel parts. The magnitude and the sign (compressive or tensile) is dependent on the individual treatments.

3. Applied stress gradients: This essentially depends on the method of stressing and local design details.

The interaction of these three gradients determines the fatigue strength of case hardened steel components. An increase in the inherent fatigue strength and a compressive residual stress will result in a high fatigue strength. The factors which contribute to increasing inherent fatigue strength and compressive residual stress will therefore increase the effective fatigue strength of the case hardened part. It may therefore be appropriate to discuss the effect of surface treatments and their parameters on the fatigue strength gradient and the residual stress distribution.

In the following discussion, an effort is made to describe the effect of case hardening treatment, viz. thermochemical and thermal treatments, on notched and unnotched fatigue specimens. The treatments considered are:

1. Carburising
2. Carbonitriding and ferritic nitrocarburising
3. Induction hardening.

3.2 Carburising

Carburising may be regarded as a process that introduces carbon into a solid ferrous alloy by heating the material in contact with a carbonaceous material-solid, liquid or gas, to a temperature range and holding in that temperature range for a specific length of time. This is normally followed by quenching or some form of hardening treatment, which produces a hard case. The microstructure of surface layers of the case consists of martensite, retained austenite and carbides.

The fatigue strength gradient in carburised steel is partly a result of carbon content of the case increasing from the core to its maximum value at the surface, assuming that decarburisation does not occur. The microstructural constituents retained austenite and carbides, also affect the inherent fatigue strength. The examination of the fatigue limits of the quenched and tempered steels shows that the fatigue limit does not increase significantly with carbon content beyond 0.3% carbon, there being a maximum value of 600 MPa [50]. When compared with a typical level of fatigue strength of carburised and quenched steel, which is 700 MPa [50], it shows that the inherent fatigue strength of the case contributes significantly towards the fatigue strength of case carburised parts. The effect of surface carbon on the fatigue strength is in fact due to increase of inherent fatigue strength.

In the investigation carried out by Fomenko [51] the samples with surface carbon content varying between 0.77% and 1.3% were tested in bending fatigue. The samples were subjected to low temperature quenching prior to tempering which would eliminate effects of other important parameters. The fatigue strength was found to increase from 700 MPa with the surface carbon of 0.77% to 750 MPa with the surface carbon of 0.9%. Further increase in the surface carbon content was not beneficial. The case depth for all samples was between 1.0 - 1.2 mm.

The argument still persists regarding the beneficial or detrimental effects of retained austenite on the fatigue strength of case carburised steels. On the basis of the inherent strength of the material alone the amount of retained austenite seemed to be beneficial as shown by Richman and Landgraf [52] and other investigators [49,53]. Low cycle fatigue tests carried out on high carbon steels in order to simulate the behaviour of the case showed that, in general, samples heat treated to produce lower amounts of retained austenite showed lower ductility and fatigue resistance over the entire life range than the samples with higher retained austenite. Richman and Landgraf [52] suggested that the retained austenite transforms to martensite when subjected to stress or strain. Such a transformation is associated with enhanced ductility because the transformation shear is an extra deformation mechanism. Further, the product martensite itself is more ductile than the thermally formed martensite.

Other investigators [54,55] found an opposite effect of retained austenite on high cycle bending fatigue. Apple and Krauss [54] demonstrated that large amounts of retained austenite, lower surface hardness and the coarse prior austenite grain size that accompany a coarse plate martensite contribute to a lower fatigue strength. Diesburg and Eldis [55] examined several steels with the surface carbon content of 0.8% and 1.0%. In all cases, samples with the surface carbon content of 1% showed a lower fatigue limit than those with 0.8% C. This apparent contradiction was explained by Krauss [56] on the basis of the morphological differences in the martensite-austenite microstructure produced by the variation in carbon content, alloying and/or heat treatment. Examination of microstructural classification of the martensites that form in Fe-C system shows that high carbon (>1%) austenite forms plate martensite on transformation. Low carbon (<0.6% C) austenite forms lath martensite. A mixture of lath and plate martensite is present if austenite with carbon content between 0.6% and 1.0% transforms. The plate martensite is associated with large amount of retained austenite and microcracks. The transformation of high carbon austenite thus results in two constituents which have opposite effects on the fatigue properties. In the reports cited [49,51-55] the carbon content of the surface was higher than 1%. Thus samples heat treated to produce lower retained austenite may have had microcracks which could result in lower fatigue strength [52]. The samples with higher retained austenite were chemically polished exposing the micro-

crack to the surface which lowered the fatigue strength [54]. Whether the deformation induced transformation of high carbon austenite is associated with microcracks is not known. However, the residual stresses generated due to transformation would improve the fatigue strength. The data collected by Diesburg and Eldis [55] suggests that the decrease in surface carbon content from 0.80% to 0.60% improves the fatigue strength from 770 MPa to 840 MPa. This is also supported by the fatigue tests carried out by Richman and Landgraf [52] which showed that the surface carbon content of 0.76% results in higher fatigue strength than 1.26% C. Whether the improvement is due to a reduction in the retained austenite, as suggested by Diesbury and Eldis [55], or is due to a reduction in the formation of microcracks cannot be established. Data collected by Parish [57] indicates a general trend such that the bending fatigue limit of the case carburised steels falls by about 10% for each 30% of retained austenite. A range of 10% - 25% of retained austenite is suggested as being optimum, provided it is fine and evenly distributed.

The second microstructural feature of the case which affects the inherent fatigue strength of the case is carbides. The effect of carbides in the case was discussed by Fomenko [51], Robinson [58] and Macorski [59]. In general, excess carbide in the form of a discontinuous network was found to have no adverse effect on the fatigue strength of the case carburised parts. Finely dispersed carbides were found to improve the fatigue strength of the case carburised parts.

The second gradient, namely that of residual stress, is affected by factors such as retained austenite, case depth and carbon gradient. The development of compressive residual stresses in a carburised case is complicated and it is necessary to attain the appropriate temperature profiles in the specimen at the end of the carburising. Under such conditions a sequential transformation from the core to the surface will occur. The surface having the maximum amount of carbon will transform to martensite last and will develop compressive residual stress.

Koistinen [60] pointed out that the failure of austenite to transform during quenching means that the volume expansion which accompanies the austenite to martensite transformation will not occur. Therefore, it can be envisaged that the development of residual stress will be, in some way, related to the amount of retained austenite in the carburised case, i.e. the higher the retained austenite, the lower the compressive residual stresses. Maximum volume change and therefore maximum compressive residual stress will be observed at some distance below the surface where the martensite transformation will be essentially total. As pointed out before, the retained austenite transforms to martensite when subjected to stress or strain. This, in effect, changes the residual stress distribution during the test performed to determine the fatigue strength. The residual stresses generated during the transformation are compressive and increase the fatigue strength of the case carburised part. The values of the residual stresses generated by the strain induced transformation were found to increase

with the amount of retained austenite [52]. Diesburg[61] evaluated the residual stress distribution in two case carburised steels. The values of the residual stresses were plotted against the retained austenite at the same location. Though the plot showed a poor correlation it indicated that the locations where retained austenite was large did not develop large compressive residual stress. However, it was also found that a low level of retained austenite did not guarantee a high compressive residual stress. It was suggested that the retained austenite contents in excess of 45% should be avoided, as such an amount may generate a tensile residual stress, which would reduce the fatigue strength.

Coleman and Simpson [62] examined a series of variables to establish their effects on the residual stress distribution in the case carburised steel. It was found that, in general the highest stresses were developed with the lower core hardness material. Increasing the case depth increased the depth of the stressed layer. Tempering, even at moderately low temperatures, reduced the compressive residual stresses. The data collected by Ebert [63] also showed that increasing the case depth, increases the maximum compressive residual stress, though the value at the surface remains the same. The increase in compressive residual stress values and an improved residual stress distribution due to increased case depth is generally reflected in improved fatigue strength. The

influence of case depth on the fatigue properties of the case carburised samples was discussed by DePaul [64], Aida et al[65] and Raj and Dhar [66]. Aida et al[65] and Raj and Dhar [66] found that the bending fatigue limit shows a maximum which is associated with a particular case depth and case/core ratio. DePaul [64] compared fatigue limits for two case depths and found that the bending fatigue limit increases with the case depth. This behaviour was explained on the basis of residual distribution, though it was not supported quantitatively. It was suggested that for case depths lesser than the optimum, the location of maximum tensile stress occurs in the core. Thus the fatigue strength of the core controls the effective fatigue strength. For a case thicker than the optimum, the transformation characteristics could develop tensile residual stresses and form microcracks, thus reducing the fatigue strength. Data collected by others [1,67] suggests a similar trend of increase in the fatigue strength with the increasing case depth. It is pointed out however that the trends should be examined in conjunction with the case/core ratio.

Only a few investigators have carried out a systematic investigation of the effect of case carburising on the stress concentration of increasing severity. Data collected by Frost et al [1], Child [50], Mattson and Robinson [67] and Forrest [68], essentially refers to geometries with stress concentration factor values less than 3. It suggests that the notched condition is more favourably affected than

a plain sample. On the notched specimens the improvements of between 82% and 230% were observed compared to unnotched specimens where the improvements ranged between 32% and 105%. A typical level of the fatigue strength in a case carburised sample was quoted as being 500 MPa for a K_t of 3.0 [50]. The rotating bending tests carried out by Raj and Dhar [66] on the case carburised specimens with stress concentration factors varying between 1.2 and 2.2 showed a decrease in the fatigue strength from 590 MPa to 400 MPa.

3.3 Carbonitriding and Ferritic Nitrocarburising

Both the processes involve simultaneous diffusion of carbon and nitrogen into the surface of the material being processed. Conventional carbonitriding is carried out in the austenitic, ferritic condition at temperatures between 800°C - 950°C. The microstructure of the surface layer of a carbonitrided component consists of martensite, retained austenite, carbides, nitrides and carbonitrides. These latter components, nitrides, carbonitrides and carbides can only be resolved with electron microscopy.

The fatigue strength gradient in the case of a carbonitrided sample will be partly due to the variation in the carbon and nitrogen and the microstructural variation due to heat treatment. The retained austenite found in the case of a carbonitrided sample is higher than the case of a carburised sample for the same level of carbon content. The higher amount of retained austenite has been found to be beneficial to the fatigue properties [69-76]. The bending fatigue test carried out on the gear teeth showed that the increase in

the retained austenite from 20% to 53% resulted in the increase in the fatigue limit from 680 MPa to 1000 MPa[74]. The residual stress distribution in the case of carbonitrided components was studied by Diament [70] and Ericsson [71]. In general, low retained austenite contents in the surface layers were found to be advantageous for low cycle fatigue applications [71].

The fatigue properties of carbonitrided parts were determined by many investigators [69-75]. Improvements in the fatigue limits of between 60% and 100% were obtained on plain specimens tested in rotating bending. For notched samples improvements between 100% and 240% were reported [70-73]. It was suggested that the subsurface defects associated with excessive surface nitrogen contents (>0.5%) should be avoided, as they are detrimental to the fatigue properties [71,73,74,75].

The ferritic nitrocarburising treatment is carried out mainly on mild steel in as rolled or normalised condition. The fatigue properties are found to improve if quenching succeeds the treatment to retain nitrogen in solid solution in steel. The treatment temperature is usually 570°C. The process develops a thin layer of (10 μm to 20 μm thick) iron carbonitrides [$Fe_2(CN)$]. This layer has virtually no effect on the fatigue strength [77]. In addition to the ε-carbonitride [$(Fe_2(CN)$] layer, a 'diffusion zone' is also present due to diffusion of nitrogen into the steel. On the optical metallography basis this layer is indistinguishable from the untreated steels, as the nitrogen is

largely retained in the solid solution. A low temperature nitride 'α' ($Fe_{16}N_2$) precipitates during the ageing of the sample at the room temperature. This precipitate, along with the compressive residual stresses generated during quenching, is responsible for the increase in the fatigue strength [72,77,78]. The effect of the thickness of the diffusion layer on the fatigue properties was evaluated by Sachs and Clayton [78]. The increase in the depth of the diffusion layer from 0.076 mm to 0.2 mm increased the bending fatigue limit by 150%. The fatigue limit of nitrocarburised sample with 0.076 mm case depth was found to be equal to the fatigue limit of the hardened and tempered sample. The rotating bending fatigue tests carried out by Bavaro et al [80] on nitrocarburised plain samples with different case depths showed an improvement of 30% with the maximum case depth over a hardened, tempered sample. Similar improvements in the fatigue limit were reported by many investigators, as a result of nitrocarburising [72,77-82]. In general, the improvement in the bending fatigue limit due to nitrocarburising a plain sample is between 80% to 150%. The rotating bending fatigue strength of notched specimens after nitrocarburising was reported by Ito et al [81]. For the stress concentration factor increased from 1.4 to 3.57, the fatigue strength decreased from 460 MPa to 320 MPa. In general, the fatigue limit increase due to the treatment ranged between 140% and 205%. Similar improvements are also reported by Kiessling [72] and Bavaro et al [80], for a stress concentration factor of 2.2, the improvement increasing with the depth of diffusion zone.

3.4 Induction Hardening

The improvement of fatigue strength of steel by induction hardening is a consequence of the microstructural changes and residual stresses induced by the volume changes. Since no compositional change occurs, the fatigue strength gradient will be dependent on the microstructural variation in conjunction with the composition of the steel itself. The compressive residual stresses generated at the surface generally result in a higher bending fatigue strength, but the tensile residual stresses generated at the case-core interface can be harmful. Kern [83] proposed that for the induction hardened layer to have a compressive residual stress, the minimum depth of the hardened layer should be 2.00 mm. The microstructure should contain 90% martensite with no ferrite visible in the microstructure at a magnification of 500. Nishioka [84] showed that tempering after induction hardening results in a considerable decrease in the bending fatigue strength, which was attributed to a reduction in compressive residual stresses due to tempering. Hayashi [85] investigated the effect of case depth in the bending fatigue strength of the induction hardened component. The rotating bending fatigue strength showed a maximum at a case depth of 3.00 mm, though higher residual stresses were observed at the lesser case depths. This behaviour was attributed to the combination of microstructure, which was completely martensitic, and the compressive residual stresses present. Yamada et al [86] investigated the micro-structural effects on the fatigue behaviour of induction

surface hardened steel. It was shown that the retained ferrite in the microstructure governs the fatigue behaviour. The slip markings,and the microcracks were found to originate in the retained ferrite. The first slip marking appeared when about 1% of the life was spent. A typical level of bending fatigue strength of a surface induction hardened plain sample is 600 MPa which is 20% to 50% improvement in comparison with hardened tempered specimen [50].

3.5 Engineering Analysis of Case Hardened Steel

Most of the investigations to evaluate the fatigue resistance of surface hardened members have concentrated on the case carburised components [49,58,87,88,89]. The models and the technique developed can be easily extended to other surface hardening techniques. Krotine et al [87] and McGuire et al [49] approached the problem by viewing the surface hardened component as a composite consisting of a high strength low,ductility case and a higher ductility, low strength core. Though a simplified view, it is a reasonable starting point for understanding the behaviour of case hardened components.

The relative importance of the case and core properties and the depth of case will vary with the type of loading. In simple tension or shear, where the load is uniform throughout the cross-section, the behaviour of the case hardened component will be limited by the core properties, especially in HCF region. The core yielding constitutes failure in some applications. Thus an improvement in core

properties will result in increased load carrying capacity. Another method of improving the fatigue strength is to reduce the tensile residual stresses in the core by optimising the case:core ratio.

If loading is such as to produce a stress which varies from the surface inwards (torsion, bending) case depth and core hardness may be of considerable importance and must be considered together. The relationship of case depth and core strength in this type of loading is shown schematically as suggested by Woodvine [88]. Figure 5 shows a limiting stress condition, where the applied stress just equals the fatigue strength at the case-core junction. Obviously, an increase in either the case depth or the core fatigue strength will increase the load carrying capacity of the part. It was also suggested by Woodvine[88], that the optimum case depth could be calculated on the basis of equal probability of failure in the case and the core. At such a limiting condition the applied stress will equal the fatigue strength of the core at the case-core junction and simultaneously equal the inherent fatigue strength of the surface. This condition stems from the fact that the maximum stresses occur at the core-case interface and at the surface for the core and the case respectively. For the geometry in Figure 5

$$\frac{\sigma_{f_1}}{D} = \frac{\sigma_{f_2}}{D-d} \qquad \ldots\ldots\ldots\ldots\ldots\ldots (24)$$

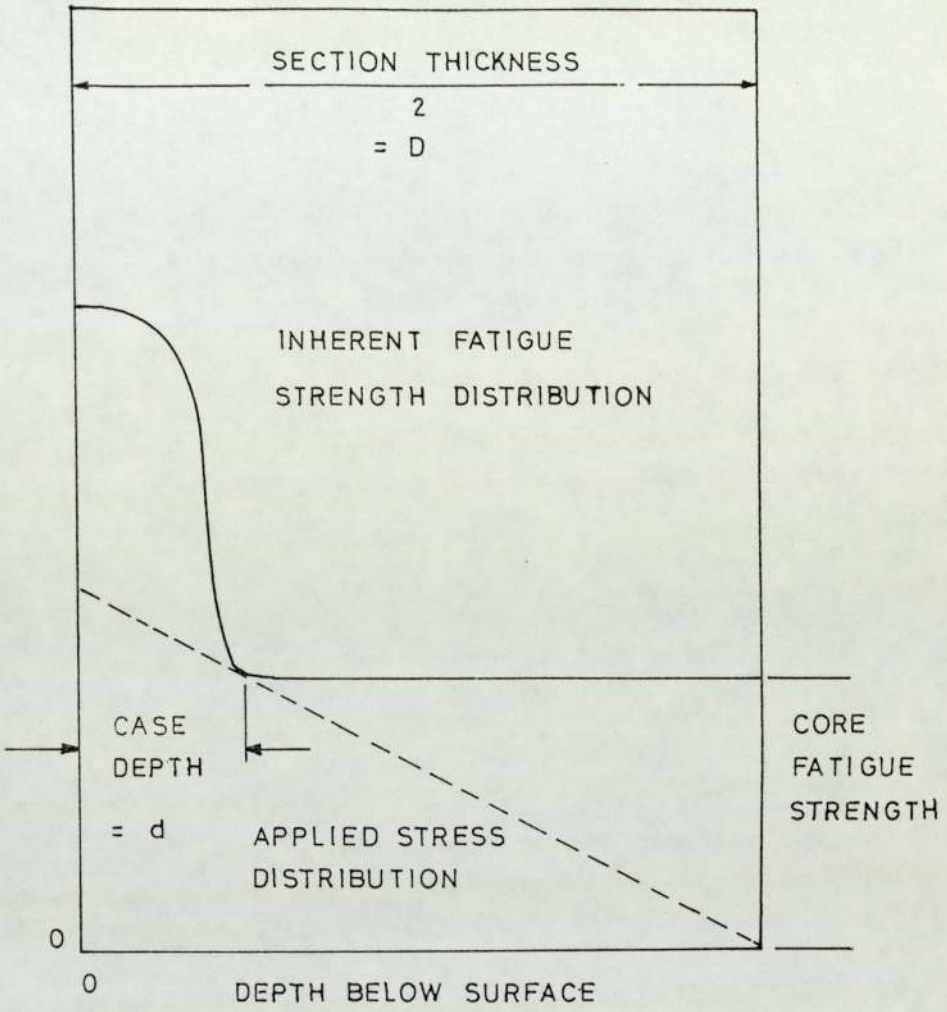

FIGURE 5 Schematic representation of stress patterns in the tension side of a case-carburised bar in bending (88)

σ_{f_1} = fatigue strength of the case

σ_{f_2} = fatigue strength of the core

D = diameter or width of the specimen

d = case depth

rearranging

$$d = D\left(1-\frac{\sigma_{f_2}}{\sigma_{f_1}}\right) \qquad \text{.....(25)}$$

In addition to the variation in material fatigue strength observed throughout the cross section of a carburised part, volume changes associated with case hardening generate residual stresses, which vary in a somewhat opposite manner to the fatigue strength gradient, as shown schematically in Figure 6, curve a. Robinson incorporated the residual stresses in the Woodvine analysis. It can be seen that the allowable applied stress in the component increases considerably. It was suggested that the redistribution of residual stresses is necessary when stresses in excess of the yield strength are present at any one point in the component, before this method is applied [58].

Landgraf and Richman [89] combined Woodvine [88] and Robinson [58] approach to estimate the optimum case depth for a plain bar. A modified form of the Basquin relationship (equation 1) was used to describe cyclic behaviour of the case and core

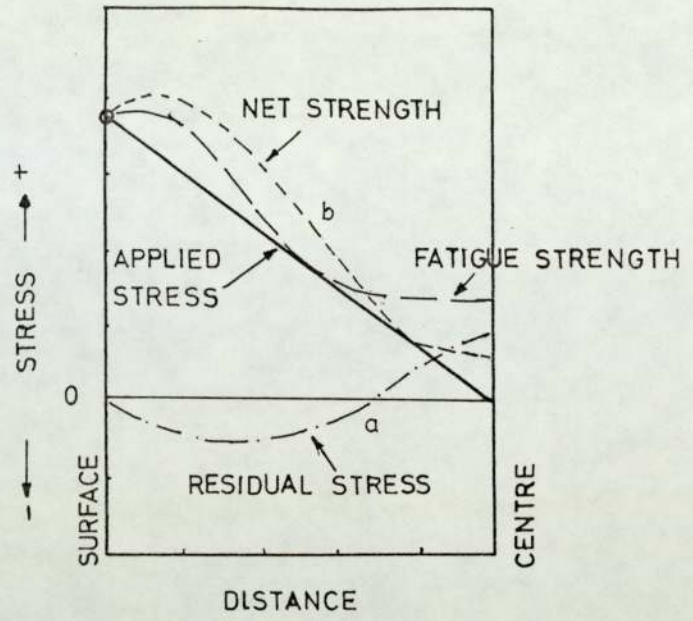

FIGURE 6 Schematic representation of stress-distribution in a case-carburised bar subjected to bending (58)

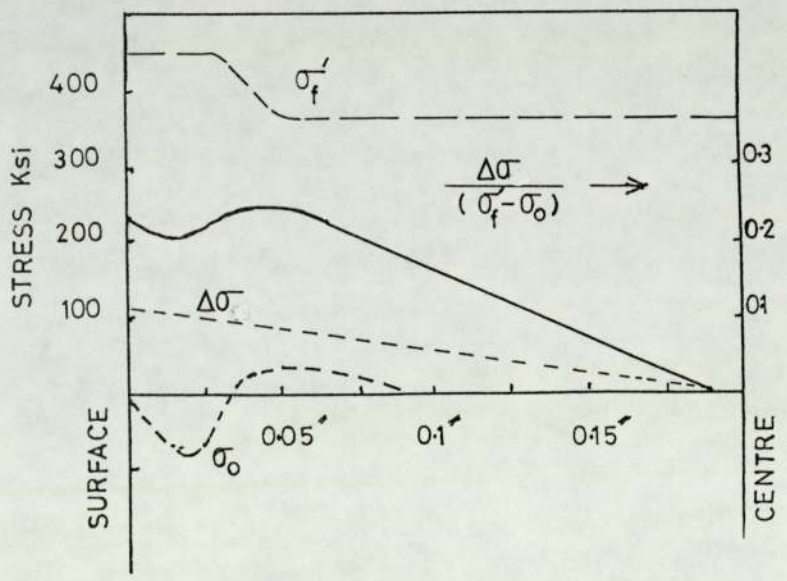

FIGURE 7 Stress-strength profiles for carburised bend specimens (89)

$$\Delta\sigma = (\sigma_f' - \sigma_o)(2N_f)^b \quad \text{.....(26)}$$

where σ_o = mean stress or residual stress

Two independent equations can be written for the case and the core

$$(2N_f)^b = \left| \frac{\Delta\sigma}{\sigma_f' - \sigma_o} \right|_{\text{core}}$$

$$(2N_f)^b = \left| \frac{\Delta\sigma}{\sigma_f' - \sigma_o} \right|_{\text{case}}$$

The value of b is independent of the microstructure and the composition of the steel. Using the Woodvine approach of equal possibility of failure

$$\left| \frac{\Delta\sigma}{\sigma_f' - \sigma_o} \right|_{\text{core}} = \left| \frac{\Delta\sigma}{\sigma_f' - \sigma_o} \right|_{\text{case}} \quad \text{.....(27)}$$

Thus

$$\frac{\Delta\sigma_{\text{core}}}{\Delta\sigma_{\text{case}}} = \frac{\sigma_f' - \sigma_o \text{ core}}{\sigma_f' - \sigma_o \text{ case}} \quad \text{.....(28)}$$

Under bending conditions the maximum stress in the core will occur at the surface, and at the case-core interface, for the case and the core respectively. Therefore the right hand side of equation 28 is in fact a ratio of $\sigma_{f_1} / \sigma_{f_2}$. Substituting in equation 25

$$d = D\left(1 - \frac{(\sigma_f' - \sigma_o)_{\text{core}}}{(\sigma_f' - \sigma_o)_{\text{case}}}\right) \quad \text{.....(29)}$$

This formula correlated well with the results for the optimum case depth. The assumptions on which the formula is based need a careful examination. Equal possiblity of failure assumes that equation 27 is valid. This may not be the case. Further, it is necessary to know the distribution of σ_f' and σ_o for the optimum case depth. This means that it is an iterative process. Moreover, the value of $\left[\frac{\Delta\sigma}{\sigma_f' - \sigma_o}\right]$ should not only be maximum but should exceed particular values at both the locations depending on the inherent fatigue strengths and the number of cycles to failure. However, this approach is more progressive in nature as the failure diagram is valid over all the HCF range, unlike the Woodvine [88] or the Robinson [58] approach where a new diagram needs to be established for each point in HCF region.

All the three approaches [58,88,89] discussed predict the initiation at or below the surface depending on the effective stress distribution. The fatigue crack is supposed to initiate at that location where the applied stress just equals the fatigue strength plus the residual stress as shown in figure 6, curve b, or where $(\frac{\Delta\sigma}{\sigma_f' - \sigma_o})$ is maximum, figure 7. Other investigators [67, 71,75,90,91,92] have also reported subsurface fatigue crack initiation in case hardened steels. The examination of the reports shows that subsurface crack initiation occurs essentially at long lives. It means that yielding of the core is unlikely. The subsurface initiation occurrence is independent of the type of loading, i.e. it is found to occur under axial tension, bending, rotating

bending and torsional fatigue. Further, the initiation fatigue crack is found to occur around an inclusion [58, 67,89,90,92]. Moveover, the location of initiation is near the case-core junction or in the core. Most of the investigators explain this behaviour by comparing the fatigue behaviour of the case and core material. It is found that the S-N curves for the case and the core, established by testing steels which simulate case and core material, cross each other at a particular level. In the HCF region, i.e. when stresses are lower than the stress at the cross-over, the simulated case shows higher fatigue properties than the simulated core. The explanations of the subsurface crack initiation based on the residual stress distribution are inconclusive as the residual stress distribution cannot be established for the same sample.

3.6 Summary

The main object of the heat treatment is not only to increase the surface hardness, but also to employ a correct process which produces a hardened contour of sufficient depth to carry contact loads and leaves a residual stress system which favours a high bending resistance. These constraints are further complicated by the presence of a geometric discontinuity and when close tolerances are required.

Thus no one treatment can be regarded as universal. Carburising is used for applications involving high bearing pressure, whereas carbonitriding has special merit that the hardened case resists tempering and the

wear resistance is higher than the carburised part. Ferritic nitrocarburising can develop high scuffing resistance under lubricant starved conditions even when low carbon unalloyed steels are used. Fillet induction hardening can give greatly improved fatigue resistance with a carbon steel at the same time maintaining a close dimensional tolerance. From the literature discussed, it becomes clear that the data collected does not help the designer to choose the best possible treatment though it can serve as a guideline. Comparative fatigue data for different heat treatments are presented in Table 2.

By investigating the fatigue behaviour of carbon steels, case hardened by different treatments, it will be possible to choose a cheaper steel suitable for a specific purpose. The proposal by Landgraf and Richman [89], to calculate an optimum case depth could be used as a starting point. In engineering design where the stress concentrations of varying degree are encountered, whether such an optimum case can be established analytically, is not known. By extending the fracture mechanics approach to the initiation and propagation of a fatigue crack to the case hardened components, it may be possible to overcome this difficulty.

TABLE 2 ROTATING BENDING FATIGUE STRENGTH OF CASE HARDENED STEELS

Treatment	Typical level of Fatigue strength MN/m^2		Change in the fatigue strength due to heat treatment	
	Plain	Notched	Plain	Notched
Carburised	770	550	32-105	82-230
Carbonitrided plain carbon	690	470	60-100	100-240
Ferritic nitrocarburised mild steel	550	300	80-150	140-250
Induction hardened	600	-	20-50	

Notch strengths are achievable with stress concentration factors up to about 3

4. FATIGUE CRACK MONITORING

4.1 Methods of Detection

There are many methods available for detecting fatigue crack initiation and measuring fatigue crack growth. These include

1. Acoustic emission
2. Electrical potential methods
3. Infra red crack detection
4. Optical measurement
5. Strain gauges
6. Ultrasonic measurements.

At the present time the most popular method appears to be the electrical potential method. Other methods listed above suffer from disadvantages either in detection sensitivity, reproducibility, difficulties in specimen preparation or the extensive or expensive peripheral equipment required. Further, they are unsuitable for continuous measurement of crack length.

4.1.1 Electrical Potential Methods

At present two methods are available for continuous measurement of crack length.

1. Direct current potential drop, DCPD
2. Alternating current potential drop, ACPD.

The electrical potential method is based on the fact that a growing crack alters the potential distribution in a specimen, through which a constant current is being passed.

This change in the potential distribution can be measured in terms of the potential difference across the crack faces as it grows and then related to the instantaneous crack length (or area). A calibration curve can be established, relating the potential difference measured to the instantaneous crack length, which can be used as a standard for subsequent tests. The calibration curves can be developed by experimental techniques [93,94,95] or using theoretical methods [96,97,98]. A review of these methods was done by Holder [35]. It was pointed out that the calibration curve is a complex function of specimen geometry, position of probes, electrical current magnitude and mode of application, material and potential measurement equipment.

The effect of the various factors mentioned above could be summarised as follows. The electrical potential distribution is analogous with the stress distribution. Any factor which changes the stress distribution can therefore be expected to change the potential distribution. The presence of a notch in a finite geometry therefore affects the calibration curve significantly [99]. For maximum sensitivity and reproducibility, the best probe positions are across the notch or crack faces, farthest away from the notch or crack tip [100]. The creation of approximately parallel equipotential lines by application of current farthest from the zone of perturbance results in optimum sensitivity and reproducibility [98]. The magnitude of current used is dependant on the material under consider-

ation, e.g. a material with low resistivity like aluminium needs a higher magnitude of current than steel to achieve the same probe potential difference. The magnitude of current between 10 amperes and 50 amperes is suitable for most materials. Such a magnitude is also found to keep heating effects and subsequent variation in the potential difference to a minimum. The potential developed across the crack faces is between 200 μv and 1000 μv for the current ranges specified above. A voltage offset source is therefore necessary so that the increase in the potential can be measured with maximum sensitivity. An instrument or a chart recorder with a full scale deflection of 50 μv can be regarded as suitable for this purpose.

A lack of universally applicable potential-crack length calibration can thus be attributed to the factors mentioned above. Further, the experimental or theoretical methods refer to a crack in a two dimensional body [93-98]. To ensure that the notch shape and the thickness of the body are taken into account, establishment of an experimental calibration using actual size specimens is essential. It is necessary therefore to obtain an accurate experimental calibration before attempting any study of initiation and growth of fatigue crack.

Alternating current potential drop method (ACPD) has been developed recently and has an enormous advantage over

direct current potential drop methods (DCPD) when the crack growth is to be monitored in large structures. Since the alternating current used to monitor the crack growth has a frequency of 8 KHz, the current is carried in the skin of the metal only and so relatively small currents and small power sources are required. However, induced currents present many problems. A careful examination of all the factors which affect the alternating current potential calibration curve is therefore necessary.

4.2 Problems Associated with Monitoring Initiation and Early Growth of Fatigue Crack from Notches

A crack is viewed to have been initiated when it is approximately 0.5 mm long and 0.15 mm deep (Figure 8). When a component is subjected to stresses near the fatigue limit, the fatigue crack initiates only at one position, but at higher stresses multiple initiation is found to occur [11,13]. The nucleated cracks generally have an elliptical shape, which subsequently becomes semicircular [13,101]. If the initiation and growth of the fatigue crack is monitored by the electrical potential method, whether the increase in potential refers to the maximum depth or to an average depth is not known, since the three dimensional theory of electrical potential distribution has not been developed. With multiple nucleation the problem becomes much more complicated. The theoretical calibrations mentioned earlier are unsuitable as these do not account for variations in shapes of cracks or multiple

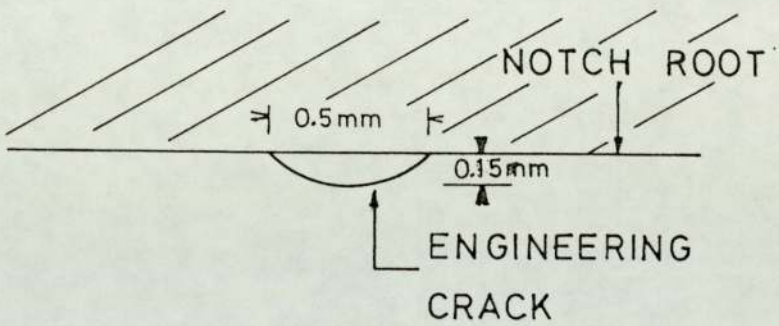

FIGURE 8 Schematic diagram of an engineering crack

cracks. Further growth in the case of multiple nucleation merges the cusps and a through thickness crack forms early in the total life of a component. The crack front in such a case will be straight, at least on macroscopic scale, from early stages. (It should be noted that these comments need not always apply to a component with a circular cross section.) Moreover, the fatigue crack front does not progress as an entity, but small pockets of striations emanate from the macroscopic front which at any instant is irregular. Such behaviour may not affect measured macroscopic crack growth significantly at long crack lengths, where the shape of the crack front could be assumed to be straight. However, for a small thumbnail crack at the notch root differences in the crack growth rates, if different at various points along the crack front, could affect the macroscopic crack growth rate significantly. Whether a macroscopic crack growth rate can be defined for such a crack is open to question. If the electrical potential technique is employed to monitor the growth of such a small crack, the increase in potential measured seems to relate to the increase in the area of the crack. The experimental calibration therefore refers to a through thickness crack which has the same area as that of the cusp or cusps. The calculated crack growth rate would therefore refer to such a crack rather than the actual cusp or cusps. Improved resolution or sensitivity of electrical potential technique will not be of much assistance as it cannot define the shape of the crack front.

Another factor which affects the electrical potential increase significantly in the early stages of crack growth is the plasticity at the tip of the notch. The effect of plastic zone size on the potential increase was discussed by Plumbridge [102]. It was suggested that the crack growth increment Δa was the sum of true crack extension Δa_T plus a fictitious increment Δa_p due to plastic deformation at the notch tip. Δa_p was found to vary with the plastic zone size and the material, i.e. for two materials with the same plastic zone size, Δa_p will depend on the change in the resistivity. The change in the resistivity itself depends on the amount of plastic deformation and for the same amount of plastic deformation, one material shows higher change in resistivity than the other. For the same plastic zone size, Δa_p constitutes as much as 80% of Δa for materials which show higher changes in the resistivity with the plastic deformation.

Thus, before employing the approaches currently used to analyse stage II crack growth data to early crack growth from notches a careful examination of the conditions under which such an analysis is done should be carried out.

5. EXPERIMENTAL WORK

5.1 The Materials

The steels chosen for this experimental programme were 080M15 (En32) and 080A47 (En43B). These steels were chosen as they are commonly used case hardening steels for low priced end products.

The compositions, as determined by wet chemical analysis and the mechanical properties of untreated materials are presented in Table 3. The uniaxial tensile properties were obtained using No. 13 Hounsfield tensile test pieces tested in a Hounsfield tensometer at a cross head speed of 0.1 cm/min.

5.2 Heat Treatment

The specimens were case hardened by four different case hardening techniques. 080M15 (En32) was case hardened by chemico-thermal method, viz. carburising, carbonitriding and nitrocarburising. 080A47 (En43B) was induction hardened.

5.2.1 Chemico-thermal Method

The specimens of 080M15 (En32) were gas-carburised by Joseph Lucas Industries using industrial case hardening methods. The two case depths chosen were 0.38 mm (0.015") and 0.76 mm (0.03") for carburising and carbonitriding, which represented the case depths normally encountered in engineering practice [50]. The specimens were case hardened on all six faces. The details are as follows:

TABLE 3

MATERIAL COMPOSITION AND MECHANICAL PROPERTIES

Material	Composition				Mechanical Properties		
	C%	Mn%	Si%	P & S%	σ_{ys} MN/m^2	σ_{UTS} MN/m^2	% El
080M15	0.13	0.55	0.16	0.05 max	465	511	24
080A47	0.46	0.78	0.20	0.05 max	619.4	820.7	17

a. Carburising:

case depth 0.38 mm: 925°C; 1 hour 15 minutes at 1.1% carbon potential. Quench in oil, temper for 1 hour at 160°C.

case depth 0.76 mm: 925°C; 3 hours 15 minutes at 1.1% carbon potential. 15 minutes at 0.8% carbon potential. Quench in oil; temper for 1 hour at 160°C.

b. Carbonitriding:

case depth 0.38 mm: 925°C; 1 hour 15 minutes at 1.1% carbon potential plus 5% NH_3. Quench in oil; temper for 1 hour at 160°C.

case depth 0.76 mm: 925°C; 3 hours 15 minutes at 1.1% carbon potential plus 5% NH_3, 15 minutes at 0.8% carbon potential plus 5% NH_3. Quench in oil; temper for 1 hour at 160°C.

c. Nitrocarburising (Ni-temper)

570°C, 2 hours, 50% endothermic natural gas plus 50% NH_3. Quench in oil.

5.2.2. Induction Hardening

The specimens of 080A47 (En43B) were induction hardened on a Birlec high frequency set. The frequency was 450 KHz, and the power input was between 6 to 9 Kw. A case depth of 2.00 mm was chosen as such a case depth is

normally encountered in practice [50]. The heating time required for this case depth was calculated as follows[50]:

Overall depth of penetration is given by

$$d_o = d_{800} + d_c$$

where d_{800} = the depth of penetration of current at 800°C

d_c = the depth of penetration resulting from conduction

Further, $d_{800} = 500/\sqrt{f}$

where f = frequency of the power supply in Hz,

and $d_c = 0.2 * \sqrt{t}$

where t = the heating time in seconds.

Rearranging

$$t = 25 * \left[d_o - \frac{500}{\sqrt{f}}\right]^2$$

For the required case depth of 2.00 mm this formula yielded a heating time of 39 seconds.

A copper coil (4 mm outer diameter and 2.5 mm inner diameter) was wound to the shape shown in Plate 1. A schematic diagram of the experimental set up is shown in Figure 9. To locate the samples exactly in the same position in coil an asbestos former was used. After the calculated heating time of 39 seconds, the samples were quenched in brine (10% NaCl). The current used was 3½ amperes. For each quenching, new solution was made so as to ensure similar quenching conditions. The use of brine

PLATE 1 Copper coil used for induction hardening

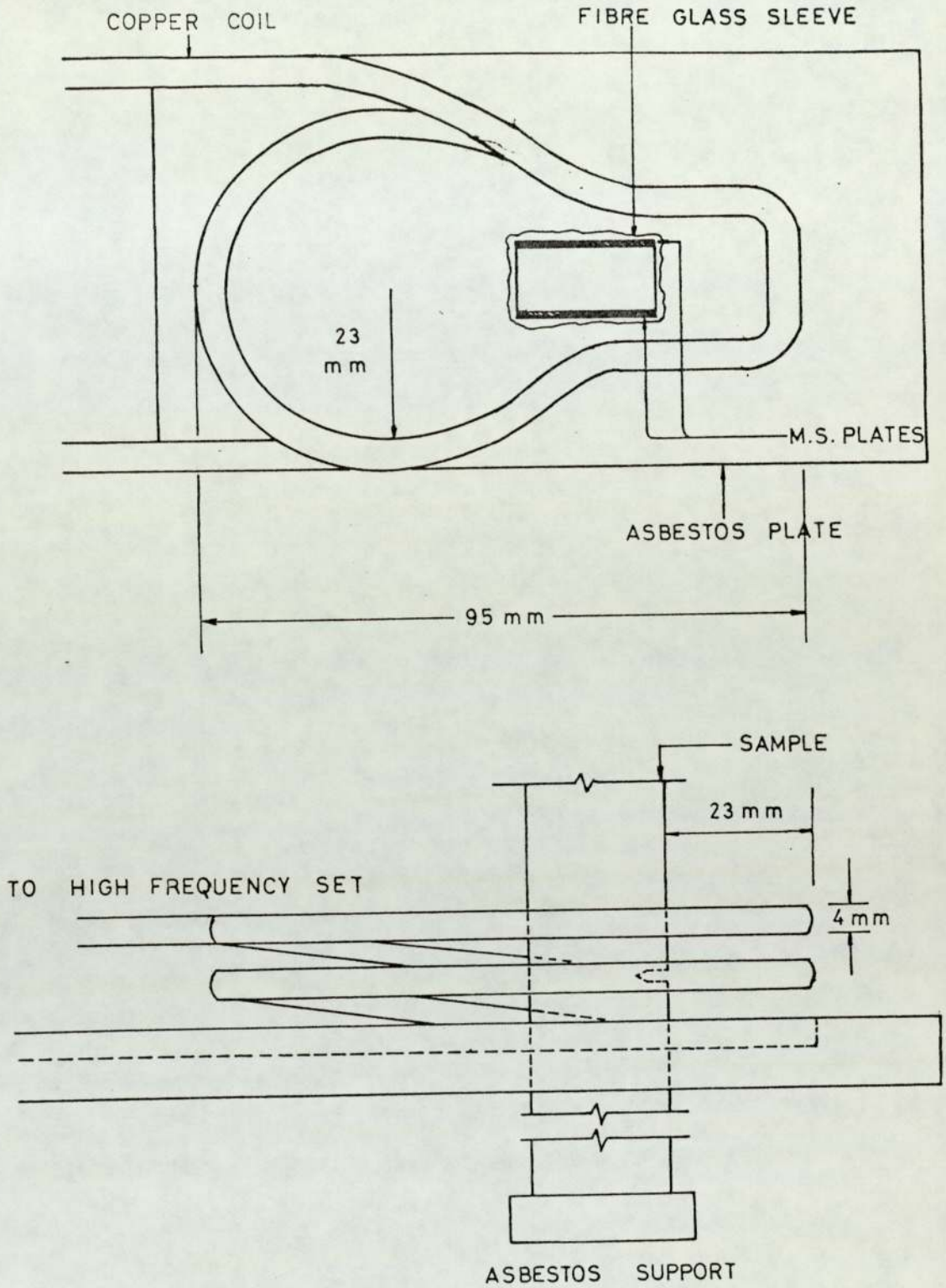

FIGURE 9 Schematic diagram of induction hardening set-up

solution for quenching necessitated manual quenching. The quenching operation took approximately 2-3 seconds.

To complement the formulae used to calculate the heating time and to ensure that the temperature did not drop significantly during the manual quenching operation, the temperature was monitored by a thermocouple. Initially for some samples from each notch group thermocouples were spot welded at the root of the notch and at the mid-section. The temperature was measured using a calibrated chromel-alumel thermocouple. The temperature measured at the root of the notch after a heating time of 39 seconds was 890°C for all samples. The temperature dropped to approximately 870°C after 2 seconds.

Initial experiments showed that the profile of the hardened case at the root of the notch was curved. To obtain a more straight profile, two plates of mild steel (2.5 mm thick), with appropriate notch profiles cut, were placed in close contact with the specimen being induction heated. It was necessary to clamp them together at the ends with glassfibre thermocouple sleeves (Figure 9). Metal clamps could not be used as the metal clamps were simultaneously heated with specimen and the close contact between the specimen and the plates was lost. The specimen was quenched with the plates in position. This ensured that the hardened case had a straight profile below the notch.

All the samples were then tempered at 160°C for one hour.

5.3 The Specimens

The effect of case hardening on the fatigue properties of steel is maximum when subjected to bending loads. The specimens, therefore, were to be tested in three point bending with a central notch.

The specimen dimensions for all the tests in the experimental programme were selected to satisfy two criteria. Firstly, the specimen should be tested essentially under conditions of plane strain. This condition is met when the plastic zone size at the crack tip is less than 2% of the thickness. Further, the plastic zone size in fatigue is one fourth of the monotonic plastic zone size. For both the materials, in treated and untreated conditions, the plastic zone size is calculated according to the following relationship:

$$r_y = \frac{1}{4 \times 5.6\pi} \left[\frac{\Delta K_I}{\sigma_{ys}}\right]^2$$

To establish a maximum value of r_y in fatigue a maximum value of the stress intensity factor range ΔK_I needs to be specified. The maximum value of ΔK_I is generally 60% of the critical value of the stress intensity factor. For the materials under consideration the values of K_{IC} are not known. However, it is known that the values exceed 100 $MN/m^{3/2}$ for the untreated 080M15 and 080A47 in normalised condition. Assuming that the maximum value of ΔK_I is 60 $MN/m^{3/2}$ the above formula produces a minimum thickness requirement of 10 mm.

The second criterion was to achieve the case to core ratios normally encountered in practice. This also stipulates that the thickness should be 10 mm for the two case depths, as stated in previous section. The width of the specimen is normally twice the thickness. The width in the present programme was chosen to be 22 mm. The stress intensity factor calibration curves available [103] are calculated for a span to width ratio of four. This value gave the span length of 88 mm. The overhang requirements [103] dictated that the total length of the sample should be 100 mm.

The notches were designed to represent the range of the stress concentrations factors normally encountered in practice. The notches were essentially deep hyperbolic notches with zero flank angle. The stress concentration factors were calculated by Wood and Richards [104], using finite element technique. The specimen dimensions and the stress concentration factors are presented in Table 4 and Figure 10.

5.4 Design of the Experimental Programme

5.4.1 Fatigue Crack Initiation

In the early stages of work is was decided to correlate the initiation life with a stress concentration parameter $K_t \Delta s$ or a fracture mechanics stress intensity factor range parameter $\frac{\Delta K}{\sqrt{\rho}}$. The fibre stress Δs at the root of the notch was calculated using

TABLE 4

SPECIMEN DIMENSIONS AND STRESS CONCENTRATION FACTORS

Root radius mm	Notch depth a mm	Notch width w mm	K_t
0.13	5	1.5	7.59
0.36	5	1.5	4.65
0.76	5	1.5	3.42
1.52	10	3.05	2.26
3.17	10	6.35	1.69

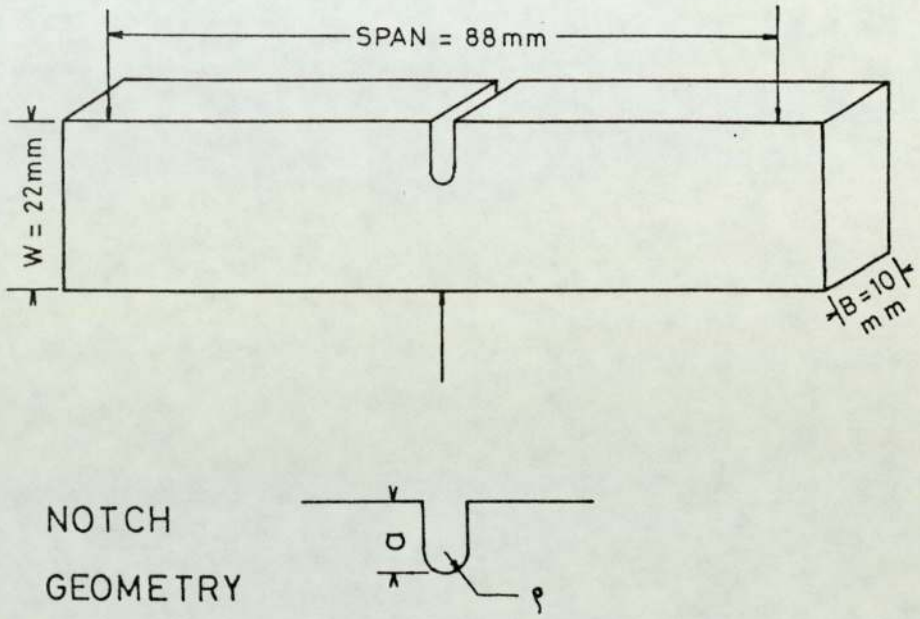

FIGURE 10 Specimen geometry of fatigue specimens

$$\Delta S = \frac{6\Delta PW}{B(W-a)^2}$$

ΔP = load range

W = width of the specimen

B = breadth of the specimen

a = notch depth

The stress intensity factor range ΔK was calculated from the following formula:

$$\Delta K = \Delta P * Y_L * \sqrt{a+c} / (B*W) \quad \ldots\ldots\ldots (30)$$

ΔP = load range

a = notch depth

c = crack length

B = breadth of the specimen

W = width of the specimen

Y_L = stress intensity factor coefficient

$$= \frac{1.99-2.15*(a/W)+6.08*(a/W)^2-6.67*(a/W)^3+2.7*(a/W)^4}{(1+2*(a/W)) * (1-(a/W))^{1.5}}$$

As indicated in the previous section, these factors essentially estimate stress at the root of the notch with root radius ρ. Previous work on the case hardened steels has been presented in the form of an S-N curve. After examination of the S-N curves of untreated and treated materials under consideration, it was decided that the majority of tests should have a finite fatigue life, preferably less than 10^6 cycles.

The minimum stress range Δs should be such that $K_t \Delta s$ was not less than 110% of the uniaxial fatigue limit of the material. Further, the lower limit for the factor $\frac{\Delta K_I}{\sqrt{\rho}}$ was calculated from [105]:

$$\frac{\Delta K_{th}}{(\sigma_{ys})^{2/3} * \sqrt{\rho}} = 5.0$$

for the steels with σ_{ys} between 276 MN/m^2 and 965 MN/m^2. The minimum value of the load range ΔP was selected so as to satisfy both the conditions.

The maximum value of the load range ΔP was such that the value of the fibre stress at the root of the notch was less than the net section yield stress; calculated using the following equation:

$$P_L = 1.216 * \sigma_{ys} * \frac{B(W-a)^2}{4W}$$

Thus the minimum value of load range for a 5 mm deep notch was approximately 2000 Newtons and the maximum value was 19000 Newtons. The two limits on the stress range having been determined, intermediate values were selected such that entire second stage crack growth range was covered.

5.4.2 Fatigue Crack Propagation

The determination of the stress intensity factor coefficient as indicated in section 2, the crack growth rate data should be obtained over as wide range as possible

so as to estimate the values of constants in the Paris equation as accurately as possible. The samples with the smallest root radius were chosen for this purpose. The upper limit of the second stage of the fatigue crack growth rate is dependent on the cyclic fracture toughness of the material. As stated before, the maximum value of the stress intensity factor range ΔK_I was 60 $MN/m^{3/2}$. The fatigue crack growth threshold in steels occurs around 5 $MN/m^{3/2}$. The test performed at such a low stress intensity factor range have very low crack growth rates. A minimum ΔK of 10 $MN/m^{3/2}$ was therefore selected for tests on specimens with a notch root radius of 0.13 mm and proportionally higher values for blunter notches.

Due to the size of the specimen it was not possible to measure the fatigue crack growth rates for the whole range of the stress intensity factor range ΔK. Therefore, the load ranges were chosen so that the maximum value of ΔK for one group of specimens became starting value of ΔK for the next. The crack growth rates in the first one mm of crack were ignored as the intensity factor coefficient for short cracks eminating from notches was not known. The value of the parameter was calculated using equation (30).

5.4.3 Fatigue Crack Initiation and Propagation in Case Hardened Specimens

To assess the effect of case hardening treatments on the threshold values of $K_t \Delta s$ or $\frac{\Delta K}{\sqrt{\rho}}$ for initiation of a fatigue crack a complete factorial experiment was run. Each test

was triplicated for each combination of geometry and the heat treatment. The procedure explained in section 5.4.1 could not be followed as the values of yield strength are not available or could be evaluated. Thus to start with the starting value of load range was calculated assuming only 50% improvement in the threshold value of the stress intensity factor parameter $\frac{\Delta K_I}{\sqrt{\rho}}$ or the stress concentration parameter $K_t \Delta s$. The test was then run for 1,000,000 cycles. If the initiation of fatigue crack was not observed then the load range was increased by 5% of the previous load or by 200 Newtons, whichever was minimum and the test run for 1,000,000 cycles. (The load increments lower than 200 Newtons were not possible on the machines used). The procedure was repeated till initiation of fatigue crack was observed.

For the nitrocarburised materials however, the fatigue strength improvements reported in the literature are not as high as those observed in carburising or carbonitriding. Thus an improvement of only 30% was assumed and the procedure described above was repeated.

5.5 The Equipment and Test Methods

5.5.1 The Equipment

The fatigue tests were carried out in three point bending in a $\pm$20 KN, Amsler Vibrofore and on a $\pm$50 KN capacity electrohydraulic machine (Servotest 177-F8). The wave-form in both cases was sinusoidal. The test frequency

in Amsler Vibrofore was 85 Hz, whereas in servohydraulic machine was 20 Hz. In both cases the fatigue machine and other equipment was switched on for at least 30 minutes before start of a test. This was necessary to ensure complete thermal and electrical stabilization of the electrical and electronic systems.

The initiation and the propagation of the fatigue crack was monitored by measuring the potential difference across the notch faces. The constant current supply necessary for this purpose was Farnell (F2111M 7/50 ST), with an output variable between zero and 50 amperes. A current of 30 amperes was chosen so as to obtain maximum sensitivity and minimal heating in the specimen and at the contacts.

The current was introduced in the specimen using tool makers clamps covered with 1 mm thick annealed electrical purity copper. Welding cable was then brazed to the copper cladding on the tool makers clamps, other end of which was brazed to a 1 mm thick copper sheet for attaching to the power supply. The clamps were then attached to either ends of the specimen. The specimen was insulated from the machines by placing bakelite pieces between the knife-edges and the machine.

To measure the potential, 0.15 mm diameter nichrome wire was spot welded to the specimen. The wires were spot welded at either side of the notch opening (Figure 11). This particular position was chosen as it was shown to

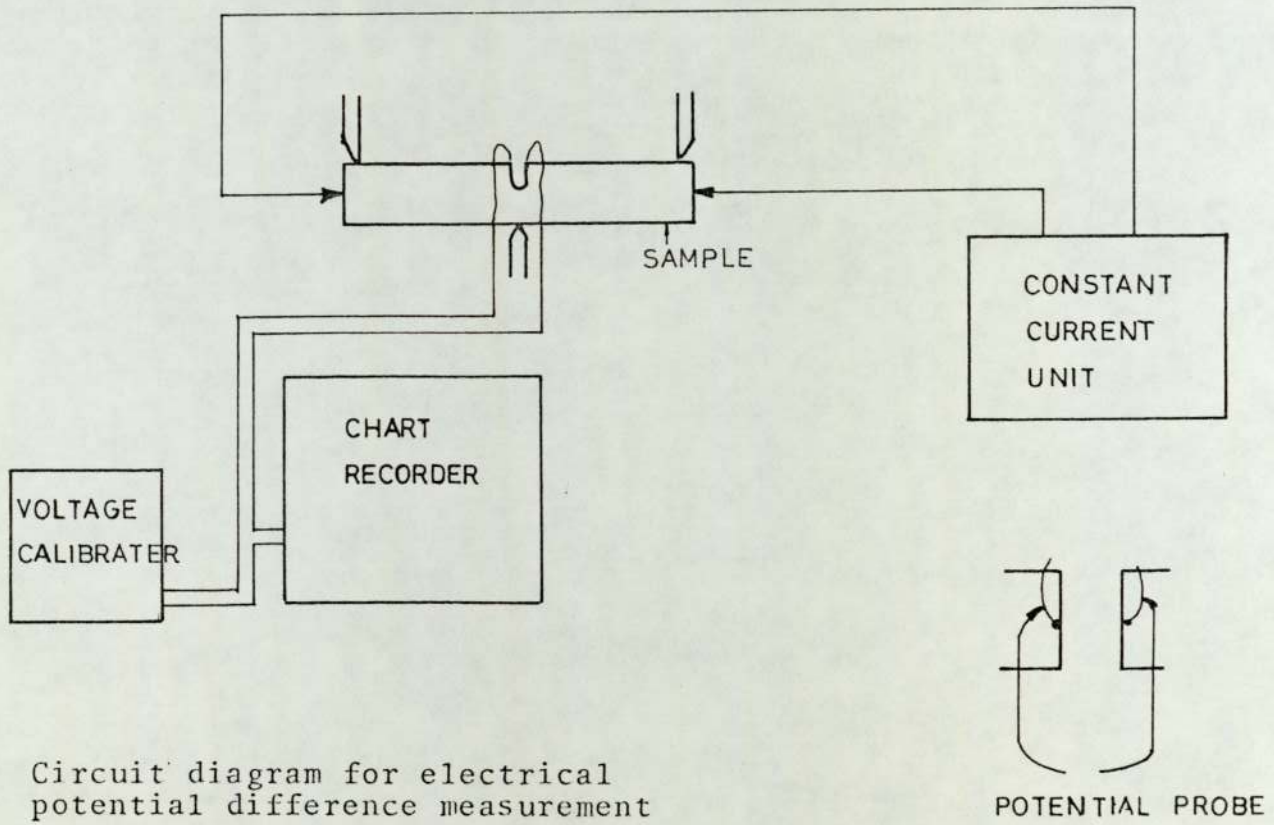

FIGURE 11 Circuit diagram for electrical potential difference measurement system

achieve maximum sensitivity and minimum effect of plasticity at the root of the notch [99].

The voltage was measured using a direct current chart recorder (Tekman 200) with a maximum sensitivity of 0.5 μv and 50 μv full scale deflection. The potential difference across the notch was found to depend on the notch depth and root radius, e.g. for a notch depth of 5 mm and root radius of 0.13 mm, the potential difference was 300 μv. This was opposed by a variable millivolt source (Time electronics Type 2003, %0.006), so that the further increase in the potential difference could be measured with the maximum sensitivity available on the chart recorder. The power supply source and Tekman chart recorder was switched on with the fatigue machine to ensure electrical stabilization.

A general view of the fatigue (servotest) machine and other equipment used is shown in Plate 2. A closer view of the specimen complete with the potential leads and clamps, in the three point bend rig is shown in Plate 3. A schematic diagram of the electrical system to measure the potential difference is as shown in Figure 11.

5.5.2 Test Methods

5.5.2.1 Specimen Preparation

All the specimens were lightly polished with a silicon carbide paper down to 400 grade finish. Small amounts of flash in the notch were removed, if present. The notch

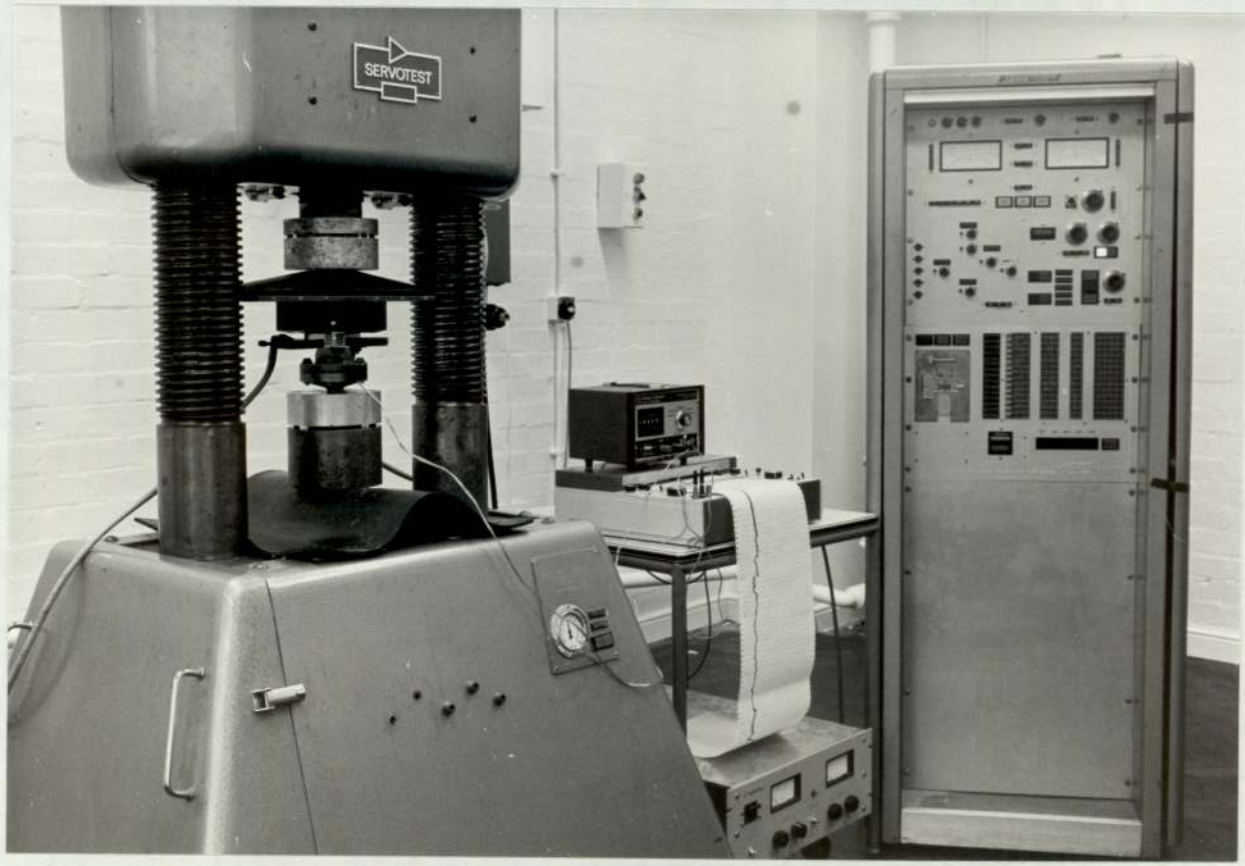

PLATE 2 General view of the fatigue machine and other equipment

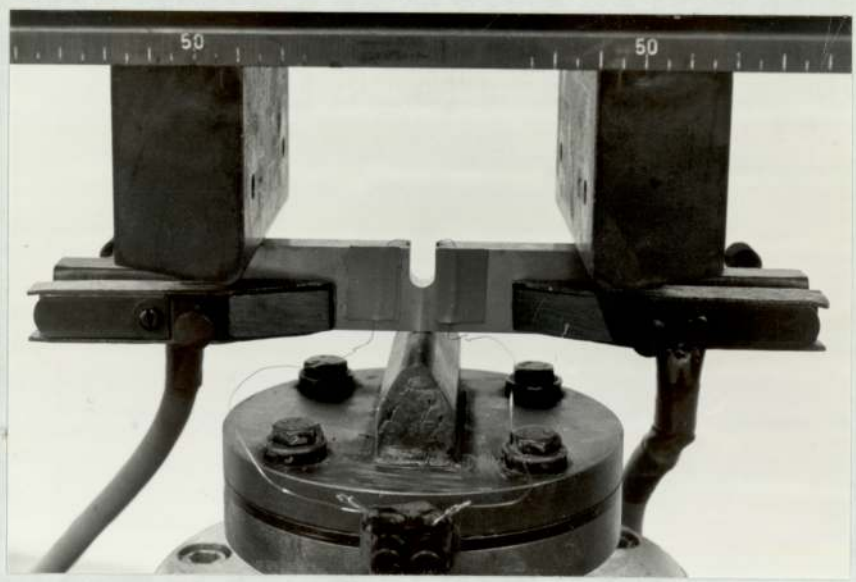

PLATE 3 Closer view of 3 point bend rig and the specimen

depth and the notch width were measured with a travelling microscope with an accuracy of 0.01 mm.

The notch root area was examined in a projection microscope or a profile projector at the highest possible magnification. The notch root was then traced and the notch root radius was determined according to the following method. A chord was constructed across the tracing. This chord was then bisected and vertical distance between this point and the notch root was measured. The notch root radius was then calculated using the following equation:

$$\rho = \frac{a^2+b^2}{2bm}$$

where a = the semichord length

b = the vertical distance from the chord to the notch root

ρ = the notch root radius

m = magnification of the tracing.

5.5.2.2. Fatigue Crack Initiation and Propagation

After spot welding the potential probes and attaching the current input clamps at the ends of the specimen, the specimen was placed inside the machine. The current was then adjusted to 30 amperes. The potential probes were then connected to the chart recorder through a terminal block. The voltage on the variable voltage

source was adjusted so that the difference recorded on the chart was between 10 μv and 25 μv. It was found necessary to wait for 30 minutes so that potential measured on the chart recorder was constant. The potential measured on the chart recorder invariably changed by 2 μv to 5 μv during this time.

The required mean load was then applied to the specimen and the machine switched to 'RUN' mode to achieve the required load amplitude. The minimum load in all tests was 200 Newtons or such as to maintain the R value of 0.05. This was necessary to prevent the specimen judder and subsequent displacement.

The test was continued till the potential across the notch increased to a predetermined value.

5.5.2.3 Electrical Potential Calibration

It was decided that the calibration curve relating the crack length to the potential increased as derived by Gilbey and Pearson [97] should be complimented by experimental values as the geometry under consideration was different to the one for which the analytical expression was developed.

A number of specimens for 080M15 (En32) and 080A47 (En43B), for each root radius were fatigue cracked to potential difference increases from 5 μv to 400 μv in 25 μv intervals. The specimens were then broken open in fast fracture.

For the fatigue cracks which were cusps, the area of the fatigue crack was traced using a profile projector at the highest possible magnification. The area of the crack was then estimated using a planimeter. This area was then devided by the thickness of the sample and an equivalent crack length was established. The through thickness crack lengths were estimated using a travelling microscope and measuring the crack length at ten positions along the crack front. This was complemented by examining the specimen in the scanning electron microscope and measuring the crack length at the same position as that measured by the travelling microscope.

The potential V_o was measured for untreated materials by placing the probes at the midthickness position and at 5 mm on either side of the centerline on an unnotched specimen. It was also measured by placing potential probes at the midthickness and midway between the specimen end and the notch edge, 10 mm apart.

The results were then plotted as suggested by Gilbey and Pearson [97], in terms of Va/V_oW versus a/W; where Va = potential measured across the notch face at any crack + notch length. V_o = potential gradient in an unnotched sample. W = width of the specimen, mm.

5.6 Hardness and Composition Gradient

After the fatigue cracks were grown to a certain length in the case hardened samples, the samples were fractured by carrying out fracture toughness tests in three point bend.

The fracture surface was then separated from the specimen and mounted in conducting bakelite. This was then polished to 1 μ diamond polish. The polished specimen was used to establish the hardness and the carbon gradient for each root radius and treatment condition.

The hardnesses were measured on the Vicker's microhardness tester with a pyramid diamond indentor. The load used was 100 grammes. This particular load was chosen so as to give maximum sensitivity as the minimum distance allowed between the two indentations was approximately 25 μm for the size of the indentations observed throughout the case and the core. Further increase in load either necessitated increase in distances between the two indentations or reduction in the sensitivity of the measurement. For some samples the hardness gradient was determined using higher loads available. It was found that increasing the load did not improve the sensitivity or reproducibility.

The carbon gradient was determined using the electron microprobe analyser (Cambridge Instruments Microscan 5). All the measurements were obtained using 15 Kv beam potential to achieve optimum conditions, i.e. minimum penetration and maximum number of counts. The crystal used was barium stearate. The machine was set up using graphite standard. As the number of electrons absorbed and the depth of penetration is different for graphite and steel,it becomes necessary to establish a calibration curve to estimate the

variation in the carbon percentage in the case, by using steel samples with known carbon percentages and establishing a correlation between number of counts per unit of time and percent weight of carbon.

The polished samples were then analysed and the number of counts obtained in one second were displayed on a chart recorder continuously. The sample was moved at a speed of 30 μm/min. A continuous graph of the number of counts at various distances below the notch was thus obtained. Using the established calibration this graph can then be used to obtain the variation in the carbon percentage below the notch root.

5.7 Metallography and Fractography

The specimens used for determination of hardness gradients and composition gradients were subsequently used for metallographic examination. The specimens were polished to 1 μm diamond polish and etched in 2 percent nitric acid in alcohol. Some specimens were not broken open, but were ground so as to remove the case hardened layer. This was done to compliment the fractographic studies to observe the influence of microstructure on the crack path.

The fracture surfaces of specimens representing each root radius andtreatment condition were examined in the scanning electron microscope. Fractographs of representative features of the fracture surface from the slow crack growth region close to the notch to final fracture were taken for

comparison purposes. The fracture surface of case and case-core boundary region was closely examined to locate crack initiation sites. In some cases fractographic collage was produced to indicate variation in the fracture morphology.

6. RESULTS

6.1 Electrical Potential Calibration

The calibration curves obtained for various notch geometries under consideration are plotted as a dimensionless ratio of $V_a/V_o W$ versus $(a+c)/W$ in Figure 12. The Gilbey and Pearson solution [97] for a sharp crack in a finite geometry is also plotted for comparison. In the present experimental programme the current was introduced at different points to that indicated in the Gilbey and Pearson report [97]. The solution will have to be modified to accommodate the change in the position of the input leads.

The curves presented in figure 12 may be described by a polynomial of the form

$$(a+c)/W = K_o + K_1\left(\frac{Va}{V_o W}\right) + K_2\left(\frac{Va}{V_o W}\right)^2 + K_3\left(\frac{Va}{V_o W}\right)^3 \quad \ldots\ (31)$$

The values of constants K_o, K_1, K_2 and K_3 for individual notch geometries are presented in Table 5. The curves obtained for individual geometries are independent of the materials under consideration. The values of V_o, the value of the potential gradient in an uncracked geometry, for the materials under consideration are presented as an inset in the figure 12a.

It was found that till the crack was approximately 1 mm long it could be in the form of a cusp or cusps depending on whether the crack nucleated at one location or multiple nucleation was observed. Plate 4 shows such a nucleated cusp formed which showed a 5 μv increase in the potential difference. The area of the cusp shown is 1.52 mm^2, which

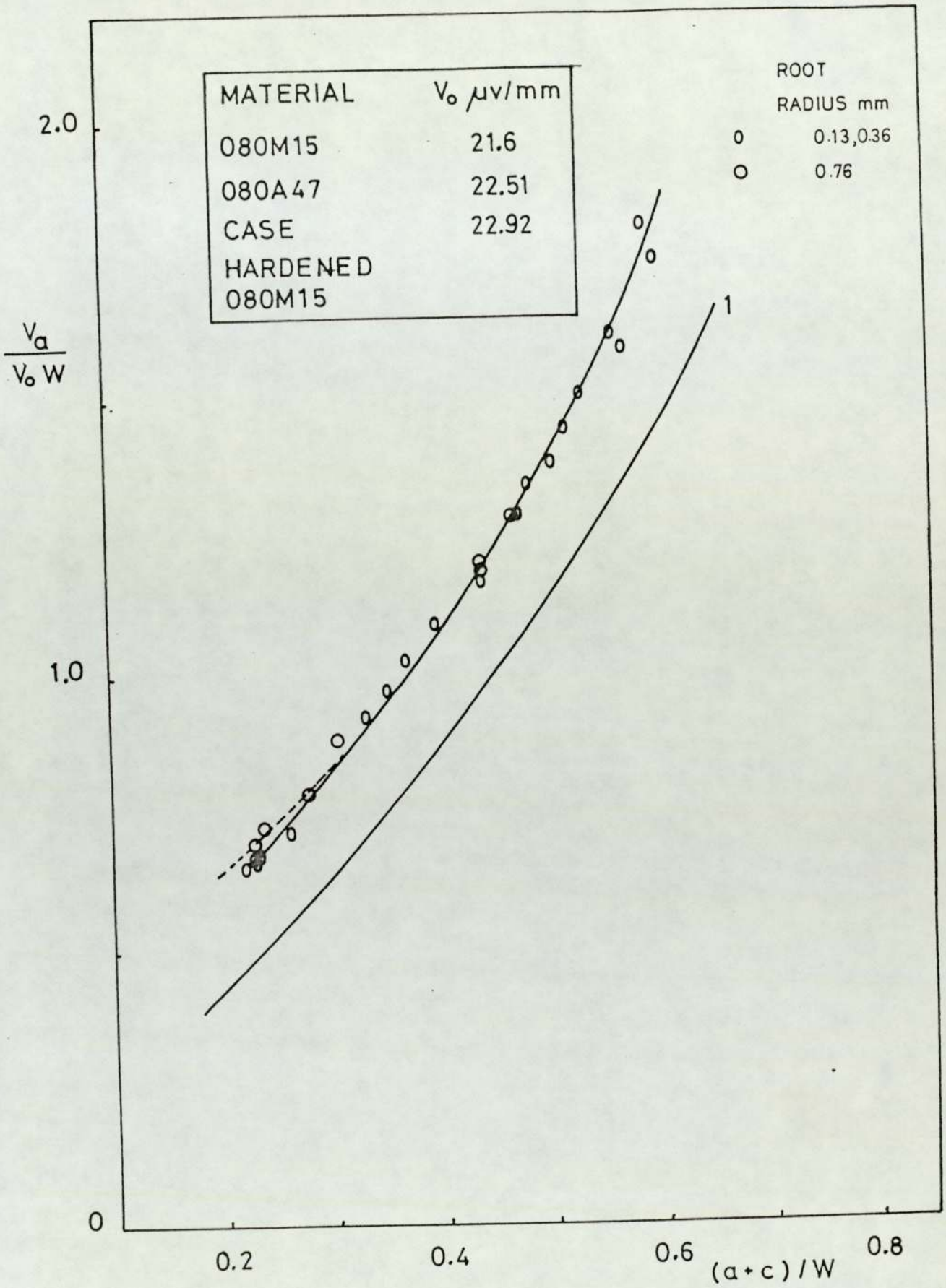

FIGURE 12a Experimental electrical potential calibration curves (notch depth 5 mm, root radii 0.13 mm, 0.36 mm and 0.76 mm, curve 1 represents theoretical calibration [97])

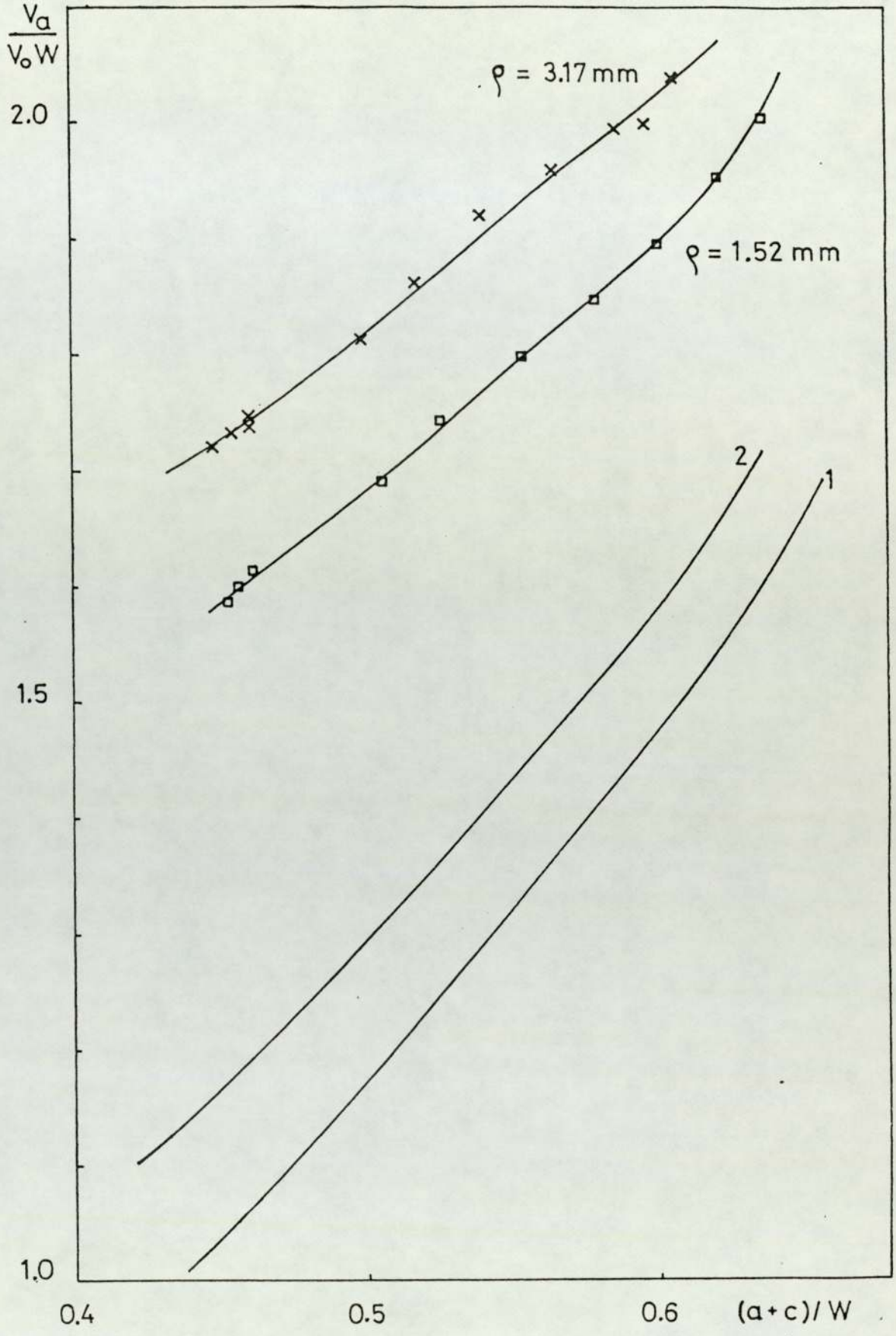

FIGURE 12b Experimental electrical potential calibration curves (notch depth 10 mm, root radii 1.52 mm and 3.17 mm, curve 1 and 2 represent theoretical calibrations for 1.52 mm and 3.17 mm root radius respectively)

TABLE 5

CONSTANTS OF EQUATION 31 FOR VARIOUS NOTCH GEOMETRIES

Constants	Notch geometry Root Radius			
	0.13	0.76	1.52	3.17
K_o	-0.1438	-0.3447	7.2993	-11.809
K_1	0.6560	1.1332	-12.641	18.893
K_2	-0.1535	-0.5183	7.5221	-9.8767
K_3	0.01066	0.1011	-1.4338	1.7649

PLATE 4 Fatigue crack shape at initiation in O8OA47 specimen (magnification x24)

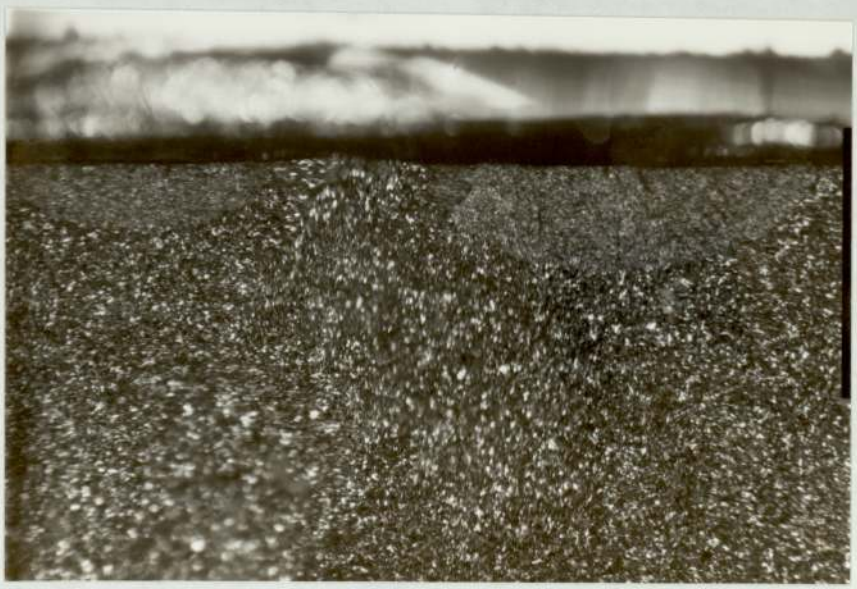

PLATE 5 Fatigue crack shape at initiation in O8OA47 specimen (magnification x24)

gives an equivalent through thickness crack length of 0.152 mm. Plate 5 shows a multiple initiation situation. The macrophotograph shows 2 cusps formed. The total area of the two cusps is 1.56 mm^2, which gives an equivalent through thickness cracklength of 0.156 mm. The increase in the potential difference observed in these cases was 5 μv. An experimental calibration based on cusps was established as the cracks emanating from notches less than 1 mm, in the present experiments, were cusps.

For some through thickness cracks, areas of cracks were calculated using a planimeter after tracing the area using a profile projector. Equivalent crack lengths were then established. The average values of crack lengths were then compared with the equivalent crack lengths obtained as described above. The results are presented in Table 6. It can be seen that the values of cracklengths calculated by the two methods are almost the same. The cracklength measured or estimated thus correlated to the area of the crack.

The sensitivity of the technique is based on the material resitivity, recorder sensitivity, current flow and the position of the probes. Examination of theoretical calibration curves suggests that the voltage difference ΔV is much higher for the same increment in crack length at a longer crack length, than at a shorter crack length. Similar behaviour was observed in the present experiments. The sensitivity at any crack length could be obtained by

TABLE 6

CALCULATED CRACK LENGTHS USING DIFFERENT METHODS

Average of 10	ASTM [103]	Eq. Area
3.342	3.713	3.591
3.632	3.77	3.784
4.154	4.3	4.18
3.658	3.92	3.775
3.634	3.82	3.732
3.722	4.003	3.957
4.156	4.74	4.407

differentiating the polynomial with respect to voltage V. The values of the sensitivity are plotted as an increment in crack length per 5 μv versus the notch plus crack length (a+c) (Figure 13).

It can be seen that when the crack length c is small the increase in the potential difference of 5 μv indicates an increment of crack length of 0.1 mm. As the minimum value of voltage that can be recorded is 0.5 μv, detection sensitivity could be estimated to be as high as 0.01 mm.

The maximum error observed in predicting the total crack length (a+c) was 0.14 mm. However, as indicated above the increment in the crack length Δ(a+c) could be predicted with an accuracy of 0.01 mm .

6.2 Determination of Stress Intensity Factor Coefficient for the Notch plus Crack Geometry

6.2.1 Propagation of Fatigue Cracks

As described in section 2.4.3, it is necessary to determine the values of constants C and n of the Paris equation. A summary of fatigue crack growth data for 080M15 and 080A47 is presented in Figures 14 and 15. The data can be represented by Paris equation:

$$\frac{da}{dN} = C(\Delta K)^n$$

The values of the constants are

	C	n
080M15	$1.2966*10^{-9}$	3.0458
080A47	$2.0697*10^{-10}$	3.574

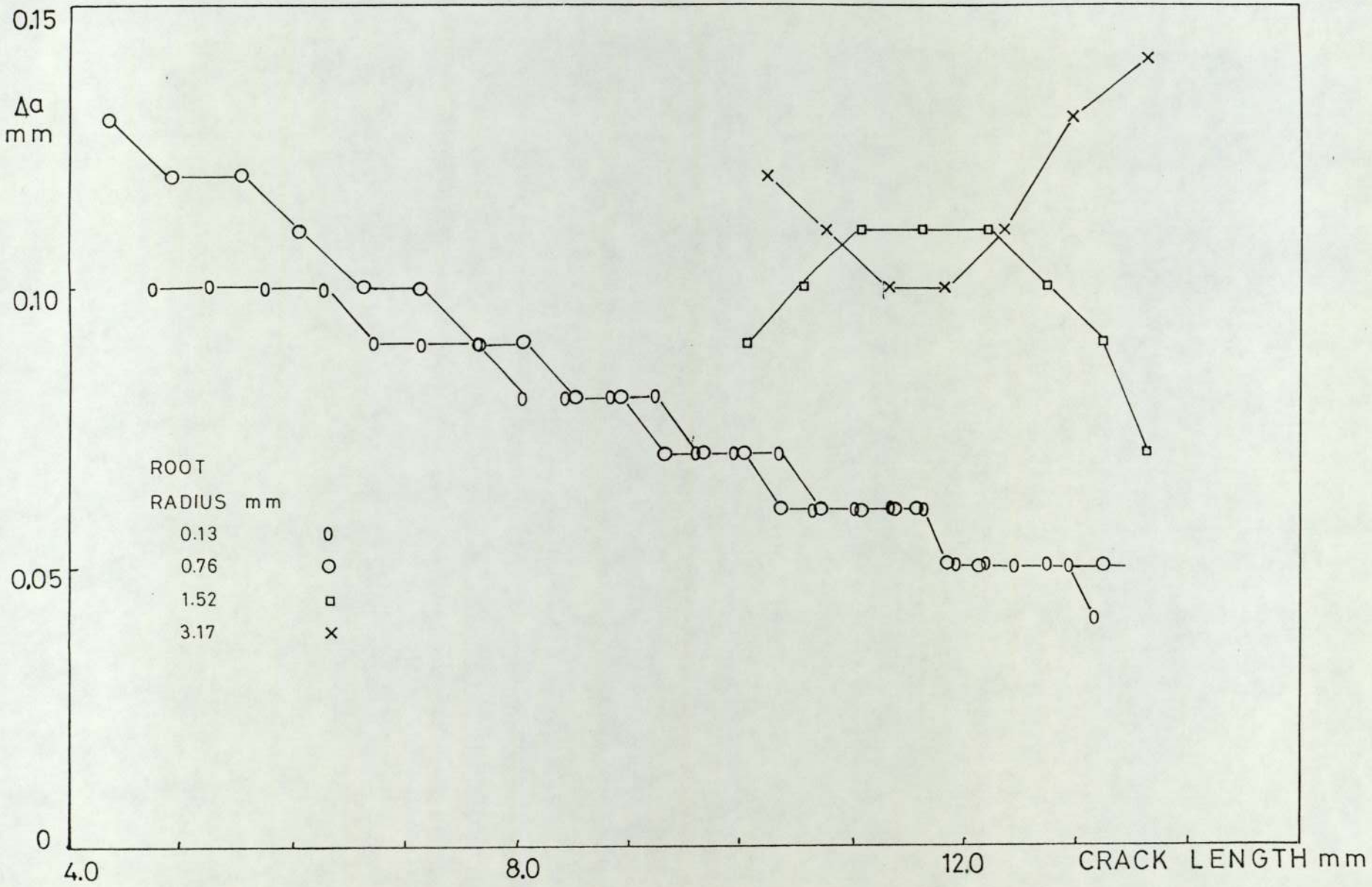

FIGURE 13 Sensitivity of experimental electrical potential calibration curves

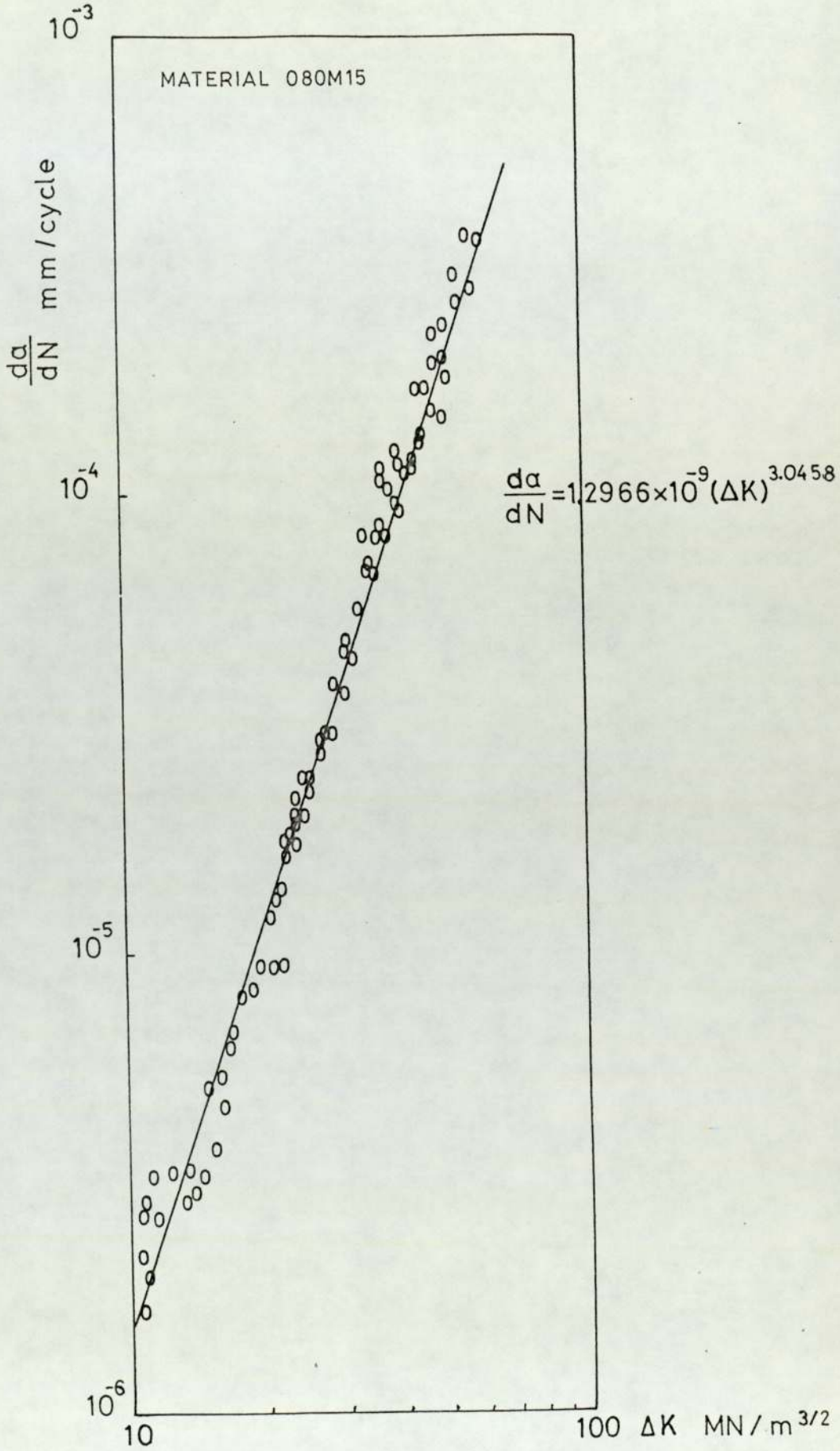

FIGURE 14 Fatigue crack growth data for BS970 080M15 (En32)

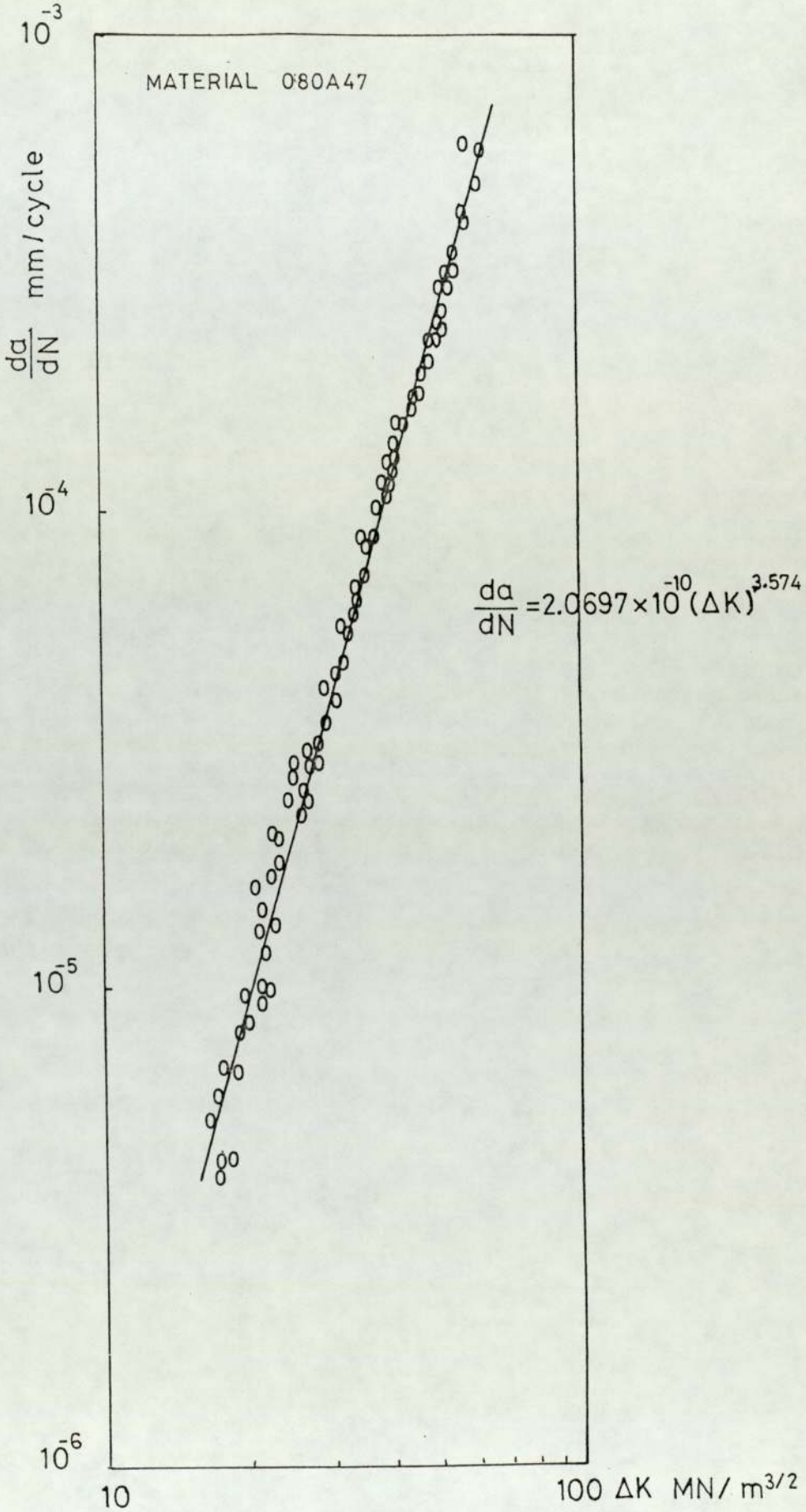

FIGURE 15 Fatigue crack growth data for BS970 080A47 (En 43B).

The upper and the lower limits of the crack growth rates are 10^{-3} mm/cycle and 10^{-6} mm/cycle. The units of the stress intensity factor range are $MN/m^{3/2}$.

The data presented here was obtained from the fatigue tests carried out on the notch with sharpest root radius (notch length a = 5 mm and root radius ρ = 0.13 mm). The crack growth occurring in the first mm is ignored to ensure that the crack growth is not affected by the notch geometry.

To determine the crack growth rates the number of cycles elasped for particular values of voltage differences were obtained from the chart recorder. In the initial stages of crack growth the number of cycles was calculated at 5 μv intervals until the increase in the potential drop was 50 μv. For the further increase in potential difference of 300 μv, the interval was maintained at 10 μv, after which it was 20 μv. This method was adopted so as to maintain uniform sensitivity throughout the crack growth region under consideration. Using the calibration curves (Figure 12a and b or equation 31), values of the crack lengths for the potential differences were obtained. These values of the crack lengths a were then plotted against number of cycles N to obtain a versus N plot.

The crack growth rates were determined using two techniques. The first involved constructing tangents at various crack lengths on the crack length versus number of cycles curve. The slopes of these tangents are the crack growth rates $\frac{da}{dN}$.

The K-calibration curve [103] was then used to obtain the results in the form of $\frac{da}{dN}$ versus ΔK.

The second method entailed the use of a simple finite difference technique suitable for computer processing. The measurements required were the same as those in the method described above, i.e. potential difference and the corresponding number of cycles. In addition to this, the specimen dimensions and load range needed to be specified. The crack lengths were calculated using the appropriate calibration curve. The values of crack growth rates were calculated using the following equation:

$$\frac{da}{dN} = \frac{a_2 - a_1}{N_2 - N_1}$$

where a_1 and a_2 were estimated crack lengths at N_1 and N_2 cycles respectively. The stress intensity factor range ΔK was calculated for the mean of the two crack lengths a_1 and a_2. The output was in the form of the crack growth rates da/dN, the crack length, the notch plus crack length and the stress intensity factor range.

The method using computer programme was convenient. However, the first technique was used periodically to check the accuracy and the algorithm of the computer programme.

6.2.2 Propagation of Fatigue Cracks from Blunt Notches

The same procedure as described in the previous section was followed to determine the crack growth rates in blunt notches. The growth rates were determined from the root of the notch. The values of the constants C and n in Paris Law were determined for O8OM15 and O8OA47 in the previous section. These constants were used to determine the stress intensity factor range and subsequently the value of the stress intensity factor coefficient as described in section 2.4.3. Figures 16, 17 and 18 show the variation in the ratio of the stress intensity factor coefficients for the notch plus crack geometry and the crack of the same length as notch plus crack. The stress intensity factor coefficient for the crack was determined from the Srawley equation [103]. The equation by Jergeus[42] is also plotted for comparison with the experimental results. The value of the crack length Co beyond which the ratio becomes one and the notch plus crack combination could be treated as a long crack could not be estimated experimentally. However, the experimental results suggest that Co could be calculated from 0.5 $\sqrt{a\rho}$ The experimental points lie well below the plots of the equations suggested by Jergeus [42].

The experiments carried out to establish the electrical potential drop calibration showed that the cracks which are less than one mm in length are seldom through thickness cracks. The crack growth rates calculated for crack lengths

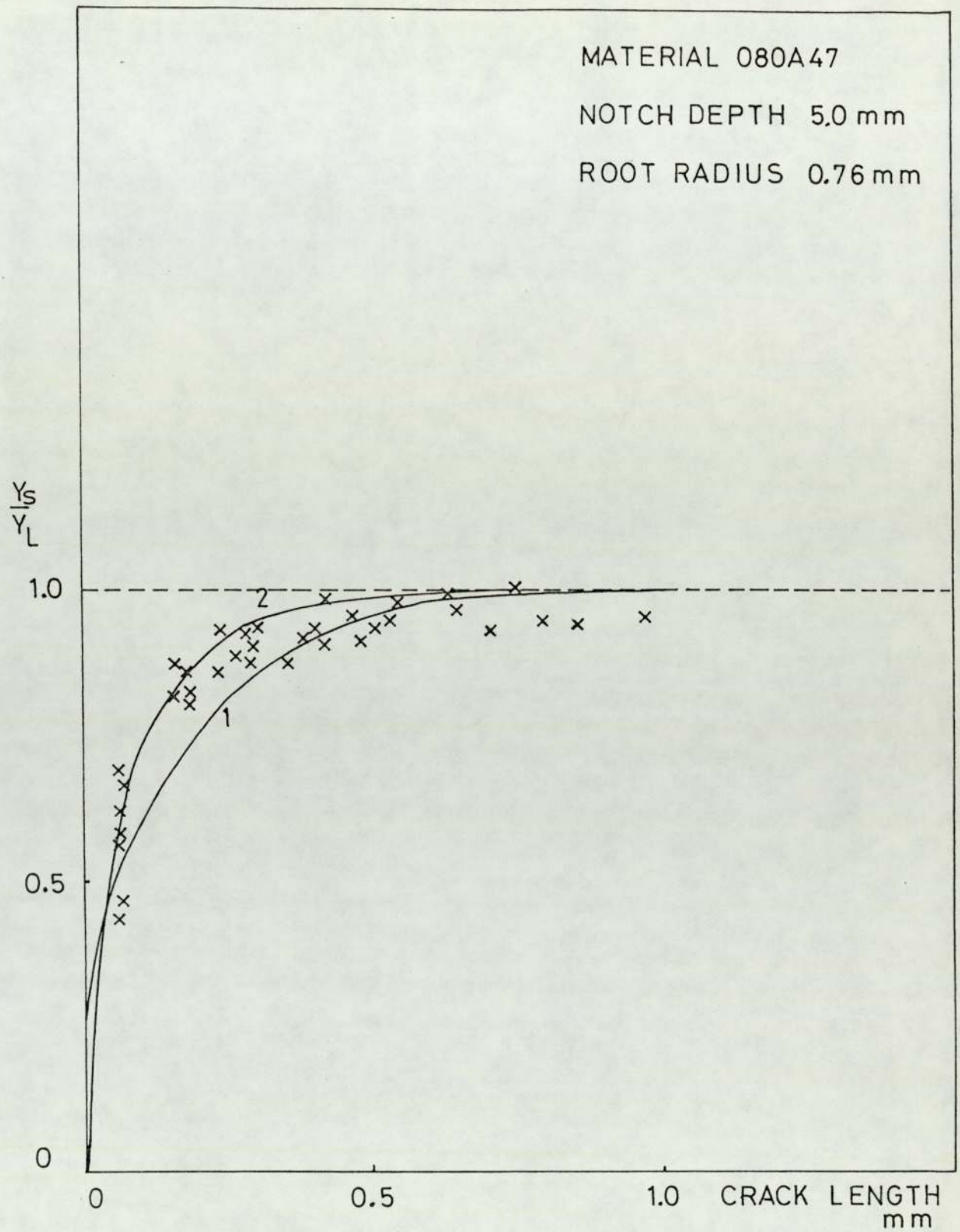

FIGURE 16 Comparison between proposed equation (curve 1), Jergeus equation (curve 2)[42] and experimental data. (Notch depth 5 mm and root radius 0.76 mm)

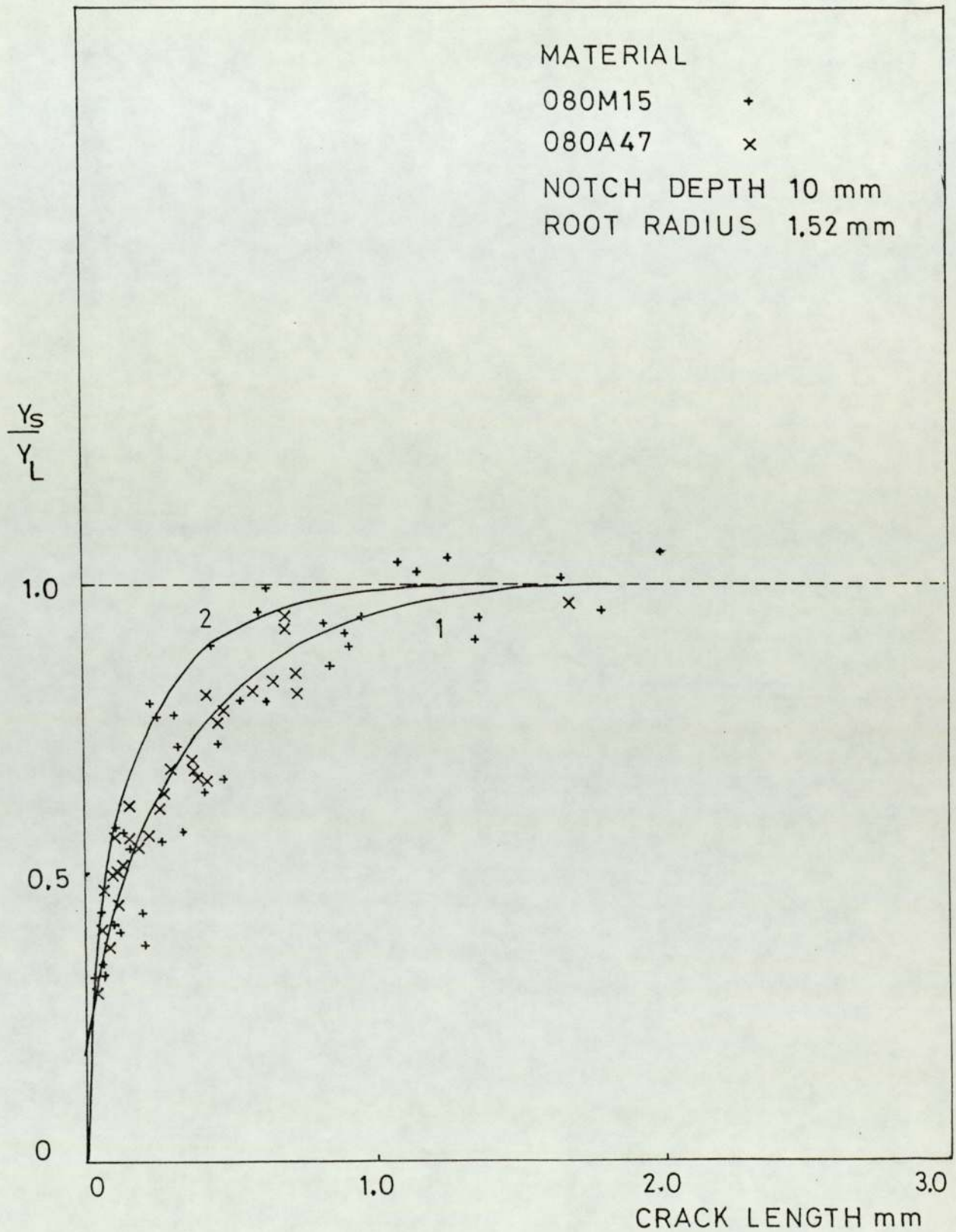

FIGURE 17 Comparison between proposed equation (curve 1), Jergeus equation (curve 2)[42] and experimental data (Notch depth 10 mm and root radius 1.52 mm)

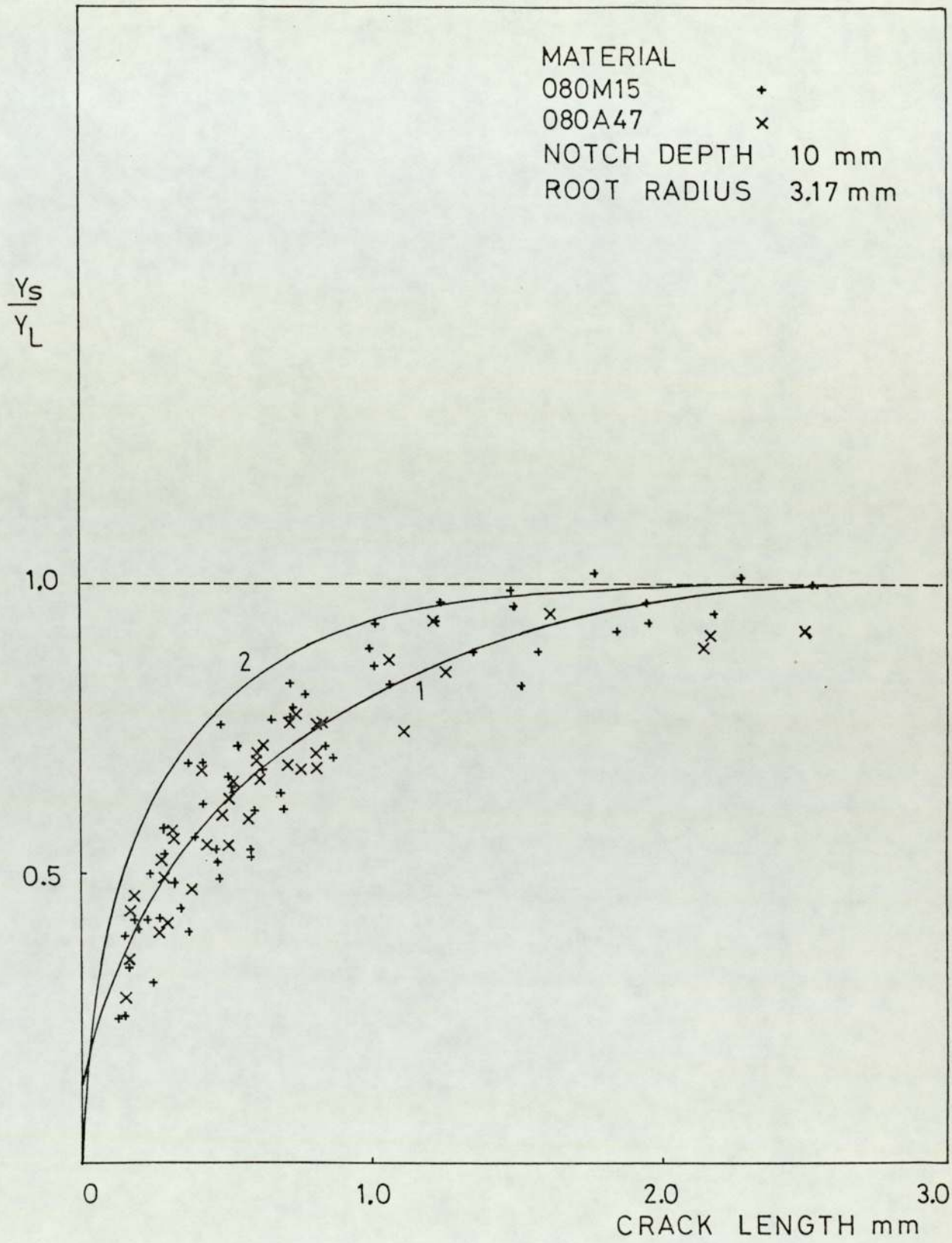

FIGURE 18 Comparison between proposed equation (curve 1), Jergeus equation (curve 2)[42] and experimental data (notch depth 10 mm and root radius 3.17 mm)

smaller than one mm were in fact the crack growth rates estimated for a through thickness of the same area of the cusp. The crack in reality could be growing in the thickness direction and in the directions which are at an angle to the expected direction of macroscopic crack growth.

A modified form of the Jergeus equation [42], equation (32), is proposed to describe the experimental data. The equation is as follows:

$$\frac{Y_s}{Y_L} = \sqrt{\frac{a \tanh\left[\frac{(2^* \sqrt{(1+a/\rho)} * (c+C_B)}{\sqrt{a\rho}}\right] + c+C_B}{a + c}} \quad \ldots.(32)$$

where Y_s = the stress intensity factor coefficient for the notch plus crack geometry

Y_L = the stress intensity factor coefficient for the crack with the same geometric length as that of the notch plus crack

a = notch depth

c = crack length

ρ = root radius

C_B = empirical constant dependent on the material properties and microstructure.

For the curves plotted in Figures 16, 17 and 18 describing equation (32), C_B has the value of 22 μm, which is the grain size for 080M15 and the mean free path in ferrite in 080A47.

6.3 Fatigue Crack Initiation

6.3.1 Fatigue Crack Initiation in 080M15 and 080A47

The results are presented in Tables 7 and 8 which list the notch depth and the root radius, the load range, the crack length at initiation, the parameters $K_t \Delta S$, $\frac{\Delta K}{\sqrt{\rho}}$ and ΔK_B and the number of cycles to initiation Ni. The results are plotted graphically in Figures 19-24. For all the samples the initiation was defined as the first 5 μv increase in the potential difference. This was necessary as the long duration tests show a drift in the potential difference time record of approximately 2-4 μv.

The values of $K_t \Delta S$ and $\frac{\Delta K}{\sqrt{\rho}}$ were calculated as indicated in section 5.4.1. The values of ΔK_B were calculated using equation (30) in conjunction with equation (32). The equation is as follows:

$$\Delta K_B = \Delta P * Y_s * \sqrt{a+c} \; / \; (B*W)$$

$$Y_s = Y_L \sqrt{\frac{a \tanh\left[\frac{2*(\sqrt{1+a/\rho})*(c+C_B)}{\sqrt{a\rho}}\right] + c + C_B}{a + c}} \quad \ldots(33)$$

The value of C_B for 080M15 was 22 μm which was the ferrite grain size and for 080A47 was 22 μm which was the mean free path in ferrite.

The data obtained could be represented by equations of the form.

$$N_i = B_o(\Delta K_B)^m$$

$$N_i = B_1 \left(\frac{\Delta K}{\sqrt{\rho}}\right)^{m_1}$$

$$N_i = B_2 (K_t \Delta s)^{m_2}$$

The linear regression analysis of the results obtained gave the following values of B_o, B_1, B_2 and m, m_1, m_2

Materials 080M15

	Calculated	Estimated
B_o	$1.845*10^{10}$	-
m	-4.438	-
B_1	$4.273*10^{13}$	$1.2134*10^{15}$
m_1	-2.8802	-3.600
B_2	$3.616*10^{15}$	$1.202*10^{14}$
m_2	-3.4099	-3.321

Material 080A47

	Calculated	Estimated
B_o	$1.329*10^{10}$	-
m	-4.354	-
B_1	$-3.207*10^{16}$	$2.756*10^{17}$
m_1	-3.898	-4.162
B_2	$9.5371*10^{17}$	$1.0021*10^{18}$
m_2	-4.2455	-3.872

Holder [35] proposed equations to estimate the values of B_1, B_2, m_1 and m_2.

TABLE 7 FATIGUE CRACK INITIATION DATA FOR 080M15

Sample No.	Notch Depth mm	Notch Root radius mm	Crack length at initiation mm	Load range KN	$K_t \Delta s$ MN/m^2	$\frac{\Delta K}{\sqrt{\rho}}$ MN/m^2	ΔK_B $MN/m^{3/2}$	Ni
131	4.94	0.13	0.11	2.989	1010.08	881.50	9.91	690,000
132	4.96	0.13	0.11	2.989	1013.42	885.07	9.94	600,000
133	4.86	0.13	0.13	5.978	1989.79	1742.52	19.77	37,000
134	4.89	0.13	0.11	5.978	1998.52	1745.22	19.62	29,750
135	4.86	0.13	0.13	6.377	2134.76	1866.17	21.15	15,000
136	4.93	0.13	0.13	6.377	2143.87	1880.42	21.29	29,030
137	5.00	0.13	0.11	6.377	2180.76	1902.66	21.39	31,270
138	4.94	0.13	0.13	9.964	3357.06	2938.23	33.30	3,280
139	5.03	0.13	0.11	9.964	3395.99	2965.08	33.30	4,320

TABLE 7 (CONTINUED)

Sample No.	Notch Depth mm	Notch Root radius mm	Crack length at initiation mm	Load range KN	$K_t \Delta s$ MN/m^2	$\frac{\Delta K}{\sqrt{\rho}}$ MN/m^2	ΔK_B $MN/m^{3/2}$	Ni
1521	10.06	1.52	0.10	3.587	725.18	570.53	9.32	693,830
1522	9.98	1.52	0.12	3.587	740.50	582.79	10.27	730,400
1523	10.05	1.52	0.08	4.583	959.21	748.86	11.62	390,500
1524	9.94	1.52	0.11	4.583	939.93	739.78	12.95	246,000
1525	10.04	1.52	0.08	5.978	1232.63	962.70	14.30	46,670
1526	10.00	1.52	0.08	5.978	1212.69	946.54	14.06	32,000
1527	10.00	1.52	0.08	8.071	1675.02	1311.04	20.19	18,000
1528	9.98	1.52	0.12	8.071	1667.79	1312.85	23.34	22,400

TABLE 7 (CONTINUED)

Sample No.	Notch Depth mm	Notch Root radius mm	Crack length at initiation mm	Load range KN	$K_t \Delta s$ MN/m^2	$\frac{\Delta K}{\sqrt{\rho}}$ MN/m^2	ΔK_B $MN/m^{3/2}$	Ni
3171	9.9	3.17	0.120	5.6	851.57	623.29	11.93	838,130
3172	9.9	3.17	0.123	5.6	852.44	622.67	12.06	602,830
3173	9.9	3.17	0.131	5.6	850.41	624.41	12.41	287,890
3174	9.9	3.17	0.139	6.2	943.76	692.73	14.08	163,200
3175	9.9	3.17	0.120	6.2	944.71	690.07	13.21	196,800
3176	9.9	3.17	0.130	6.2	942.82	690.20	13.64	302,400
3177	9.9	3.17	0.132	7.8	1189.71	869.94	17.29	64,000
3178	9.9	3.17	0.129	7.8	1187.31	868.83	17.17	48,090
3179	9.9	3.17	0.136	7.8	1183.74	868.21	17.50	57,600

TABLE 8 FATIGUE CRACK INITIATION DATA FOR O80A47

Sample No.	Notch Depth mm	Notch Root radius mm	Crack length at initiation mm	Load range KN	$K_t \Delta s$ MN/m^2	$\frac{\Delta K}{\sqrt{\rho}}$ MN/m^2	ΔK_B $MN/m^{3/2}$	Ni
131	4.79	0.36	0.10	4.4	914.98	781.64	11.82	972,210
132	4.86	0.36	0.10	4.4	920.75	784.95	11.87	371,800
133	4.85	0.36	0.10	4.4	921.40	787.59	11.91	414,220
134	4.84	0.36	0.10	4.6	968.60	826.61	12.50	132,600
135	4.85	0.36	0.10	4.6	962.60	820.66	12.41	287,990
136	4.84	0.36	0.10	4.6	962.13	823.30	12.45	251,530
137	4.85	0.36	0.10	5.8	1216.11	1036.24	15.67	64,190
138	5.16	0.36	0.10	5.8	1261.22	1068.64	16.16	82,170
139	4.85	0.36	0.10	5.8	1215.42	1035.58	15.66	90,550
1310	4.86	0.36	0.10	11.0	2298.08	1967.99	29.76	7,720
1311	4.88	0.36	0.10	11.00	2317.84	1976.59	29.89	7,490
1312	4.90	0.36	0.10	11.00	2319.93	1975.27	29.87	7,410

TABLE 8 (CONTINUED)

Sample No.	Notch Depth mm	Notch Root radius mm	Crack length at initiation mm	Load range KN	$K_t \Delta s$ MN/m^2	$\frac{\Delta K}{\sqrt{\rho}}$ MN/m^2	ΔK_B $MN/m^{3/2}$	Ni
761	5.12	0.76	0.12	5.597	888.21	712.17	12.31	302,900
762	4.95	0.76	0.14	5.8	903.80	725.48	13.42	66,570
763	5.16	0.76	0.12	5.8	927.44	742.42	12.71	163,910
764	5.21	0.76	0.12	5.8	934.00	746.81	12.95	220,450
765	5.20	0.76	0.12	7.8	1252.06	1004.02	17.41	42,100
766	5.14	0.76	0.12	7.8	1240.0	994.53	17.41	48,600
767	5.18	0.76	0.12	7.8	1245.87	999.66	17.61	44,800
768	5.20	0.76	0.12	9.0	1442.73	1156.09	20.27	58,080
769	5.08	0.76	0.12	9.0	1421.25	1140.60	20.03	34,440
7610	5.10	0.76	0.12	9.0	1428.91	1145.34	20.05	51,770

TABLE 8 (CONTINUED)

Sample No.	Notch Depth mm	Notch Root radius mm	Crack length at initiation mm	Load range KN	$K_t \Delta s$ MN/m^2	$\frac{\Delta K}{\sqrt{\rho}}$ MN/m^2	$\Delta K_{B_{3/2}}$ MN/m	Ni
1521	10.01	1.52	0.10	3.986	829.89	649.21	10.58	270,000
1522	10.00	1.52	0.10	3.986	829.32	647.95	10.61	292,000
1523	10.03	1.52	0.10	4.583	958.56	750.13	12.40	265,000
1524	10.13	1.52	0.10	4.583	974.78	759.74	12.47	239,000
1525	10.01	1.52	0.08	5.978	1247.36	973.23	14.76	78,000
1526	10.12	1.52	0.08	5.978	1269.89	988.22	15.18	57,050
1527	10.00	1.52	0.09	7.971	1658.70	1295.33	20.15	17,000
1528	10.06	1.52	0.08	7.971	1678.80	1308.19	19.84	14,200
1529	9.97	1.52	0.08	9.967	2063.02	1612.44	25.02	6,620
15210	10.15	1.52	0.09	9.964	2122.03	1649.88	26.18	6,400

TABLE 8 (CONTINUED)

Sample No.	Notch Depth mm	Notch Root radius mm	Crack length at initiation mm	Load range KN	$K_t \Delta s$ MN/m^2	$\frac{\Delta K}{\sqrt{\rho}}$ MN/m^2	ΔK_B $MN/m^{3/2}$	Ni
3171	9.96	3.17	0.12	5.579	864.06	628.51	11.89	242,000
3172	9.99	3.17	0.12	5.579	866.65	630.34	11.96	242,000
3173	10.04	3.17	0.11	5.978	952.40	688.72	12.68	185,000
3174	9.98	3.17	0.11	5.978	927.17	673.64	12.63	447,000
3175	9.98	3.17	0.11	5.978	929.03	676.41	12.72	212,000
3176	9.97	3.17	0.12	7.971	1234.16	897.57	16.98	50,000
3177	9.98	3.17	0.11	7.971	1238.70	899.29	16.81	62,000
3178	9.99	3.17	0.12	7.971	1239.53	900.90	16.99	49,000
3179	9.99	3.17	0.11	9.964	1546.30	1123.79	20.88	23,000
31710	10.08	3.17	0.11	9.964	1576.10	1142.49	20.97	18,000
31711	9.98	3.17	0.11	9.964	1548.38	1126.78	20.55	19,000

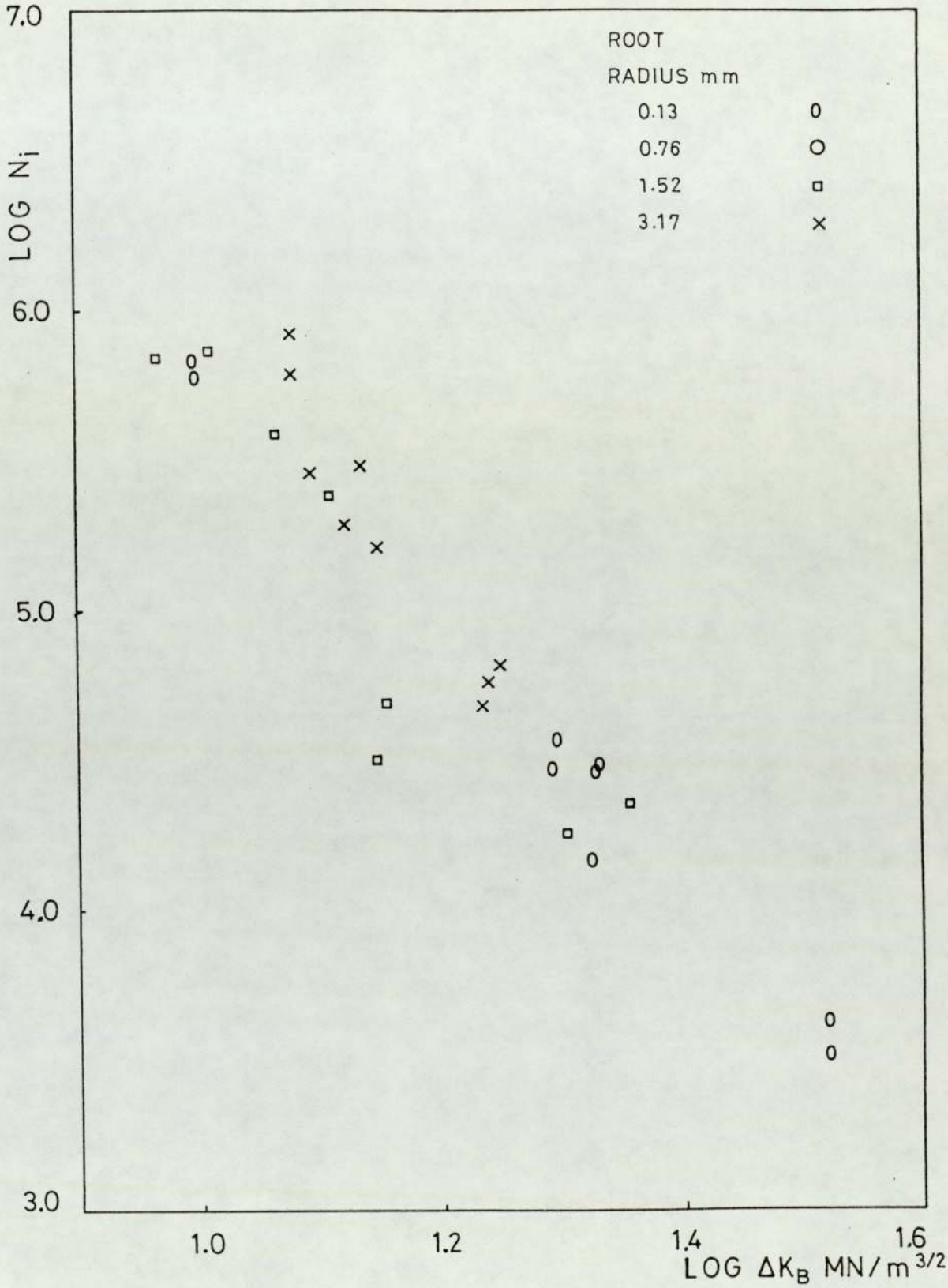

FIGURE 19 Fatigue crack initiation data for 080M15: parameter ΔK_B

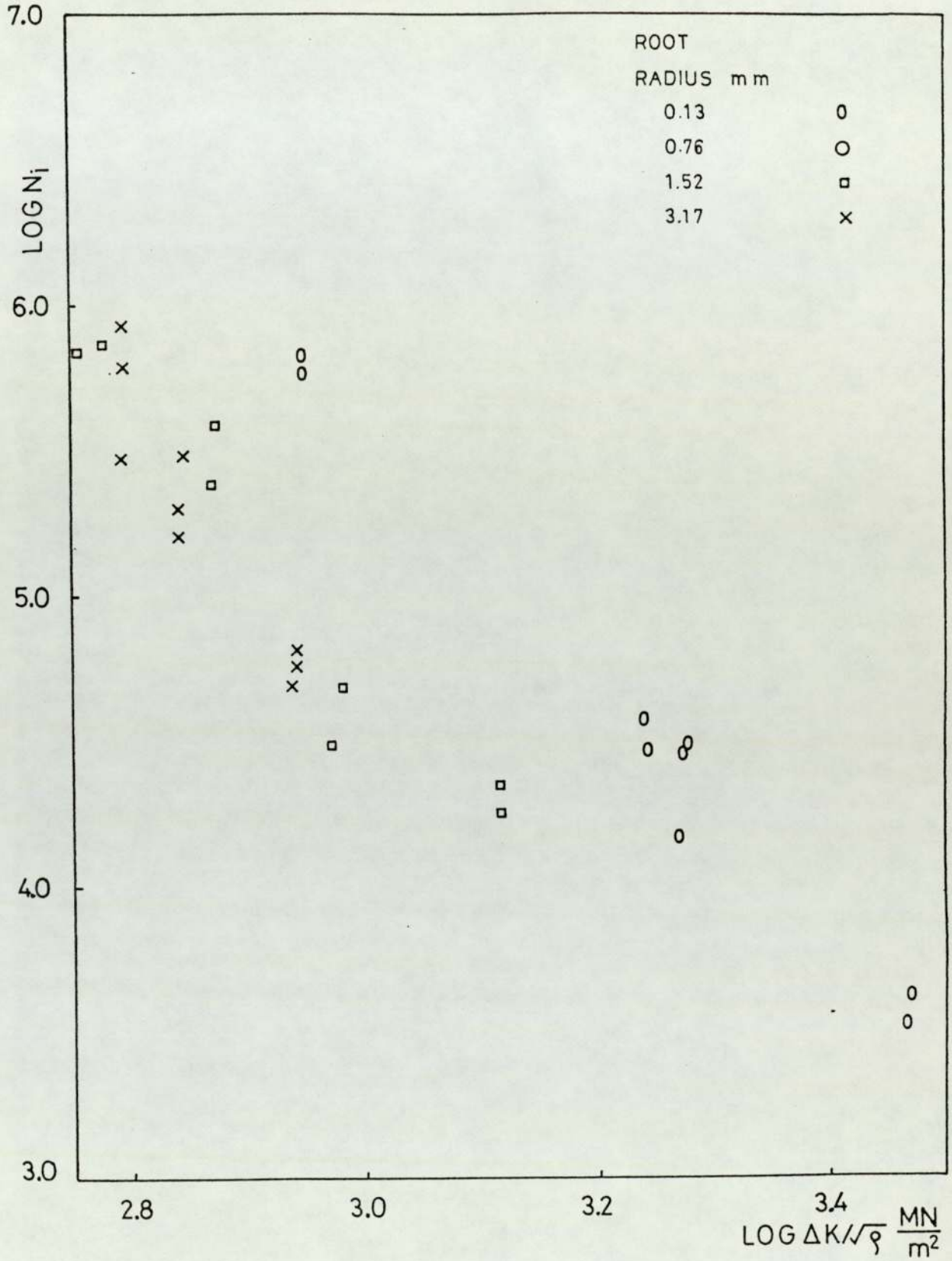

FIGURE 20 Fatigue crack initiation data for 080M15: parameter $\Delta K/\sqrt{\rho}$

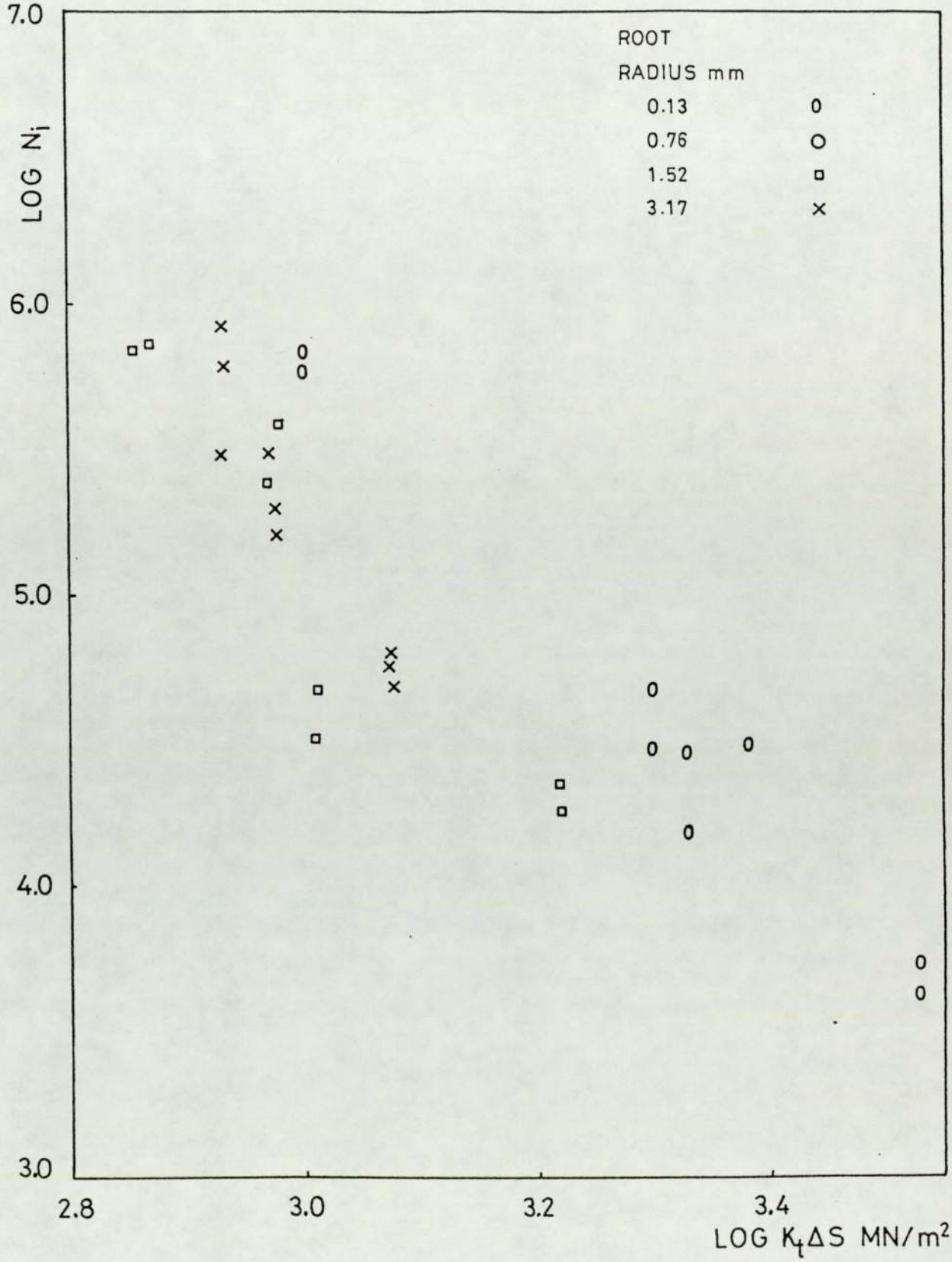

FIGURE 21 Fatigue crack initiation data for 080M15: parameter $K_t\Delta S$

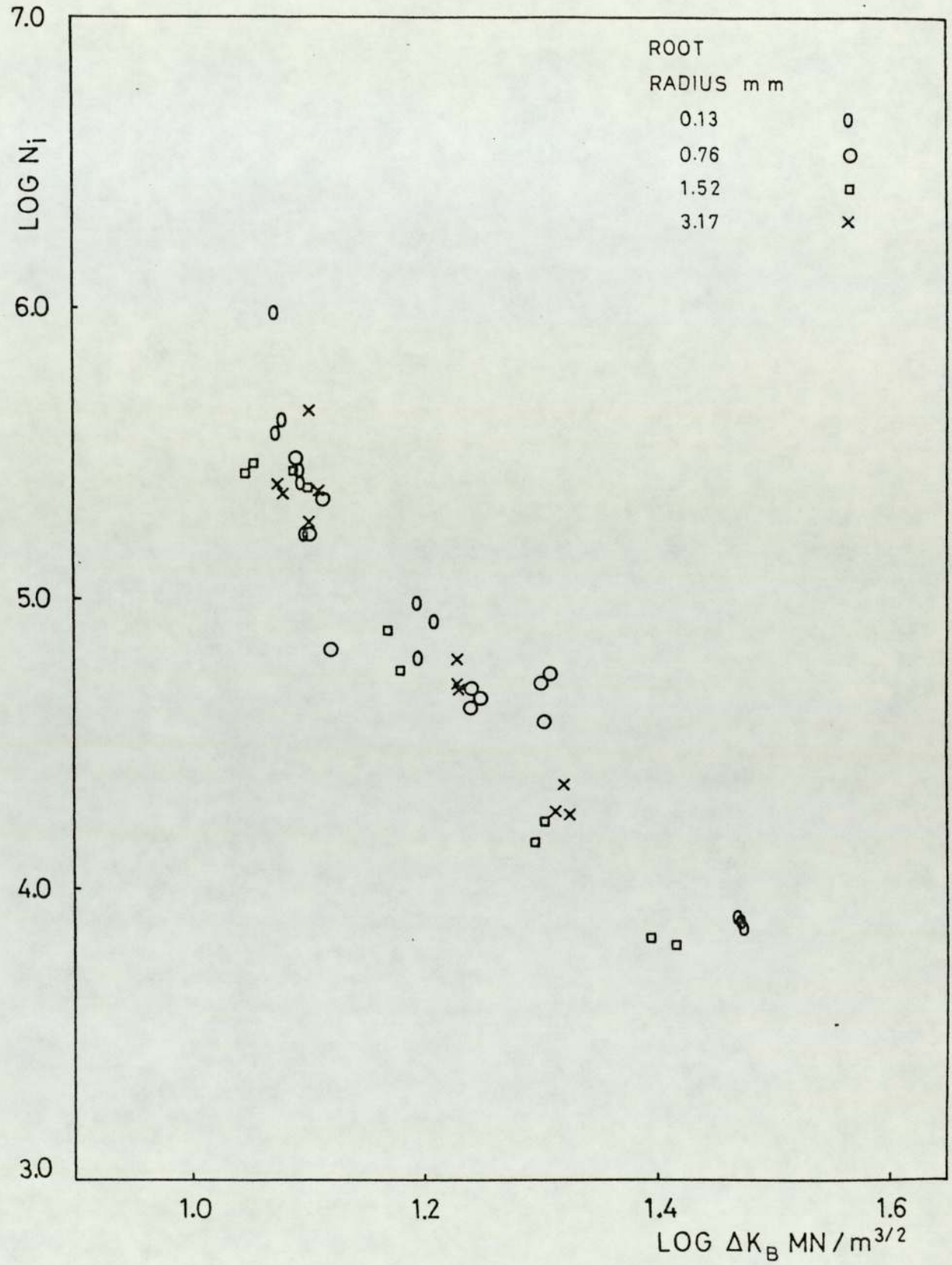

FIGURE 22 Fatigue crack initiation data for 080A47: parameter ΔK_B

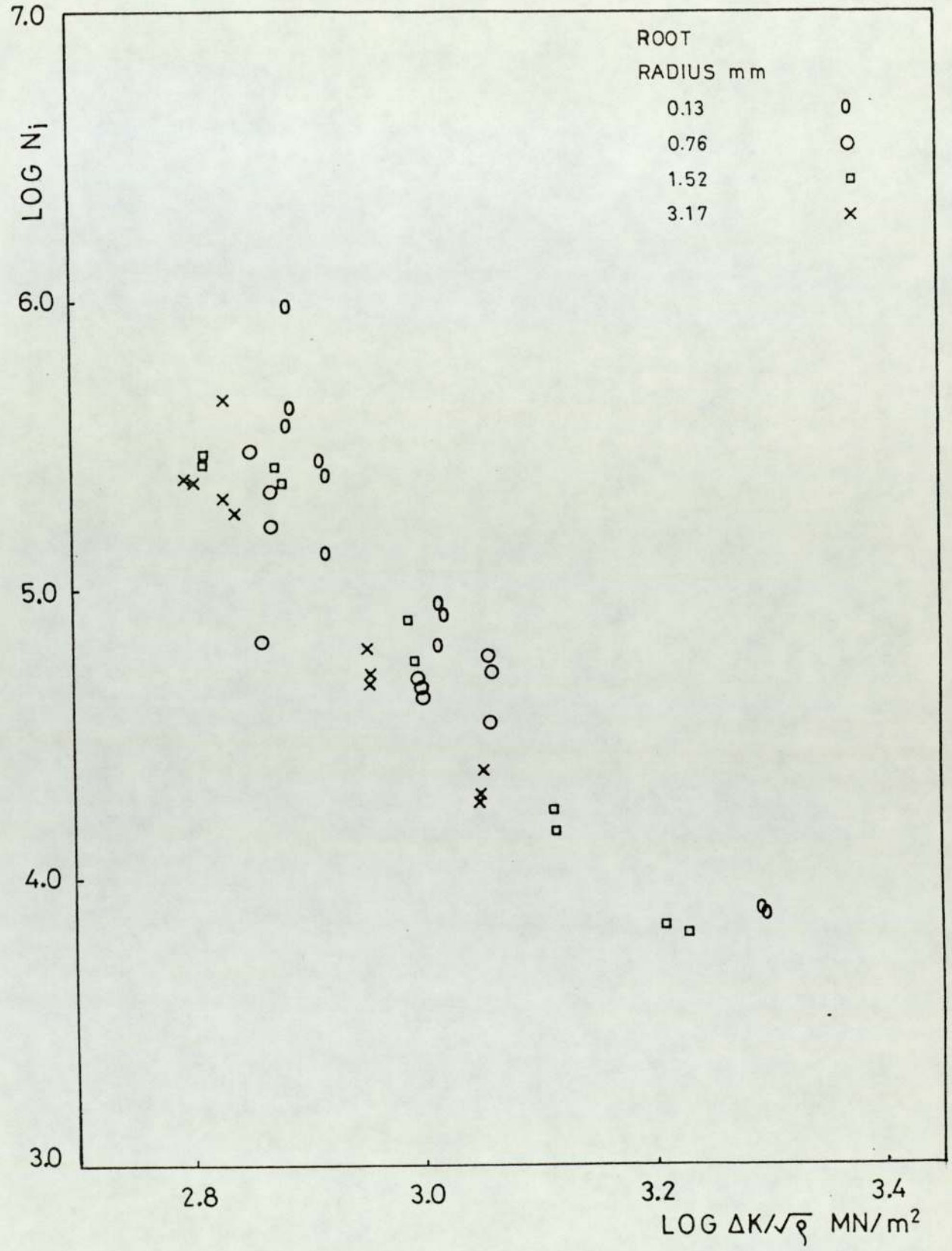

FIGURE 23 Fatigue crack initiation data for 080A47: parameter $\Delta K/\sqrt{\rho}$

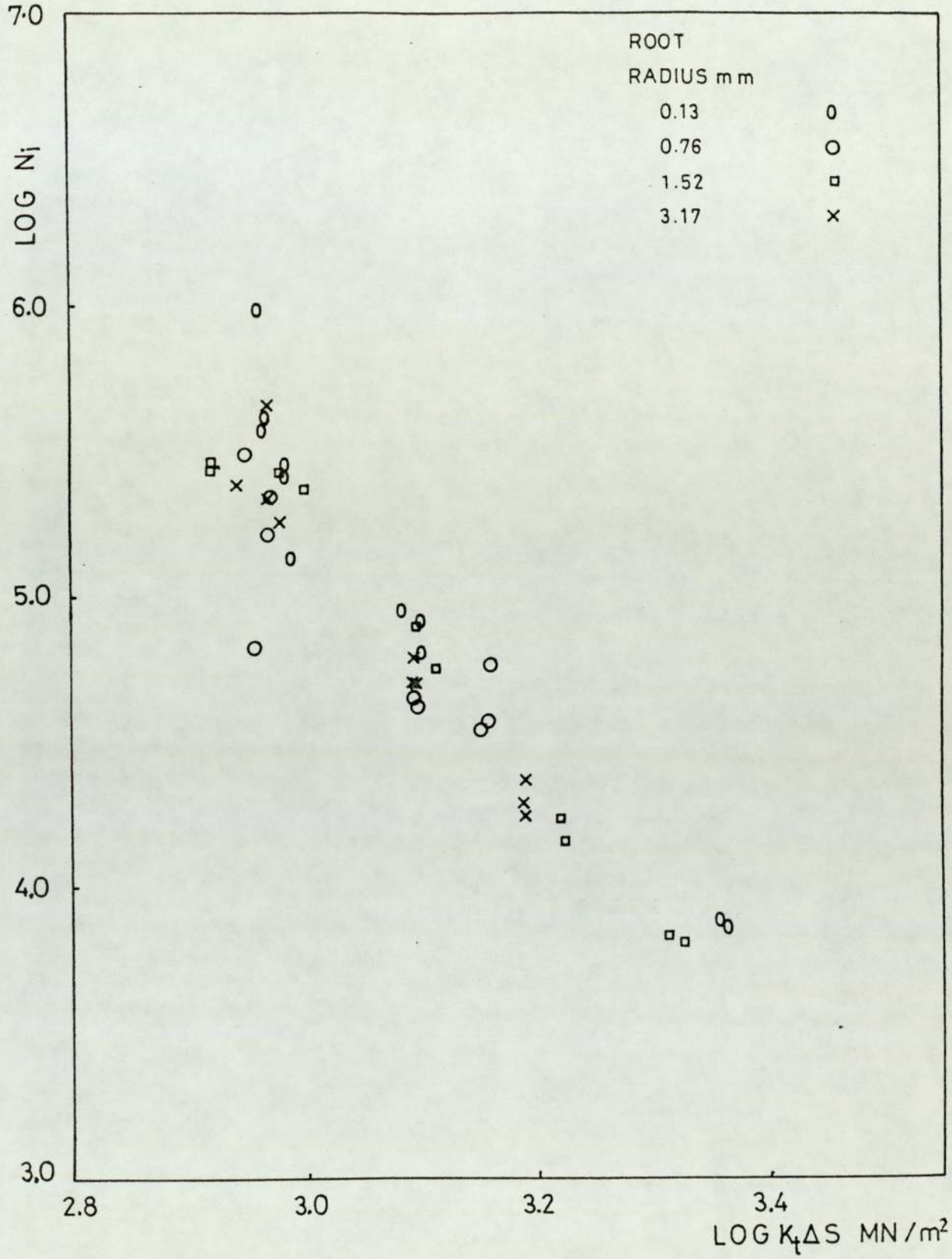

FIGURE 24 Fatigue crack initiation data for 080A47: parameter $K_t \Delta S$

$$m_1 = - \frac{\text{Yield strength MN/m}^2}{275} - 1.91$$

$$m_2 = - \frac{\text{Yield strength MN/m}^2}{280} - 1.66$$

$$B_1 = - 4.19 * m_1$$

$$B_2 = - 4.24 * m_2$$

The estimated values are calculated from these equations.

The value of the crack length at the initiation is calculated from equation (31). The average value of the crack length at initiation is 0.11 mm. This is the length of the through thickness crack at initiation. The actual geometric shape of the crack at initiation could not be established in every sample.

6.3.2 Initiation of Fatigue Crack in Case Hardened 080M15

The results are presented in Table 9 which lists the notch depth and the root radius, the load range, the crack length at initiation, the parameters $K_t \Delta S$, $\frac{\Delta K}{\sqrt{\rho}}$ and ΔK_B and the number of cycles to initiation N_i. The results are plotted graphically in Figures 25-30. The initiation criterion was the same as that for the untreated material. The method of calculation for various parameters and the crack length at initiation is as indicated in section 6.3.1

The data obtained could be represented by the equations of the form:

$$N_i = B_o (\Delta K_B)^m$$

$$N_i = B_1 \left(\frac{\Delta K}{\sqrt{\rho}}\right)^{m_1}$$

$$N_i = B_2 (K_t \Delta S)^{m_2}$$

The data is banded and the notches of shorter length show a distinctly different behaviour compared to that of deeper notches, when log number of cycles to initiation is plotted against log of the stress intensity factor range calculated for notch plus crack geometry. For the other two parameters $K_t \Delta S$ and $\frac{\Delta K}{\sqrt{\rho}}$, however, only the sharpest notch with ρ = 0.13 mm shows a different behaviour to that of the notches of other notch root radii.

The linear regression analysis of the initiation data of the carburised and carbonitrided 080M15 gave the following values of B_o B_1 and B_2, and m, m_1 and m_2 for the parameter ΔK_B:

	Notch depth 5 mm ρ = 0.13 and 0.76	Notch depth 10 mm ρ = 1.52 and 3.17
B_o	$2.052 * 10^{10}$	$8.032 * 10^{13}$
m	-3.6903	-7.107

For parameters $K_t \Delta S$ and $\frac{\Delta K}{\sqrt{\rho}}$

	Notch depth 5mm, ρ = 0.13	Notch depth 5mm. ρ = 0.76 10mm. ρ = 9.52 ρ = 3.17
B_1	$4.167 * 10^{25}$	$1.751 * 10^{11}$
m_1	-6.053	-1.9856
B_2	$1.89 * 10^{26}$	$2.79 * 10^{15}$
m_2	-6.141	-3.261

The linear regression analysis of the initiation data from different groups showed significant correlation between the two respective variables at 1% level.

TABLE 9a FATIGUE CRACK INITIATION DATA FOR CARBURISED 080M15, CASE DEPTH 0.38 mm

Sample No.	Notch Depth mm	Notch Root radius mm	Crack length at initiation mm	Load range KN	$K_t \Delta s$ MN/m^2	$\frac{\Delta K}{\sqrt{\rho}}$ MN/m^2	ΔK_B $MN/m^{3/2}$	Ni
CR381	4.90	0.13	0.11	7.8	2634.49	2298.50	25.84	209,550
CR382	4.97	0.13	0.11	7.8	2630.16	2295.83	25.81	429,940
CR383	4.92	0.13	0.065	7.8	2640.64	2293.99	24.56	152,770
CR384	4.93	0.13	0.11	8.0	2705.38	2350.98	26.43	108,000
CR385	4.95	0.13	0.11	8.0	2711.76	2361.65	26.55	90,630
CR386	4.90	0.13	0.11	9.0	3012.17	2626.73	29.53	70,300
CR387	4.89	0.13	0.11	9.0	3010.8	2627.62	29.54	66,030
CR388	4.87	0.13	0.11	9.0	2999.49	2626.73	29.53	53,400

TABLE 9a (CONTINUED)

Sample No.	Notch Depth mm	Notch Root radius mm	Crack length at initiation mm	Load range KN	$K_t \Delta s$ MN/m^2	$\frac{\Delta K}{\sqrt{\rho}}$ MN/m^2	ΔK_B $MN/m^{3/2}$	Ni
CR3812	9.92	1.52	0.09	7.0	1395.78	1094.55	17.24	62,050
CR3813	9.95	1.52	0.09	7.0	1420.86	1114.42	17.64	46,854
CR3814	9.92	1.52	0.08	7.0	1407.53	1103.87	16.44	118,470
CR3815	9.92	1.52	0.08	7.0	1397.58	1095.39	16.57	122,260
CR3816	9.90	1.52	0.09	7.4	1467.19	1156.41	18.53	179,820
CR3817	o.99	1.52	0.08	8.0	1611.19	1261.15	18.93	28.830
CR3818	9.93	1.52	0.08	8.0	1604.15	1275.42	19.07	20,000
CR3819	9.98	1.52	0.09	8.0	1638.27	1283.10	20.51	43,000

TABLE 9a (CONTINUED)

Sample No.	Notch Depth mm	Notch Root radius mm	Crack length at initiation mm	Load range KN	$K_t \Delta s$ MN/m^2	$\frac{\Delta K}{\sqrt{\rho}}$ MN/m^2	ΔK_B $MN/m^{3/2}$	Ni
CR389	5.00	0.74	0.13	9.6	1481.82	1205.25	21.18	231,000
CR3810	5.00	0.74	0.13	9.2	1419.06	1155.17	20.30	294,000
CR3811	5.08	0.74	0.13	9.2	1451.86	1153.96	20.31	197,780
CR3820	9.95	3.17	0.11	7.8	1181.8	859.67	15.88	370,800
CR3821	10.02	3.17	0.11	8.4	1248.35	927.76	17.29	210,000
CR3822	10.00	3.17	0.11	8.2	1244.48	903.71	16.74	354,200

TABLE 9b FATIGUE CRACK INITIATION DATA FOR CARBURISED 080M15 CASE DEPTH 0.76 mm

Sample No.	Notch Depth mm	Notch Root radius mm	Crack length at initiation mm	Load range KN	$K_t \Delta s$ MN/m^2	$\frac{\Delta K}{\sqrt{\rho}}$ MN/m^2	ΔK_B $MN/m^{3/2}$	Ni
CR761	4.90	0.13	0.11	8.0	2693.99	2349.52	26.36	423,300
CR762	4.90	0.13	0.11	7.6	2539.31	2215.35	24.88	295,800
CR763	4.92	0.13	0.11	7.2	2413.62	2104.94	23.64	241,000
CR764	5.01	0.74	0.12	9.4	1435.99	1167.56	20.20	229,000
CR765	5.02	0.74	0.12	8.8	1344.61	1094.19	19.02	633,600
CR766	5.00	0.74	0.12	8.6	1307.47	1064.16	18.44	261,000
CR767	10.0	1.52	0.11	7.2	1476.84	1158.95	19.61	305,700
CR768	o.97	1.52	0.11	7.2	1451.55	1141.34	19.49	168,840
CR769	9.98	1.52	0.11	7.2	1447.33	1147.17	19.50	302,400
CR7610	9.93	3.17	0.11	8.4	1263.82	915.05	16.95	51,600
CR7611	9.98	3.17	0.12	8.2	1235.20	901.76	17.11	107,000
CR7612	9.92	3.17	0.11	8.6	1282.63	933.74	17.40	193,210

TABLE 9c FATIGUE CRACK INITIATION DATA FOR CARBONITRIDED 080M15 CASE DEPTH 0.38 mm

Sample No.	Notch Depth mm	Notch Root radius mm	Crack length at initiation mm	Load range KN	$K_t \Delta s$ MN/m^2	$\frac{\Delta K}{\sqrt{\rho}}$ MN/m^2	ΔK_B $MN/m^{3/2}$	Ni
CN381	4.98	0.13	0.11	7.2	2430.7	2121.86	23.83	459,120
CN382	4.95	0.13	0.11	7.2	2393.96	2148.97	24.11	639,460
CN383	5.04	0.13	0.11	7.2	2478.74	2161.45	24.25	872,850
CN384	4.97	0.76	0.13	8.8	1352.61	1084.83	19.23	363,240
CN385	5.00	0.76	0.12	9.0	1389.58	1114.41	19.57	505,000
CN386	5.04	0.76	0.13	8.6	1334.07	1070.67	18.92	418,370
CN387	9.97	1.50	0.10	7.2	1447.64	1136.16	18.87	158,650
CN388	10.03	1.50	0.09	7.0	1442.69	1128.45	17.95	199,060
CN389	10.07	1.50	0.10	6.8	1388.52	1087.05	17.80	257.000
CN3810	9.95	3.17	0.11	7.8	1182.97	861.68	16.01	242,670
CN3811	10.0	3.17	0.11	7.6	1165.71	846.23	15.58	144,750
CN3812	9.95	3.17	0.11	7.6	1156.06	840.80	15.48	211,200

TABLE 9d FATIGUE CRACK INITIATION DATA FOR CARBONITRIDED 080M15 CASE DEPTH 0.76 mm

Sample No.	Notch Depth mm	Notch Root radius mm	Crack length at initiation mm	Load range KN	$K_t \Delta s$ MN/m^2	$\frac{\Delta K}{\sqrt{\rho}}$ MN/m^2	ΔK_B $MN/m^{3/2}$	Ni
CN761	4.97	0.13	0.11	7.2	2420.75	2113.48	23.76	168,770
CN762	5.01	0.13	0.11	6.8	2297.04	2002.79	22.47	244,290
CN763	4.96	0.13	0.11	6.8	2281.93	1992.51	22.40	177.550
CN764	5.00	0.76	0.12	8.0	1226.34	982.66	16.85	292.500
CN765	5.02	0.76	0.12	7.6	1177.03	944.61	16.51	173,780
CN766	5.02	0.76	0.12	7.8	1197.34	961.03	16.85	168,000
CN767	9.97	1.5	0.11	5.6	1136.78	894.87	15.63	185,000
CN768	9.97	1.5	0.11	5.8	1170.45	920.57	15.72	363,380
CN769	9.98	1.5	0.07	5.8	1166.68	913.50	13.32	195,900
CN7610	9.99	3.17	0.17	8.0	1205.63	885.37	19.79	241,270
CN7611	9.85	3.17	0.12	7.6	1119.13	818.67	15.81	835,630
CN7612	9.97	3.17	0.12	7.6	1140.43	831.61	16.06	156,000

TABLE 9e FATIGUE CRACK INITIATION DATA FOR NITROCARBURISED 080M15

Sample No.	Notch Depth mm	Notch Root radius mm	Crack length at initiation mm	Load range KN	$K_t \Delta s$ MN/m^2	$\frac{\Delta K}{\sqrt{\rho}}$ MN/m^2	ΔK_B $MN/m^{3/2}$	Ni
NC371	4.94	0.13	0.11	4.4	1515.80	1319.15	14.83	191,000
NC372	4.98	0.13	0.11	4.4	1489.39	1300.5	14.65	195,000
NC373	4.97	0.13	0.11	4.4	1483.69	1294.7	14.57	188,000
NC374	5.05	0.76	0.13	7.0	1077.3	865.42	15.46	610,000
NC375	4.95	0.76	0.13	7.0	1072.03	860.81	15.52	862,880
NC376	4.98	0.76	0.14	6.8	1038.93	834.85	15.19	481,000
NC377	10.01	1.52	0.11	5.2	1060.55	832.14	14.21	646,250
NC378	9.95	1.52	0.10	5.2	1040.80	817.58	13.26	610,570
NC379	9.90	1.52	0.09	5.4	1078.72	847.63	13.45	182,000
NC3710	10.01	3.17	0.12	7.2	1108.39	804.82	15.18	191,000
NC3711	9.97	3.17	0.12	7.2	1098.85	801.33	15.43	180,000
NC3712	10.03	3.17	0.12	7.2	1084.44	789.67	15.25	155,000

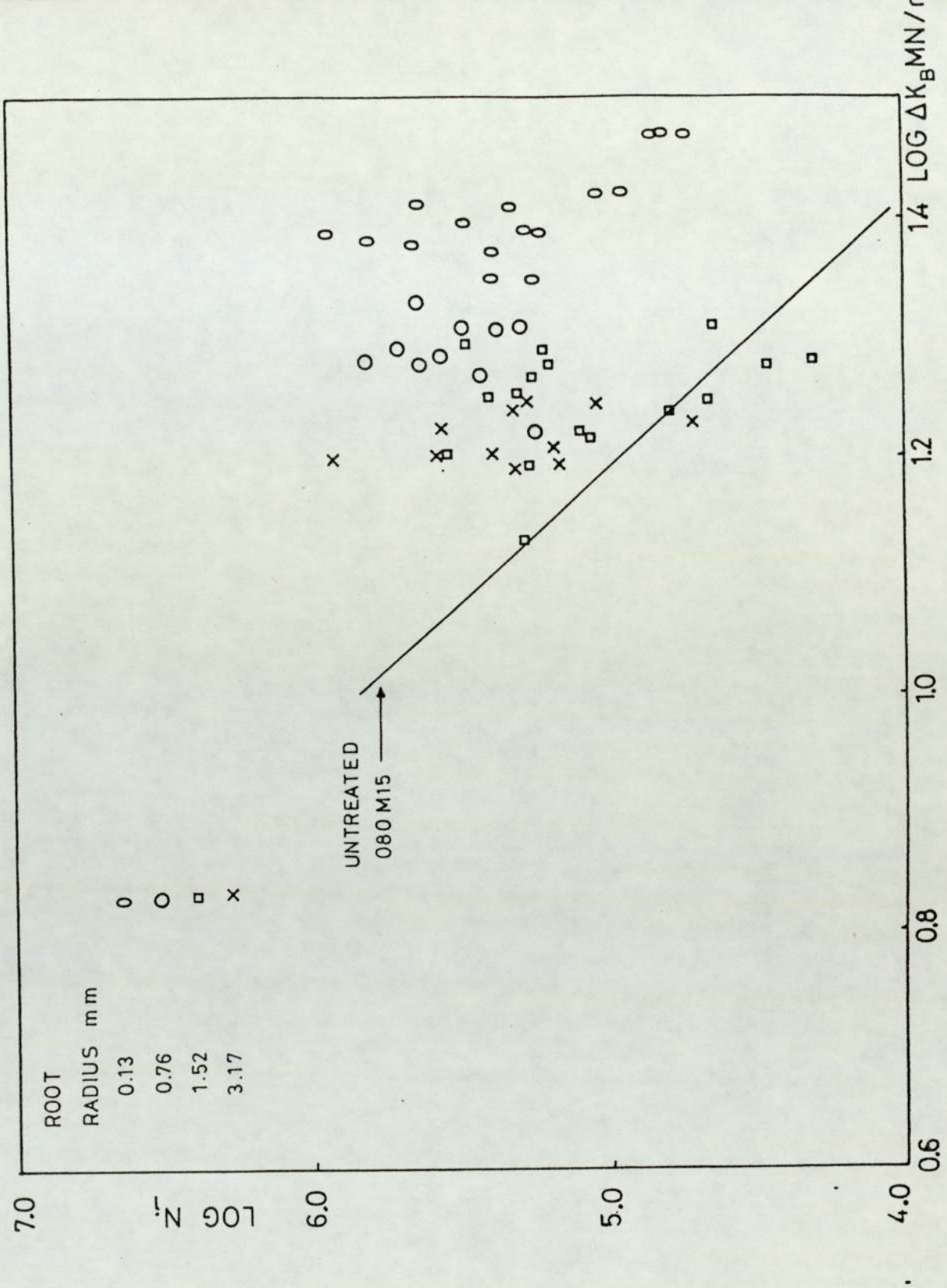

FIGURE 25 Fatigue crack initiation data for carburised and carbonitrided 080M15: parameter ΔK_B

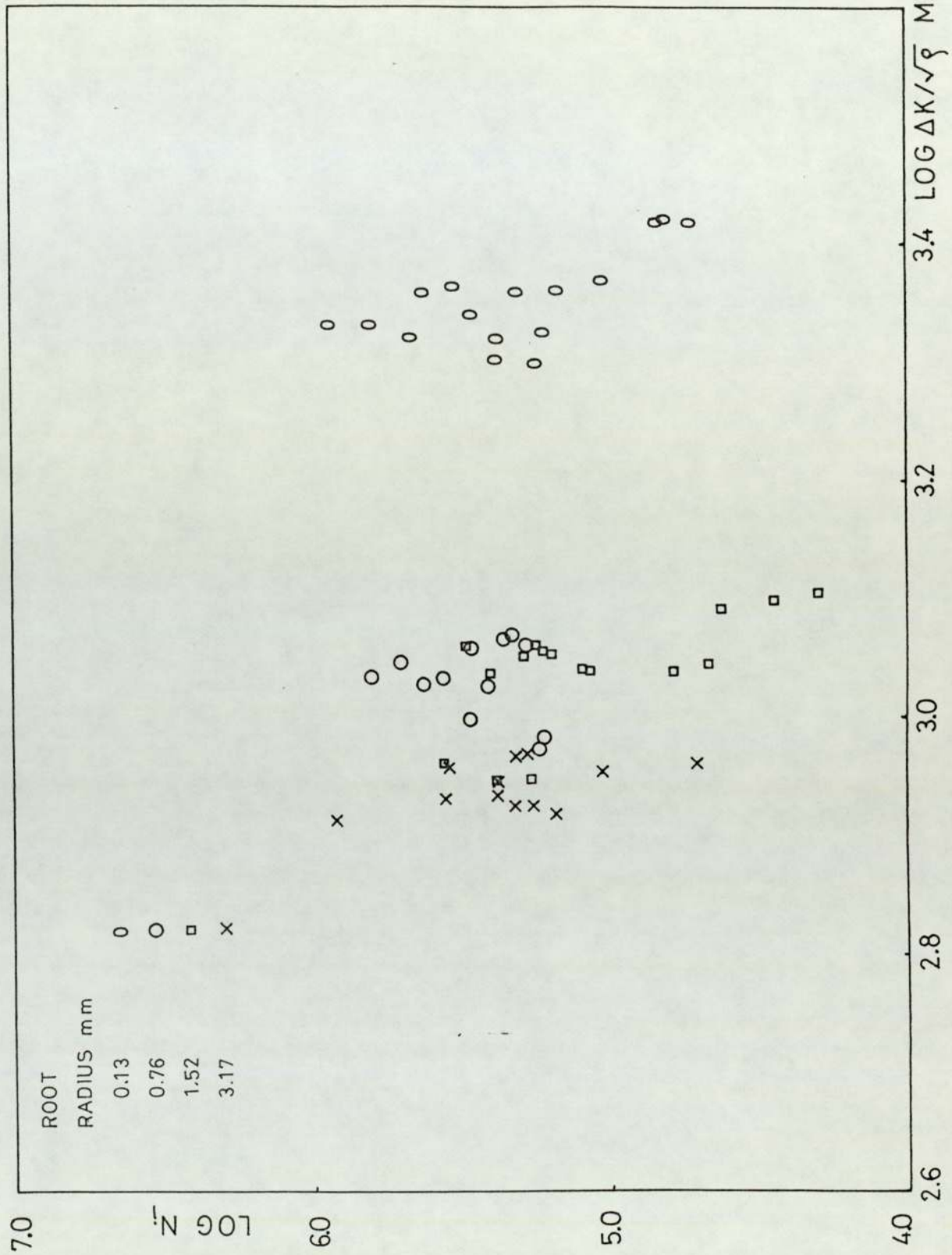

FIGURE 26 Fatigue crack initiation data for carburised and carbonitrided 080M15: parameter $\Delta K/\sqrt{\rho}$

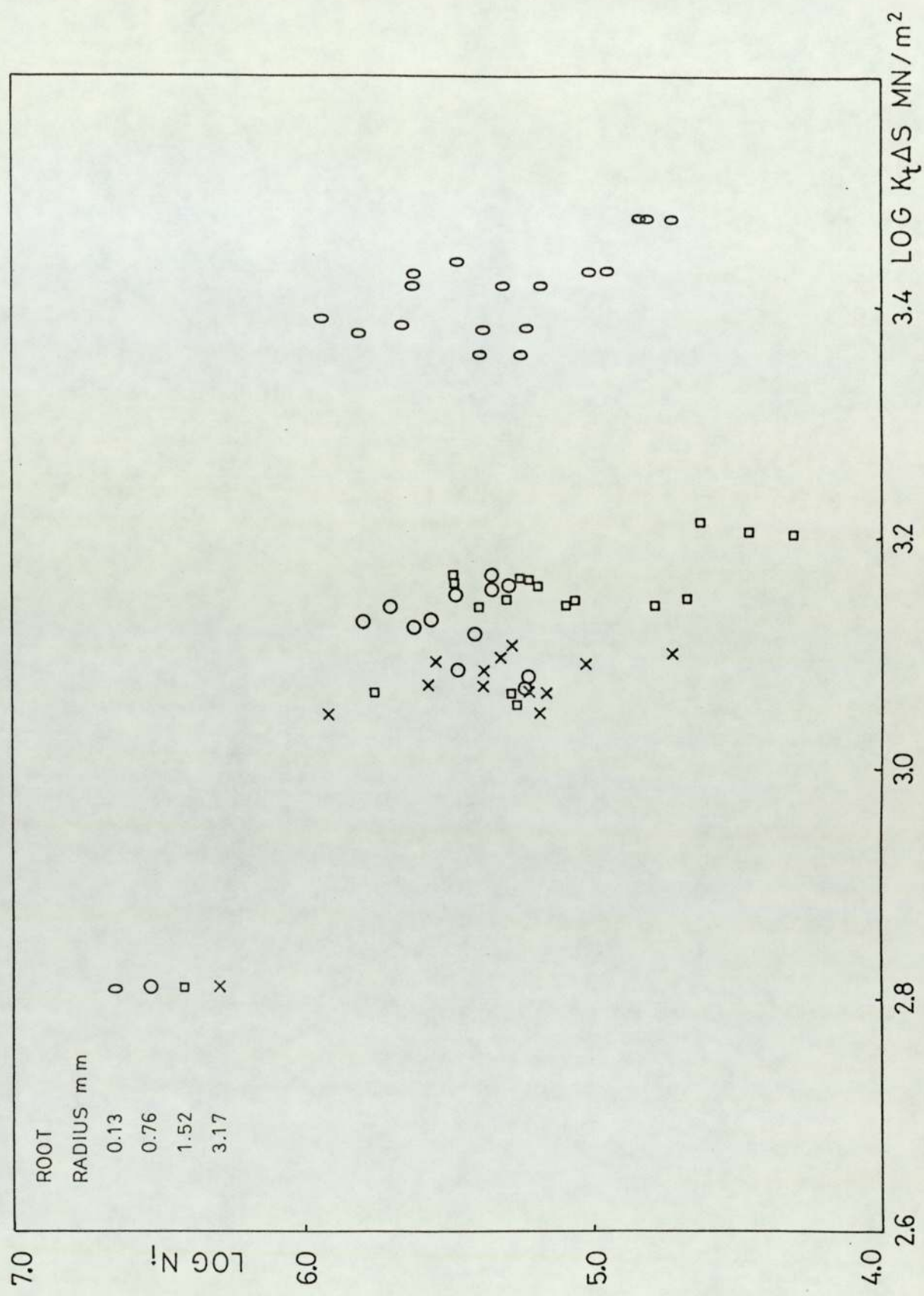

FIGURE 27 Fatigue crack initiation data for carburised and carbonitrided 080M15: parameter $K_t\Delta s$

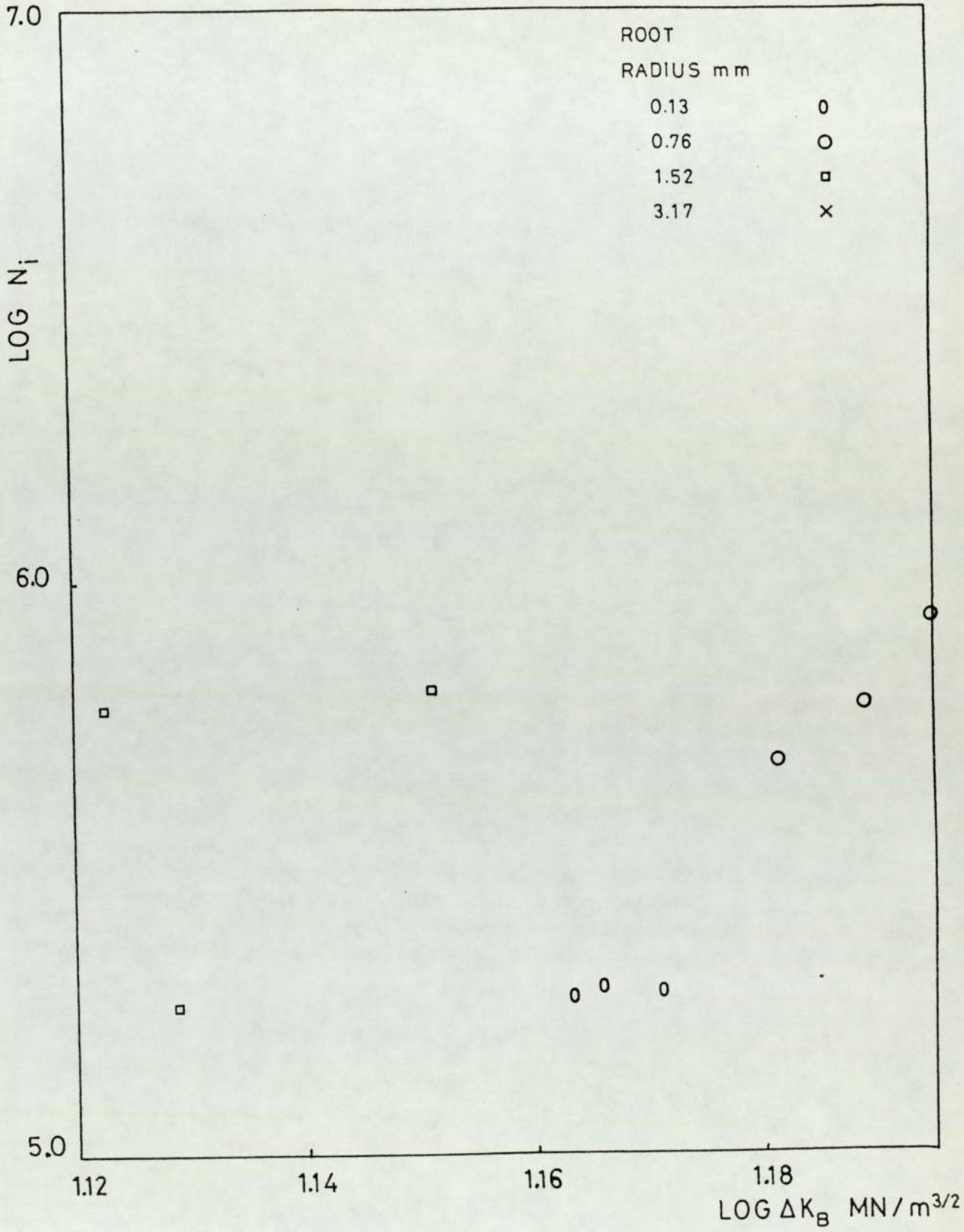

FIGURE 28 Fatigue crack initiation data for nitrocarburised 080M15: parameter ΔK_B

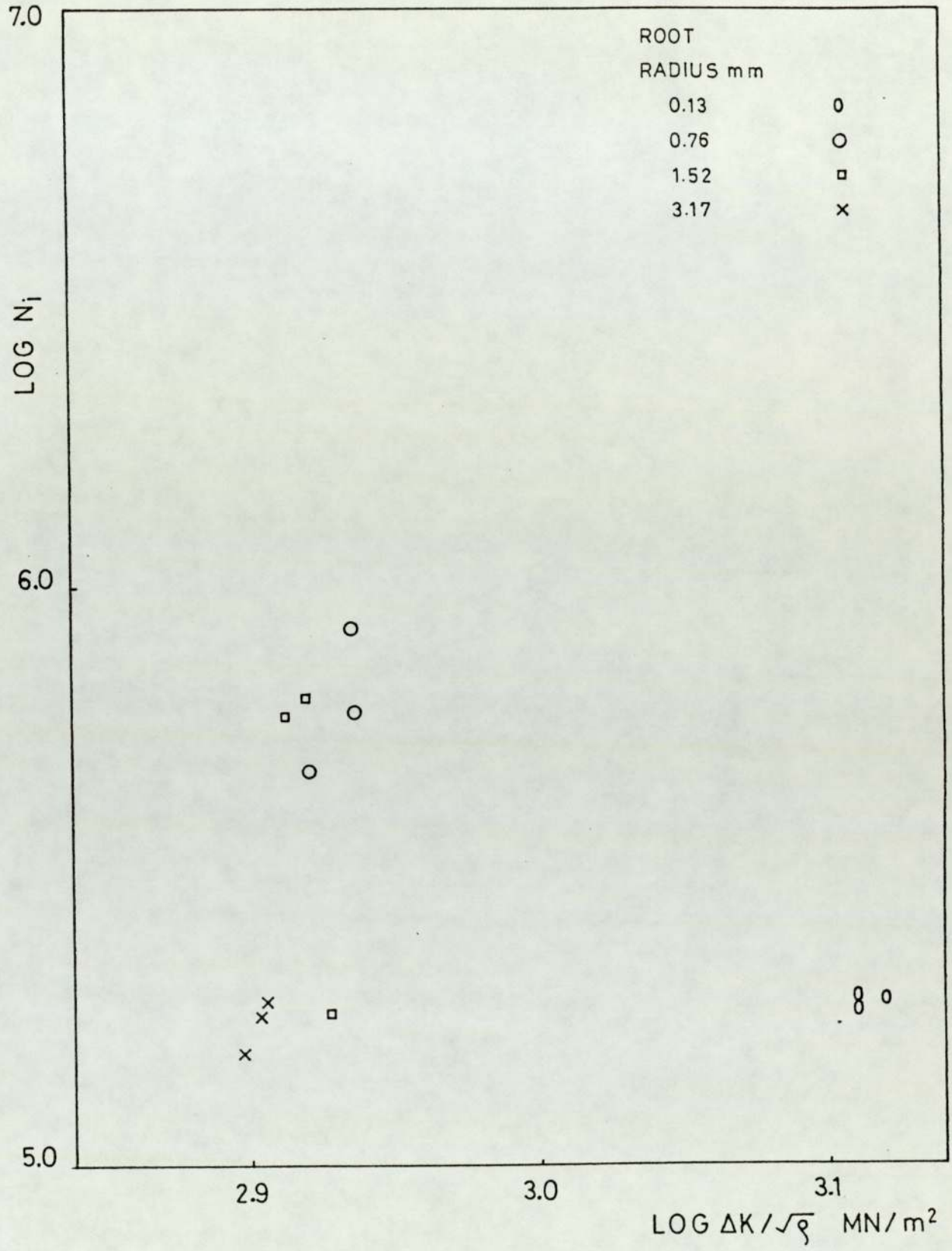

FIGURE 29 Fatigue crack initiation data for nitrocarburised 080M15: parameter $\Delta K/\sqrt{\rho}$

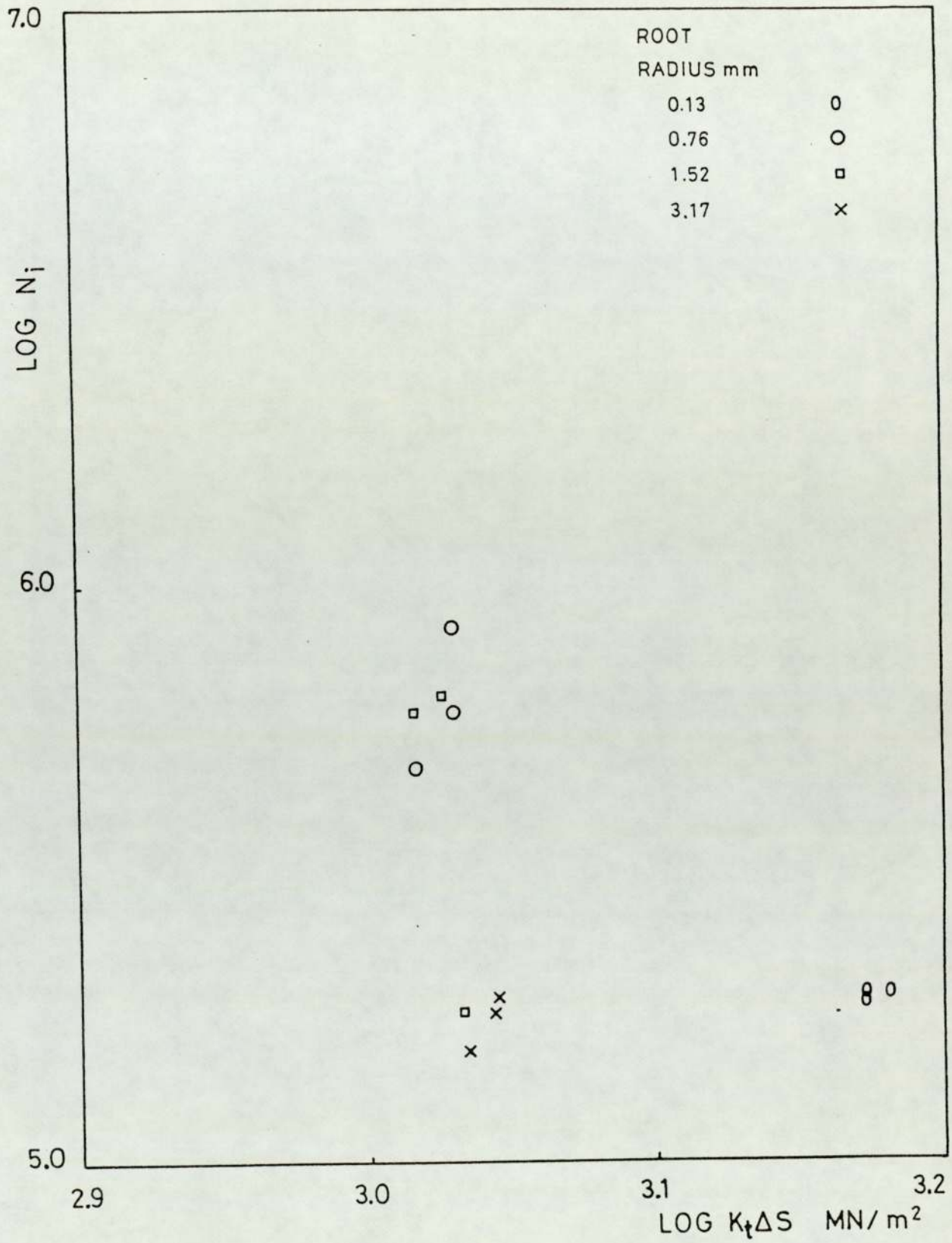

FIGURE 30 Fatigue crack initiation data for nitrocarburised 080M15: parameter $K_t\Delta s$

The linear regression line for the untreated 080M15 is also plotted for comparison. It can be seen that above a certain level of the parameter the untreated material shows higher values of Ni, the number of cycles to initiation, than does the case hardened material.

The initiation data for the nitrocarburised 080M15 did not show correlation between the number of cycles to initiation and the parameters $K_t\Delta s$ and $\frac{\Delta K}{\sqrt{\rho}}$. For the parameter ΔK_B, however, a horizontal line was obtained. This indicates that the number of cycles to initiation is unaffected by the parameter ΔK_B in the range of ΔK_B considered.

6.3.3 Initiation Fatigue Crack in Case Hardened 080A47

The results are presented in Table 10 which lists the notch depth, root radius, load range, the parameters $K_t\Delta s$, $\frac{\Delta K}{\sqrt{\rho}}$ and ΔK_B, and the number of cycles to initiation N_i. The results are presented graphically in Figures 31 to 33. The value of the material parameter C_B is the experimentally determined prior austentic grain size (22 μm). The initiation of a crack resulted in final fracture in very few cycles. Thus initiation and failure could be treated as virtually simultaneous events. The initiation criterion was therefore the first deflection observed on the electrical potential versus time trace. The scatter observed in the test results made analysis of these results on the statistical basis irrelevant.

TABLE 10 FATIGUE CRACK INITIATION DATA FOR INDUCTION HARDENED 080A47

Sample No.	Notch Depth mm	Notch Root radius mm	Load KN	$K_t \Delta s$ MN/m^2	$\frac{\Delta K}{\sqrt{\rho}}$ MN/m^2	$\Delta K_{B_{3/2}}$ MN/m	Ni or N_f
I 131	4.90	0.36	18.0	3786.5	3196.83	21.91	248,000
I 132	4.90	0.36	18.0	3794.12	3203.24	21.95	221,000
I 133	4.90	0.36	18.0	3805.56	3213.90	22.02	254,000
I 134	4.88	0.36	17.0	3568.90	3013.59	20.65	700,000
I 135	4.85	0.36	17.0	3557.34	3004.37	20.60	820,000
I 136	4.85	0.36	17.0	3560.04	3005.85	20.61	754,000

TABLE 10 (CONTINUED)

Sample No.	Notch Depth mm	Notch Root radius mm	Load KN	$K_t \Delta s$ MN/m^2	$\frac{\Delta K}{\sqrt{\rho}}$ MN/m^2	ΔK_B $MN/m^{3/2}$	Ni or N_f
I 761	5.08	0.76	20.0	3164.66	2501.11	17.76	90,000
I 762	5.18	0.76	20.0	3187.34	2519.36	17.87	220,000
I 763	5.15	0.76	20.0	3178.34	2511.75	17.82	150,000
I 764	5.15	0.76	18.0	2859.74	2259.46	16.03	377,000
I 765	5.13	0.76	18.0	2846.71	2250.76	15.97	408,000
I 766	5.16	0.76	18.0	2866.20	2266.61	16.08	385,000

TABLE 10 (CONTINUED)

Sample No.	Notch Depth mm	Notch Root radius mm	Load KN	$K_t \Delta s$ MN/m^2	$\frac{\Delta K}{\sqrt{\rho}}$ MN/m^2	ΔK_B $MN/m^{3/2}$	Ni or N_f
I 1521	10.14	1.7	10.0	2110.39	1536.05	10.99	780,000
I 1522	10.14	1.7	10.0	2123.04	1545.27	11.06	680,000
I 1523	10.05	1.7	10.0	2089.14	1525.02	10.92	90,000
I 1524	10.10	1.7	8.80	1857.50	1353.83	9.69	280,000
I 1525	10.15	1.7	8.8	1866.76	1361.69	9.74	242,000
I 1526	10.08	1.7	7.6	1598.95	1166.06	8.35	435,000
I 1527	10.22	1.7	7.4	1589.23	1153.72	8.25	1378,000
I 1528	10.08	1.7	7.6	1597.37	1164.89	8.34	738,000

TABLE 10 (CONTINUED)

Sample No.	Notch Depth mm	Notch Root radius mm	Load KN	$K_t \Delta s$ MN/m^2	$\frac{\Delta K}{\sqrt{\rho}}$ MN/m^2	ΔK_B $MN/m^{3/2}$	Ni or N_f
I 3171	9.97	3.17	10.0	1541.91	1105.74	8.38	21,000
I 3172	10.00	3.17	10.0	1557.27	1114.67	8.45	4,000
I 3173	10.09	3.17	8.6	1352.49	965.65	7.31	248,000
I 3174	10.24	3.17	8.6	1389.65	987.67	7.47	351,000
I 3175	10.10	3.17	7.4	1176.24	838.22	6.35	873,000
I 3176	10.05	3.17	7.6	1192.30	852.03	6.46	816,000
I 3177	10.18	3.17	7.0	1119.12	796.34	6.02	1190,000

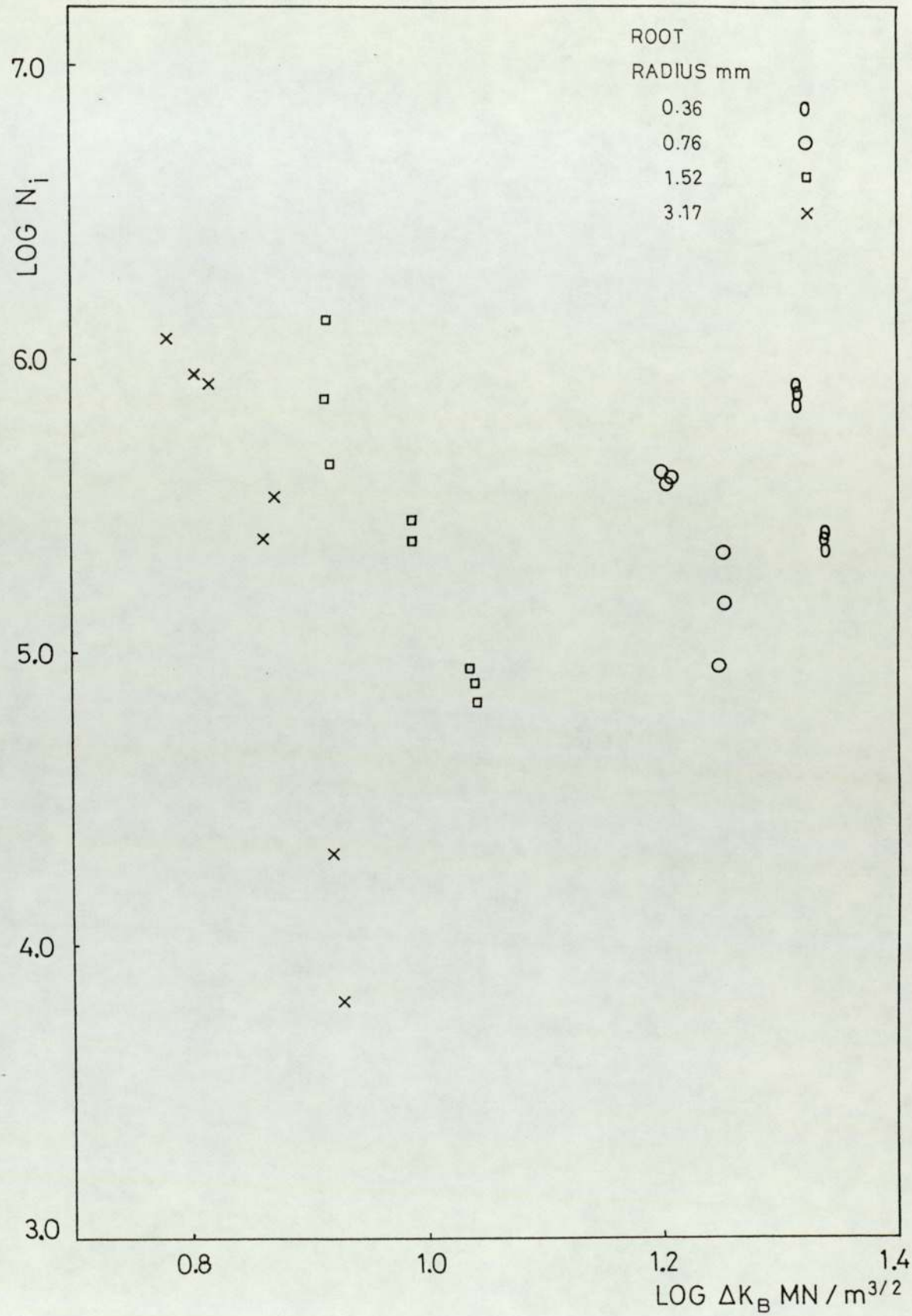

FIGURE 31 Fatigue crack initiation data for induction hardened 080A47: parameter ΔK_B

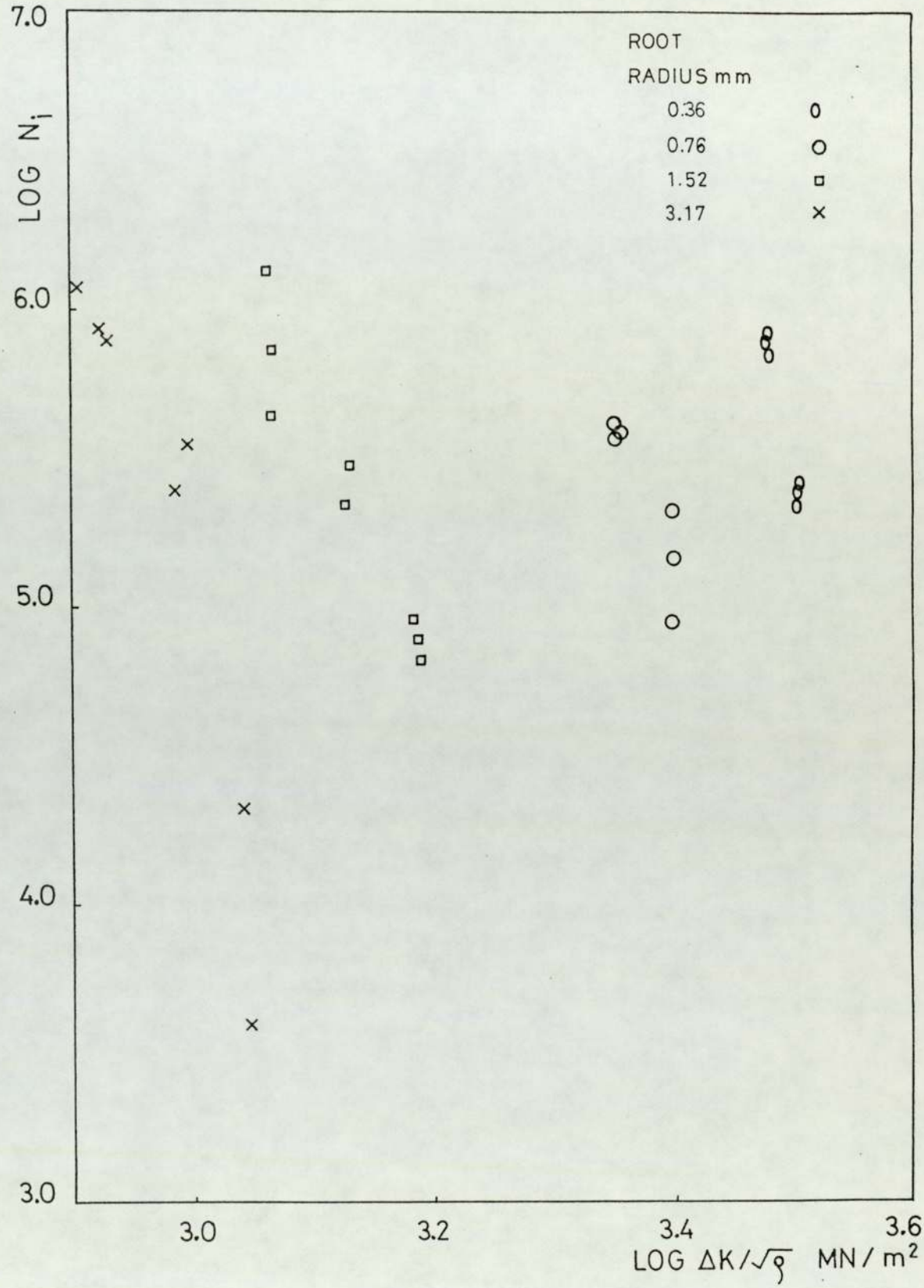

FIGURE 32 Fatigue crack initiation data for induction hardened 080A47: parameter $\Delta K/\sqrt{\rho}$

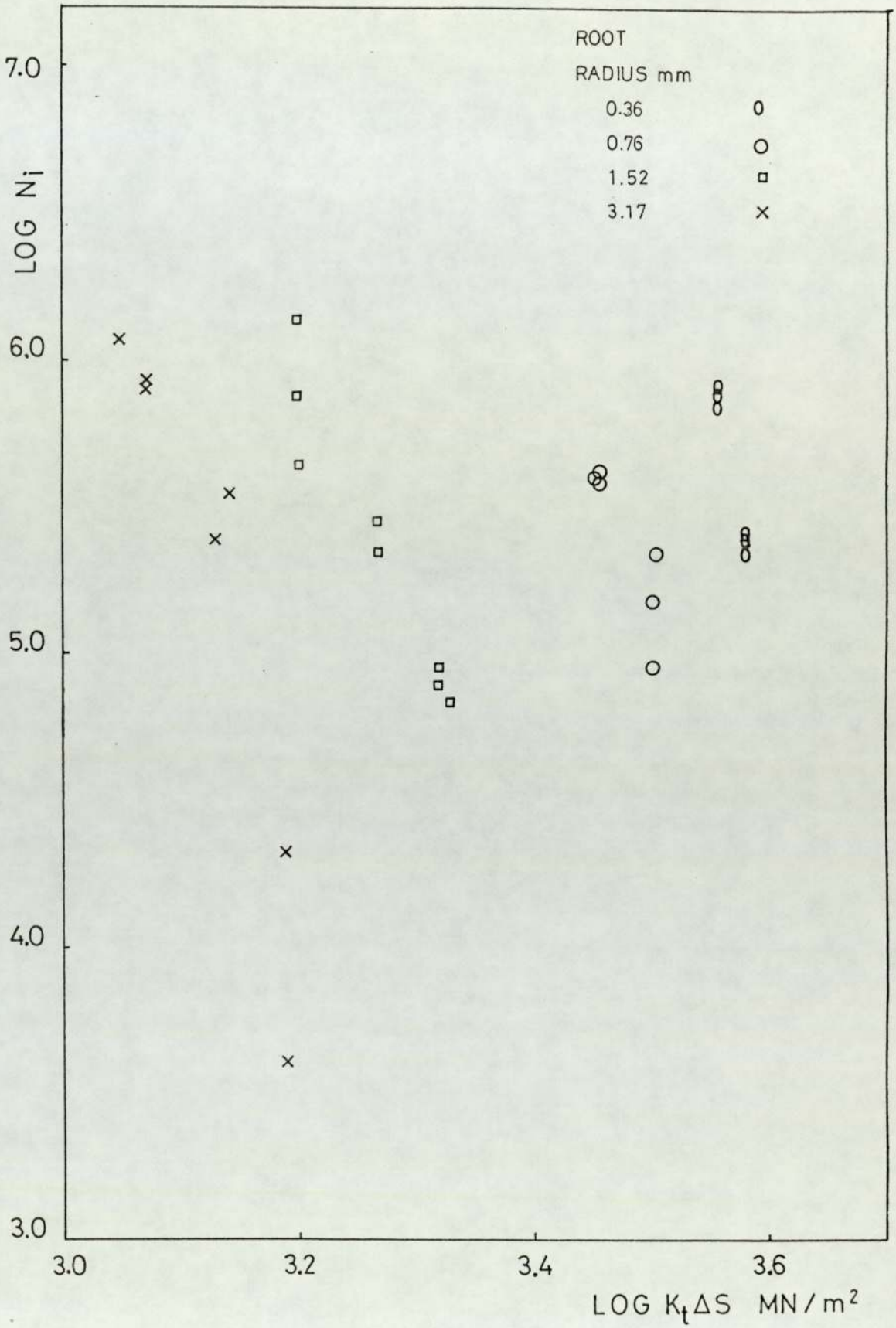

FIGURE 33 Fatigue crack initiation data for induction hardened 080A47: parameter $K_t \Delta s$

6.4 Fatigue Crack Propagation in Case Hardened 080M15

The summary of results is presented in Figures 34-38. The method of calculating the crack propagation rate is the same as that explained in section 6.2.1. The values of the stress intensity factor range were calculated by incorporating the modification factor $B_m = Y_S/Y_L$ as predicted by equation (33) or using equation (30) in conjunction with equation (32). Figure 39 illustrates the variation of the crack propagation rate $\frac{da}{dN}$ with the stress intensity factor range when the modification factor is not considered, i.e. the geometric length of notch plus crack is assumed to be a long crack. The results are plotted for different values of load ranges. It can be seen that for each load range a fatigue crack growth threshold is exhibited. The same values when the modification is incorporated are also plotted. The values with the modified stress intensity factor range lie on a straight line which can be represented by the Paris Law. The data represent the crack propagation in the first 2 mm of crack length in front of a notch. In the cited work [33,35], a point of inflection was observed in this period of crack growth. Such behaviour was not observed. Further, it was suggested [35], that this behaviour becomes more apparent when the crack propagation rates are plotted as a function of crack length. Figures 40 and 41 present the crack propagation rates of short cracks emanating from notches in carburised 080M15. The point of inflection was not observed in these cases. Similar behaviour was also observed for other case hardening treatments considered.

LEGEND FOR FIGURES 34 to 38

NOTCH DEPTH mm	ROOT RADIUS mm	
5	0.13	o
5	0.76	o
10	1.52	□
10	3.17	×

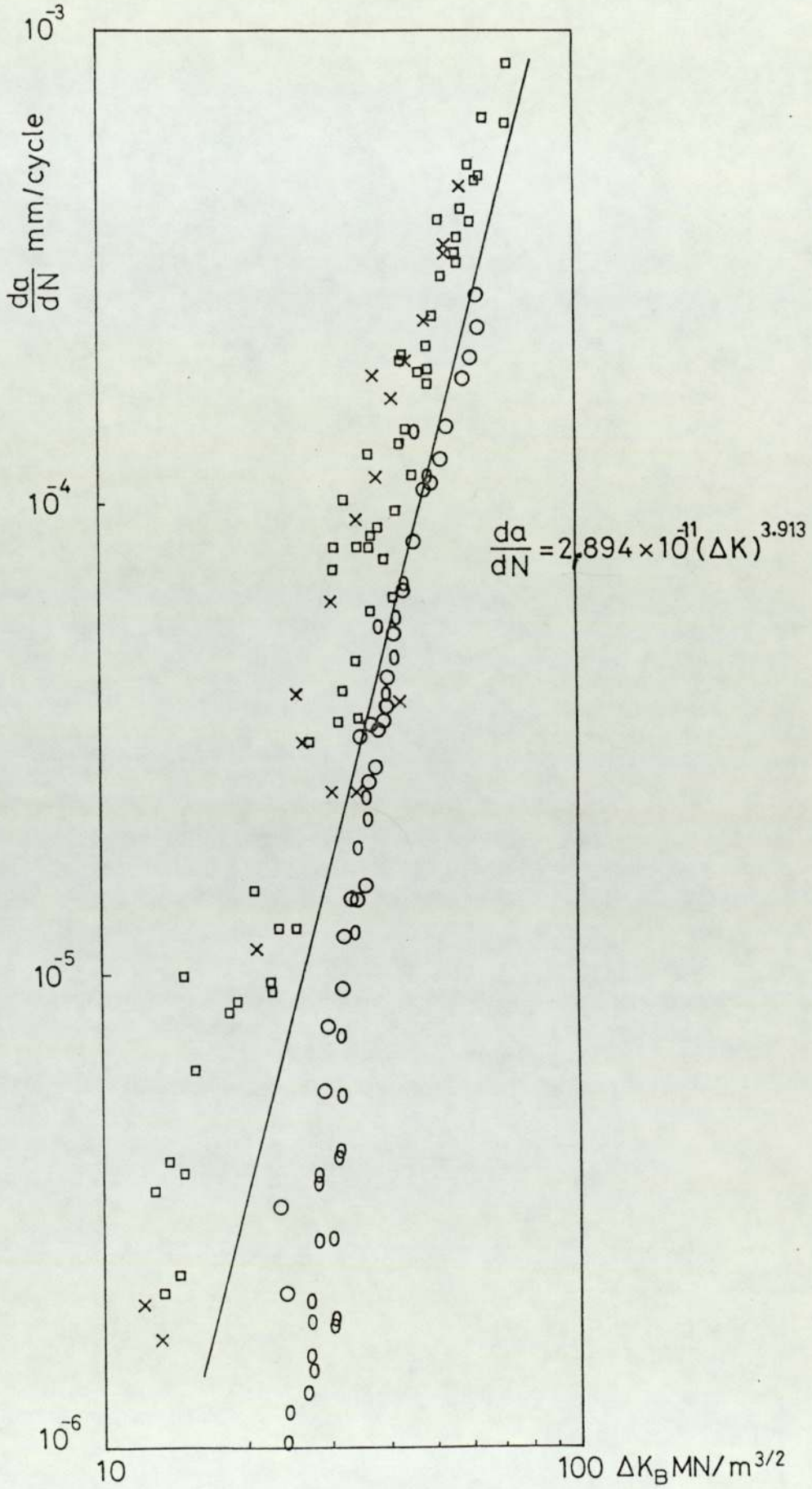

FIGURE 34 Fatigue crack propagation data of carburised 080M15: case depth 0.38 mm

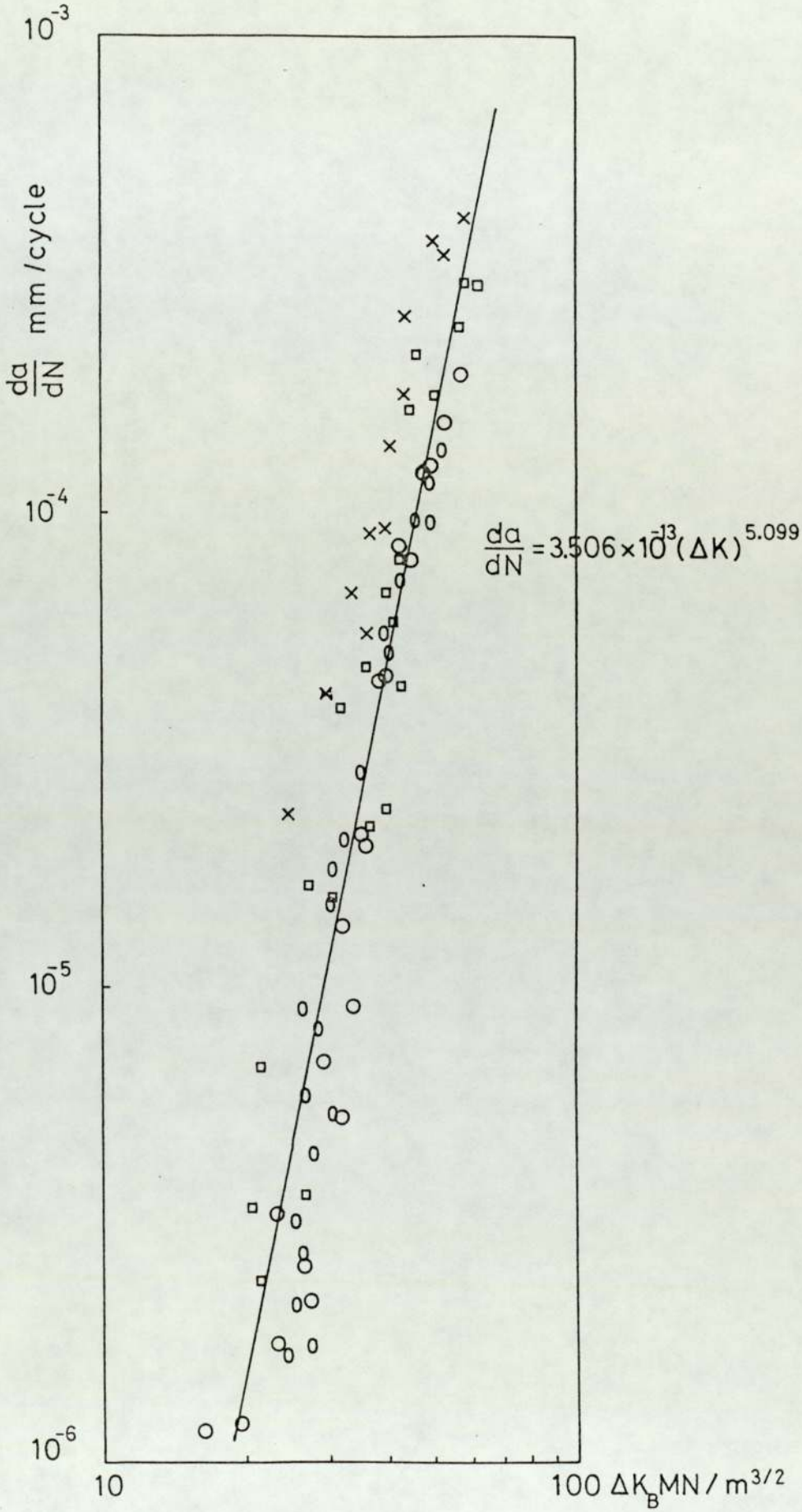

FIGURE 35 Fatigue crack propagation data of carburised 080M15: case depth 0.76 mm

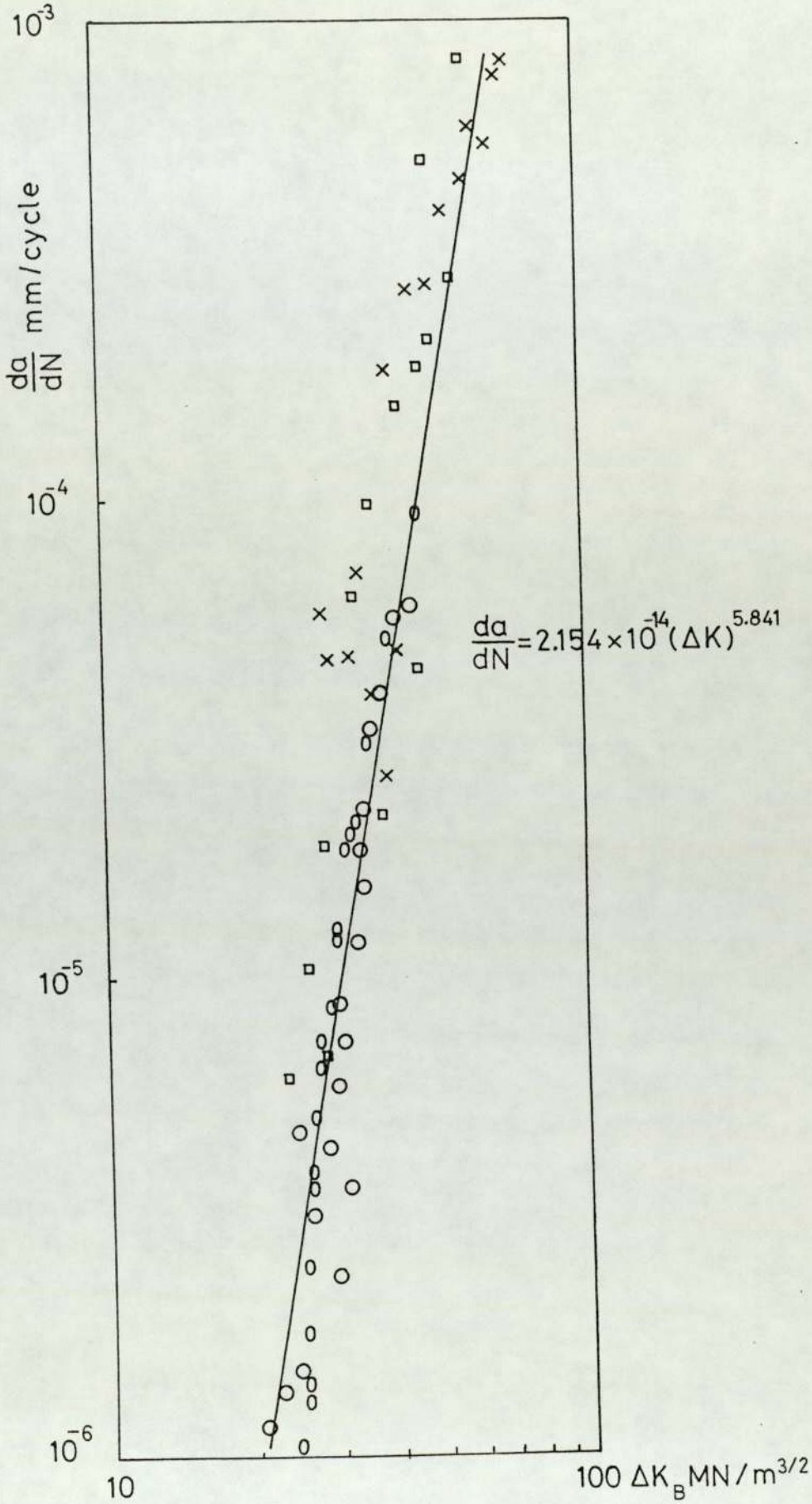

FIGURE 36 Fatigue crack propagation data of carbonitrided 080M15: case depth 0.38 mm

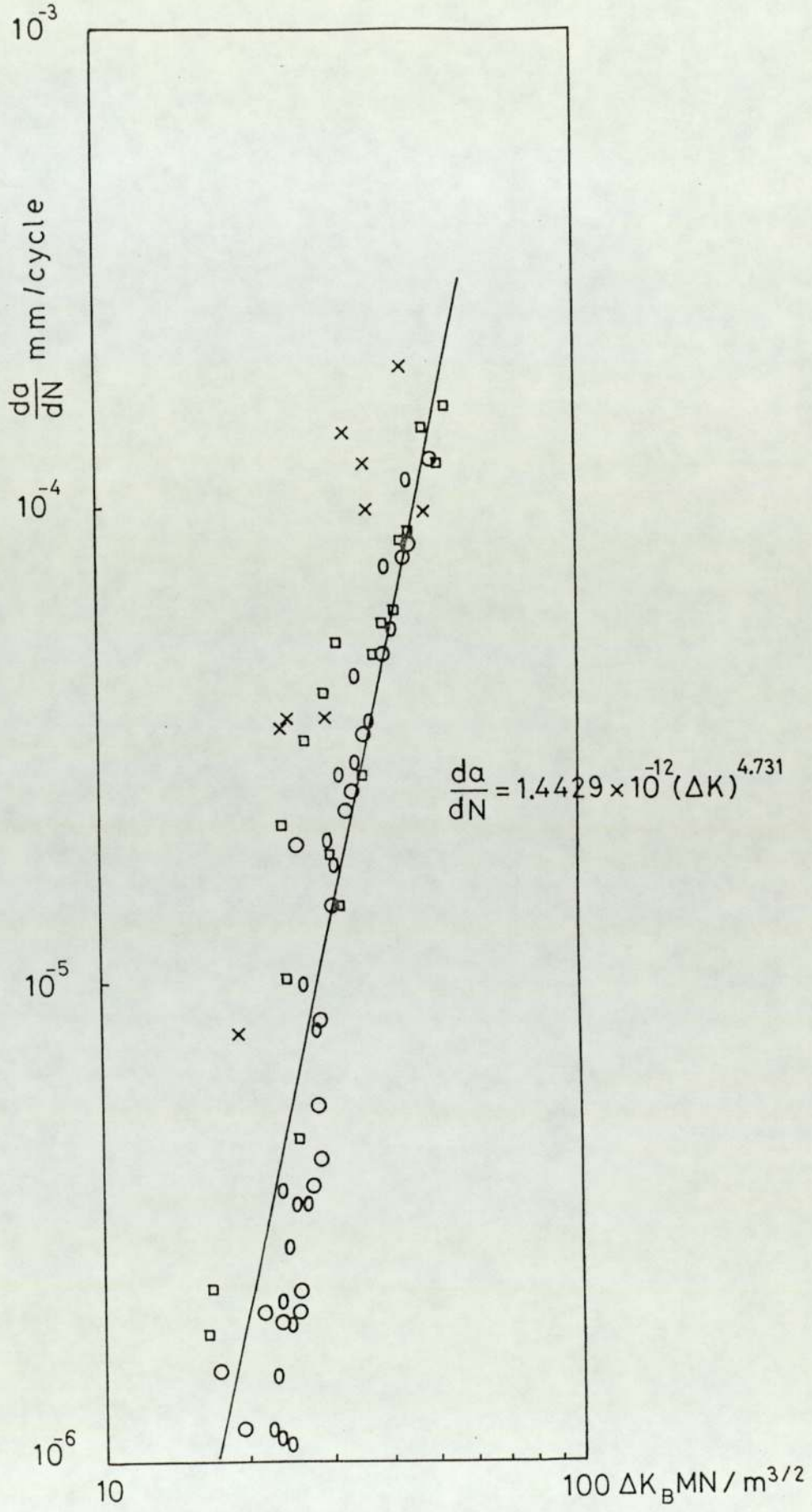

FIGURE 37 Fatigue crack propagation data of carbonitrided 080M15: case depth 0.76 mm

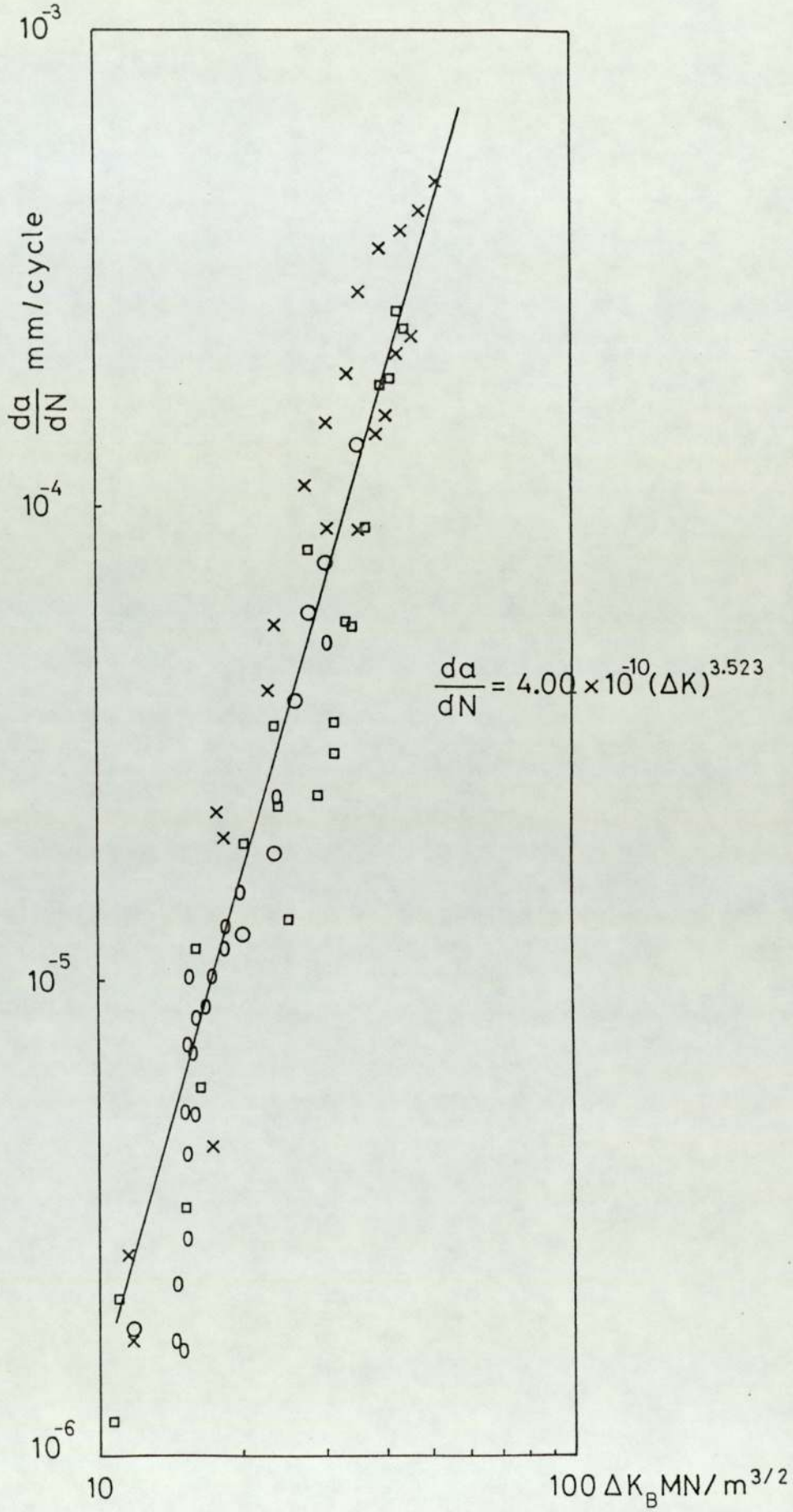

FIGURE 38 Fatigue crack propagation data of nitrocarburised 080M15

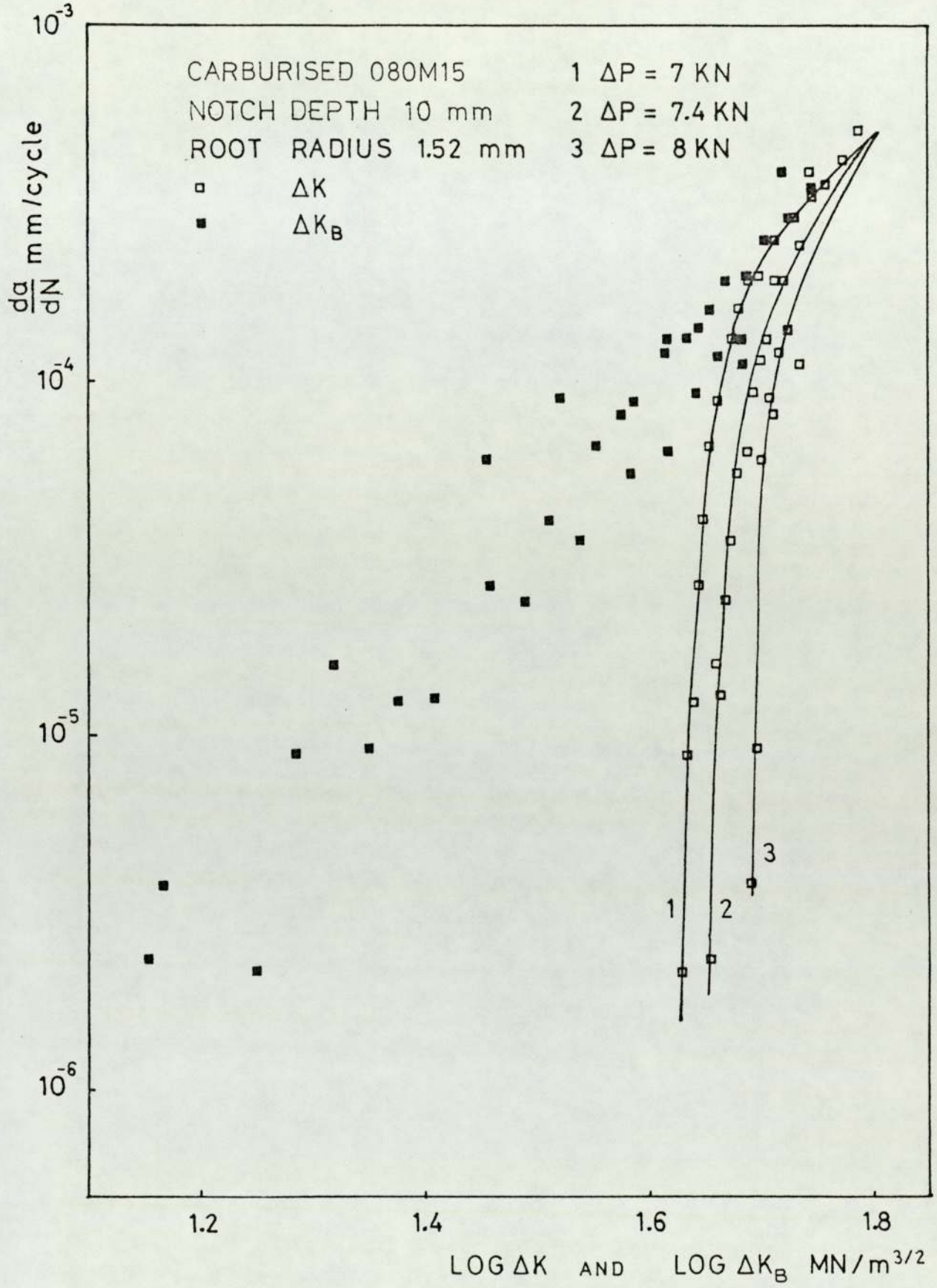

FIGURE 39 Fatigue crack propagation data of 080M15 as a function of unmodified and modified stress intensity factor range (case depth 0.38 mm, notch depth 10 mm, root radius 1.52 mm)

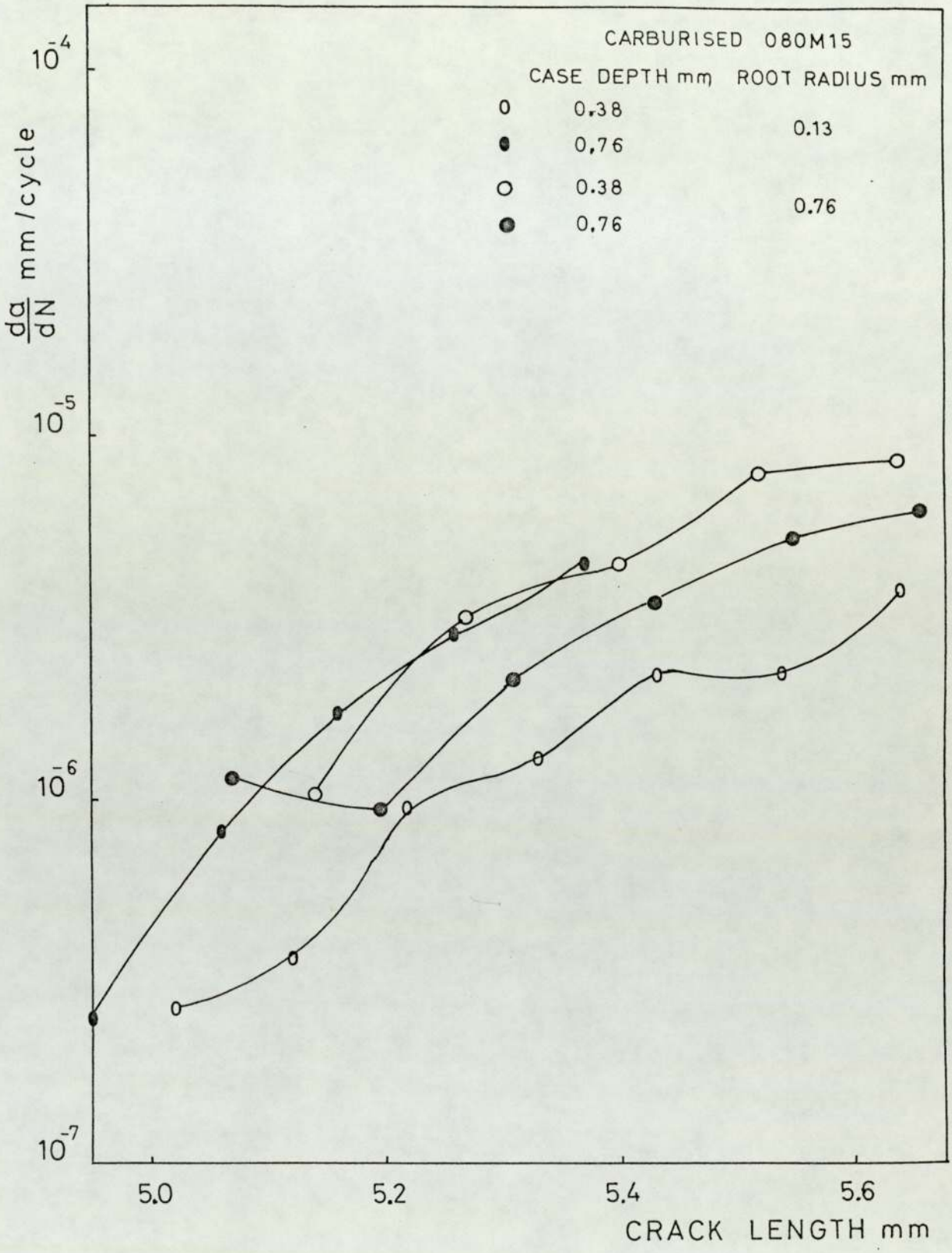

FIGURE 40 Fatigue crack propagation data of carburised 080M15 as a function of crack length (notch depth 5 mm, root radii 0.13 mm and 0.76 mm)

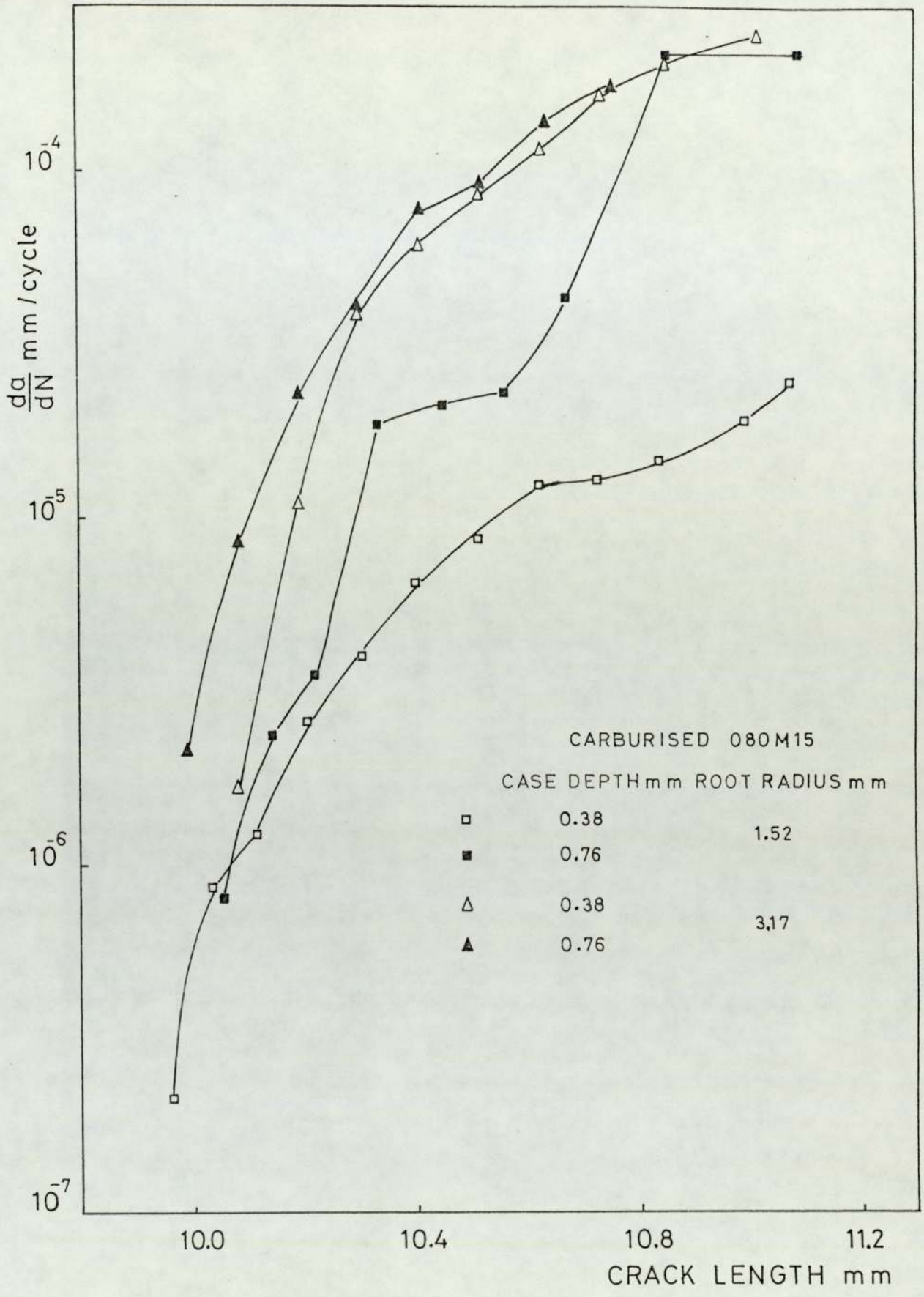

FIGURE 41 Fatigue crack propagation data of carburised 080M15 as a function of crack length (notch depth 10 mm, root radii 1.52 mm and 3.17 mm)

The fatigue crack propagation data for various case hardening treatments can be represented by the Paris equation

$$\frac{da}{dN} = C(\Delta K_B)^n$$

The value of the constants C and n are as follows:

Treatment	n	C
Carburised case 0.38 mm	3.913	$2.894 * 10^{-11}$
Carburised case 0.76 mm	5.099	$3.506 * 10^{-13}$
Carbonitrided case 0.38 mm	5.841	$2.154 * 10^{-14}$
Carbonitrided case 0.76 mm	4.730	$1.443 * 10^{-12}$
Nitempered	3.523	$4.000 * 10^{-10}$

The crack propagation rate is in mm/cycle and the stress intensity factor range is in $MN/m^{3/2}$.

6.5 Composition and Hardness Gradient

6.5.1 Carbon Gradient

The use of the electron microprobe analyser to measure the carbon content of steel is a technique which is liable to very large experimental errors if enough care is not exercised in the calibration of the equipment. This is due to the characteristic carbon X-ray emission from the sample being small, which is a consequence of a relatively low carbon concentration present in the steel and a high absorbtion of carbon X-rays by the iron matrix. This results in a small X-ray emission (counts/sec less than 150), compared to in excess of a thousand which is normally

encountered for other alloying elements in steel. The calibration curve was obtained by measuring the X-ray emission from carbon steel standards containing 0.145% C, 0.20% C, 0.265% C, 0.53% C, 0.63% C, 0.79% C, and 0.99% C. This calibration procedure was carried out before each series of carbon determination.

A typical plot of number of counts obtained at successive positions away from the notch root at the midsection is shown in Figure 42. As can be seen, the graphical output has a fairly wide scatter and the mean of this curve was taken to represent the carbon gradient. The carbon gradient was calculated using the calibration curve already established. Four such determinations were also carried out apart from the one at the midsection, for each sample to ensure that the carbon gradients did not vary depending on the position at which it was determined. It was found that the variation in the carbon gradient at different positions along the notch root was negligible.

A summary of results obtained for different heat treatments and notch geometries is presented in Figures 43-46. The total case depths obtained for different case hardening methods from Figures 43-46 is presented in Table 11. Though the total case depth for a particular treatment was the same for different notches, the variation in the carbon weight percent was different. For the carburised samples the geometry of the notch did not make an appreciable difference to the carbon gradients. In the

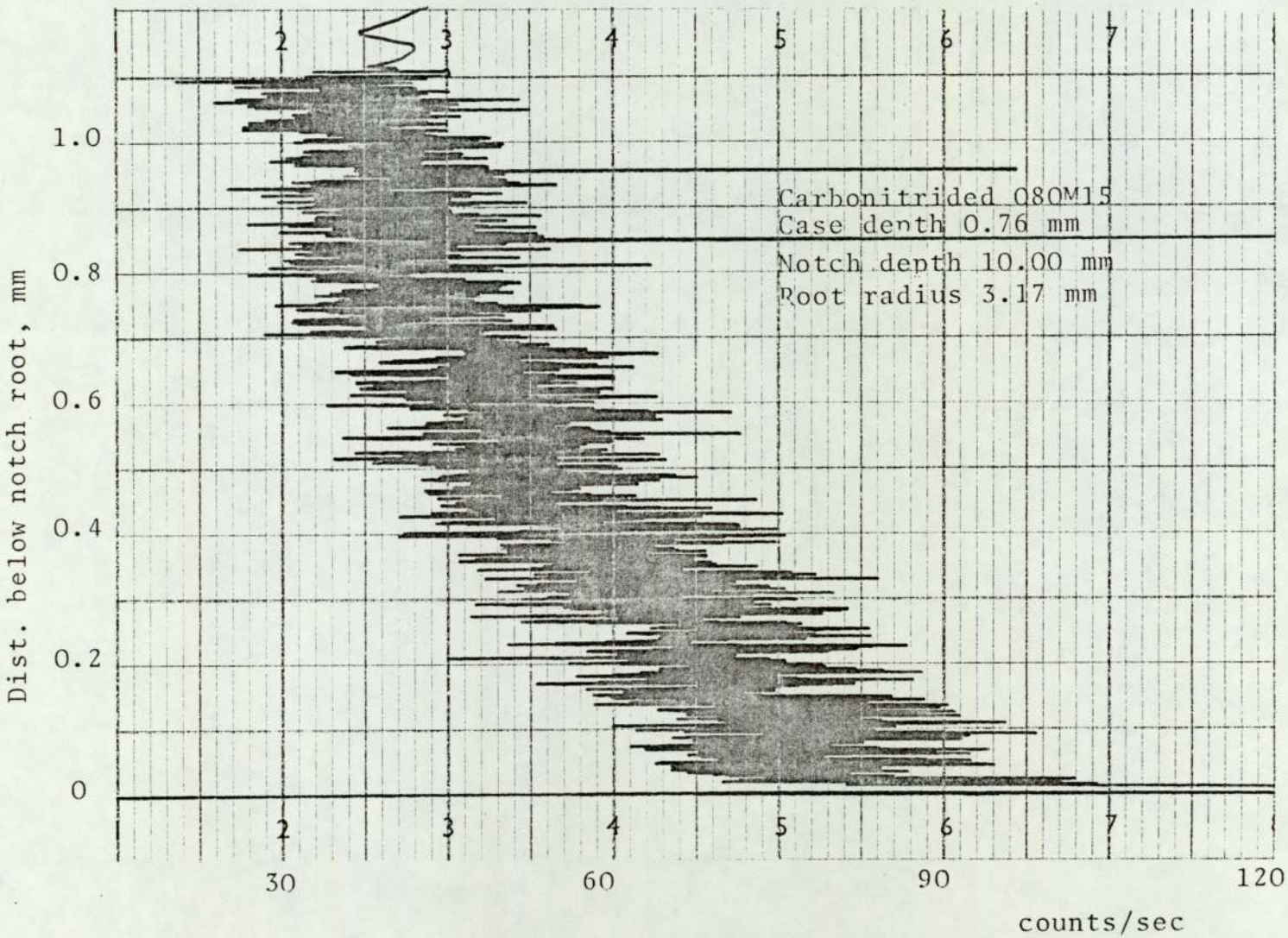

FIGURE 42 A representative plot of number of counts obtained from electron microprobe analyser to determine the carbon gradient at the notch root

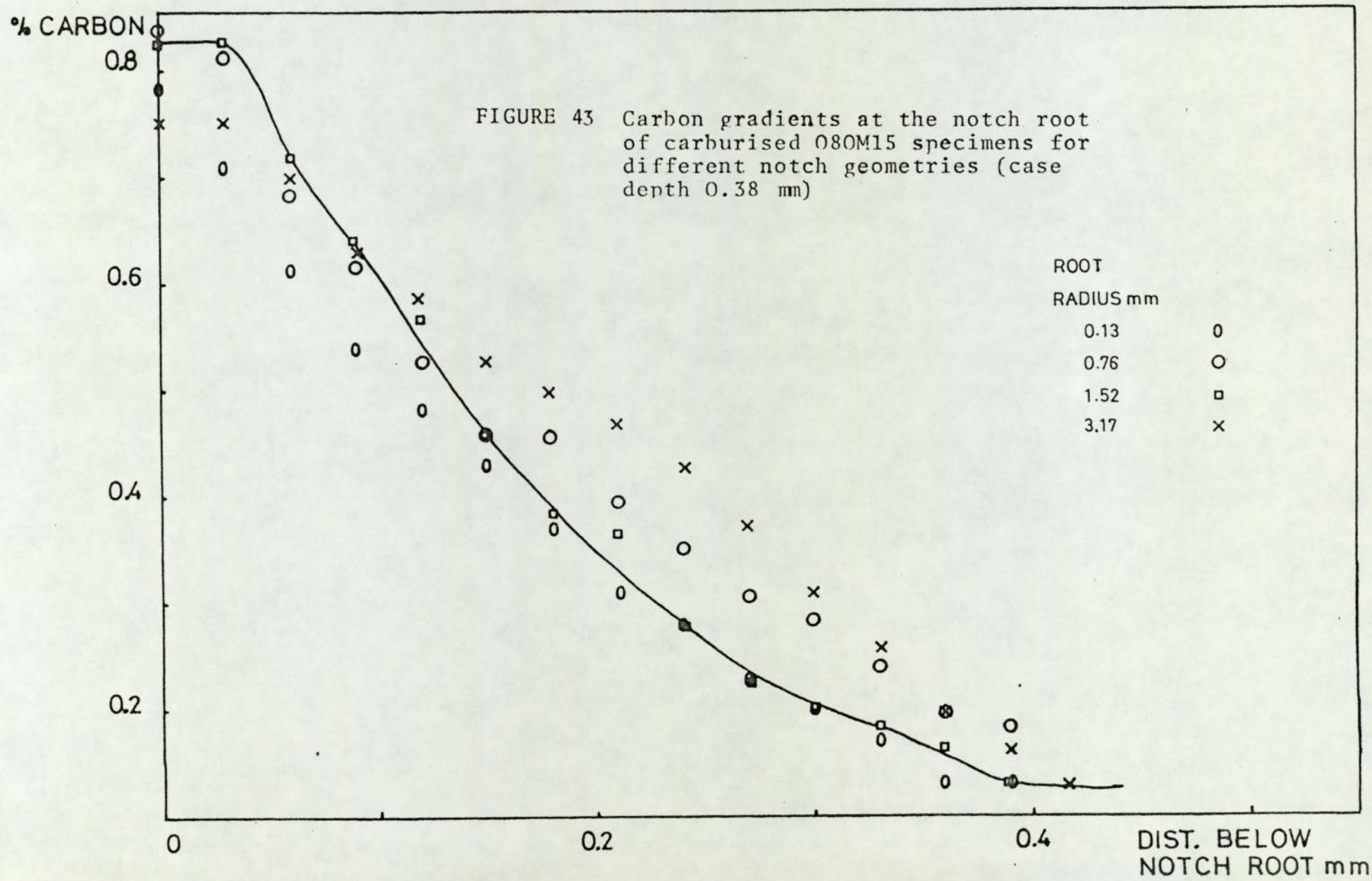

FIGURE 43 Carbon gradients at the notch root of carburised 080M15 specimens for different notch geometries (case depth 0.38 mm)

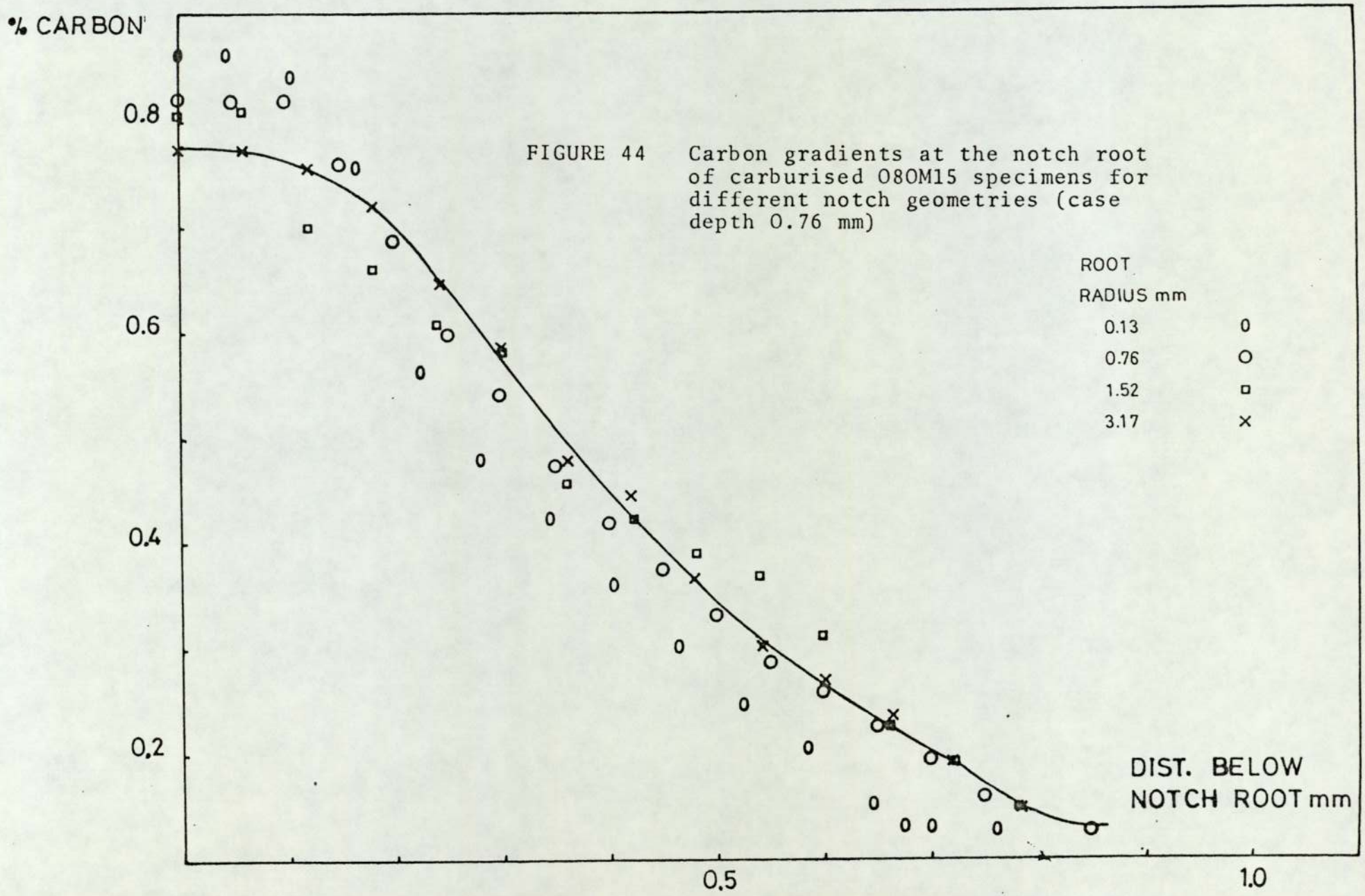

FIGURE 44 Carbon gradients at the notch root of carburised 080M15 specimens for different notch geometries (case depth 0.76 mm)

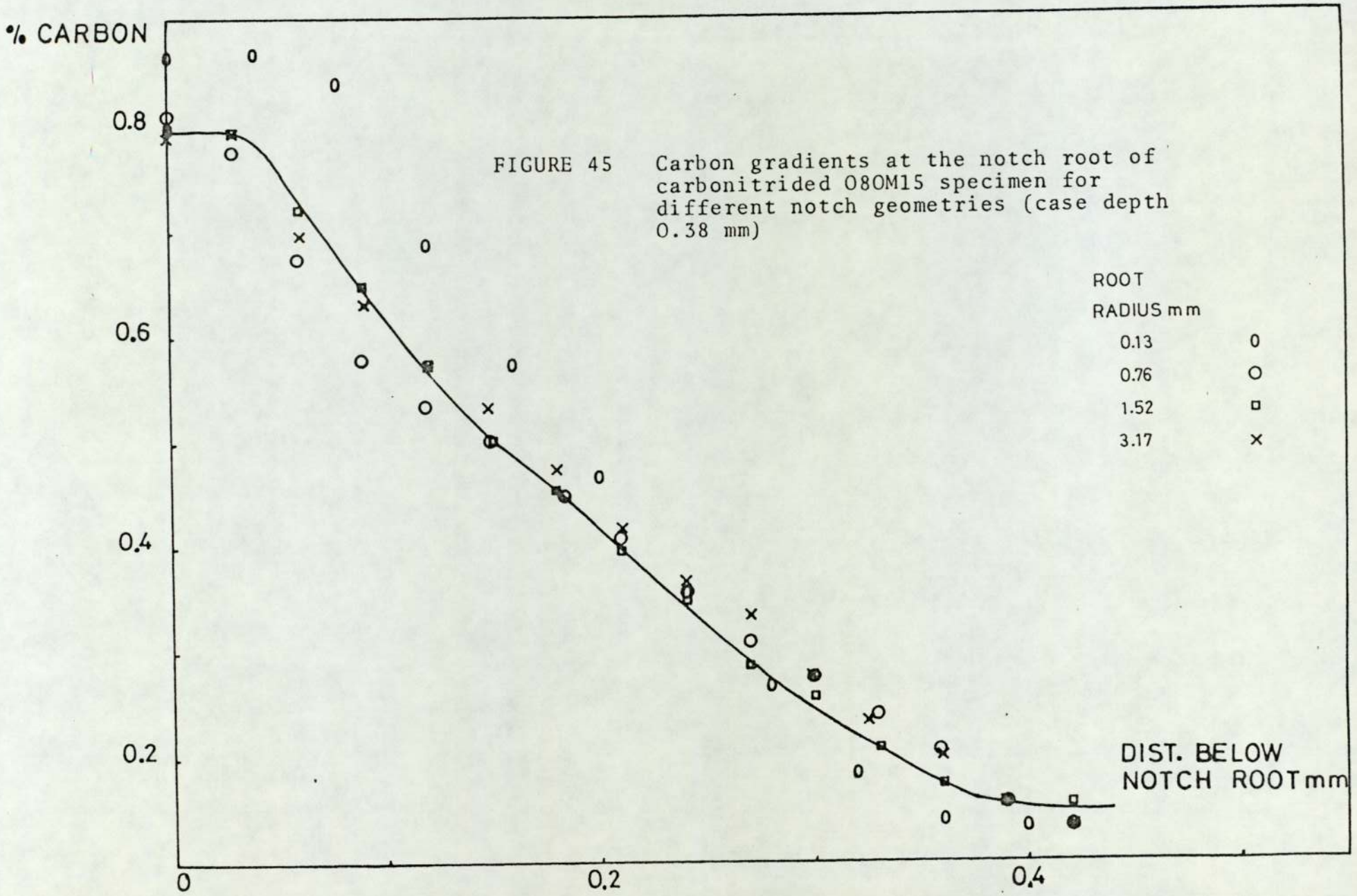

FIGURE 45 Carbon gradients at the notch root of carbonitrided 080M15 specimen for different notch geometries (case depth 0.38 mm)

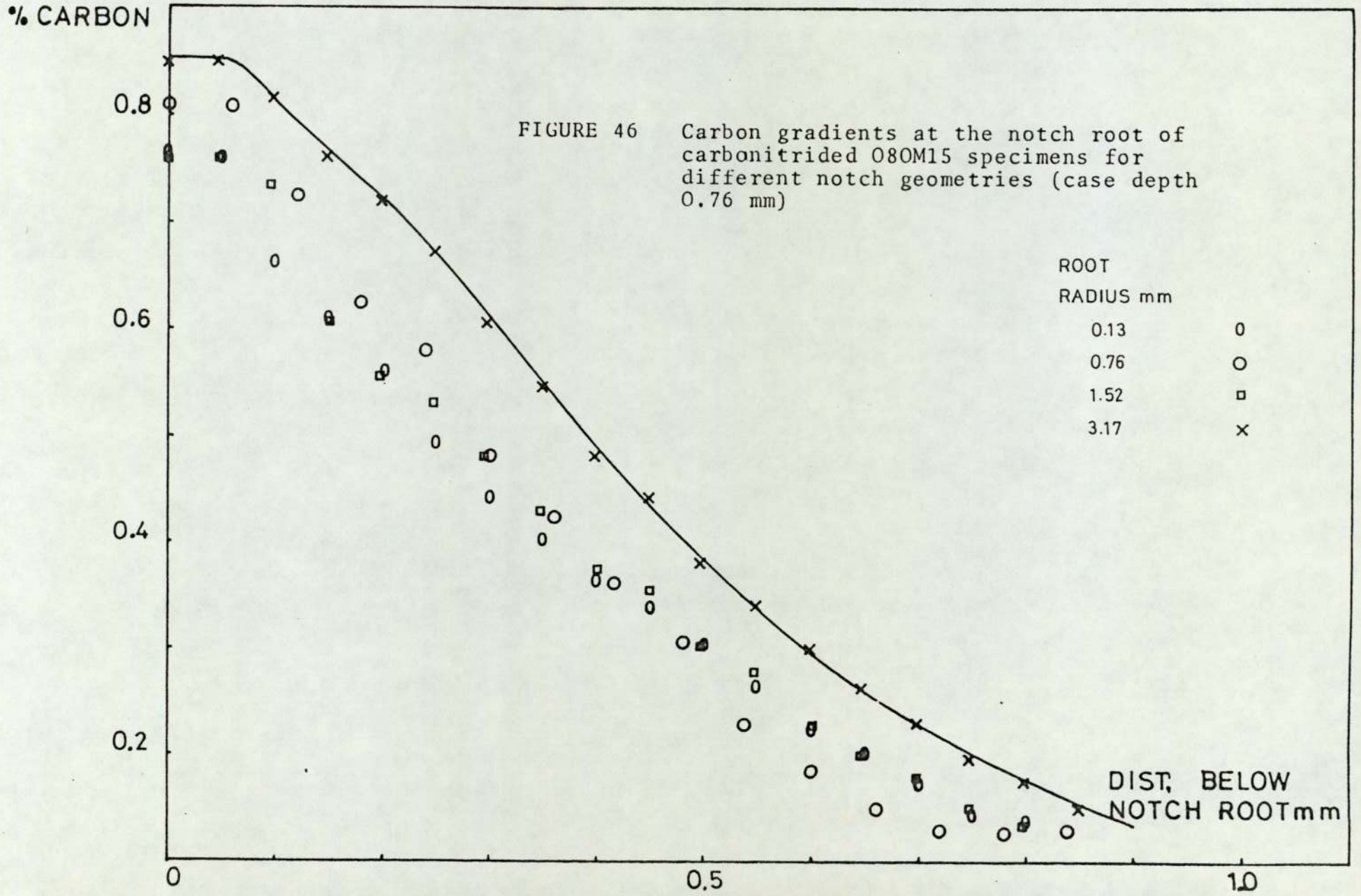

FIGURE 46 Carbon gradients at the notch root of carbonitrided 080M15 specimens for different notch geometries (case depth 0.76 mm)

TABLE 11 EFFECTIVE CASE DEPTHS FOR VARIOUS CASE HARDENING TREATMENTS (080M15)

Notch Geometry/K_t		Carburised 0.38 mm	Carburised 0.76 mm	Carbonitrided 0.38 mm	Carbonitrided 0.76 mm	Nitemper mm
Root radius 0.13	Composition	0.38	0.76	0.38	0.76	0.062
K_t 7.59	Hardness 550 Hv	0.23	0.40	0.27	0.38	0.80
Root radius 0.76	Composition	0.38	0.76	0.38	0.76	0.042
K_t 3.42	Hardness 550 Hv	0.23	0.37	0.27	0.38	0.80
Root radius 1.52	Composition	0.38	0.76	0.38	0.76	0.032
K_t 2.26	Hardness 550 Hv	0.28	0.64	0.30	0.62	0.70
Root radius 3.17	Composition	0.38	0.76	0.38	0.76	0.010
K_t 1.69	Hardness	0.28	0.64	0.32	0.62	0.70

case of carbonitriding, however, for both the case depths considered, and specimens with the notch root radius of 3.17 mm, carbon contents were higher than those obtained for lesser notch root radii at the same position.

The carbon gradients for nitempered samples are presented in Figure 47. The carbon contents at the notch root surface were found to be considerably different. The variation in carbon content away from the notch root was also different. It was, however, possible to establish the case depth of the compound layer. The values obtained are presented in Table 11.

6.5.2 Hardness Gradient

The Vicker's hardness is calculated using the following formula:

$$Hv = \frac{1834 * P}{d^2}$$

where Hv = Vicker's hardness K_p/mm^2

P = measuring load in ponds

d = length of the indentation in μm.

A set of tables are also available for converting the measured value of the diameter of indentation into Vicker's hardness at a particular load. The microhardness values are susceptible to the surface finish, cleanliness of surface, etc., and considerable care is necessary to ensure minimum error in measurement. Further, the cali-

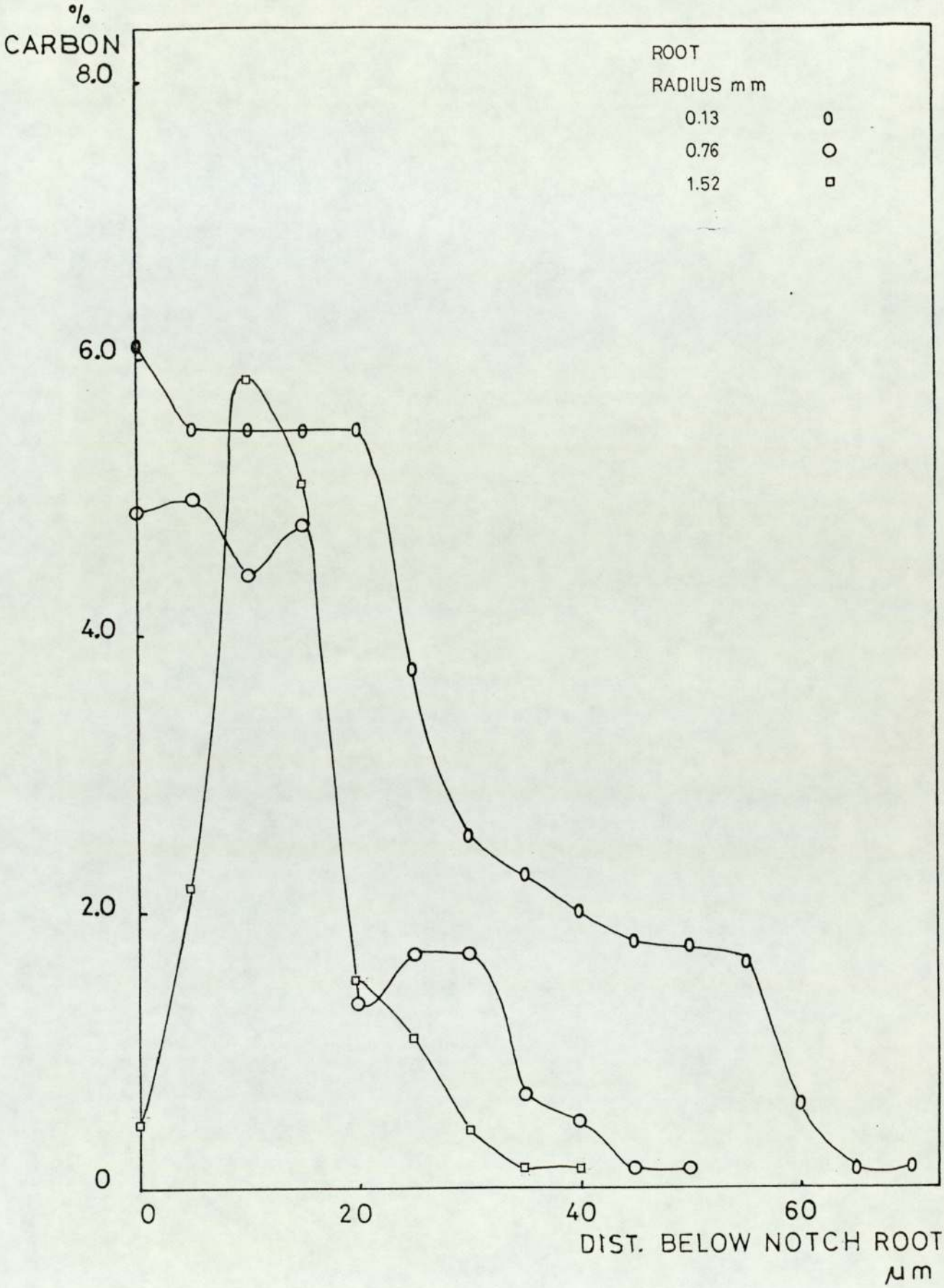

FIGURE 47 Carbon gradients at the notch root of nitrocarburised 080M15 specimens for different notch geometries

bration of hardness testing machine has to be checked using a standard test piece. To ensure minimum error, the calibration of the machine was checked for every set of hardness measurements carried out. Moreover, the sample surface was degreased before the hardness measurements were carried out.

Figures 48 to 51 show representative hardness variation below the notch root for carburised and carbonitrided samples. The effective case depth is defined as the distance from the surface at which hardness is 550 Hv[106]. The values of effective case depths for different treatment conditions and notch root geometries are presented in Table 11.

The variation in hardness for nitempered samples is presented in Figure 52. The average hardness of the compound layer was found to be 450 Hv. The thickness of the compound layer could not be established on the basis of hardness variation, as it varied between 10 μm and 60 μm for different notch geometries. The hardness gradient was, however, useful in establishing an approximate value of the diffusion layer, which plays an important role in the fatigue properties of nitempered steels [82]. The results are presented in Table 11.

The variation in hardness in the induction hardened case of 080A47, at the notch root, is presented in Figure 53. A large variation in hardness is observed at the notch

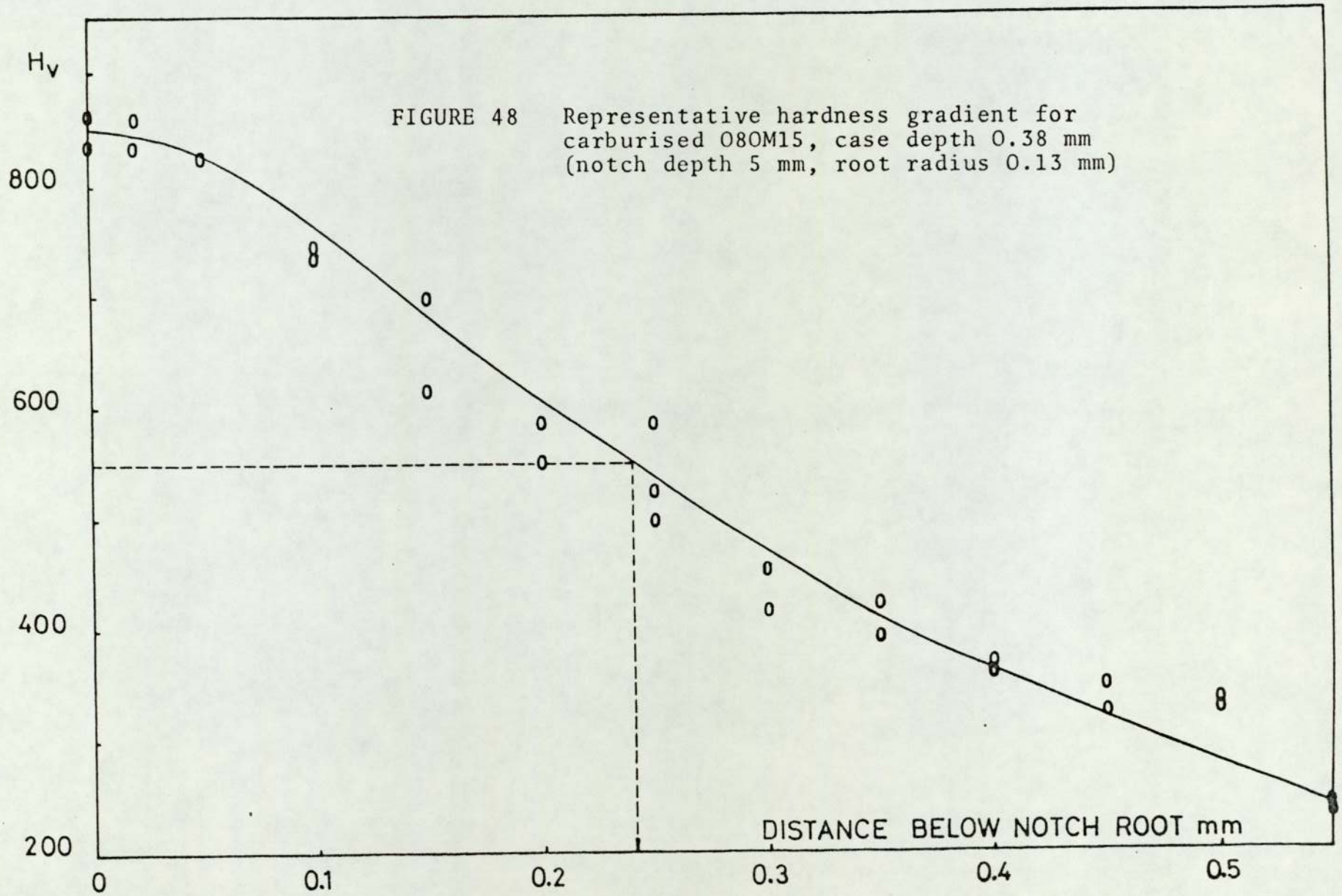

FIGURE 48 Representative hardness gradient for carburised 080M15, case depth 0.38 mm (notch depth 5 mm, root radius 0.13 mm)

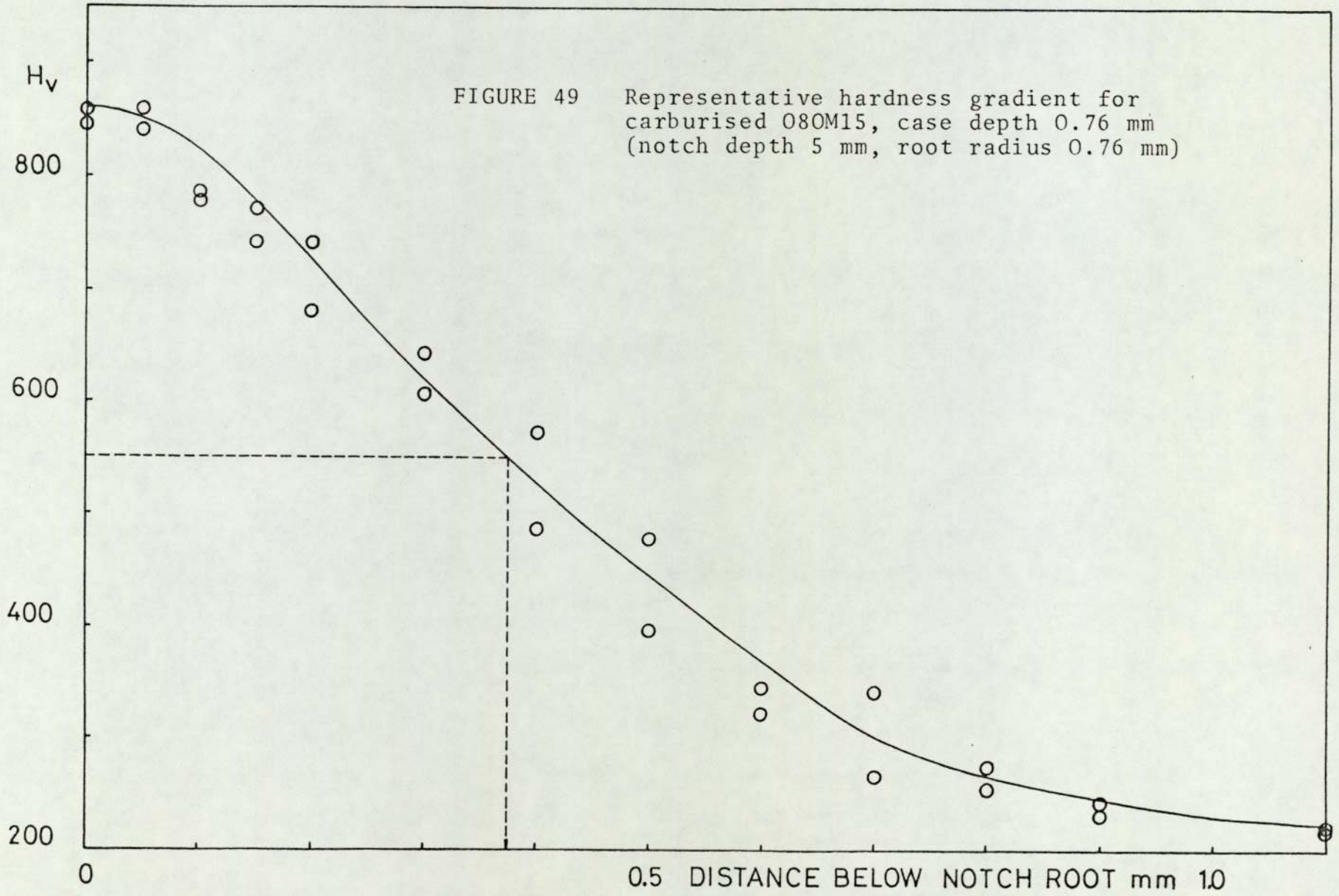

FIGURE 49 Representative hardness gradient for carburised 080M15, case depth 0.76 mm (notch depth 5 mm, root radius 0.76 mm)

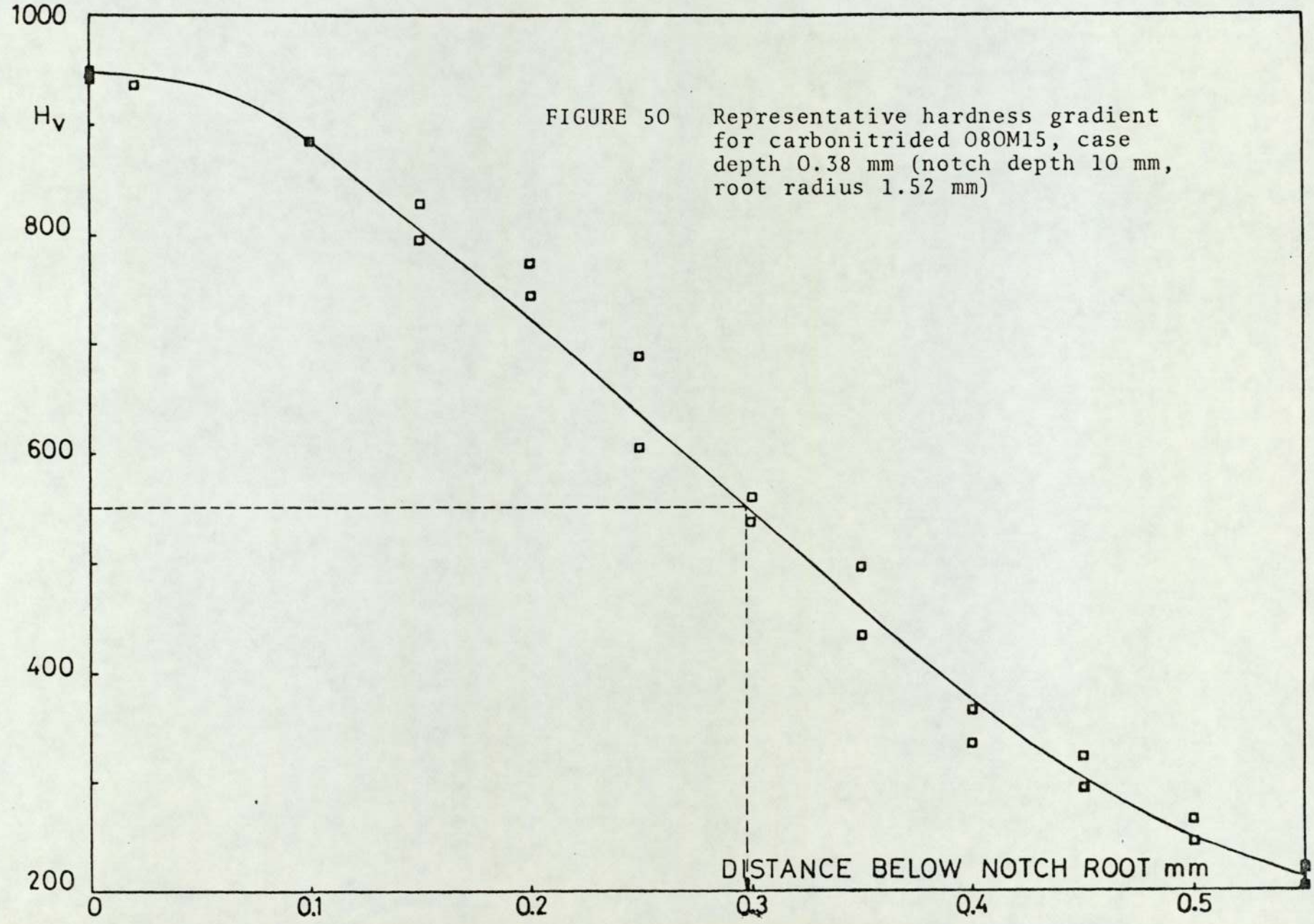

FIGURE 50 Representative hardness gradient for carbonitrided 080M15, case depth 0.38 mm (notch depth 10 mm, root radius 1.52 mm)

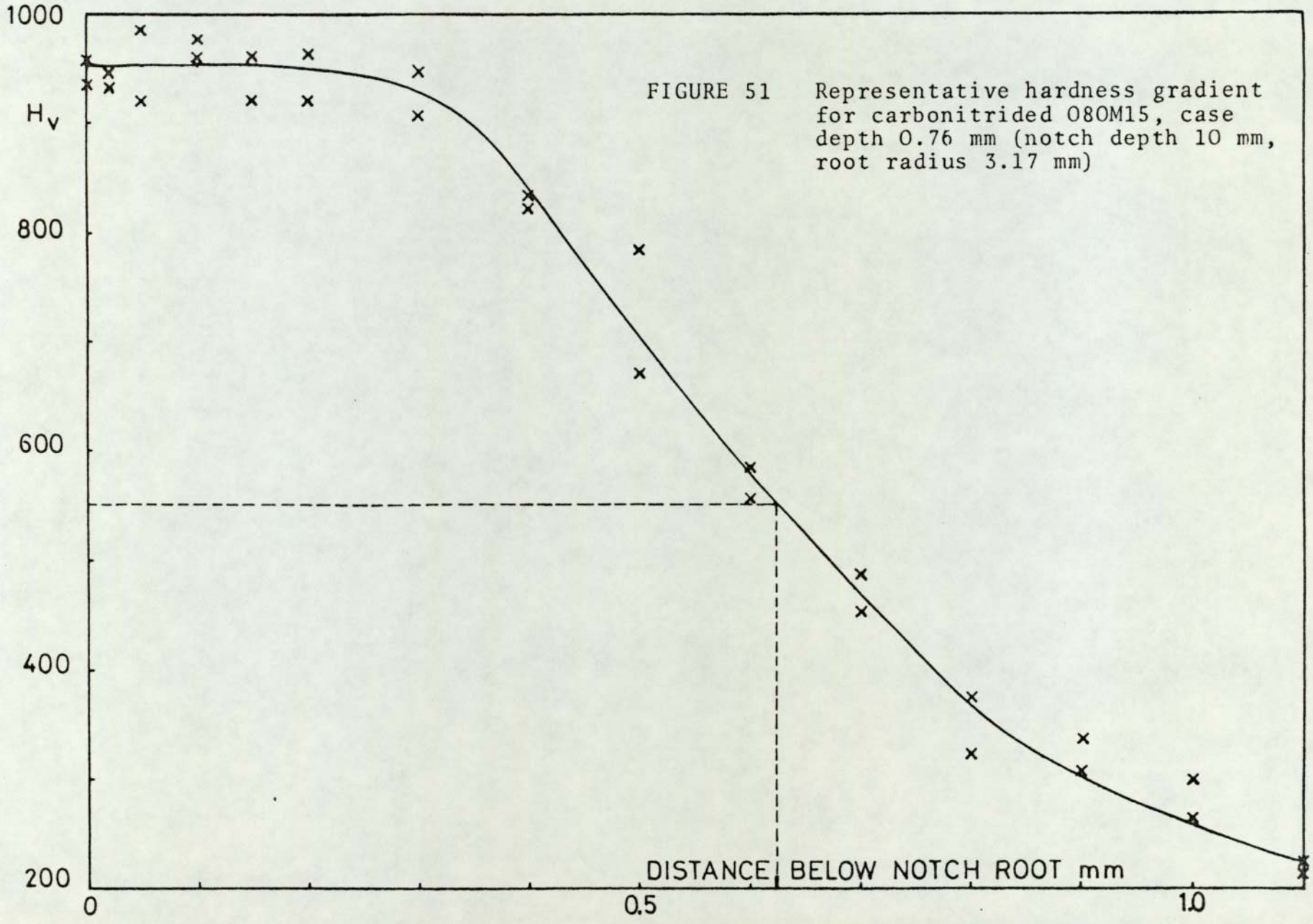

FIGURE 51 Representative hardness gradient for carbonitrided 080M15, case depth 0.76 mm (notch depth 10 mm, root radius 3.17 mm)

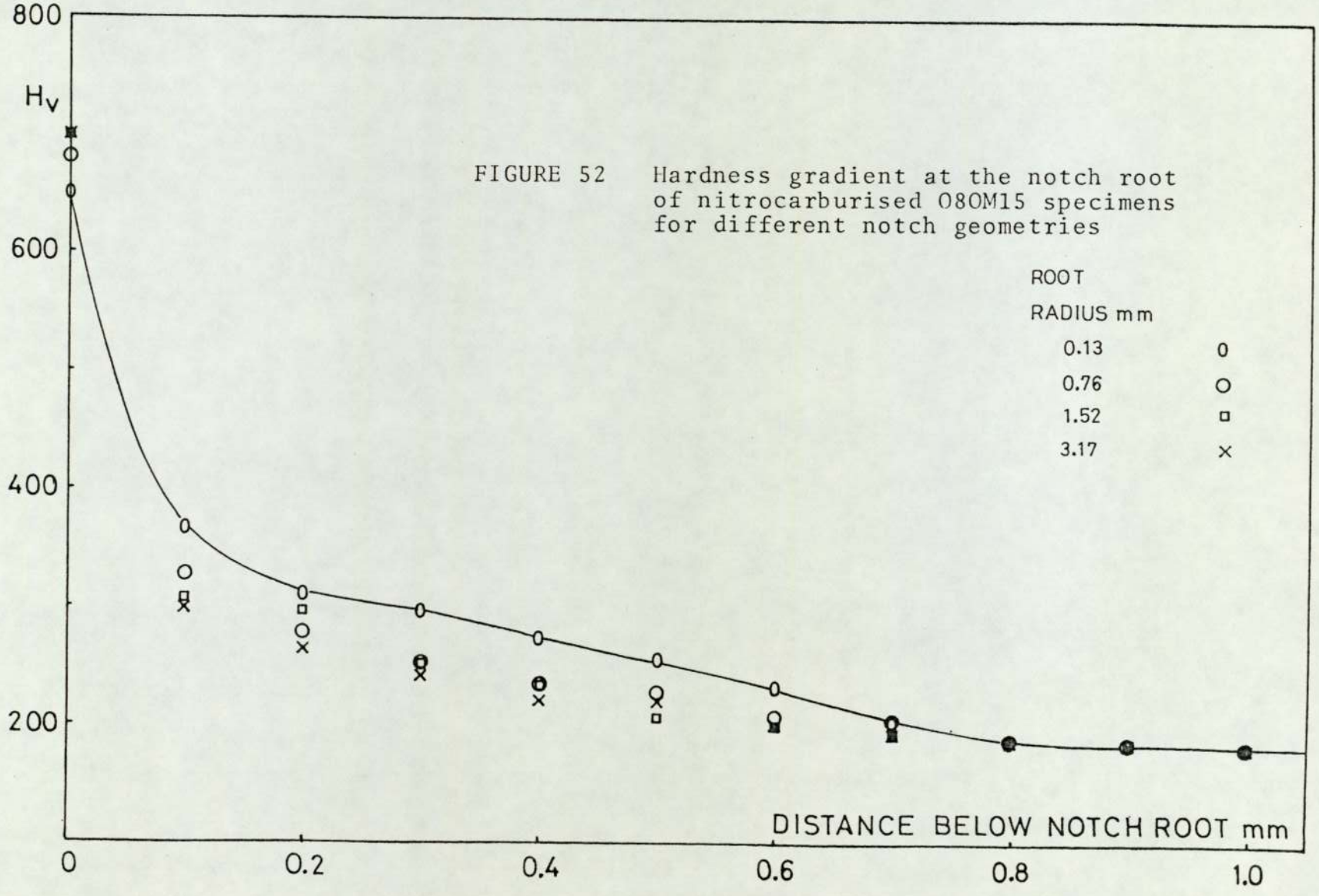

FIGURE 52 Hardness gradient at the notch root of nitrocarburised 080M15 specimens for different notch geometries

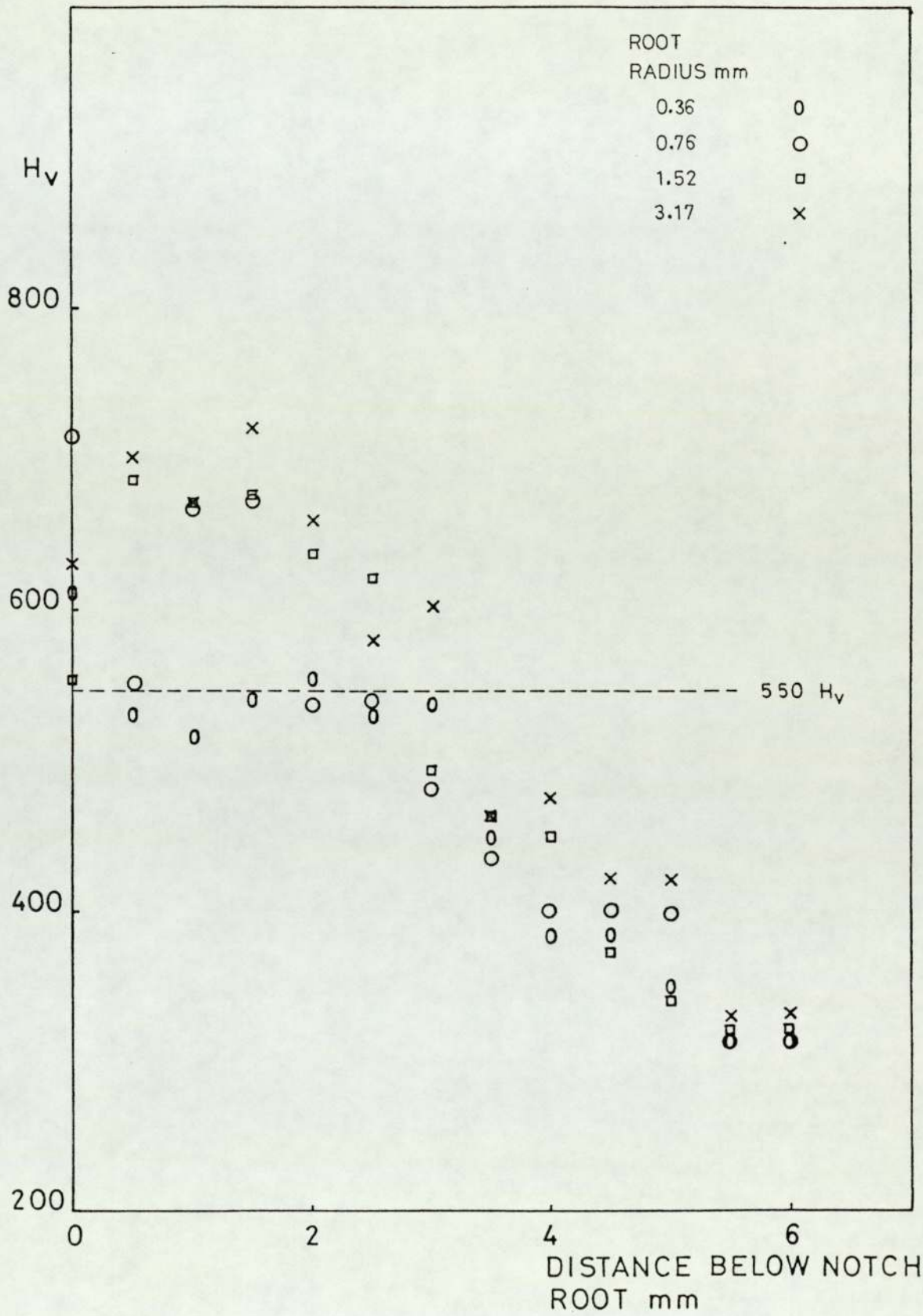

FIGURE 53 Hardness gradients at the notch root of induction hardened 080A47 specimens for different notch geometries

root. The effective case depth is 2.0 mm. Due to rapidity of heat treatment the diffusion of carbon to attain a uniform carbon percentage in the sample is not possible in induction hardening practice. The martensite formed therefore shows a variation in hardness and retained ferrite also forms if the quench is not severe. Both the factors contribute to the large variation observed in the hardness gradient across the case depth.

6.6 Metallographic and Fractographic Examination

6.6.1 Material Microstructure

6.6.1.1 Untreated material

Plates 6 and 7 show the microstructures of untreated 080M15 and 080A47. 080M15 showed fine grained ferrite-pearlite aggregates with approximately 13% volume fraction of pearlite. 080A47 also showed fine grained ferrite-pearlite aggregate with approximately 54% volume fraction of pearlite. For 080M15 the ferrite grain size and pearlite colony size was determined using the intercept method at a linear magnification of 400. 50 fields were examined. The grain size was found to vary between 10 μm and 40 μm, the mean value being 22 μm. The value of mean free path in ferrite and the pearlite colony size was determined using a Quantimet (Metals Research). The value of the mean free path in Ferrite was found to vary between 10 μm and 50 μm, the mean value being 22 μm. The pearlite colony size was found to vary between 10 μm and 30 μm, the average value being 19 μm.

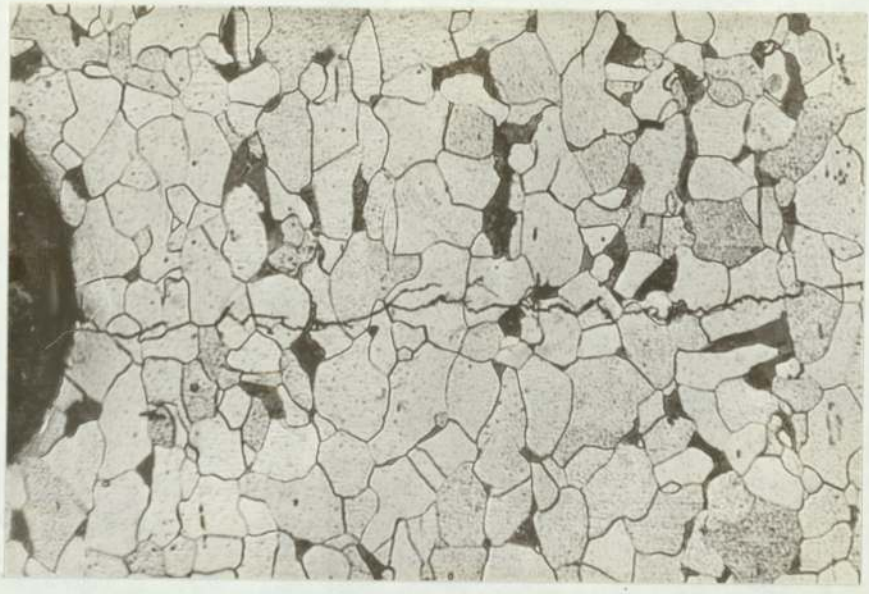

PLATE 6 Microstructure of untreated 080M15
(magnification x200)

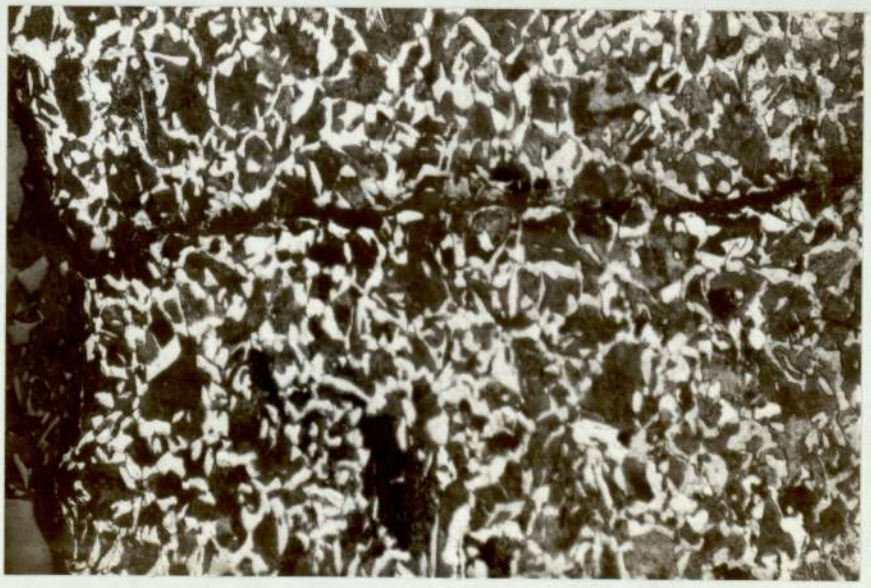

PLATE 7 Microstructure of untreated 080A47
(magnification x200)

6.6.1.2 Carburised 080M15

Plates 8 and 9 show the variation of micros tructure in case of carburised 080M15 for two case depths, 0.38 mm and 0.76 mm respectively. The micrographs shown represent the microstructures at the root of the notch. The microstructure consists of tempered martensite colonies along with pearlite which had formed along the austenitic grain boundaries. The pearlite however could not be resolved using optical microscope.

As could be seen in Plates 10 and 11, the occurrence and the amount of pearlite at the root of the notch was more pronounced in the case of sharper notch root radii than the blunt notches, especially at midsection. In the case of blunt notches the transformation to martensite was almost complete, though traces of pearlite could be found at the notch root at the midsection. Further away from the notch root, the microstructure showed increasing contents of ferrite associated with low carbon martensite. The structure of the core was accicular or widmanstäten ferrite.

In thicker cases (0.76 mm) the structure at the notch root was similar to the shallower case (0.38 mm). The amount of pearlite however was found to be higher than the shallower case for all the notch root radii, especially at the midsection (Plates 12 and 13). Further away from the notch root, the microstructure showed an increasing content of non-martensitic transformation products associated with

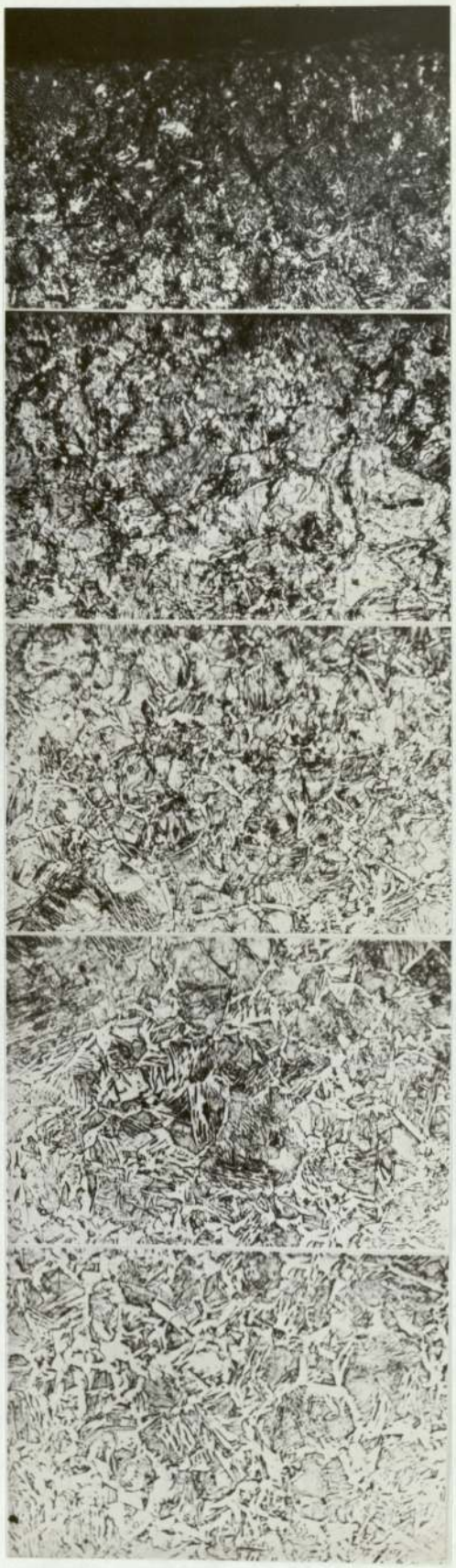

PLATE 8 Microstructure of case carburised 080M15, case depth 0.38 mm (magnification x250)

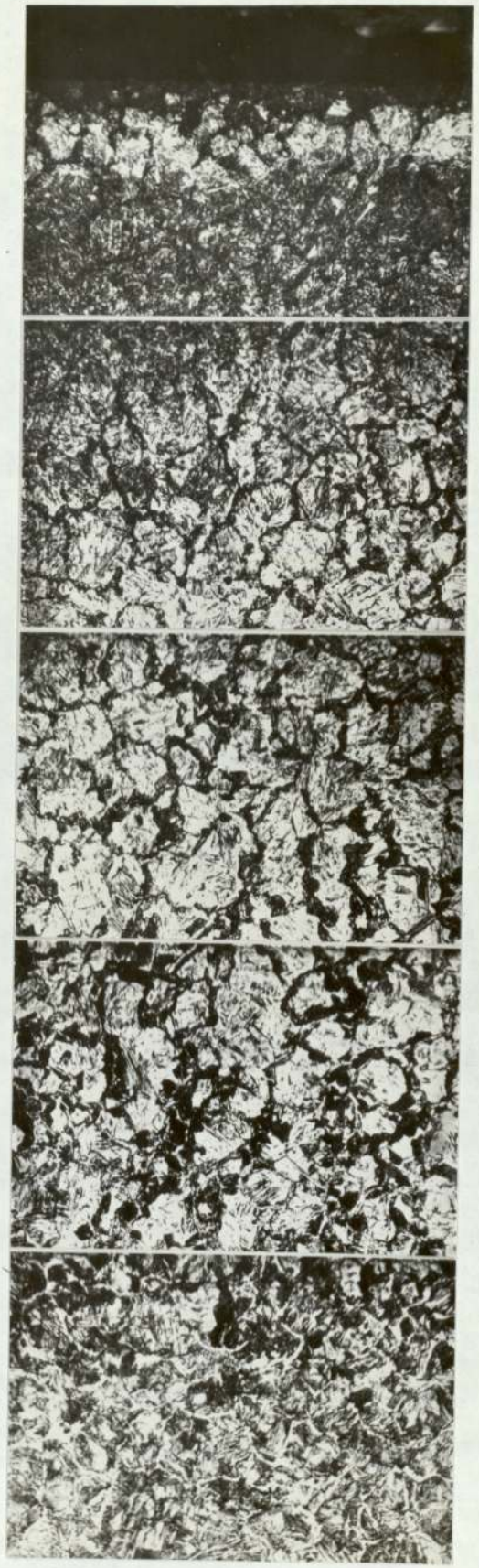

PLATE 9 Microstructure of case carburised 080M15, case depth 0.76 mm (magnification x250)

PLATE 10 Microstructure at the notch root, carburised 080M15, root radius 0.76 mm, showing non-martensitic transformation products (case depth 0.38 mm) (magnification x450)

PLATE 11 Microstructure at the notch root, carburised 080M15, root radius 3.17 mm (case depth 0.38 mm) (magnification x450)

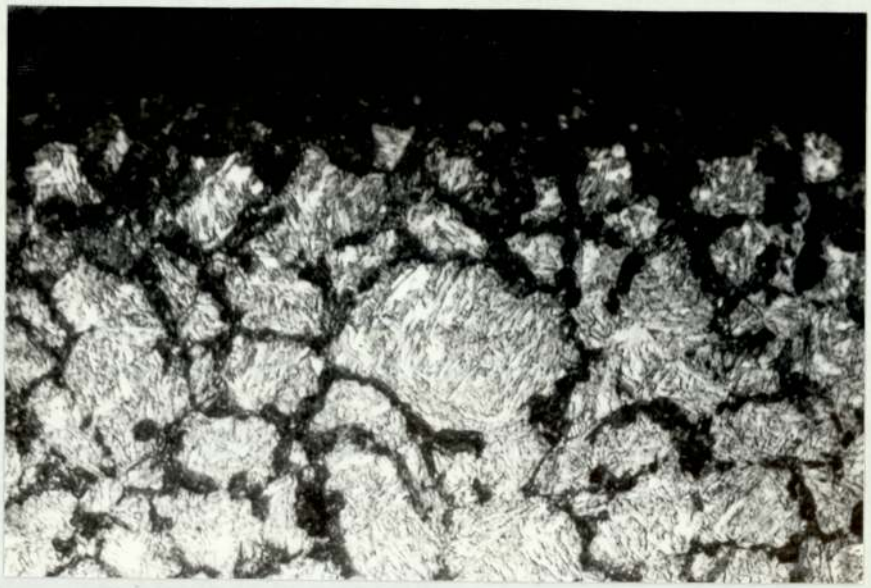

PLATE 12 Microstructure at the notch root, carburised 080M15, root radius 0.76 mm, mid section, (case depth 0.76 mm) (magnification x450)

PLATE 13 Microstructure at the notch root, carburised 080M15, root radius 3.17 mm, mid section (case depth 0.76 mm) (magnification x450)

low carbon martensite. The changes in the microstructure were more gradual than those observed in a shallower case. The microstructure of the core was acicular or Widmanstätten ferrite.

The martensitic colony size at the root of the notch was measured using the intercept method. The colony size was found to vary between 10 μm and 50 μm, the mean value being 22 μm.

The amount of retained austenite is negligible, and cannot be detected by optical microscopy.

6.6.1.3 Carbonitrided 080M15

Plates 14 and 15 show the variation in microstructure at the root of the notch for the two case depths considered, viz. 0.38 mm and 0.76 mm. The microstructure at the root of the notch consists of tempered martensite colonies and non-martensitic transformation products. The non-martensitic transformation products could not be resolved under the optical microscope. The amount of retained austenite was not large enough to be detected by the optical microscope. The size of the prior austenitic grain size as determined by the intercept method was between 10 μm and 50 μm, mean value being 22 μm.

For the shallower case depth (0.38 mm), the amount of non-martensitic transformation products formed along the prior austenitic grain boundaries was higher in the sharper notch root radii than in the case of blunter notches (Plates 16

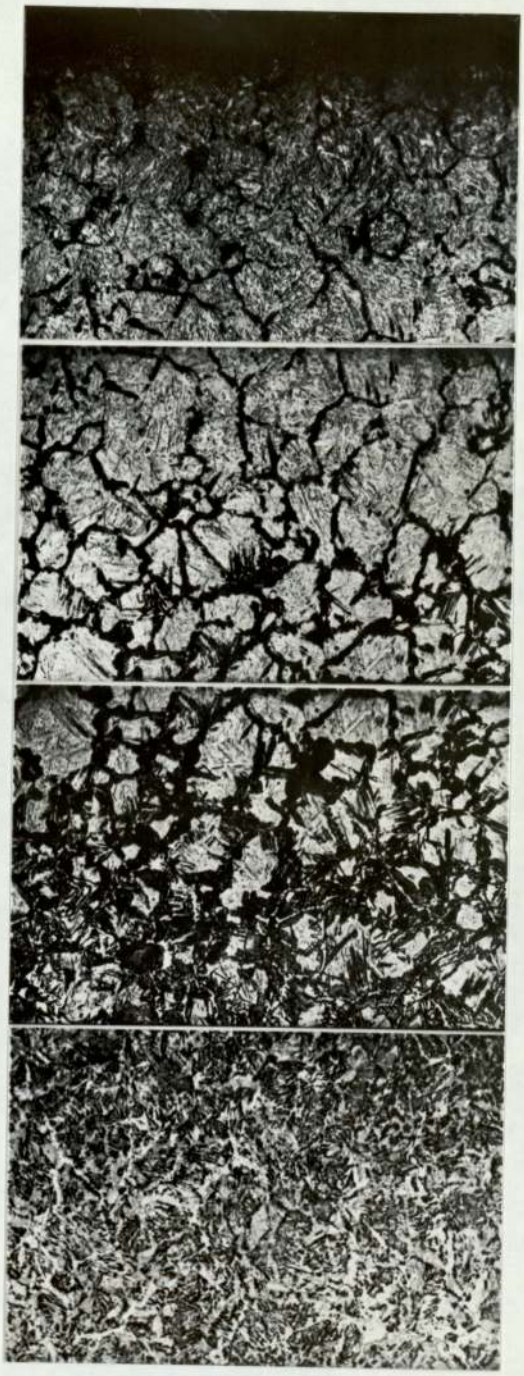

PLATE 14 Microstructure of case carbonitrided 080M15, case depth 0.38 mm (magnification x250)

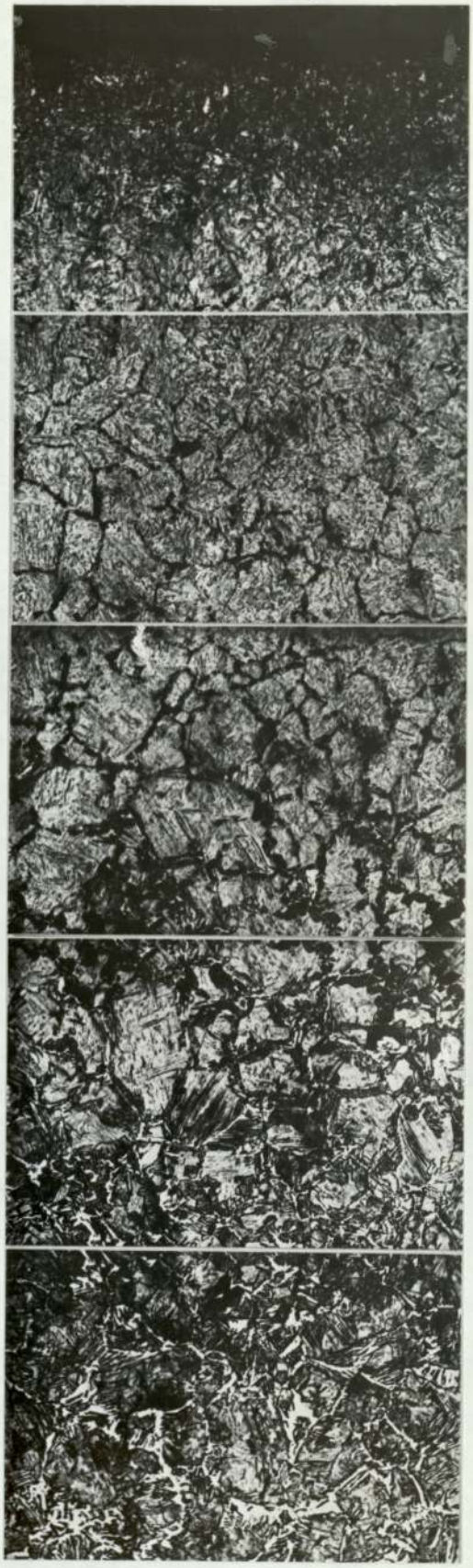

PLATE 15 Microstructure of case carbonitrided 080M15, case depth 0.76 mm (magnification x 250)

and 17). In the thicker case depth (0.76 mm) a similar observation was made except that the comparison with a similar notch root radius carbonitrided to shallower case depth showed a higher amount of non-martensitic product in the former (Plates 16, 18, 19 and 20). Further away from the notch root the microstructure showed increasing amounts of non-martensitic transformation product associated with low carbon martensite. The structure of the core was acicular ferrite.

Comparison of Plates 8 and 14 shows the effect of nitrogen in carbonitrided cases. At the same distance below the notch root, the amount of martensite in the carbonitrided case is higher than the carburised case. This could be attributed to higher hardenability associated with the presence of nitrogen in steel. (The comparison of carbon gradients for carburising and carbonitriding did not show large enough differences to justify this occurrence.)

Subsurface porosity is sometimes observed in carbonitrided cases. Unetched samples of carbonitrided 080M15 did not show the existence of subsurface porosity.

6.6.1.4 Nitrocarburised 080M15 (Nitemper)

Plates 21 and 22 show the microstructure of nitrocarburised 080M15. The micrographs show the compound layer at the root of the notch. The thickness of the compound layer was found to vary depending on the notch root radius, the

PLATE 16 Microstructure at the notch root, carbonitrided 080M15, root radius 0.13 mm (case depth 0.38 mm) (magnification x450)

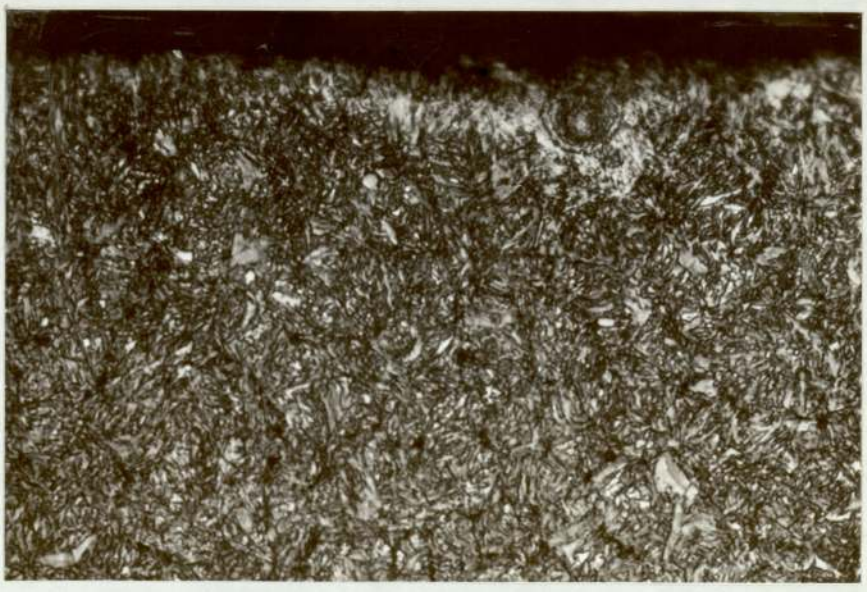

PLATE 17 Microstructure at the notch root carbonitrided 080M15, root radius 3.17 mm (case depth 0.38 mm) (magnification x450)

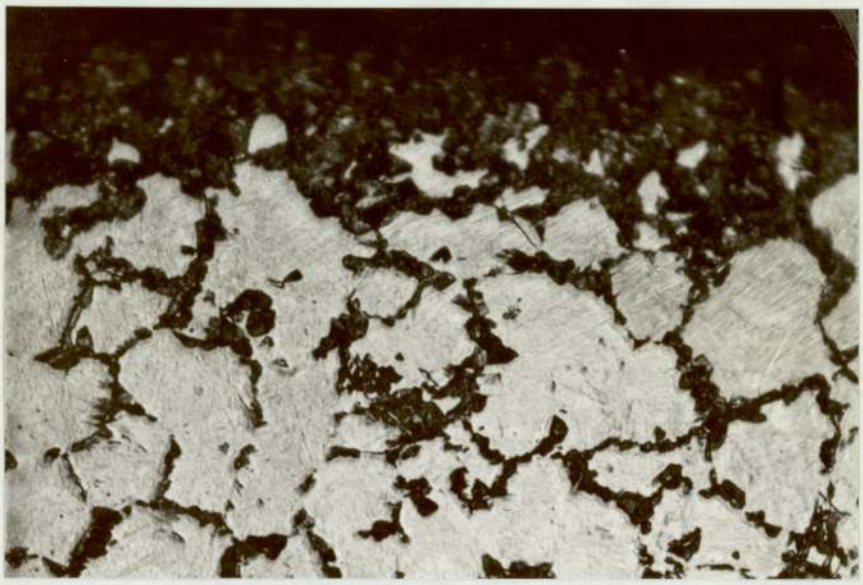

PLATE 18 Microstructure at the notch root, carbonitrided 080M15 showing non-martensitic transformation product, root radius 0.13 mm (case depth 0.76 mm) (magnification x450)

PLATE 19 Microstructure of carbonitrided 080M15, root radius 0.76 mm, (case depth 0.76 mm) (magnification x450)

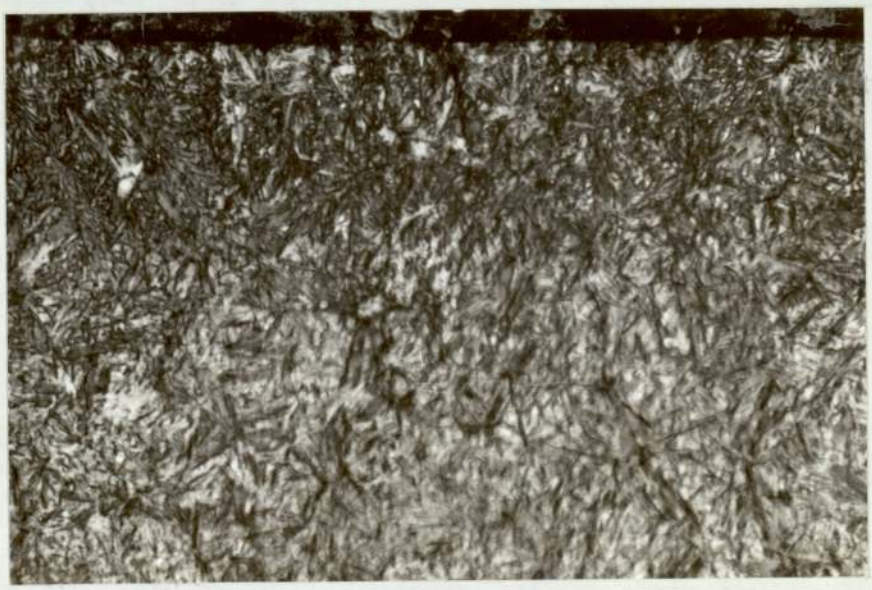

PLATE 20 Microstructure of carbonitrided 080M15, root radius 3.17 mm (case depth 0.76 mm) (magnification x450)

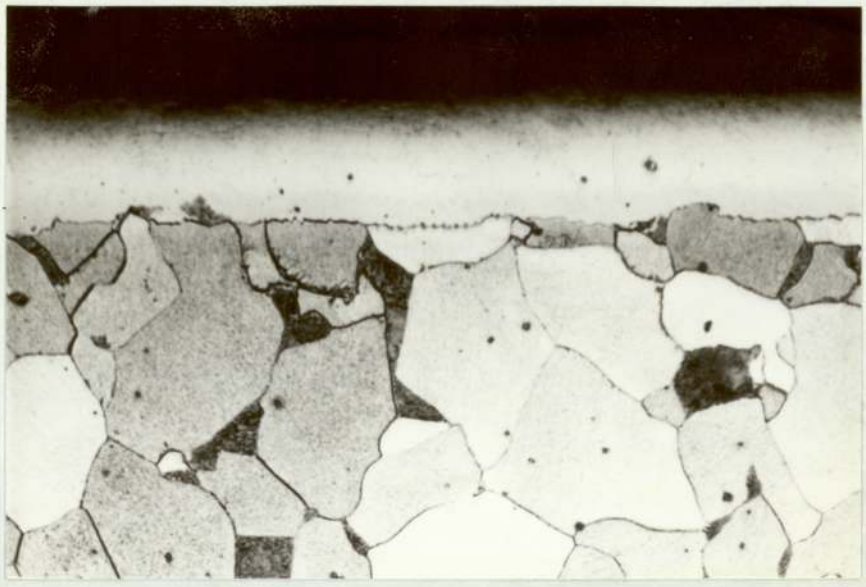

PLATE 21 Microstructure at the notch root of nitrocarburised 080M15 specimen showing compound layer, root radius 0.13 mm, (magnification x450)

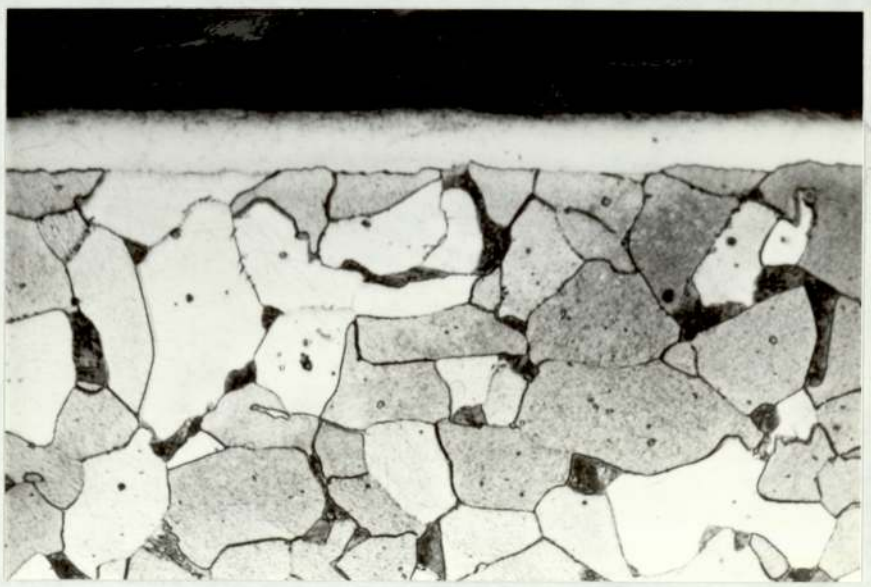

PLATE 22 Microstructure of nitrocarburised 080M15 specimen, midsection, at the notch root, root radius 3.17 mm (magnification x450)

sharpest motch having the thickest compound layer. The thickness of the compound layer varied between 60 μm for the sharpest notch (0.13 mm root radius) to 10 μm for the bluntest notch root radius (3.17 mm root radius). The diffusion zone beneath the compound layer was indistinguishable from the original matrix. The microstructure away from the notch root, below the compound layer, showed fine grained ferrite pearlite aggregate with approximately 14% volume fraction of pearlite.

The thickness of the diffusion zone could not be established using optical microscopy, The microhardness gradients and nitrogen gradient can be used to estimate the depth of the diffusion zone. In the present experiments the depth of diffusion zones for different notch geometries is presented in Table 11.

6.6.1.5 Induction Hardened 080A47

Plates 23 to 29 show microstructures of induction hardened samples. At the root of the notch the microstructure consisted of tempered martensite and non-martensitic transformation products. The non-martensitic product at the root of the notch is essentially pearlite. The amount of pearlite was found to increase towards the midsection at the root of the notch, Plates 24 and 27. Further away from the notch root the amount of pearlite was found to increase towards the core. The structure of the core consisted mainly of pearlite. In the case of deeper notches however, large patches of martensite were also found though not many

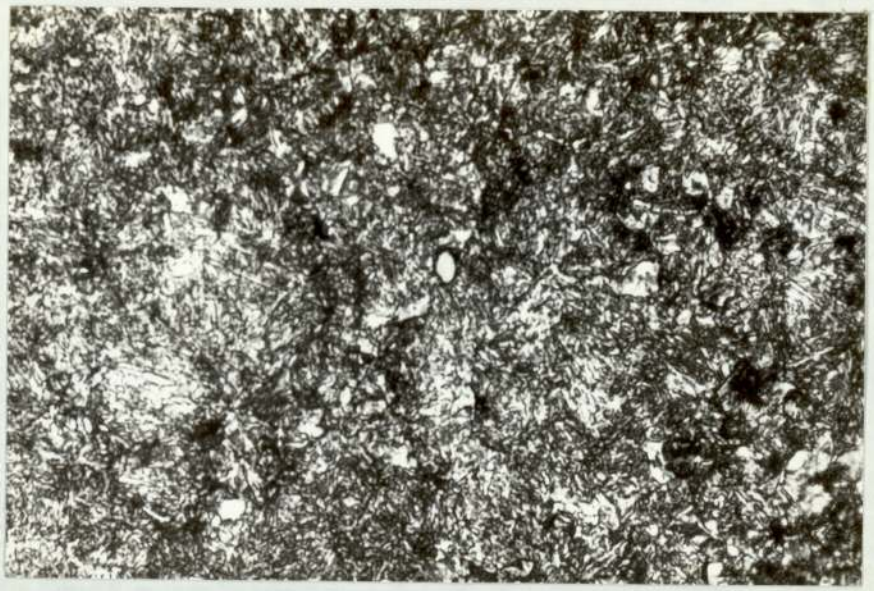

PLATE 23 Microstructure of induction hardened O80A47, at the notch root, root radius 3.17 mm (magnification x450)

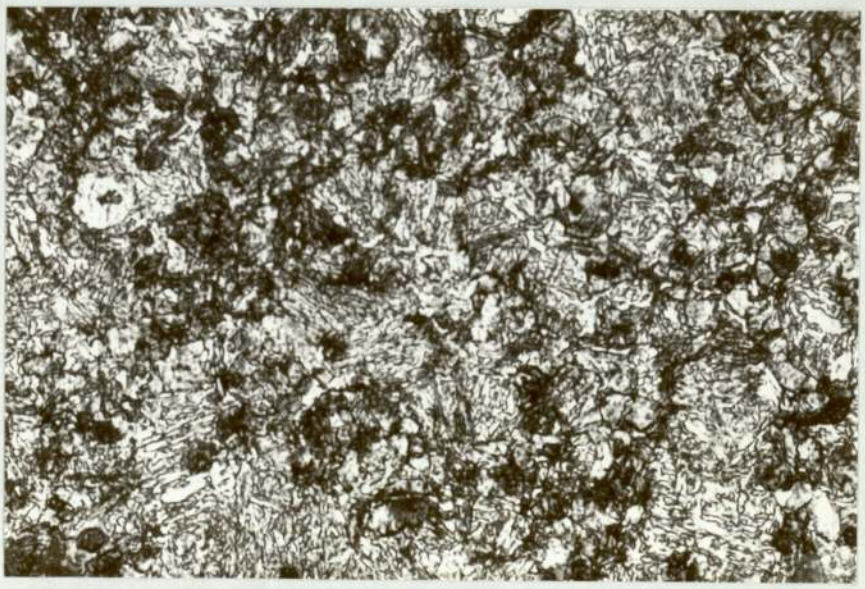

PLATE 24 Microstructure of induction hardened O80A47, at the notch root and mid-section, root radius 3.17 mm (magnification x450)

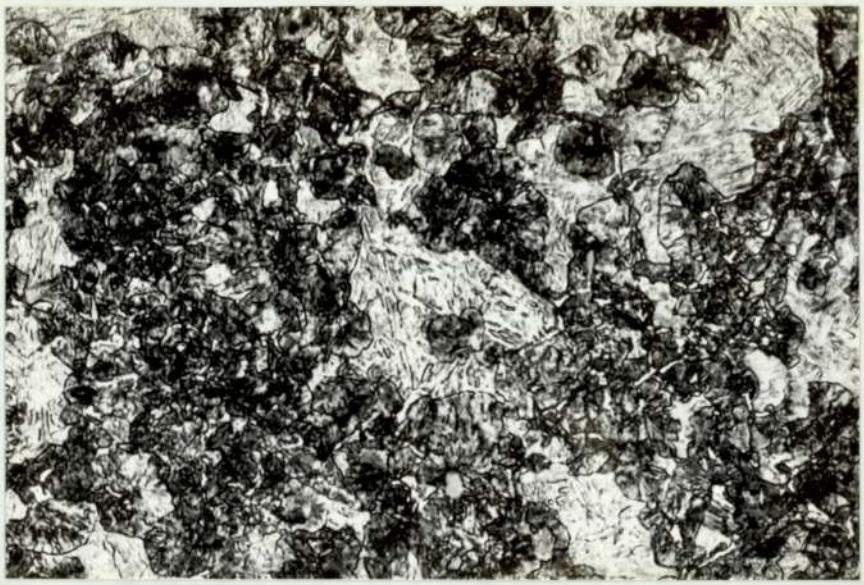

PLATE 25 Microstructure in the core of induction hardened 080A47, root radius 3.17 mm (magnification x450)

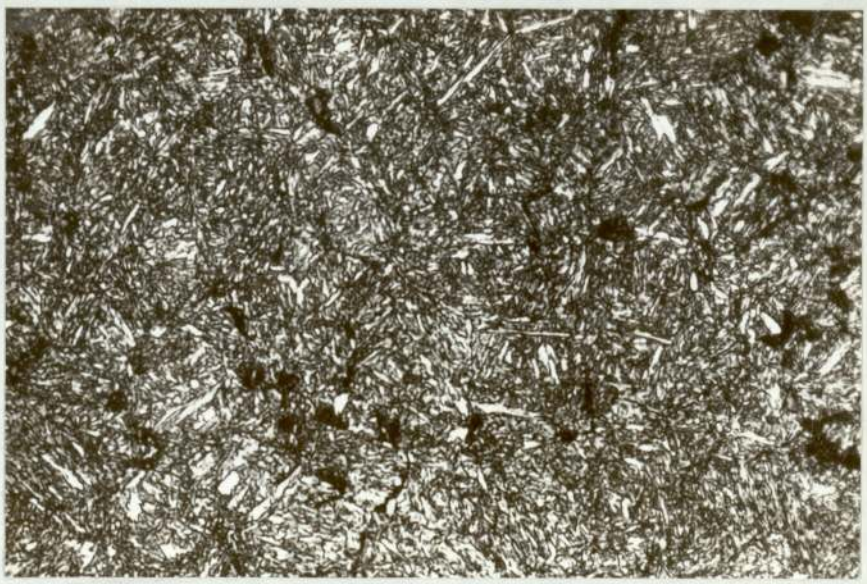

PLATE 26 Microstructure of induction hardened 080A47, at the notch root, root radius 0.36 mm (magnification x450)

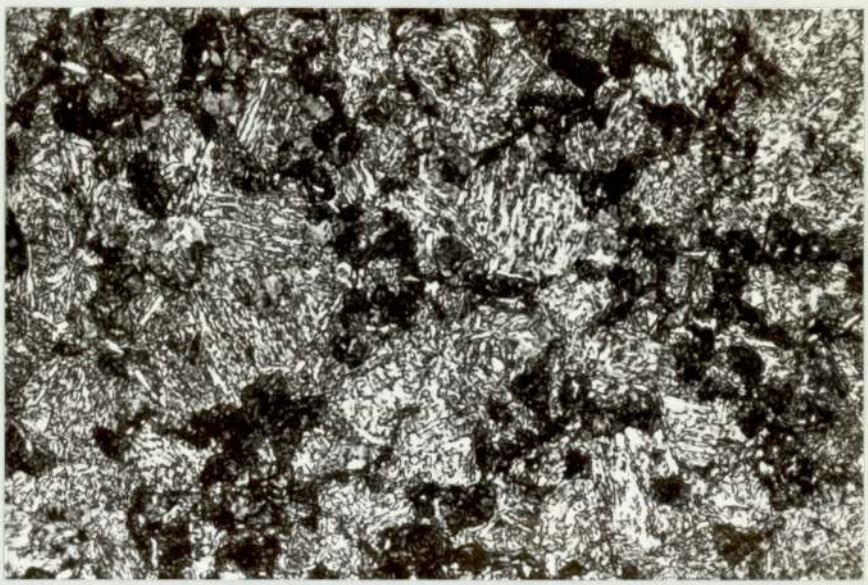

PLATE 27 Microstructure at the notch root in induction hardened 080A47, showing non-martensitic transformation product, root radius 0.36 mm, midsection (magnification x450)

PLATE 28 Microstructure in core of induction hardened 080A47 specimen (magnification x450)

PLATE 29 Microstructure in core of induction hardened 080A47 specimen (magnification x450)

were present. In sharp and shallow notches chunky ferrite grains were embedded in the matrix of pearlite. The case depth could not be established accurately with the aid of microstructure as the structural variation was smoother. A deep etch, however, confirmed the case depth established on the basis of hardness gradient.

The prior austenitic grain size was determined using the intercept method. The size varied between 15 μm to 40 μm, mean being 22 μm.

6.6.2 Fracture Surface Examination

The comparison of the stress parameters versus life to initiation of fatigue crack for untreated and treated material shows that all the samples in these experiments could be treated as the samples subjected to low stress, high cycle fatigue. For all the samples of case hardened steels the fracture surfaces of the case at the root of the notch, at the case-core interface and below the case-core interface were examined to locate the sub-surface crack initiation. In the literature cited, evidence of sub-surface crack initiation was found when the fracture surfaces were examined at low magnification (less than x 50). None of the samples examined in this series of experiments showed the existence of sub-surface crack initiation. The examination of fracture surfaces using the scanning electron microscope at different magnifications also yielded negative results.

The examination of the number of cycles to initiation versus the modified stress intensity factor range graphs suggest that the behaviour of carburised and carbonitrided notch geometries could be divided into two categories,

a. shallow and sharp notches
   notch depth = 5 mm
   root radius = 0.13 mm and 0.76 mm

b. long and blunt notches
   notch depth = 10 mm
   root radius = 1.52 mm and 3.17 mm.

6.6.2.1 Fatigue Fracture of Carburised and Carbonitrided Shallow and Sharp Notches

Plates 30 to 41 show typical fatigue fracture surface topography observed at the notch roots. The fatigue fracture at the root of the notch is predominantly transgranular. The fracture starts transgranularly in the form of cleavage of martensitic platelets. This mode suggests that the high stress and stress gradient at the root of sharp notches causes the martensite plates to fracture primarily by overloading. Under these conditions cleavage of brittle martensite can occur. Though a considerable amount of non-martensitic transformation product is present, as seen in Plates the fracture of martensite seemed to be the over-riding factor. In the literature cited, the initiation of fatigue crack in martensite was sometimes associated with slag inclusions or carbides. No evidence was found to support this.

PLATE 30 Fatigue fracture of carburised case below the notch root, case depth 0.38 mm, root radius 0.13 mm N_i = 429,940

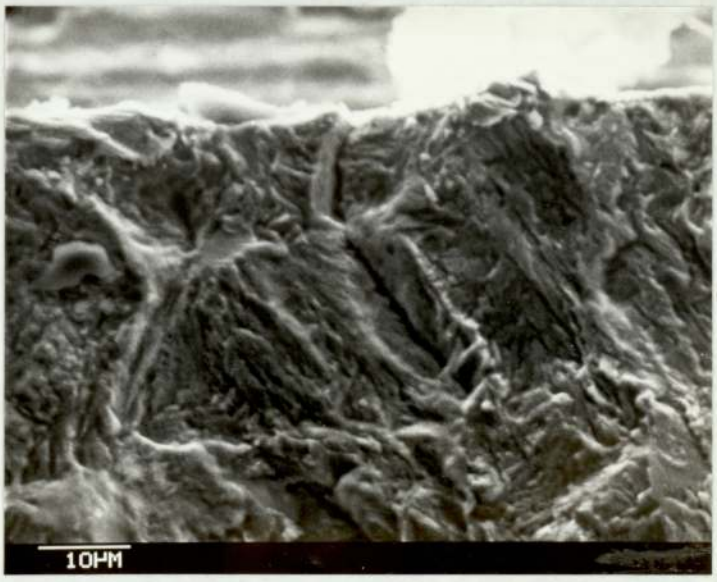

PLATE 31 Fatigue fracture of carburised case at the notch root, case depth 0.38 mm, root radius 0.13 mm, N_i = 209,550

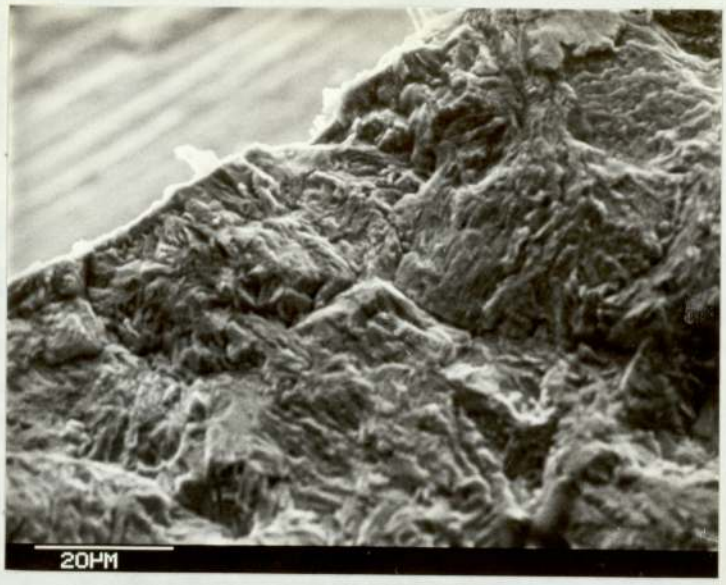

PLATE 32 Fatigue fracture of carburised case at the notch root, case depth 0.38 mm, root radius 0.13 mm, N_i = 90,630

PLATE 33 Fatigue fracture of carburised case at the notch root, case depth 0.76 mm, root radius 0.76 mm, N_i = 241,000

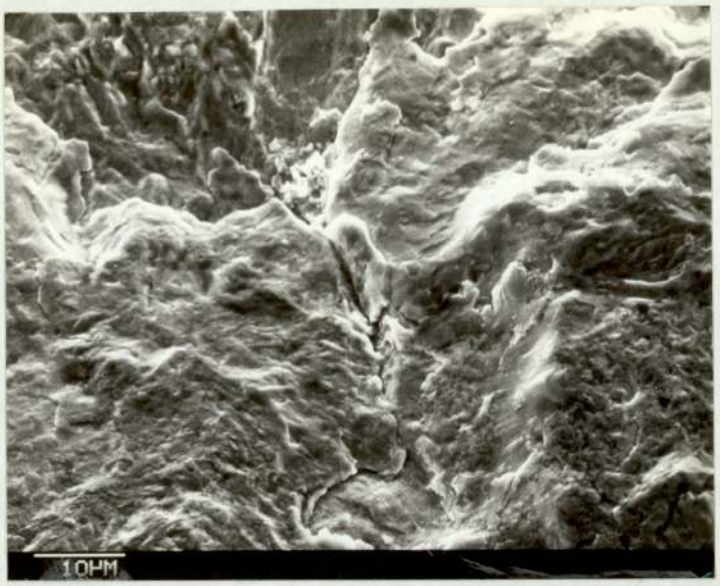

PLATE 34 Fatigue fracture of carburised case at the notch root, case depth 0.76 mm, root radius 0.13 mm, N_i = 295,800

PLATE 35 Fatigue fracture of carburised case at the notch root, case depth 0.76 mm, root radius 0.76 mm, N_i = 229,000

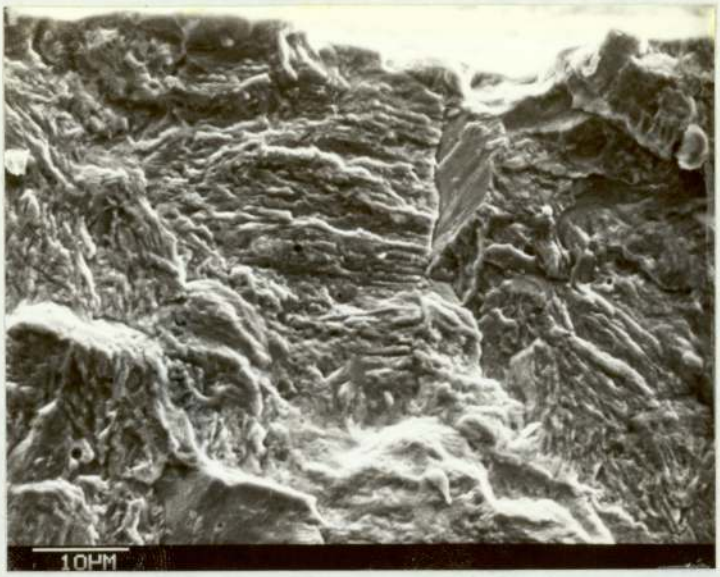

PLATE 36 Fatigue fracture in carbonitrided case at the notch root, case depth 0.38 mm, root radius 0.13 mm, N_i = 459,120

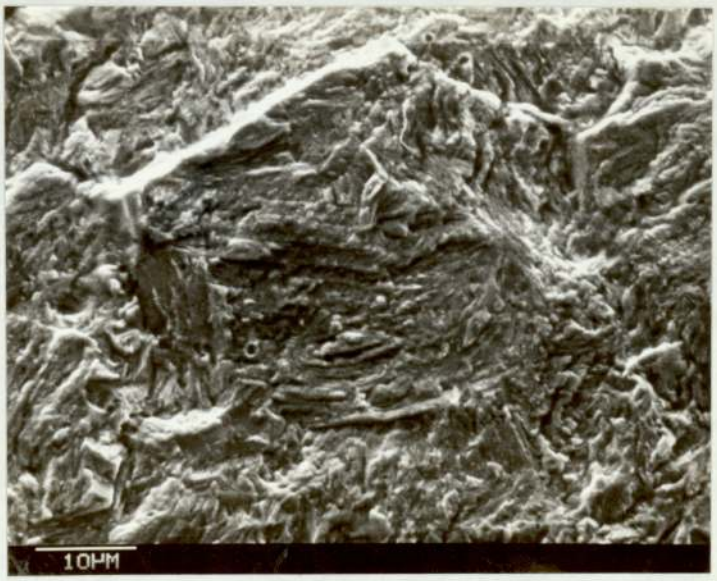

PLATE 37 Fatigue fracture in carbonitrided case at the notch root, case depth 0.38 mm, root radius 0.76 mm, N_i = 363,240

PLATE 38 Fatigue fracture of carbonitrided case at the notch root, case depth 0.76 mm, root radius 0.13 mm, N_i = 168,770

PLATE 39 Fatigue fracture of carbonitrided case at the notch root, case depth 0.76 mm, root radius 0.76 mm, N_i = 173,780

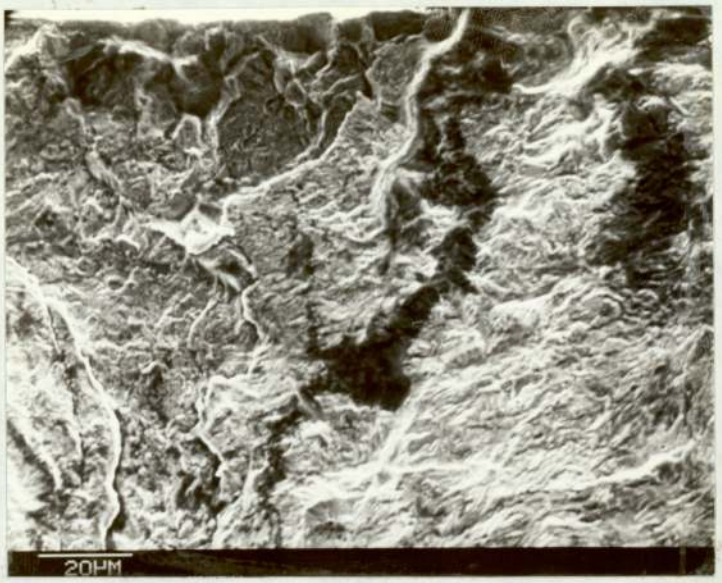

PLATE 40 Fatigue fracture in carbonitrided case below the notch root, showing sub-surface porosity, case depth 0.76 mm, root radius 0.13 mm, N_i = 168,770

PLATE 41 Fatigue fracture in carbonitrided case below the notch root, showing sub-surface porosity, case depth 0.76 mm, root radius 0.76 mm, N_i = 173,780

As can be seen in Plates 40 and 41, microcracks associated with the carbonitriding process were present. These microcracks could not be detected under the optical microscope at a magnification of x 1000. Further, a direct association of the microcracks present and the initiation of fatigue could not be made. As can be seen in Plates 38 and 39, some intergranular facets were found at the root of the notch in the carbonitride case (case depth 0.76 mm) which was not observed in other cases.

The fractographs presented also indicate that the number of cycles to initiation established for the cusp do not show any correlation to the fracture topography. Transgranular fracture is observed at the notch root irrespective of the value of Ni, the number of cycles to initiation.

6.6.2.2. Fatigue Fracture of Carburised and Carbonitrided Deep and Blunt Notches

Plates 42 to 51 show typical fatigue fracture surfaces observed at the notch root. The fatigue fracture at the notch root is predominantly intergranular. The fractographs also exhibit a certain amount of cleaved grains on the fracture surface. This could be due to the stress and stress gradient expected at the notch root, though neither are as severe as in the case of shallow sharp notches. The grain boundary separation is considered to occur along the prior austenitic grain boundaries. This could be attributed to the formation of non-martensitic transformation products (pearlite, bainite) along the prior austenitic grain

PLATE 42 Fatigue fracture of carburised case at the notch root, case depth 0.38 mm, root radius 1.52 mm, N_i = 62,050

PLATE 43 Fatigue fracture of carburised case at the notch root, case depth 0.38 mm, root radius 1.52 mm, N_i = 118,470

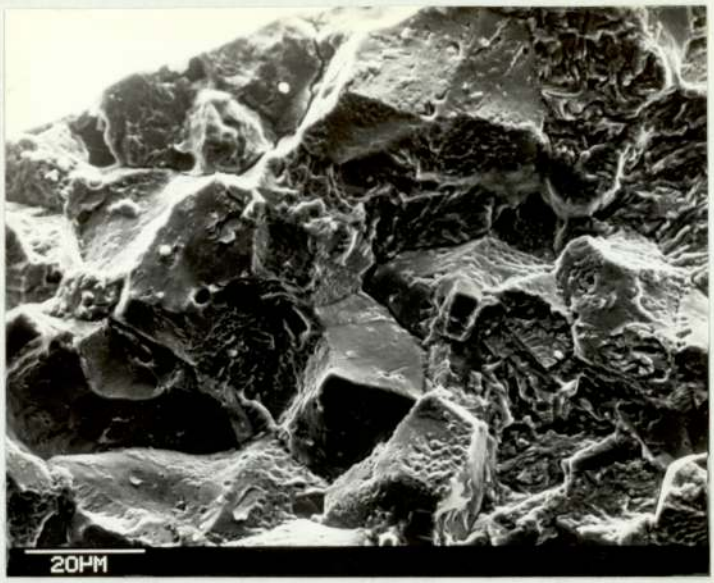

PLATE 44 Fatigue fracture of carburised case at the notch root, case depth 0.38 mm, root radius 1.52 mm, N_i = 20,000

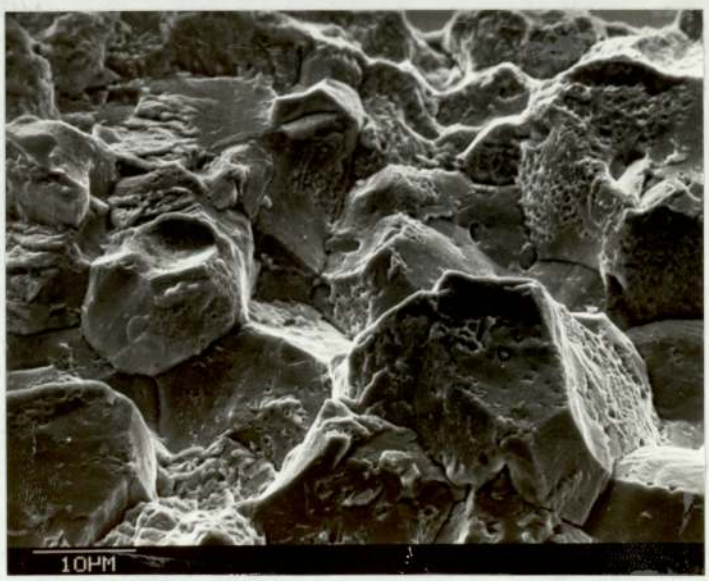

PLATE 45 Fatigue fracture of carburised case at the notch root, case depth 0.38 mm, root radius 3.17, N_i = 210,000

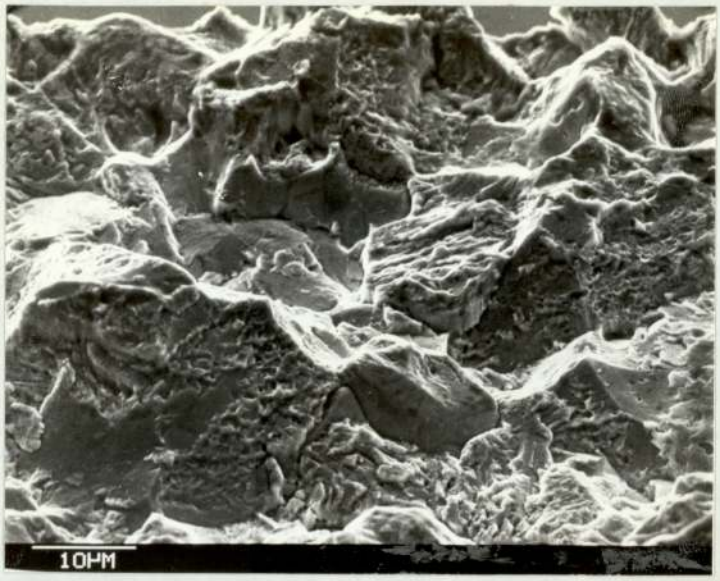

PLATE 46 Fatigue fracture of carburised case at the notch root, case depth 0.76 mm, root radius 1.52 mm, N_i = 305,700

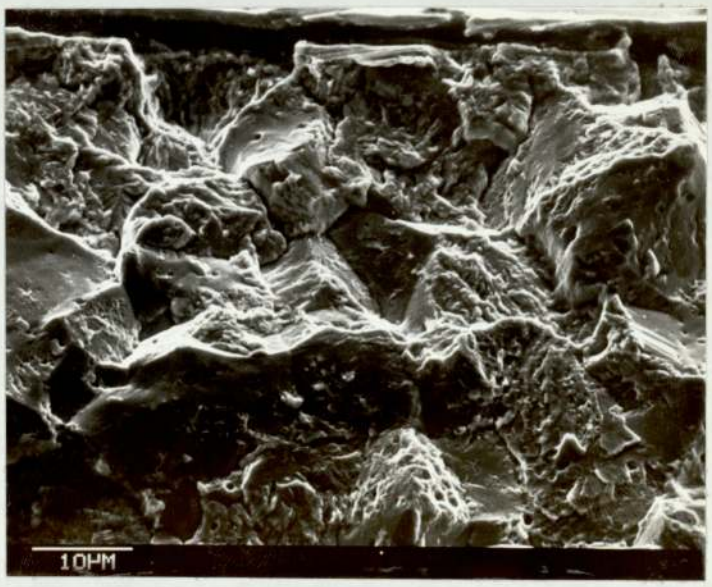

PLATE 47 Fatigue fracture of carburised case at the notch root, case depth 0.76 mm, root radius 3.17, N_i = 51,600

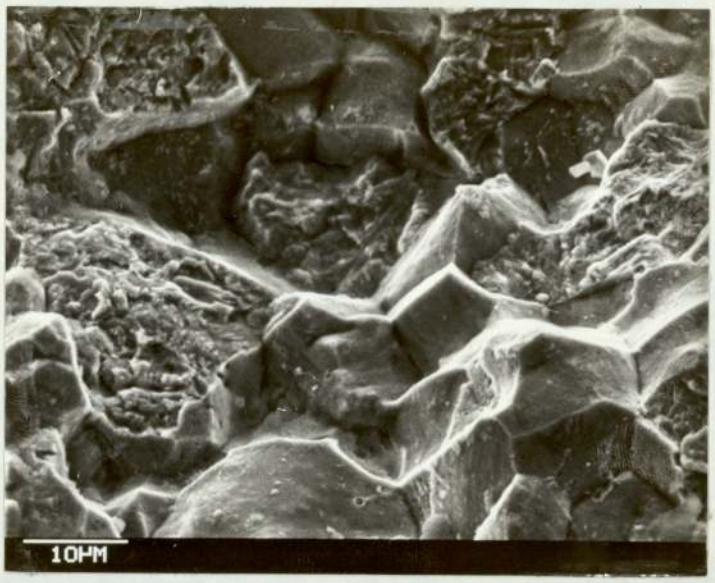

PLATE 48 Fatigue fracture in carbonitrided case below the notch root, case depth 0.38 mm, root radius 1.52 mm, N_i = 158,650

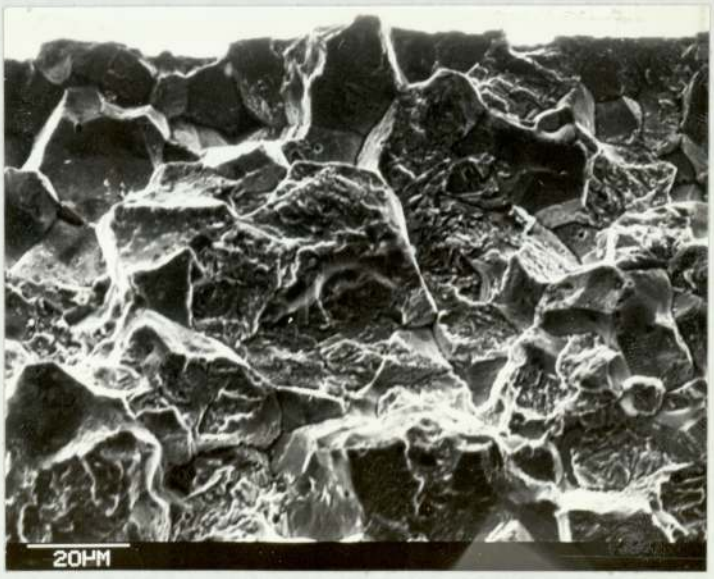

PLATE 49 Fatigue fracture in carbonitrided case at the notch root, case depth 0.38 mm, root radius 3.17 mm, N_i = 211,200

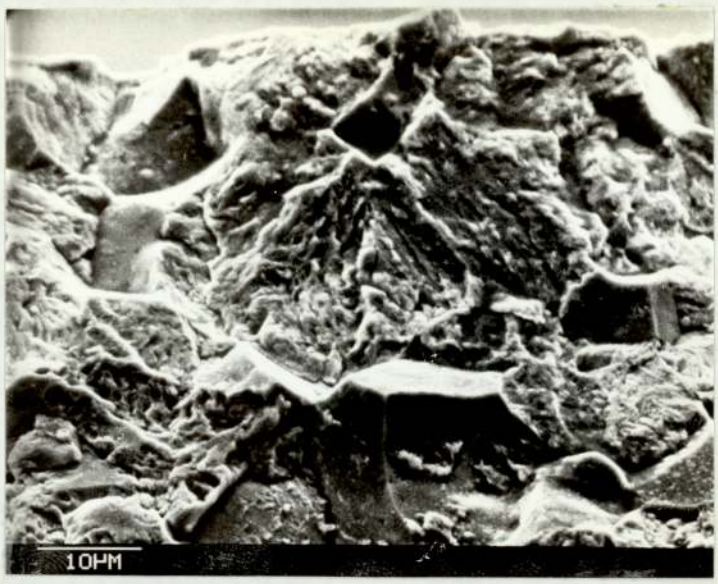

PLATE 50 Fatigue fracture in carbonitrided case at the notch root, case depth 0.76 mm, root radius 1.52 mm, N_i = 185,000

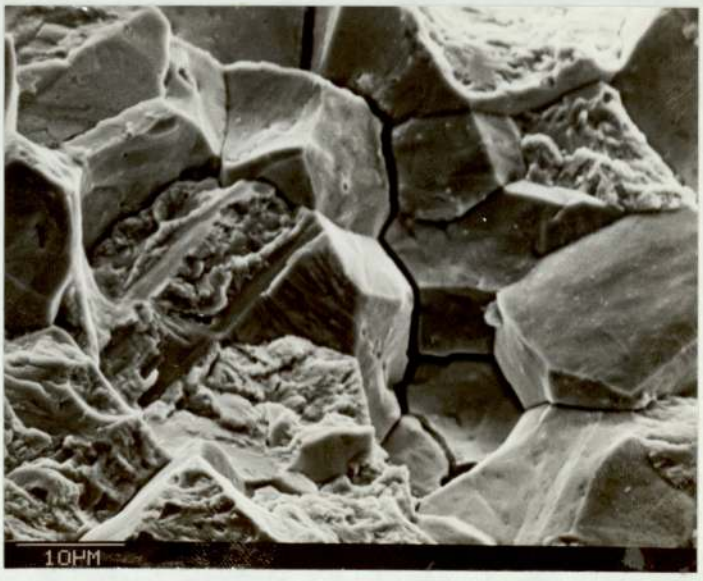

PLATE 51 Fatigue fracture in carbonitrided case at the notch root, case depth 0.76 mm, root radius 3.17 mm, N_i = 241,270

boundaries. The examination of microstructure for these notch geometries showed small amount of non-martensitic transformation product formed at the notch root. Microvoid formation and dimples are observed on most of the intergranular facets which indicate that the fatigue crack propagation occurred through the pearlite/bainite phase rather than fracture of martensite plates.

Similar to sharp and shallow notches the fracture behaviour did not seem to correlate with macroscopic fatigue crack initiation. The number of cycles to initiation Ni as established from electrical potential difference measurements is presented for each fractograph. Intergranular fracture was observed in all the specimens irrespective of the number of cycles to initiation, being large or small. Further, initiation location of fatigue could not be associated with the inclusions or carbides as was observed in other cases

The fractographs of the fatigue fracture in the core are presented in Plates 52, 53 and 54. The fracture surface was composed of dimples, tear ridges and occasional flat, quasicleavage facets. The fatigue striations were not apparent in any of the fracture surfaces of the core, in carburised or carbonitrided 080M15. The fast fracture surface through the case was always intergranular (Plate 55).

PLATE 52 Fatigue fracture of core in carburised 080M15

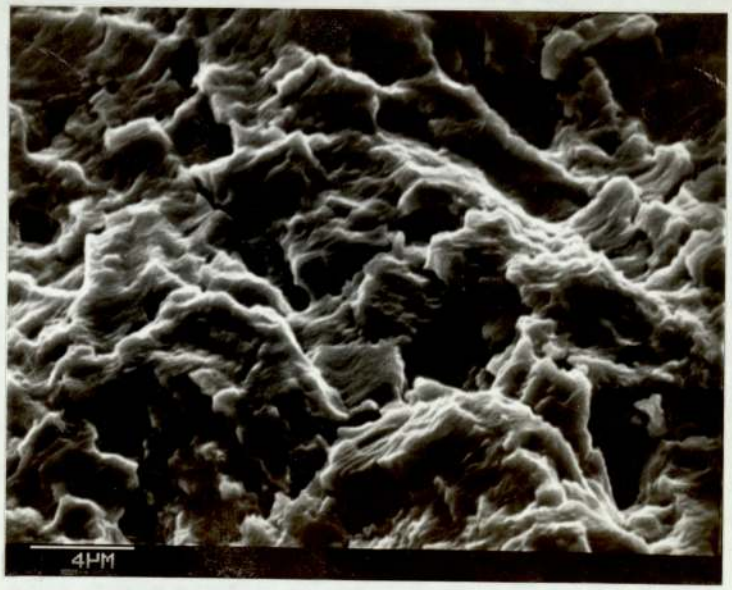

PLATE 53 Fatigue fracture of core in carburised 080M15

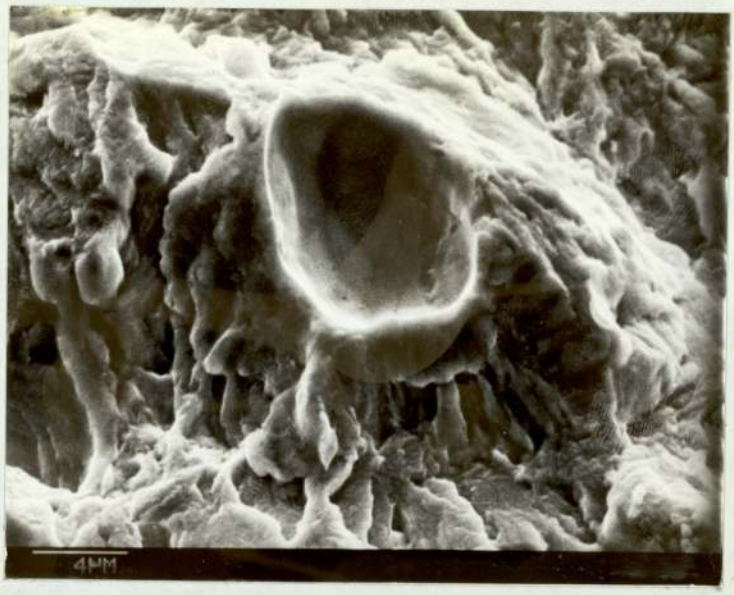

PLATE 54 Fatigue fracture of core in carbonitrided 080M15

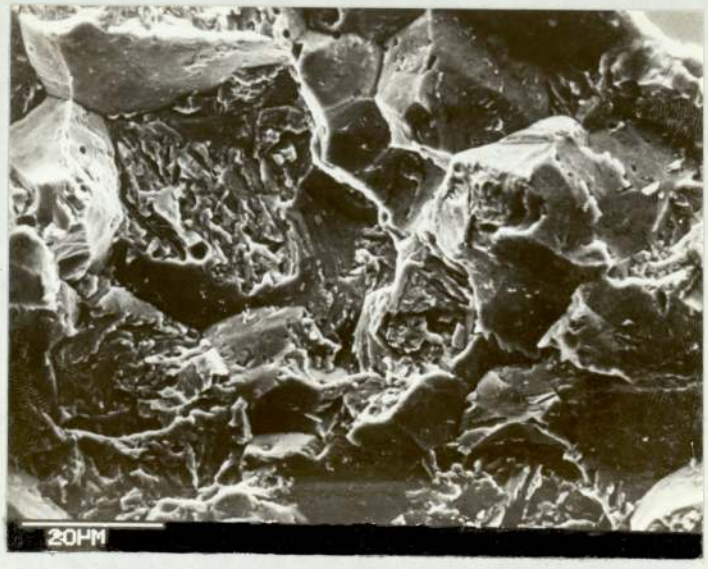

PLATE 55 Fast fracture topography of carburised case

6.6.2.3 Fatigue Fracture of Nitrocarburised 080M15

Plates 56 to 65 show typical fracture surface topography observed in nitrocarburised 080M15. The fatigue fracture of the compound layer shows a flat featureless fracture. Microporosity was evident at the notch root irrespective of the notch root radius. Further away from the notch root the fracture surface showed a mixed mode of fracture. Large cleavage facets and transgranular facets were present. Further away from the notch root the number of cleavage facets decreased considerably, transgranular facets still being evident. Fatigue fracture at the distances beyond the diffusion zone, as defined by the hardness gradient, showed microvoid coalescence and essentially flat facets (Plate 59). The striations were clearly seen on the transgranular fracture facets in the diffusion zone. However, in the core they were not so apparent.

6.6.2.4 Fatigue Fracture in Induction Hardened 080A47

Plates 66, 67 and 68 show typical fracture surface topography observed in induction hardened 080A47. The fracture surfaces at the notch root show a transgranular fracture. Evidence of subsurface crack initiation could not be found. The fracture surface essentially shows fractured martensite plates. The fracture topography was similar for all the notch geometries unlike chemico-thermally treated samples. Fatigue fracture in the core did not show any particular features. The potential difference versus time plots showed that initiation of fatigue cracks and the final fracture of the samples were

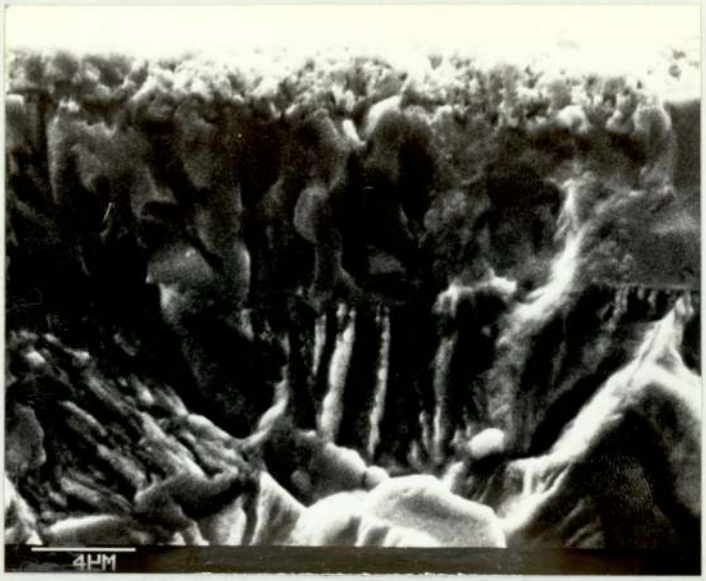

PLATE 56 Fatigue fracture of compound layer in nitrocarburised 080M15 at the notch root, root radius 0.13 mm, (midsection), N_i = 191,000

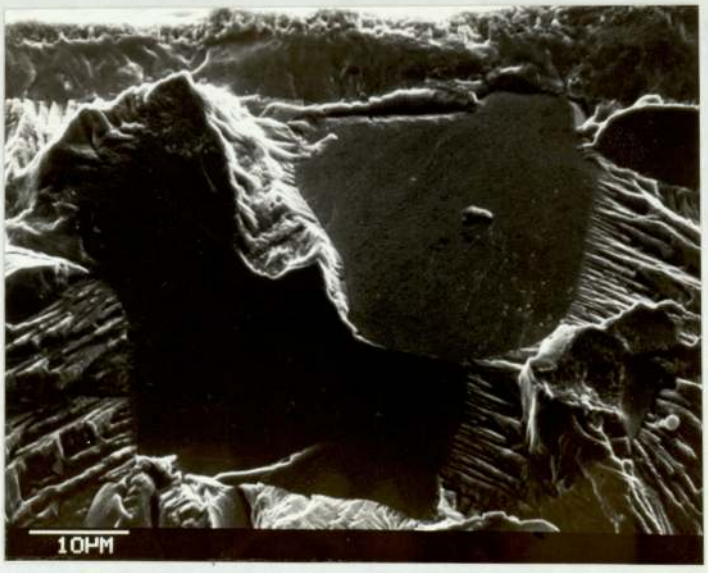

PLATE 57 Fatigue fracture of nitrocarburised case at the notch root (same area as that in plate 56, at a lower magnification), N_i = 191,000

PLATE 58 Fatigue fracture in the compound layer at the notch root, showing microporosity, nitrocarburised 080M15, root radius 0.76 mm, N_i = 610,000

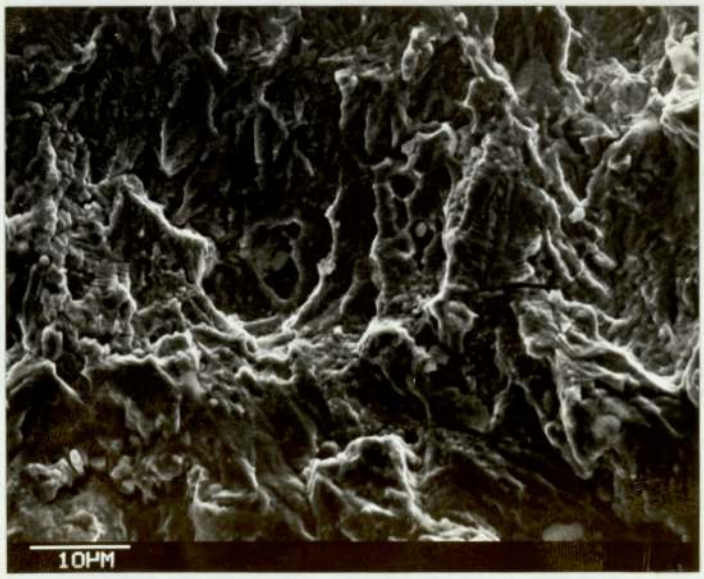

PLATE 59 Fatigue fracture of core in nitrocarburised 080M15

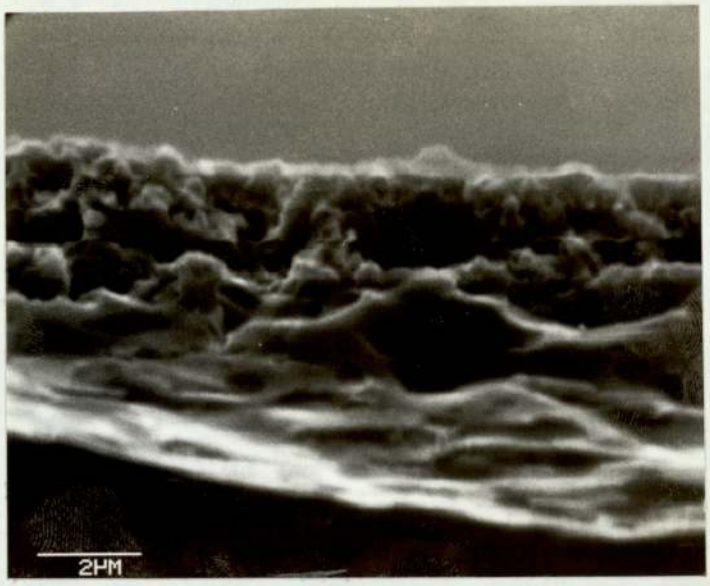

PLATE 60 Fatigue fracture in the compound layer at the notch root, showing microporosity, nitrocarburised 080M15, root radius

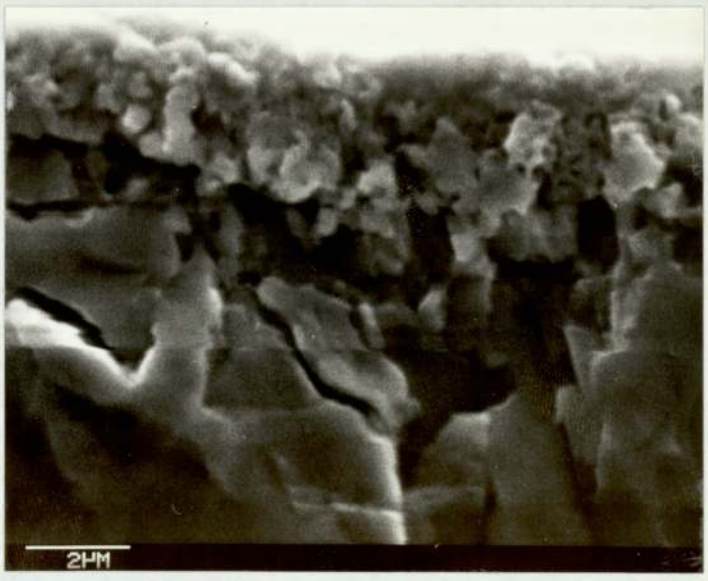

PLATE 61 Fatigue fracture in the compound layer at the notch root, nitrocarburised 080M15, root radius 1.52 mm, N_i = 646,250

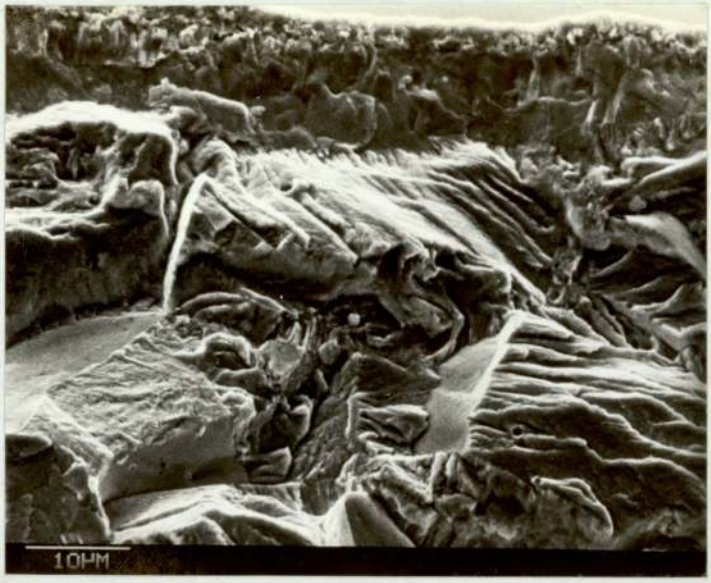

PLATE 62 Fatigue fracture in nitrocarburised 080M15 at the notch root, midsection, root radius 1.52 mm, N_i = 646,250

PLATE 63 Fatigue of compound layer at the notch root, nitrocarburised 080M15, root radius 3.17 mm, N_i = 191,000

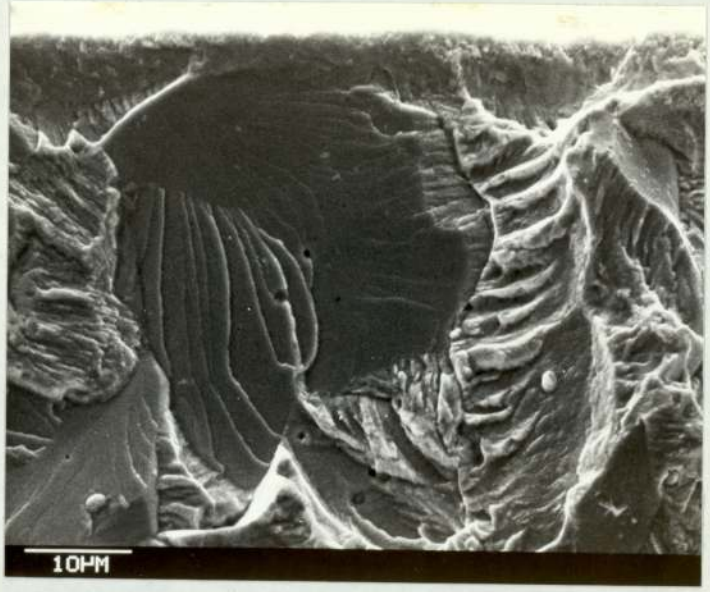

PLATE 64 Fatigue fracture in the nitrocarburised 080M15 below the notch root, midsection, root radius 3.17 mm

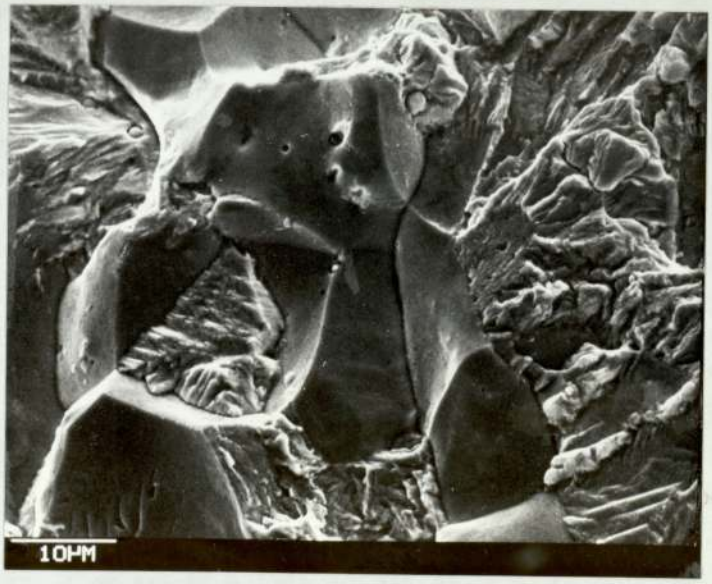

PLATE 65 Fatigue fracture in nitrocarburised case below the notch root, midsection root radius 3.17 mm

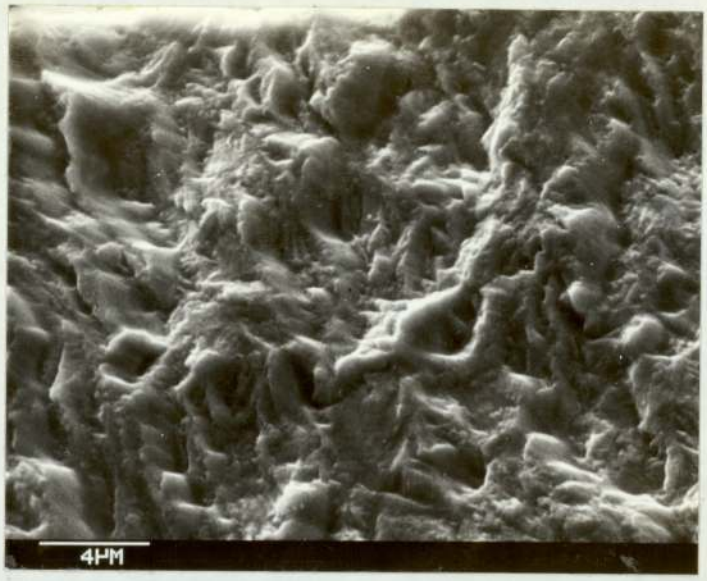

PLATE 66 Fatigue fracture of case in induction hardened 080A47, location: notch root, midsection, root radius 0.36 mm, N_i or N_f = 254,000

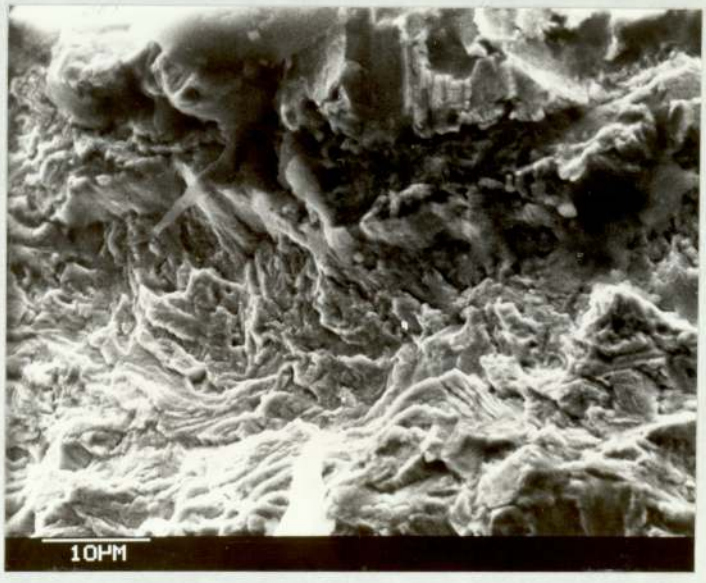

PLATE 67 Fatigue fracture of case in induction hardened 080A47, location: notch root, midsection, root radius 0.76 mm, N_i or N_f = 377,000

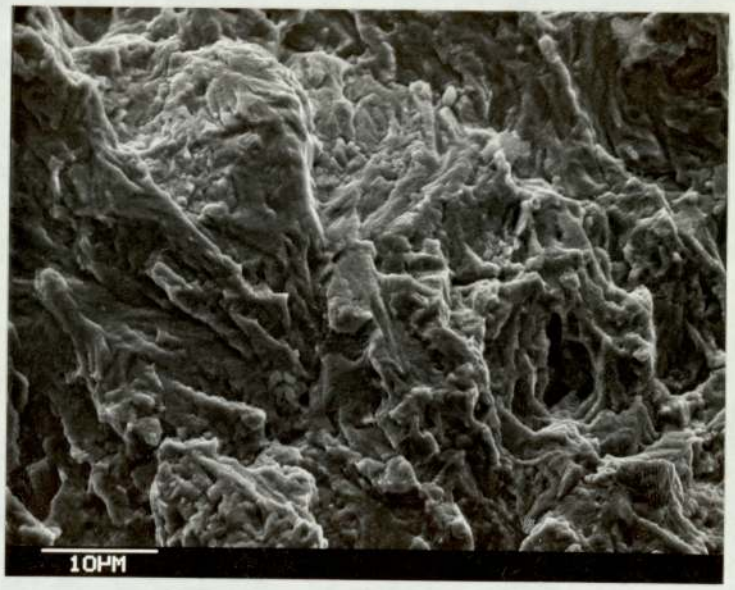

PLATE 68 Fatigue fracture in core of induction hardened 080A47

almost simultaneous. Thus the fracture surface essentially shows a fast fracture surface topography, rather than that of fatigue fractures.

6.6.3 Fracture Crack Initiation

Plates 4, 5, 69 and 70 show typical crack shapes observed at the notch root when the fatigue crack initiation was indicated by a 5 μv signal on the electrical potential difference versus time trace. The initiated cracks in untreated material, as can be seen, were larger than an engineering crack. Multiple crack initiation in case hardened steel was found to result in a through thickness crack. Further growth of crack into the core tended to result in an ellipical crack front. None of the samples examined showed sub-surface crack initiation.

The results of examination of the notch under a scanning electron microscope are presented in Plates 71 to 75. It can be seen that the crack tends to initiate in a trans-granular mode. The initiated cusp had different sizes and shapes. However, all of them conformed to the definition of an engineering crack. The area surrounding the cusps showed a mixed mode of fracture, the significant mode being intergranular. As the short and sharp notches showed a transgranular mode of fracture at all locations in the case, fractographic examination could not indicate the location of crack initiation, as in deep and blunt notches.

PLATE 69 Fatigue crack shape at initiation in carburised 080M15, case depth 0.38 mm, root radius 0.13 mm (magnification x10)

PLATE 70 Fatigue crack shape at initiation in carbonitrided 080M15, case depth 0.76 mm (magnification x10)

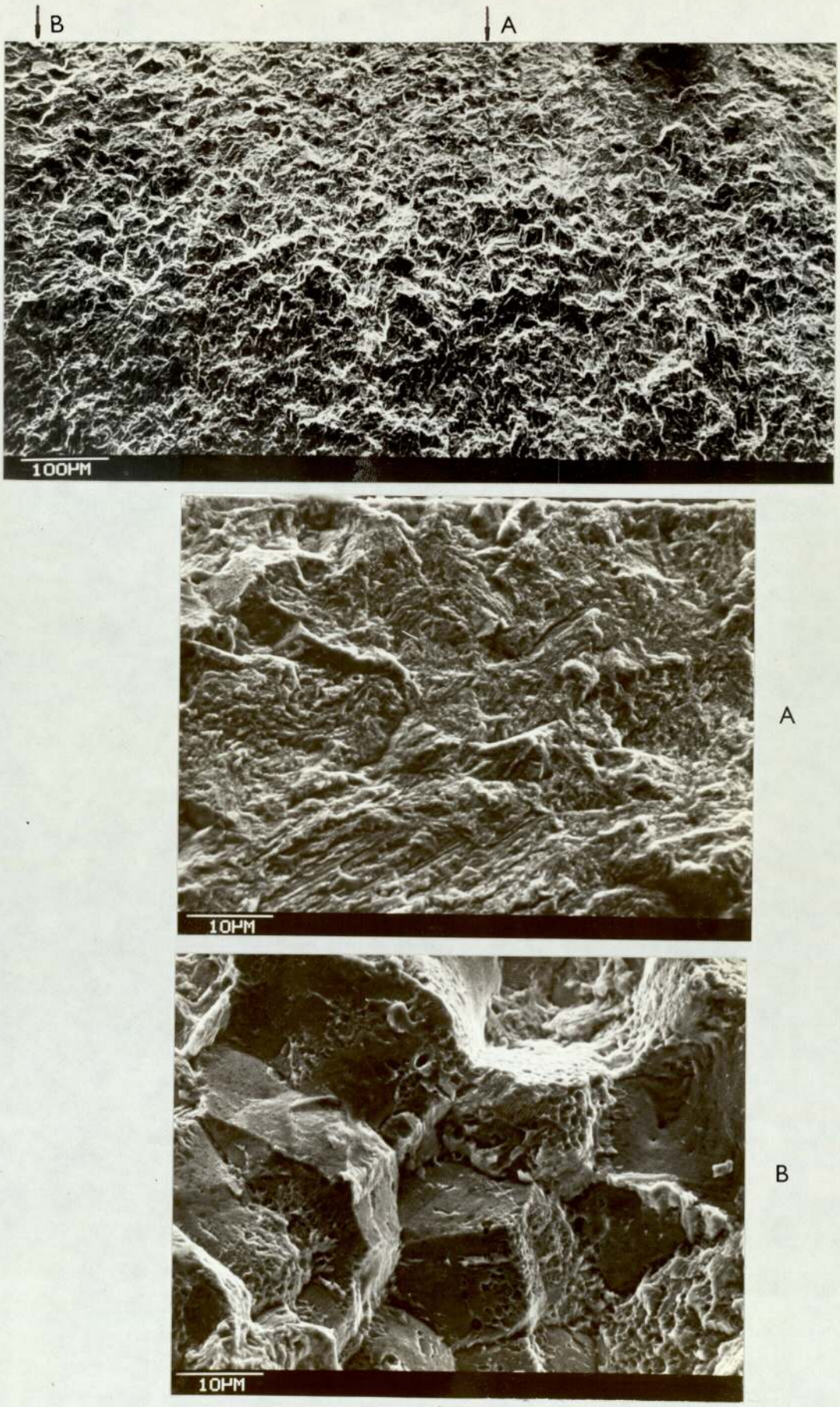

PLATE 71 Fatigue fracture of case in carburised 080M15 at the notch root, showing a cusp grown in transgranular mode. Surface topography at locations marked A and B at higher magnification is shown in plates marked A and B respectively, root radius 3.17 mm, case depth 0.38 mm, N_i = 210,000

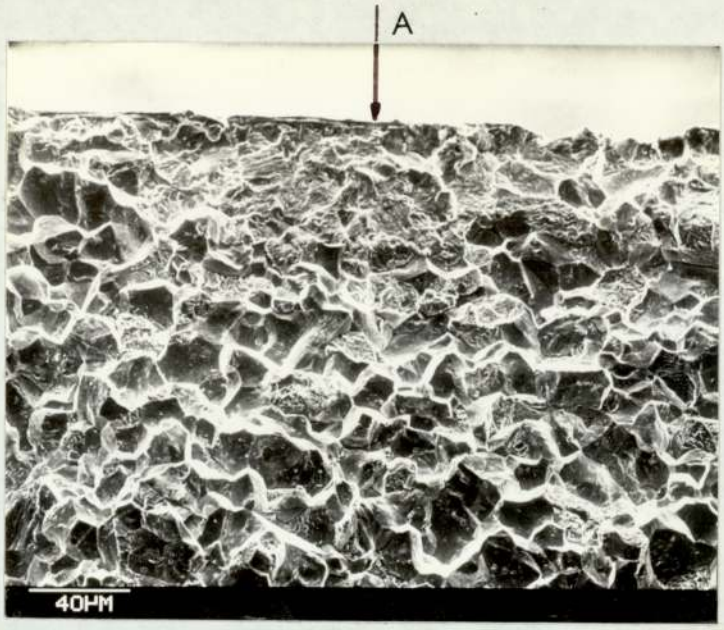

PLATE 72 Fatigue fracture of case in carburised 080M15 at the notch root, showing a cusp grown in transgranular mode, surrounded by an area fractured in intergranular mode, root radius 3.17 mm, case depth 0.76 mm, N_i = 51600

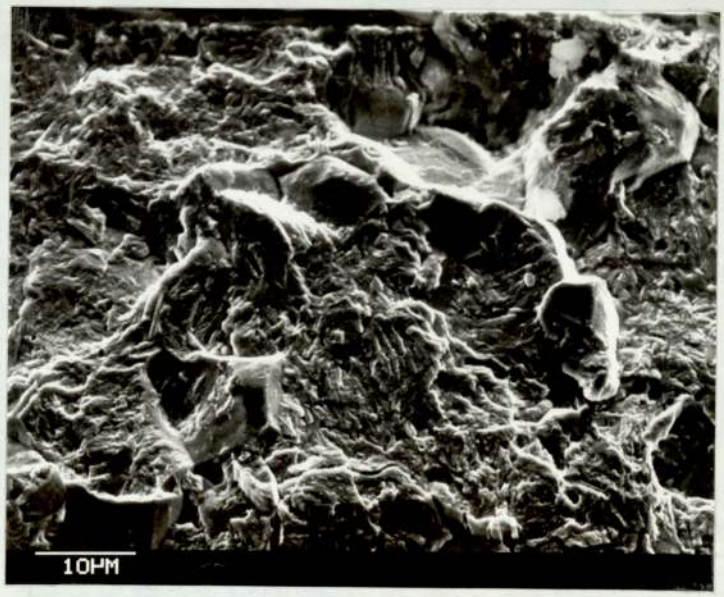

PLATE 73 Fatigue fracture of case in carburised 080M15 at the notch root, fractography of the area at location A in plate 72, at high magnification

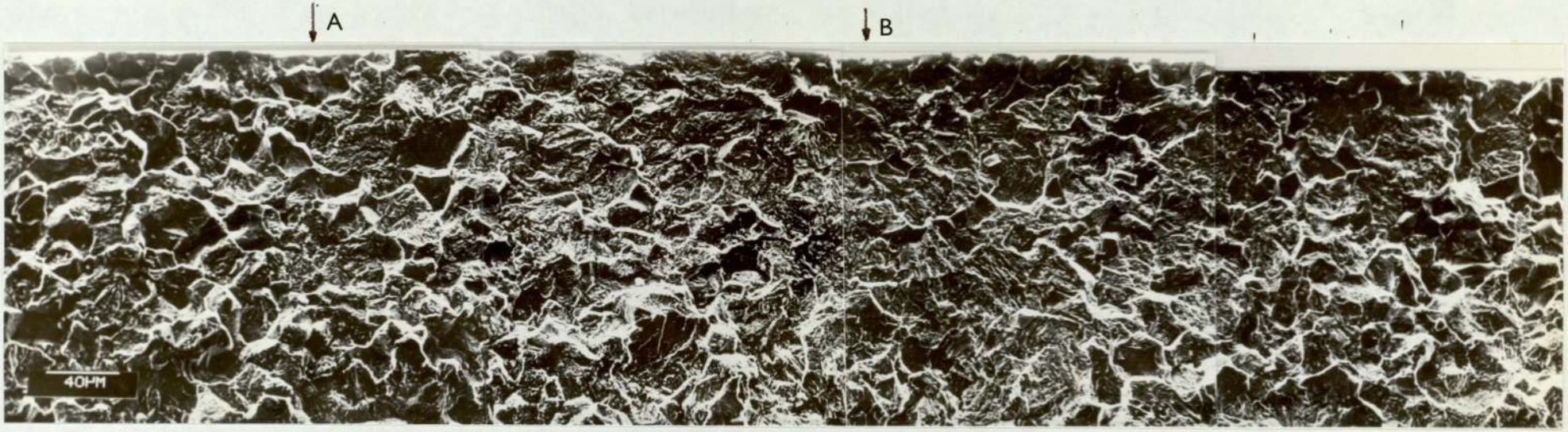

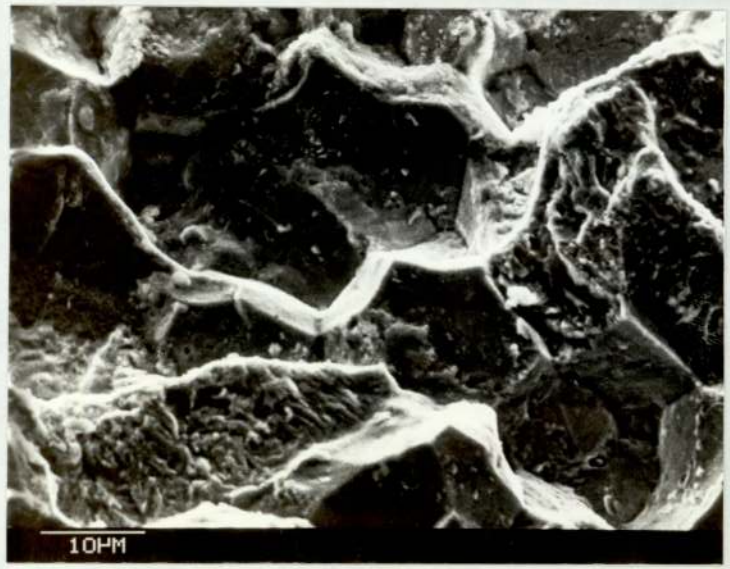

A

B

PLATE 74 Fatigue fracture of case in carbonitrided 080M15 at the notch root, showing a cusp grown in transgranular mode surrounded by an area fractured in intergranular mode. Fractography of area at locations A and B is shown at higher magnification in plates marked A and B, root radius 1.52 mm, case depth 0.38 mm, N_i = 158,650

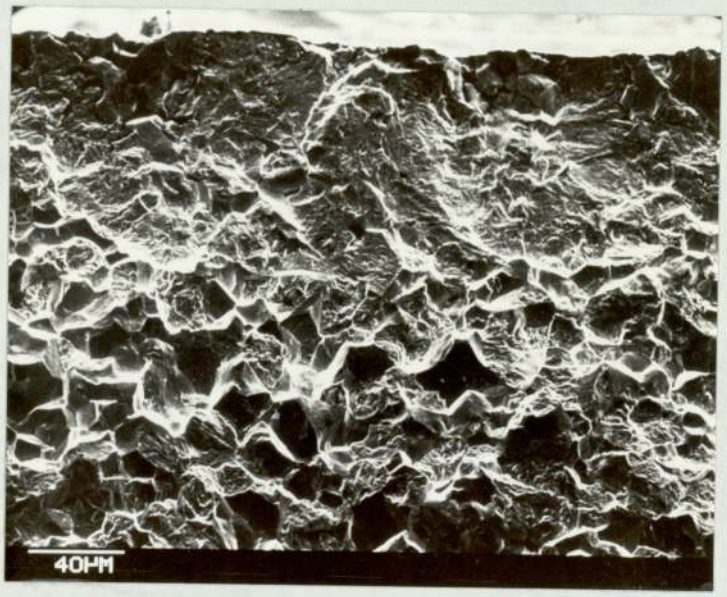

PLATE 75 Fatigue fracture of case in carbonitrided 080M15 at the notch root, showing a cusp grown in transgranular mode, surrounded by an area fractured in intergranular mode, case depth 0.76 mm, root radius 0.76 mm, N_i = 173,780

6.7 Fatigue Crack Initiation Threshold

The threshold values of the parameters Δs, the amplitude of fibre stress at the notch root, $K_t \Delta s$, the stress concentration parameter, and the stress intensity factor range parameters $\frac{\Delta K}{\sqrt{\rho}}$ and ΔK are presented in Tables 12 to 15. The values refer to the load amplitudes at which deviation was not observed on the electrical potential difference-time plot for 1000,000 cycles. Further increase in load amplitude of 200 Newtons showed initiation of fatigue crack in the samples. The increase of 200 Newtons ensured that the increase in the stress amplitude at the root of the notch was less than or equal to 5% of the threshold value of the fibre stress range Δs. The threshold value of the stress intensity factor range ΔK_B was calculated according to equation (33). The crack length c was zero and the value of the parameter C_B was approximately chosen depending on the material condition.

6.7.1 Effect of Stress Concentration or the Notch Geometry on the Threshold Value of the Parameters for Case Hardened 080M15

The variation in the threshold values of different parameters with the stress concentration factor is presented in Tables 12 to 15 and Figures 54 to 57. The threshold values of the fibre stress at the notch roots show a sharp increase beyond the stress concentration factor of 3.42 (Figure 54). The same results when plotted in terms of the stress concentration parameter $K_t \Delta s$ or the fracture mechanics parameters $\frac{\Delta K}{\sqrt{\rho}}$ and ΔK_B show a similar behaviour. The root radius 0.76 mm which has a stress concentration factor of

TABLE 12 FATIGUE CRACK INITIATION THRESHOLDS FOR CASE HARDENED 080M15 BY DIFFERENT GEOMETRIES IN TERMS OF FIBRE STRESS Δs MN/m^2

Notch Geometry/K_t	Untreated	Carburised 0.38 mm	Carburised 0.76 mm	Carbonitrided 0.38 mm	Carbonitrided 0.76 mm	Nitemper
Root radius 0.13 mm	124.62	338.99	346.07	311.35	310.08	190.68
	124.21	337.65	325.76	306.40	293.74	187.31
	123.58	338.20	309.17	317.51	291.81	186.59
K_t 7.59						
Root radius 0.76 mm	200.0	424.52	410.95	386.51	349.62	306.00
	200.0	405.91	384.22	397.28	335.10	304.50
	200.0	406.04	373.41	381.00	341.12	294.85
K_t 3.42						
Root radius 1.52 mm	303.47	579.00	635.32	622.76	485.04	451.22
	311.10	587.20	624.44	620.12	500.04	44=.82
	309.45	583.00	622.62	596.32	498.43	441.95
K_t 2.25						
Root radius 3.17 mm	468.37	681.36	730.01	682.03	695.56	637.63
	471.64	720.65	713.06	653.94	644.78	632.15
	467.26	718.42	741.30	666.06	657.06	623.35
K_t 1.69						

TABLE 13 FATIGUE CRACK INITIATION THRESHOLDS FOR 080M15 CASE HARDENED BY DIFFERENT TREATMENTS AND FOR DIFFERENT NOTCH GEOMETRIES IN TERMS OF $K_t \Delta s$ MN/m^2

Notch Geometry/K_t	Untreated	Carburised 0.38 mm	Carburised 0.76 mm	Carbonitrided 0.38 mm	Carbonitrided 0.76 mm	Nitemper
Root radius 0.13 mm	945.87	2572.93	2626.67	2363.15	2353.51	1446.88
	942.75	2562.76	2472.52	2325.58	2229.49	1421.68
	937.97	2566.94	2346.60	2409.90	2214.84	1416.22
$K_t = 7.59$						
Root radius 0.76	684.00	1451.86	1405.45	1321.86	1195.70	1046.52
	684.00	1388.21	1314.03	1358.70	1146.04	1041.39
	684.00	1388.66	1277.06	1303.02	1166.63	1008.39
$K_t = 3.42$						
Root radius 0.52	685.84	1308.54	1435.82	1407.44	1096.19	1019.76
	703.09	1327.07	1411.23	1401.47	1130.00	1000.77
	699.36	1317.58	1407.12	1347.68	1126.45	998.81
$K_t = 2.26$						
Root radius 3.17	791.55	1151.50	1233.72	1152.63	1175.50	1077.59
	797.07	1271.90	1205.07	1105.16	1089.68	1068.33
	789.67	1214.13	1252.80	1125.64	1110.33	1053.46
$K_t = 1.69$						

TABLE 14 FATIGUE CRACK INITIATION THRESHOLDS FOR 080M15, CASE HARDENED BY DIFFERENT TREATMENTS, AND FOR DIFFERENT NOTCH GEOMETRIES IN TERMS OF $\frac{\Delta K}{\sqrt{\rho}}$ MN/m^2

Notch Geometry/K_t	Untreated	Carburised 0.38 mm	Carburised 0.76 mm	Carbonitrided 0.38 mm	Carbonitrided 0.76 mm	Nitemper
Root radius	813.79	2220.38	2266.68	2039.57	2031.19	1244.08
0.13	816.36	2211.76	2133.64	2006.62	1924.22	1224.94
	819.10	2215.10	2025.09	2079.52	1911.91	1220.49
K_t = 7.59						
Root radius	649.14	1146.00	1110.31	1044.24	944.40	827.46
0.76	649.14	1096.69	1038.11	1073.38	905.19	823.38
	649.14	1096.69	1009.11	1029.43	921.46	797.29
K_t = 3.42						
Root radius	532.42	1012.86	1106.53	1093.34	851.88	788.88
1.52	544.01	1026.59	1089.47	1086.59	878.23	775.67
	541.47	1018.09	1095.39	1043.91	875.11	805.79
K_t = 2.25						
Root radius	591.54	825.84	880.96	825.28	842.29	771.37
3.17	594.20	893.30	865.99	812.74	781.97	765.71
K_t = 1.69	589.38	869.05	899.55	807.29	796.18	753.60

TABLE 15 FATIGUE CRACK INITIATION THRESHOLD FOR 080M15, CASE HARDENED BY DIFFERENT TREATMENTS AND FOR DIFFERENT NOTCH GEOMETRIES IN TERMS OF ΔK_B $MN/m^{3}/2$

Notch Geometry/K_t	Untreated	Carburised 0.38 mm	Carburised 0.76 mm	Carbonitrided 0.38 mm	Carbonitrided 0.76 mm	Nitemper
Root radius 0.13	5.36	14.62	14.93	13.43	13.38	8.20
	5.38	14.57	14.05	13.22	12.67	8.08
	5.39	14.59	13.34	13.69	12.59	8.05
K_t = 7.59						
Root radius 0.76	4.57	7.80	7.90	7.43	6.72	5.88
	4.57	7.79	7.30	7.64	6.44	5.86
	4.57	8.15	7.18	7.32	6.06	5.67
K_t = 3.42						
Root radius 1.52	3.79	7.22	7.88	7.78	6.25	5.61
	3.86	7.31	7.76	7.73	6.23	5.52
	3.87	7.25	7.80	7.42	6.39	5.73
K_t = 2.26						
Root radius 3.17	4.49	6.26	6.68	6.26	5.39	5.85
	4.51	6.77	6.57	6.16	5.94	5.81
	4.47	6.59	6.82	6.12	6.04	5.71
K_t = 1.69						

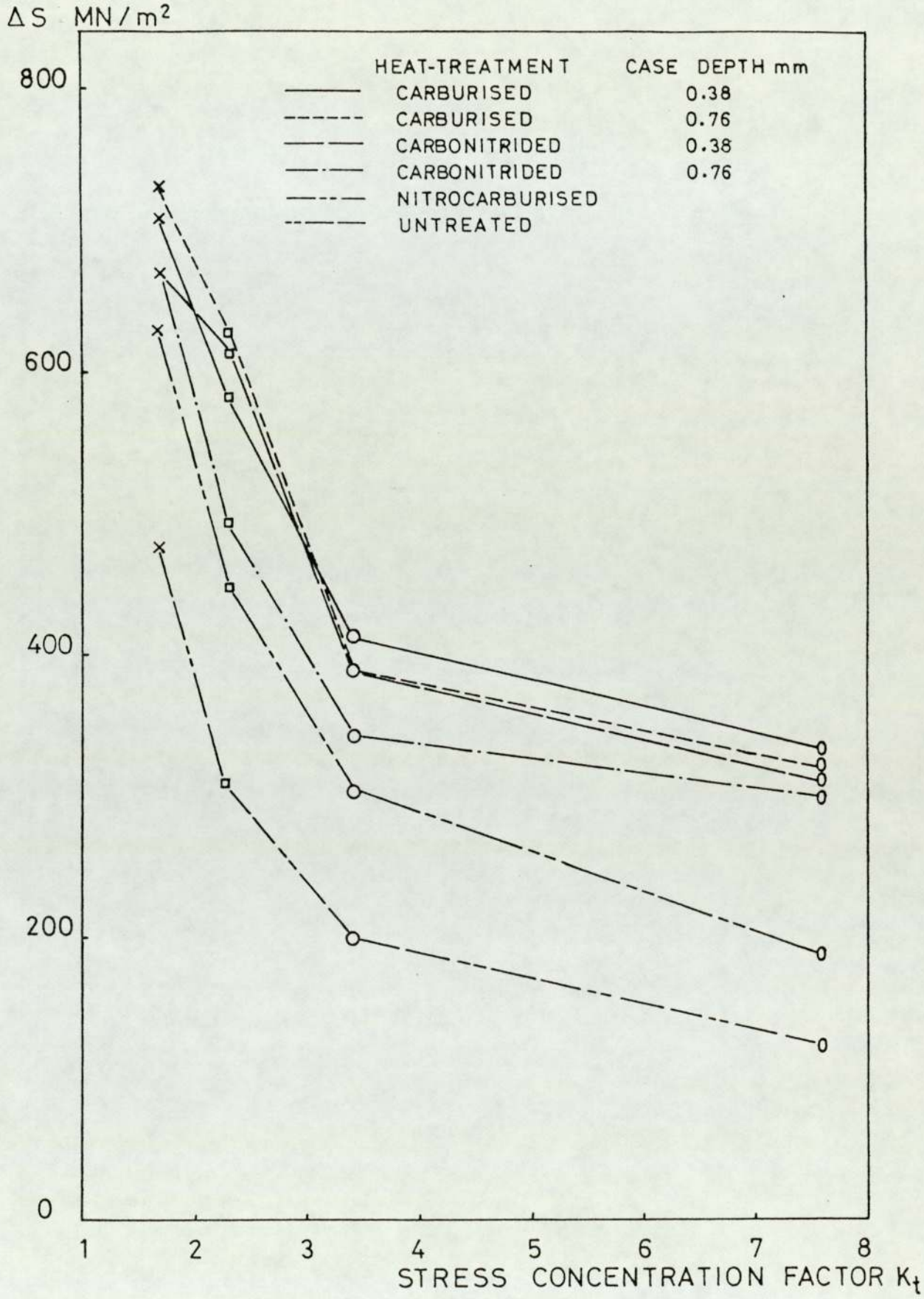

FIGURE 54 Variation in fatigue crack initiation threshold with K_t: carburised, carbonitrided and nitrocarburised 080M15: parameter Δs.

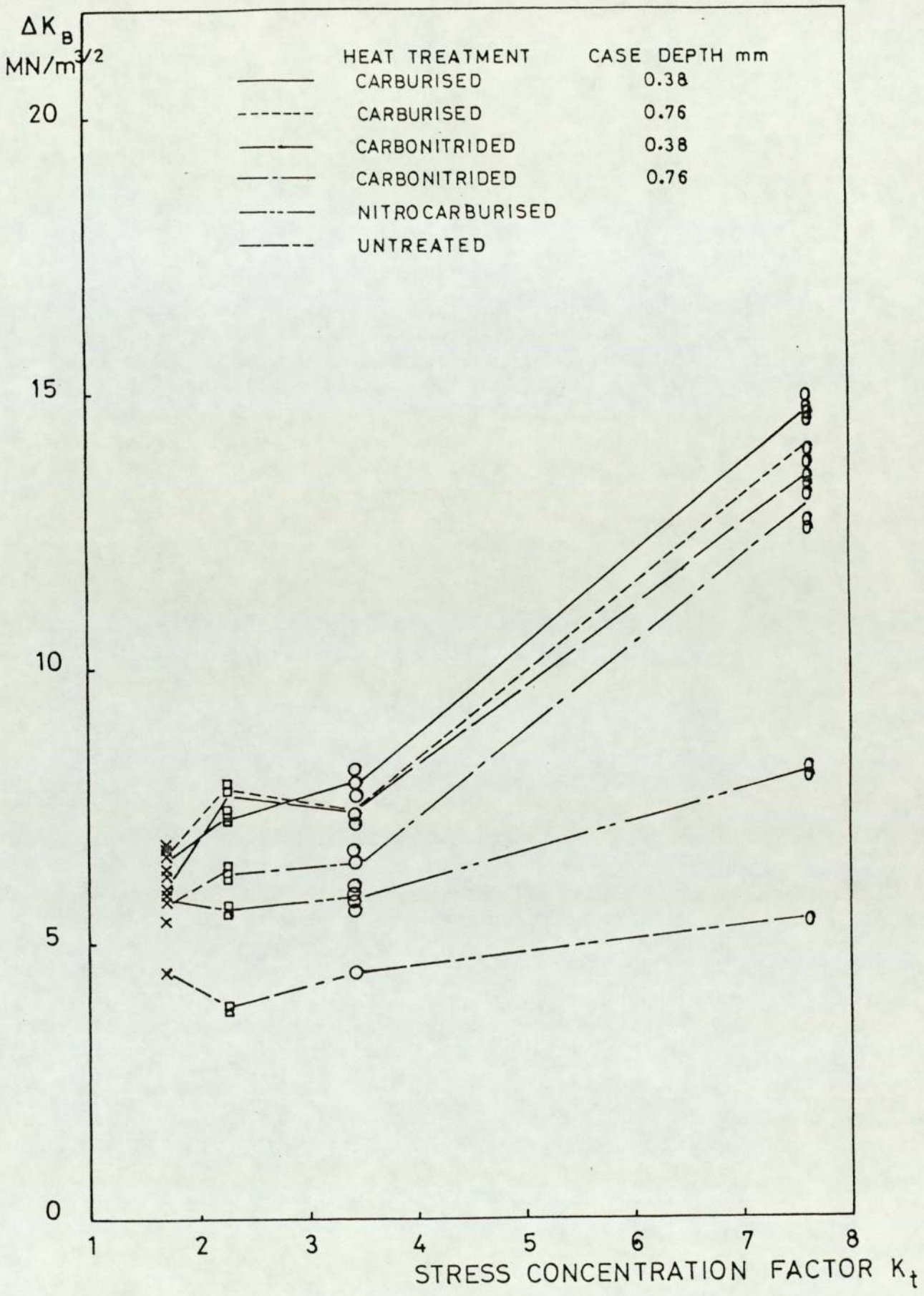

FIGURE 55 Variation in fatigue crack initiation threshold with K_t; carburised, carbonitrided and nitrocarburised 080M15: parameter ΔK_B

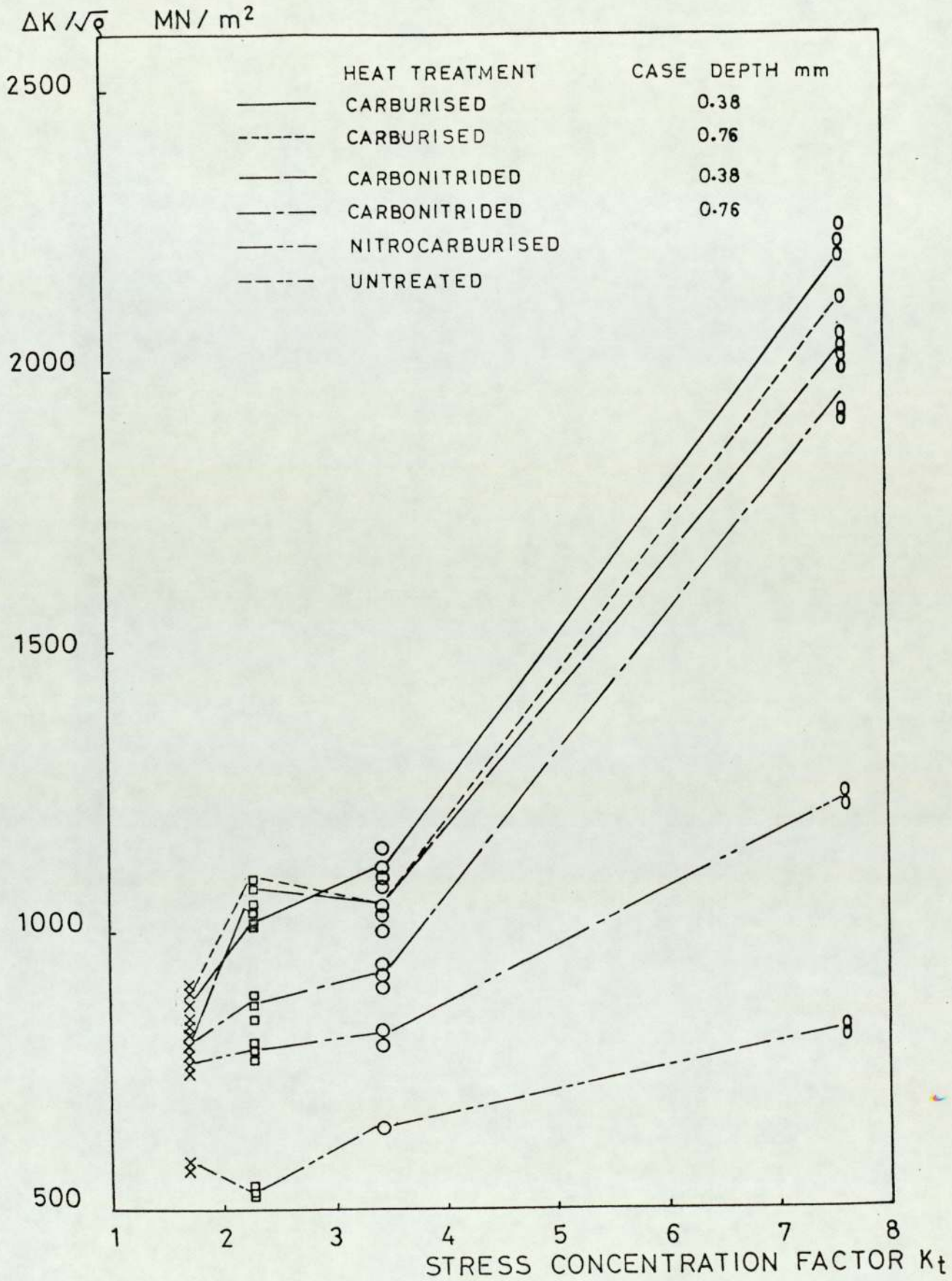

FIGURE 56 Variation in fatigue crack initiation threshold with K_t; carburised, carbonitrided and nitrocarburised 080M15: parameter $\Delta K/\sqrt{\rho}$

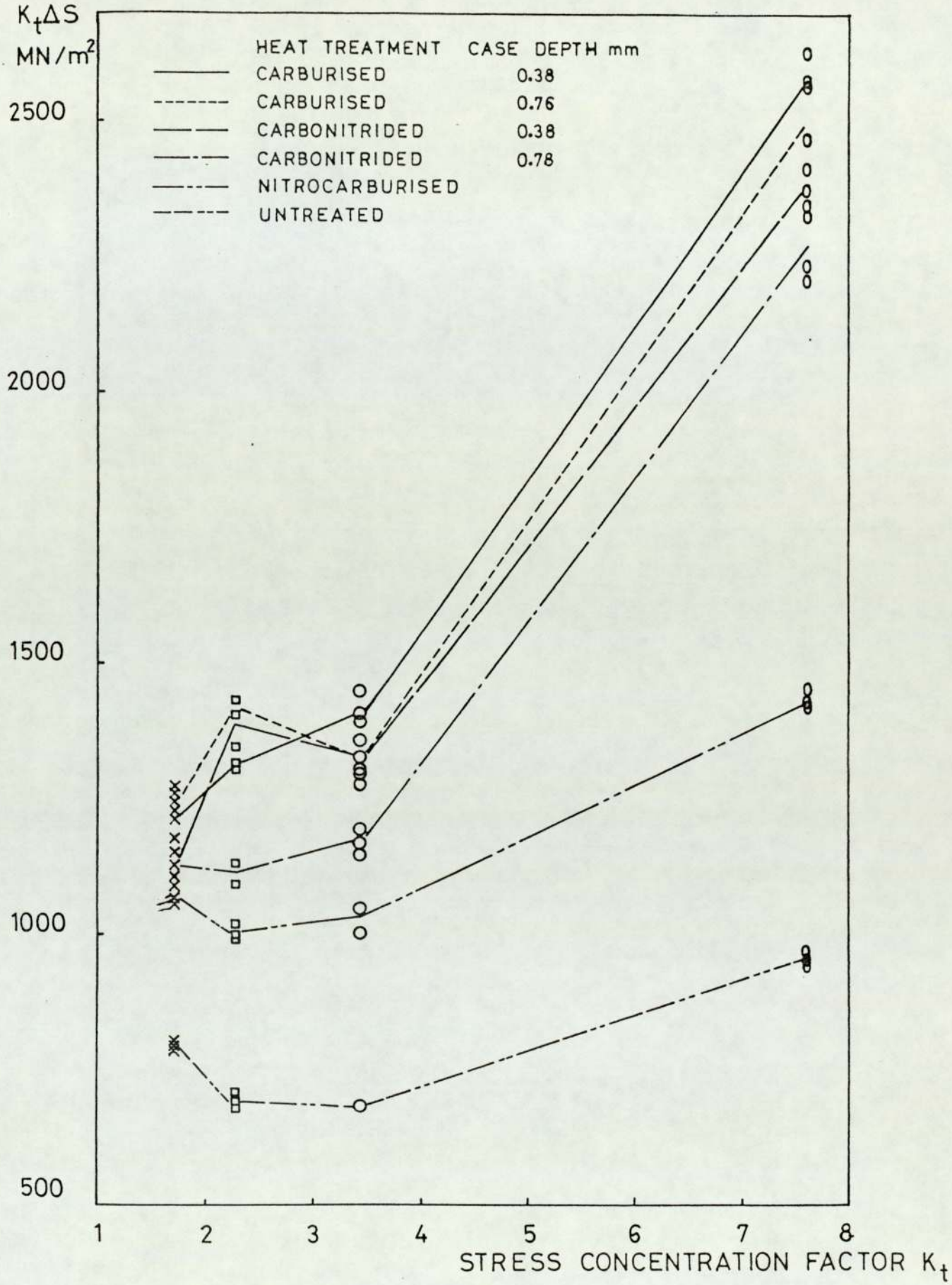

FIGURE 57 Variation in fatigue crack initiation threshold with K_t, carburised, carbonitrided and nitrocarburised 080M15: parameter $K_t\Delta s$

3.42 shows a similar threshold value to that of lesser stress concentration factors of 1.69 and 2.26. A sharp increase is however obtained when the notch root radius is decreased to yield a stress concentration factor of 7.59 (root radius 0.13 mm). The data banding decreases considerably when the values are computed in terms of the stress intensity factor range according to equation (33).

Table 16 shows the percentage increase obtained in the threshold values of different parameters for various notch roots and treatments over the untreated material. The percentage improvement obtained, when calculated in terms of the parameter $K_t \Delta s$, shows a consistent decrease in improvement in fatigue properties with decrease in the stress concentration factor. Such a trend is, however, not observed when the values are computed in terms of fracture mechanics parameters $\frac{\Delta K}{\sqrt{\rho}}$ and ΔK_B.

6.7.2 Effect of Heat Treatment and Case Depth on the Threshold Value of the Parameters for Case Hardened 080M15

Figure 53 shows the effect of treatment and case depth on the threshold values for different notch root radius. The threshold values presented here are computed in terms of the new parameter ΔK_B. As can be seen, for one particular notch geometry carburising treatment gives a marginally higher fatigue limit than the carbonitriding treatment for any one case depth. Fatigue limit values obtained for nitro-carburised material were less than both the treatments, carburising and carbonitriding. The change in the case

TABLE 16 PERCENTAGE CHANGE IN FATIGUE INITIATION THRESHOLD OF 080M15 DUE TO CASE HARDENING IN DIFFERENT NOTCH GEOMETRIES

Notch Geometry/K_t	Parameter	Carburised 0.38 mm	Carburised 0.76 mm	Carbonitrided 0.38 mm	Carbonitrided 0.76 mm	Nitemper
7.59		172.5	163.42	151.14	140.50	51.6
3.42	$K_t \Delta s$	106.00	94.76	94.13	71.00	50.9
2.26	MN/m^2	89.30	103.7	99.00	60.54	44.58
1.69		52.95	55.22	42.26	41.93	34.52
7.59		171.4	162.34	150.1	139.56	50.63
3.42	$\frac{\Delta K}{\sqrt{\rho}}$	71.48	62.14	61.6	42.3	25.71
2.26		89.00	103.4	99.3	61.0	46.5
1.69	MN/m^2	45.8	49.1	37.8	36.35	29.04
7.59		171.1	162.3	150.0	139.4	50.7
3.42		73.1	63.9	63.2	40.3	26.9
2.26	ΔK_B	89.1	103.4	99.0	64.0	46.4
1.69	$MN/m^{3/2}$	95.65	49.00	37.64	29.00	29.00

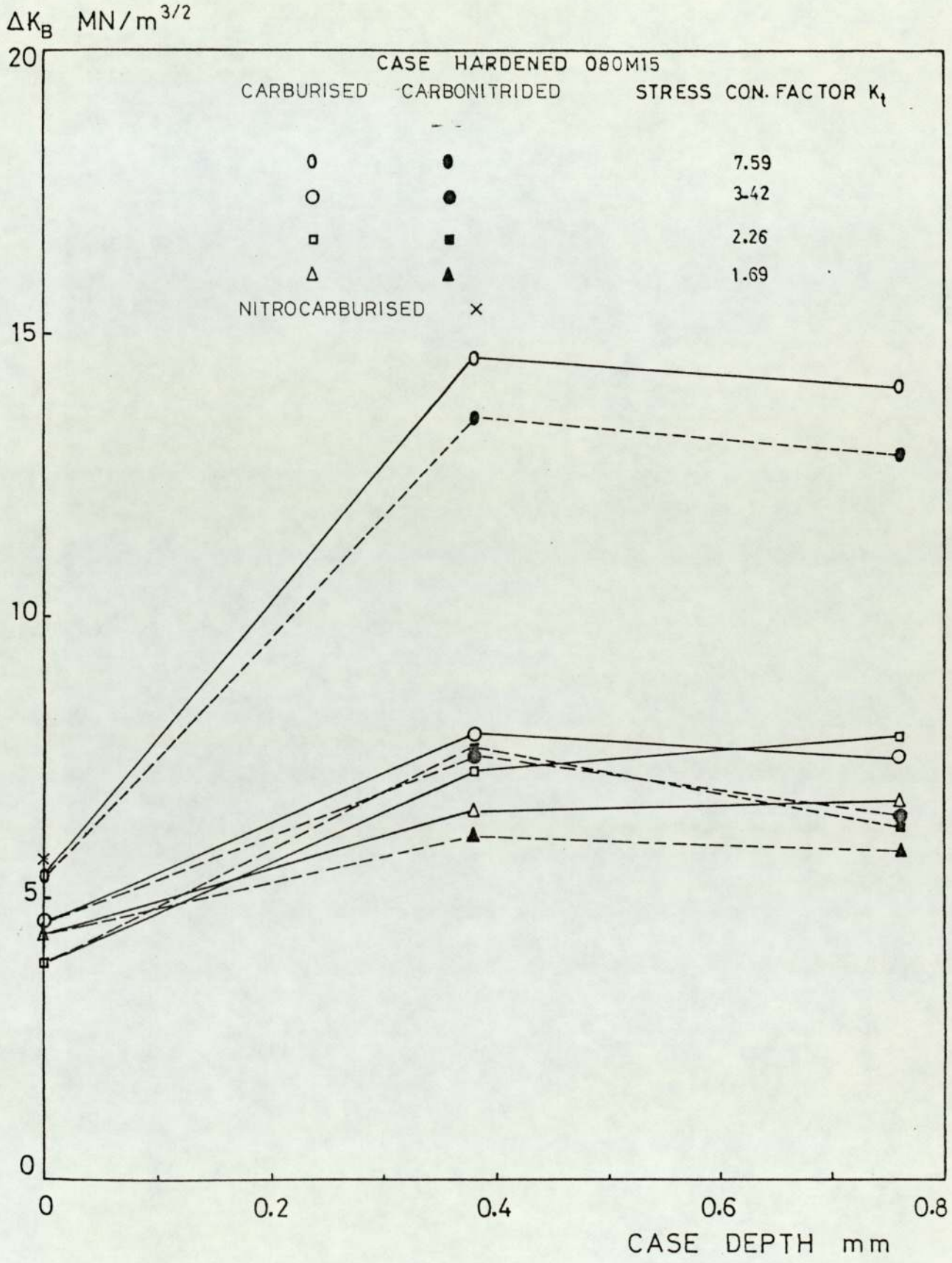

FIGURE 58 Variation in fatigue crack initiation threshold, in terms of ΔK_B, with the case depth for carburised and carbonitrided 080M15

depth does not seem to affect the fatigue limit. A consistent trend was not shown for either carburising or carbonitriding except in the case of the sharpest notch root radius (K_t = 7.59), where a slight decrease was observed in the fatigue limit.

The nitempered samples of O8OM15 with the stress concentration factors less than 3.42, all showed almost identical fatigue limits when computed in terms of the new parameter ΔK_B. The values therefore are represented by a single point in Figure 58. The thickness of diffusion layer which contributes to the fatigue properties of nitempered steels was different for samples with a root radius of 0.76 mm (K_t = 3.42) when compared with samples with larger root radii, (Table 11). This, however, does not seem to have contributed to the fatigue behaviour.

6.7.3 Effect of Induction Hardening on the Threshold Values of the Parameters for O8OA47

Fatigue crack initiation threshold values of untreated and induction case hardened O8OA47 are presented in Table 17 and Figures 59 to 61. Improvements of between 28% to 34% were obtained. Highest improvement over the untreated material observed for the notch with sharpest root radius (ρ = 0.13 mm, K_t = 7.59). The improvement observed, in fact, varied linearly with the stress concentration factor.

TABLE 17 FATIGUE CRACK INITIATION THRESHOLD DATA FOR INDUCTION HARDENED O80A47 IN TERMS OF DIFFERENT PARAMETERS

Notch Geometry/K_t	Untreated			Induction Hardened		
	$K_t\Delta s$ MN/m^2	$\frac{\Delta K}{\sqrt{\rho}}$ MN/m^{2}	ΔK_B $MN/m^{3/2}$	$K_t\Delta s$ MN/m^2	$\Delta K/\sqrt{\rho}$ MN/m^2	ΔK_B $MN/m^{3/2}$
Root radius 0.36	873.39	742.62	5.09	3149.00	2836.32	19.44
	878.90	737.32	5.06	3194.09	2827.64	19.39
	879.52	742.26	5.09	2991.35	2829.04	19.40
K_t = 4.65						
Root radius 0.76	856.95	652.06	4.63	2356.04	2148.97	15.24
	841.47	640.37	4.55	2339.96	2137.81	15.17
	863.48	657.10	4.66	2353.64	2140.69	15.19
K_t = 3.42						
Root radius 1.52	788.40	588.00	4.21	1788.79	1135.37	8.13
	787.85	577.94	4.14	1796.93	1122.54	8.03
	791.85	577.74	4.14	1787.21	1134.24	8.12
K_t = 2.26						
Root radius 3.17	833.20	600.02	4.55	1220.69	815.57	6.18
	835.70	599.19	4.54	1216.80	829.61	6.29
K_t = 1.69	857.16	600.41	4.55	1217.65	773.59	5.85

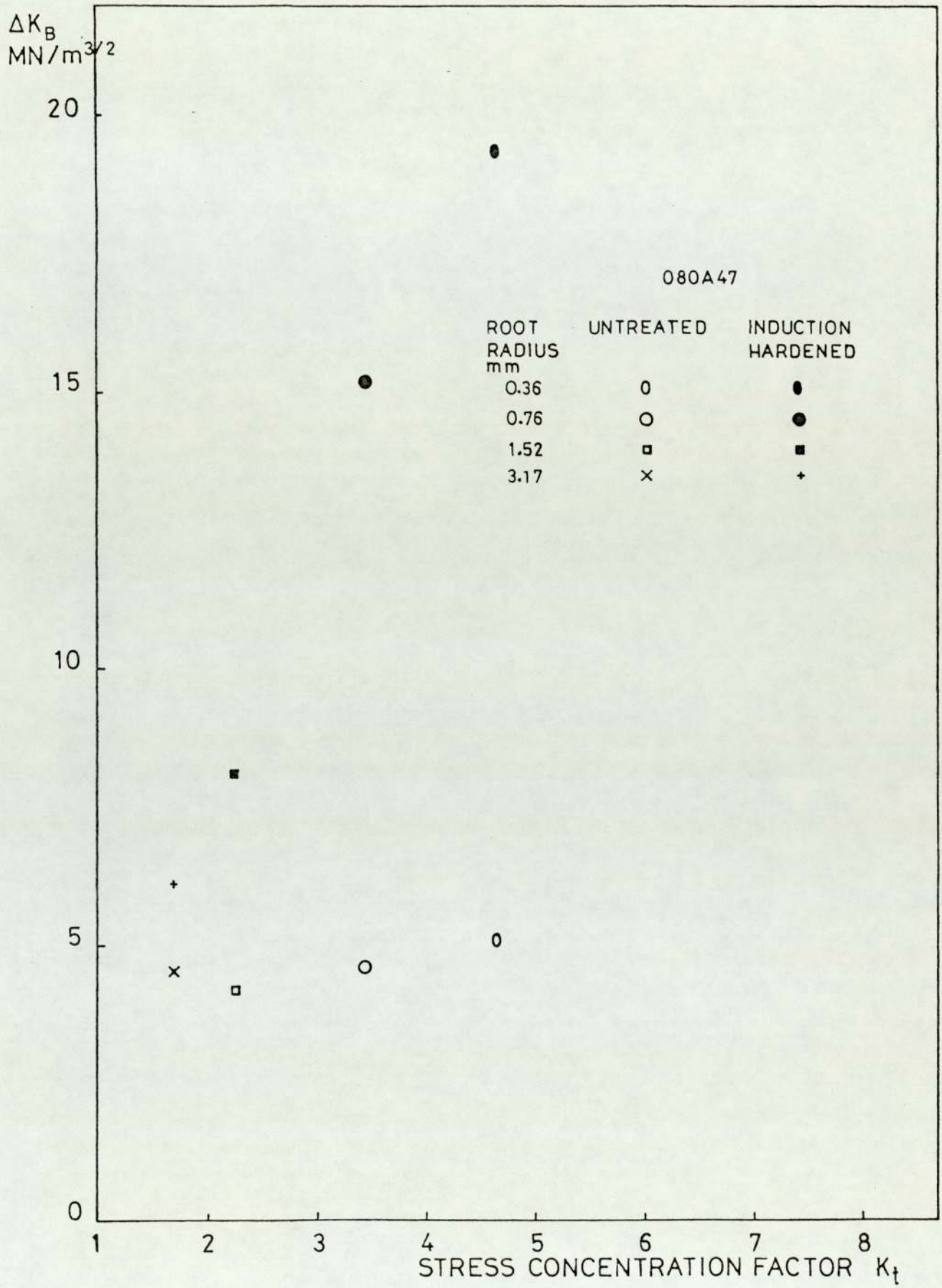

FIGURE 59 Variation in fatigue crack initiation threshold with K_t, induction hardened 080A47: parameter ΔK_B

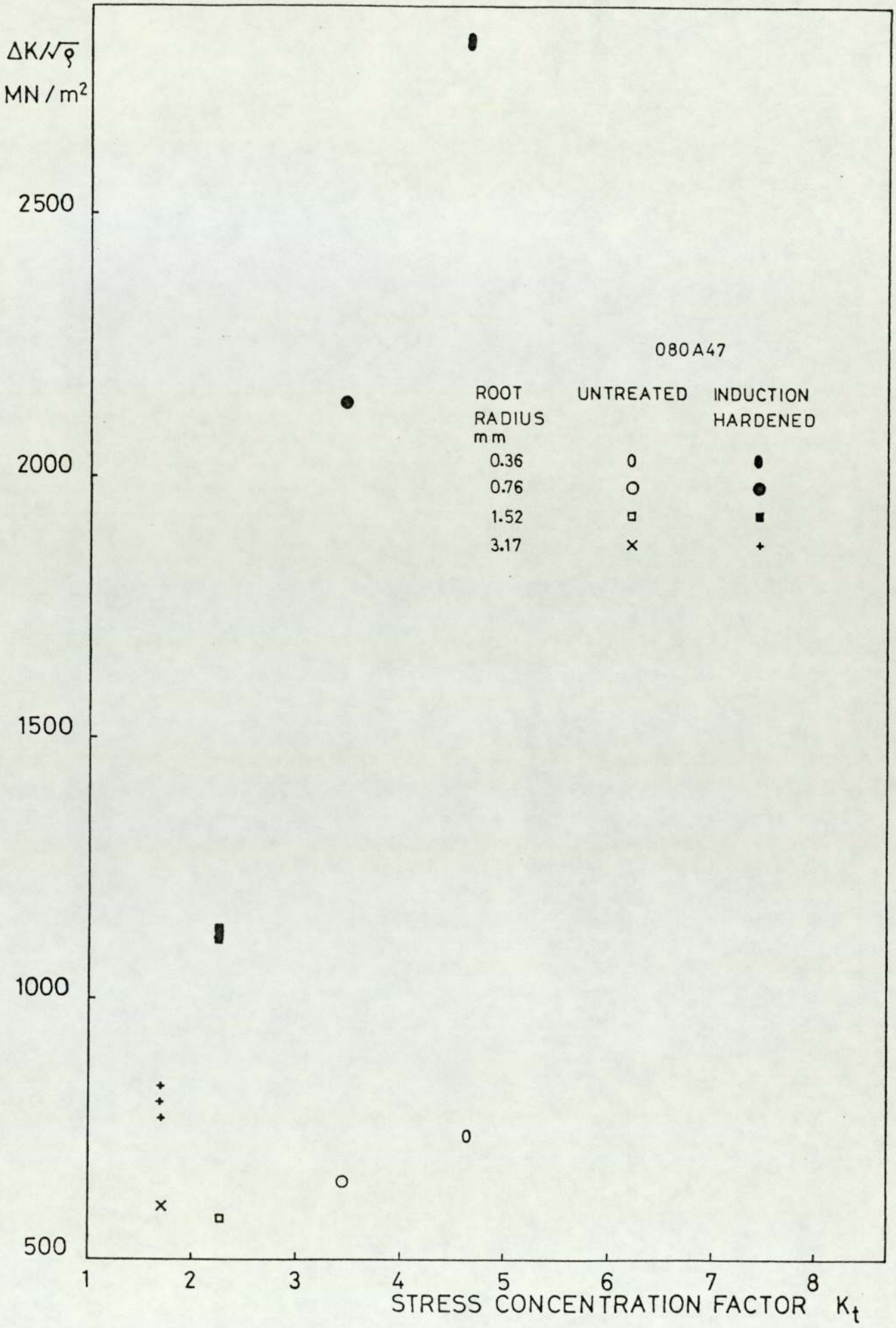

FIGURE 60 Variation in fatigue crack initiation threshold with K_t, induction hardened 080A47: parameter $\Delta K/\sqrt{\rho}$

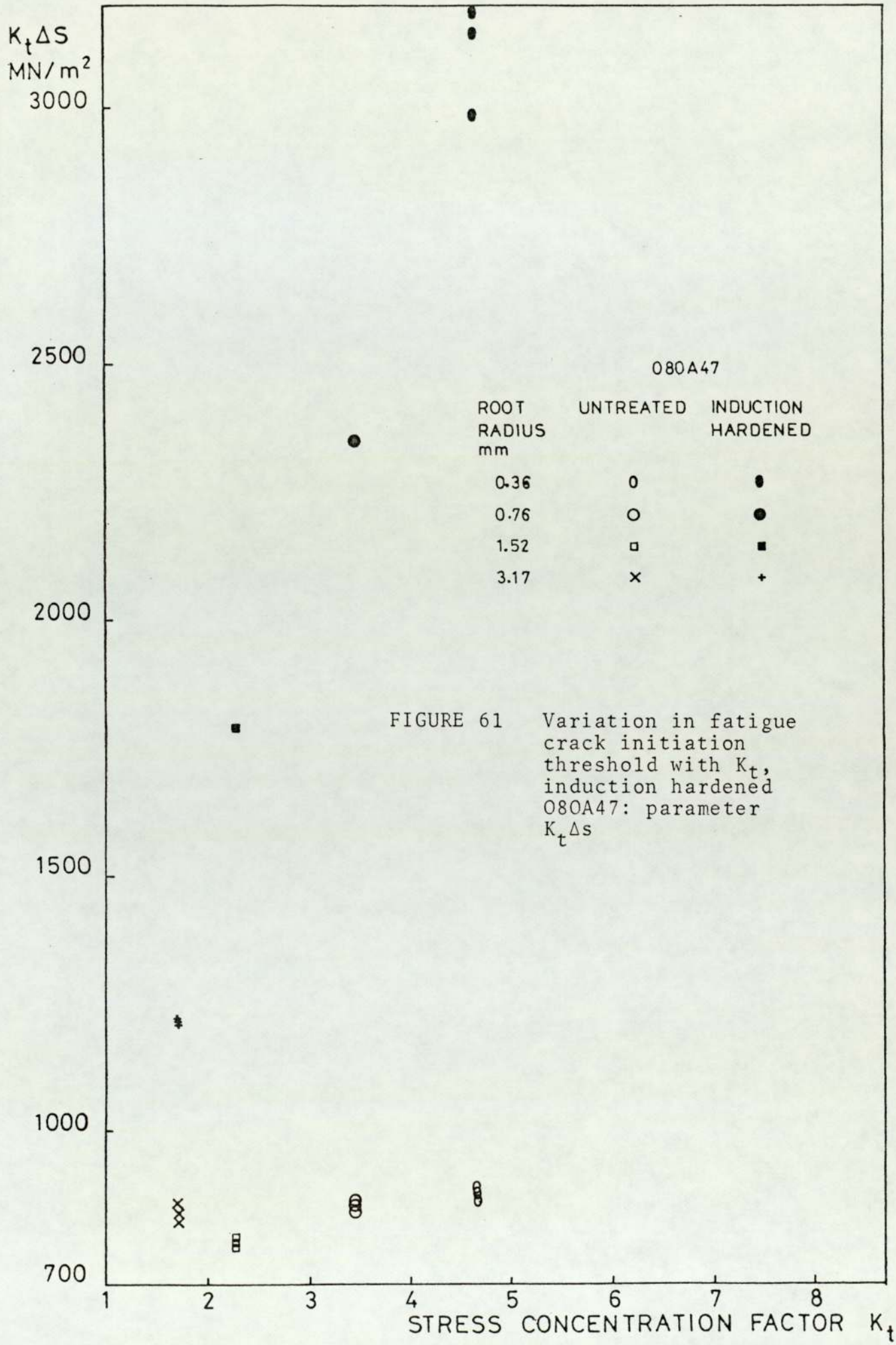

FIGURE 61 Variation in fatigue crack initiation threshold with K_t, induction hardened 080A47: parameter $K_t \Delta s$

7. DISCUSSION

7.1 Electrical Potential Difference Calibration

In the studies of metal fatigue it is necessary to estimate the length and if possible the shape of a crack. The electrical potential difference technique and the calibration curve produced have been shown to fulfil the first requirement, i.e. estimation of crack length. The procedure followed to establish the calibration is prone to many errors, which become more significant at shorter crack lengths. The same factors also influence the estimation of crack length during actual experimentation if not controlled properly. The factors involved, include crack closure, resistivity changes due to temperature fluctuations and large plastic deformation, bowing of crack front and multiple crack nucleation.

The effect of crack closure and fretting of the crack faces becomes significant when the frequencies at which the crack growth is monitored is low, i.e. below 1 Hz. In the present experiments frequencies used were 20 Hz and 85 Hz. The response of the measuring instrument being low at such frequencies the effect of crack closure or fretting could not be monitored. The effect due to temperature fluctuation is important, especially when establishing fatigue crack initiation. Increase in the electrical potential difference due to increase in temperature could be mistaken for initiation of a fatigue crack. Although

a sufficient stabilisation period was allowed before each test, for long duration tests at the lower frequency of 20 Hz the changes in temperature would be important. Further, the measuring instrument (Tekman 200, chart recorder) showed a drift of approximately 2 μv and the band observed in the potential-time record had a thickness of 0.5 μv. The initiation of a fatigue crack was therefore defined at a point when the electrical potential difference showed an increase of 5 μv. The microphotographs of such initiated cracks show that the size and shape conformed to the definition of an initiated engineering crack (section 2.3.1).

The initiated crack or cracks being thumbnail in shape, to calculate the stress intensity factor for such a geometry, it will be necessary to establish the exact shape of the crack. Multiple crack nucleation complicates the situation further. It is therefore necessary to examine the applicability of the electrical potential difference technique in predicting the crack shape and size. As shown in section 6.1, the calibration curve established can estimate the length of an equivalent through thickness crack. The technique cannot estimate the exact shape of the crack front.

Comparison of the theoretical calibration with the experimental calibration curves showed that the former are rigid as regards the geometry of the specimen. Introduction of a notch in a finite size specimen necessitates modification

of the theoretical calibration which is developed for a crack in a semi-infinite geometry. Further, the theoretical calibration curves are based on the change in the potential field due to increase in crack length. This means that the thumbnail crack or cracks in the case of single or multiple nucleation respectively should affect the potential field differently. However, it was found that the single or multiple nucleation resulted in an increase in the potential difference, equivalent to that of a through crack, so long as the total increase in area was the same. The theoretical calibration has been developed for unit thickness. Extending it to three dimension still would not change the calibration as long as the crack front remains straight and thickness remains constant. This in effect means that the parameter chosen, v/v_oW, could be related to $(a*B)/(W*B)$, where B is the thickness. This indicates that a correlation could be established between the Gilbey and Pearson [97] parameter v/v_ow and the ratio of areas of cracked and total ligament. Though the short cracks do not adhere to all the conditions necessary to use the method similar to theoretical calibration, the correlation was experimentally found to exist between v/v_ow and the ratio of areas of cracked and total ligament. Further, any anomalous behaviour arising from a change from a cusp shaped front to a straight front would have been reflected by a kink in the experimental calibration curve. As these curves show similar behaviour to that of the two dimensional theoretical calibration over the range of interest,

it could be stated that calibration established based on equivalent area is acceptable.

The sensitivity of the electrical potential method is controlled by the potential field in the vicinity of the notch root. This suggests that the sharp notch would be surrounded by a steeply changing potential field. Thus, a crack could be detected earlier as the initiation of a fatigue crack would perturb the field much more drastically than it would in the case of a blunt notch. The present calibration curves do not show this behaviour. The equivalent through thickness crack length of an initiated crack was found to be similar for all notches.

7.2 Determination of Stress Intensity Factor Coefficient

The most important part of the experimental determination of the stress intensity factor coefficient is the crack growth law and its validity. As already pointed out in section 2.4.2, the route via the inconsistent material property such as fatigue crack growth rate, the applicability of equation and effects of stress ratio and crack closure render this to be a less reliable method for the determination of the stress intensity factor coefficient. However, under the laboratory conditions of fatigue testing the fatigue crack growth law is reproducible and can be used as base line data for calculating the stress intensity factor coefficient. The data banding observed in the fatigue crack growth data for two steels 080M15 and 080A47

is very small. The variation predicted by statistical analysis in the constants C and n of the Paris law is $\pm$7%. Thus the error in the subsequent calculations will have a minimum error of 7% due to erroneous base line data.

Further errors could result from erroneous fatigue crack propagation rates obtained from the geometries for which the stress intensity factor coefficient is to be determined. This will partly depend on the electrical potential difference calibration. The calibration can predict the increase in crack length with an error of 7%. Further, it should be noted that the calculated crack growth rate is essentially the increase in the cracked area per cycle rather than the increase in the crack length per cycle. This is due to the inability of the calibration curve to predict the exact shape of the crack at any instant. Specimens with cracks shorter than one mm, when broken in fast fracture, showed thumbnail crack or cracks. This means that the data presented in Figures 16, 17 and 18 show a variation of 'effective' stress intensity factor coefficient with the crack length. The proposed equation (equation 32) will thus include the effect of notch stress field on the stress intensity factor coefficient of a short crack emanating from the notch. As the short cracks are in reality cusp shaped until they are 1 mm long the proposed equation would also include the effect of crack shape on the stress intensity factor coefficient. The experimental data, therefore, may not correlate well with the results of finite element analysis carried for the same notch geometry with straight through cracks emanating from the notch root.

A comparison with the already proposed equations of Smith et al [39] and Jergeus [42] shows that the experimental points all lie below these equations. The proposed equation (equation 32), however, fits the experimental points very well. A comparison with the Jergeus [42] equation will show that the two equations are of the same form, that is proposed equation is a modification of the Jergeus equation. Further, Smith [39] and Jergeus [42] proposals predict a value of zero for the stress intensity factor coefficient at the notch root. The proposed equation 32, however, predicts a specific value depending on the notch geometry, viz. notch depth, notch root radius and a material constant C_B. There is experimental evidence that at and even slightly below the fatigue stress limit of polycrystalline materials, fatigue slip bands and occasionally microcracks could be observed. The fatigue limit may then be understood as the set of conditions under which the nucleated microcracks can propagate. The material constant C_B can be considered as the maximum allowable distance at the location of maximum stress where a dislocation pile up can occur which will then coalesce to form a microcrack. Thus the constant C_B may have the value of the grain size or the mean free path for shear between particles. The material constant C_B constitutes an increasing fraction of the effective crack length as the total crack length decreases until at very short crack lengths it represents a crack which could propagate when subjected to fatigue limit.

The experimental values of C_o obtained for the notch geometries under consideration confirmed the previous results [42] that C_o is equal to $0.5\sqrt{a\rho}$. This means that the notch field exerts its influence on the stress over a larger crack length than predicted by others [39,43,44].

7.3 Fatigue Crack Initiation

7.3.1 Stress Concentration Approach

The results show that the life to initiation of an engineering crack may be correlated with the stress concentration parameter $K_t\Delta s$, where K_t is the stress concentration factor and Δs is the range of net section stress. The validity of such a correlation depends on whether the fatigue crack initiation is controlled by stress alone. The stress concentration factor is calculated on the basis of elastic stresses. Thus its use in a situation where limited local plasticity exists must be considered as purely empirical. Local yielding even on small scale will redistribute the stresses and the stress concentration factor will decrease. This necessitates definition of the fatigue strength reduction factor K_f. A certain measure of success has been achieved in correlating K_t and K_f which takes into account the geometry of discontinuity and the material. However, these correlations are established at the fatigue limit.

The concept of the stress concentration parameter $K_t\Delta s$ is based on the measurement of local stresses. There is, however, an accumulated evidence that the stress gradient at the surface plays an important part in the fatigue

process. The lower values of fatigue limits obtained from larger specimens as compared to those obtained from smaller specimens are due to the steeper gradients existing over a critical volume of material at the surface which is subjected to a lower average stress than the larger specimens. Similarly, comparison of elastic stress distribution at the root of sharp and blunt notches when subjected to alternating stress such that $K_t \Delta s$ is the same for both notches, shows that the stress gradients are different. The average stress over a critical distance at the notch roots will therefore be different for two notches. The elastic stress concentration parameter therefore should be used in conjunction with the stress gradient at the notch root. The complete stress distribution, which will include the effect of triaxial stresses below the notch root will probably prove more useful.

Further, the stress concentration parameter $K_t \Delta s$ does not help in the investigation of events occurring in the early stages of crack growth and does not consider structural features of the material. Initiation of an engineering crack also includes a part of stage I crack growth. The stress concentration parameter therefore cannot be considered as an appropriate parameter under such conditions.

7.3.2 Fracture Mechanics Parameters

The present work confirms the results of Jack and Price[27], in that there is a definite relationship between the number of cycles to initiation of a fatigue crack N_i and the parameter $\frac{\Delta K}{\sqrt{\rho}}$. The validity of this approach was found to extend over an order of magnitude, from a root radius of 0.13 mm to a root radius of 3.17 mm. The result of plotting N_i versus $\frac{\Delta K}{\sqrt{\rho}}$ for the two steels in untreated and treated conditions showed banding of the data points. Apart from some anomalies, generally the initiation lives for sharp notch specimens exceeded the lives for blunt notches tested at the same $\frac{\Delta K}{\sqrt{\rho}}$ level. This could be a result of two effects. Firstly, a sharp notch has a higher stress gradient resulting in lower average local stress than a blunt notch. Second, there is a lack of demarcation between the nucleation and propagation of the fatigue crack. The true initiation life, if such a phenomenon can be defined, and the number of cycles necessary till the crack grows to a detectable size, are two components of initiation life N_i. In the present experiment, the initiated engineering fatigue cracks had similar sizes for both blunt and sharp notches. This indicates that the data banding may be due to the fact that the stress gradient effect is not taken into account in the stress intensity factor parameter $\frac{\Delta K}{\sqrt{\rho}}$.

The theoretical validity of the approach is subjected to the same criticism as that applicable to the stress concentration approach. Barsom et al [14] and Clark [32] explained the parameter as the maximum stress at the root of the notch,

estimated by comparing the stress distributions in front of a crack and a notch of the same geometric length. Jack and Price [27] included the concept of ρ_o, which is dependent on the material. The effective stress intensity factor ΔK_{eff} for a notch was estimated by equating the stresses at the crack tip and at the root of a sharp notch, of the same geometric length. Though expressed in different terms, both the parameters essentially express the maximum stress range at or at a specific distance in front of the notch root; and not the stress intensity factor range for a notch. The parameter, though it ignores plasticity at the notch root, stipulates the limitations on the plastic zone size. The present experiments were carried out such that the plastic zone size will not exceed 2% of the thickness of the specimen. The effect of stress gradient and the triaxiallity of stress are ignored. Thus for a complete evaluation a more rigorous analysis is required.

The theoretical analysis carried out by Bilby and Heald [28] shows that the initiation of a fatigue crack from a crack depends on a linearly accumulated critical crack opening displacement at the crack tip. This leads to a dependence of the number of cycles to initiation on the square of the stress intensity factor range. Jack and Price [27] argued that the Bilby and Heald model [28] can be extended to fatigue crack initiation from a notch root. In the previous section (section 6.3.1), a stress intensity factor for a notch was defined (equation 33), which is dependent on the

notch geometry and the material. This parameter relates to N_i on the basis of actual physical processes involved in the formation of a fatigue crack. As mentioned earlier, the dislocation pile up occurs very early in life, when a specimen is subjected to fatigue. Such pile ups, it is assumed, are of the size of a grain. Mechanistically, therefore, it is assumed that the stress intensity controls displacement at the end of the dislocation pile up, and N_i is controlled by these displacements rather than those at the notch root. When this displacement reaches a critical value, the dislocation pile-up coalesceses to form a microcrack and this microcrack starts to extend.

As mentioned earlier, in section 6.3, the number of cycles to initiation presented in tables 7 to 10 refer to initiation of an engineering crack rather than to an initiation 'event'. The engineering fatigue crack is a cusp (plate 4). The stress concentration parameter thus may not show a good correlation as N_i includes the cycles involved in growth of a microcrack to a cusp. Holder [35] has shown that even with an arbitrary definition of initiation, the number of cycles to initiation shows a strong dependence on the parameter $\frac{\Delta K}{\sqrt{\rho}}$. The size of the initiated crack in this work [35] varied between 0.01 mm to 0.8 mm as predicted by the electrical potential calibration curve. In the present experiments, the size of the equivalent through thickness crack varied between 0.08 mm and 0.13 mm. The macrophotograph (plate 4) shows such an

initiated cusp. Both the fracture mechanics parameters were calculated for such cracks. For a particular case of plate 4, the stress intensity factor range ΔK calculated assuming it to be a surface crack in bending was 14.27 $MN/m^{3/2}$ This compares favourably with the 20.82 $MN/m^{3/2}$, stress intensity factor range calculated assuming the crack to be a through thickness crack. Calculations for other samples yielded similar results. This suggests that the correlation between N_i and the fracture mechanics parameter ΔK_B calculated from an equivalent through thickness crack is acceptable.

The fatigue crack initiation data for 080M15 and 080A47 in treated and untreated condition when plotted in terms of ΔK_B show that a definite relationship exists between the number of cycles to initiation of an engineering fatigue crack and the parameter ΔK_B. The validity of this approach was found to extend over an order of magnitude from a root radius of 0.13 mm to a root radius of 3.17 mm. Further, the data banding is reduced, improving the correlation. This could be due to the fact that the new parameter ΔK_B takes into account the local stress and the stress gradient. Recalculated results from [35] on the basis of the new parameter ΔK_B are presented in Figures 62a and 63a. For comparison the results based on the parameter $\frac{\Delta K}{\sqrt{\rho}}$ are reproduced (Figures 62b and 63b). The initiation criterion in this case was the first deflection from the electrical potential difference versus time plot. As can be seen the correlation is improved by using a new parameter ΔK_B since the data banding is reduced.

LEGEND FOR FIGURES 62 AND 63

ROOT RADIUS mm	SYMBOL
0.125	o
0.25	●
0.5	○
0.76	◉
1.25	□
3.13	■
6.36	▪
12.5	△
25.4	▲

NOTCH DEPTHS 3.5, 5.0, 6.5 AND 9.0 mm

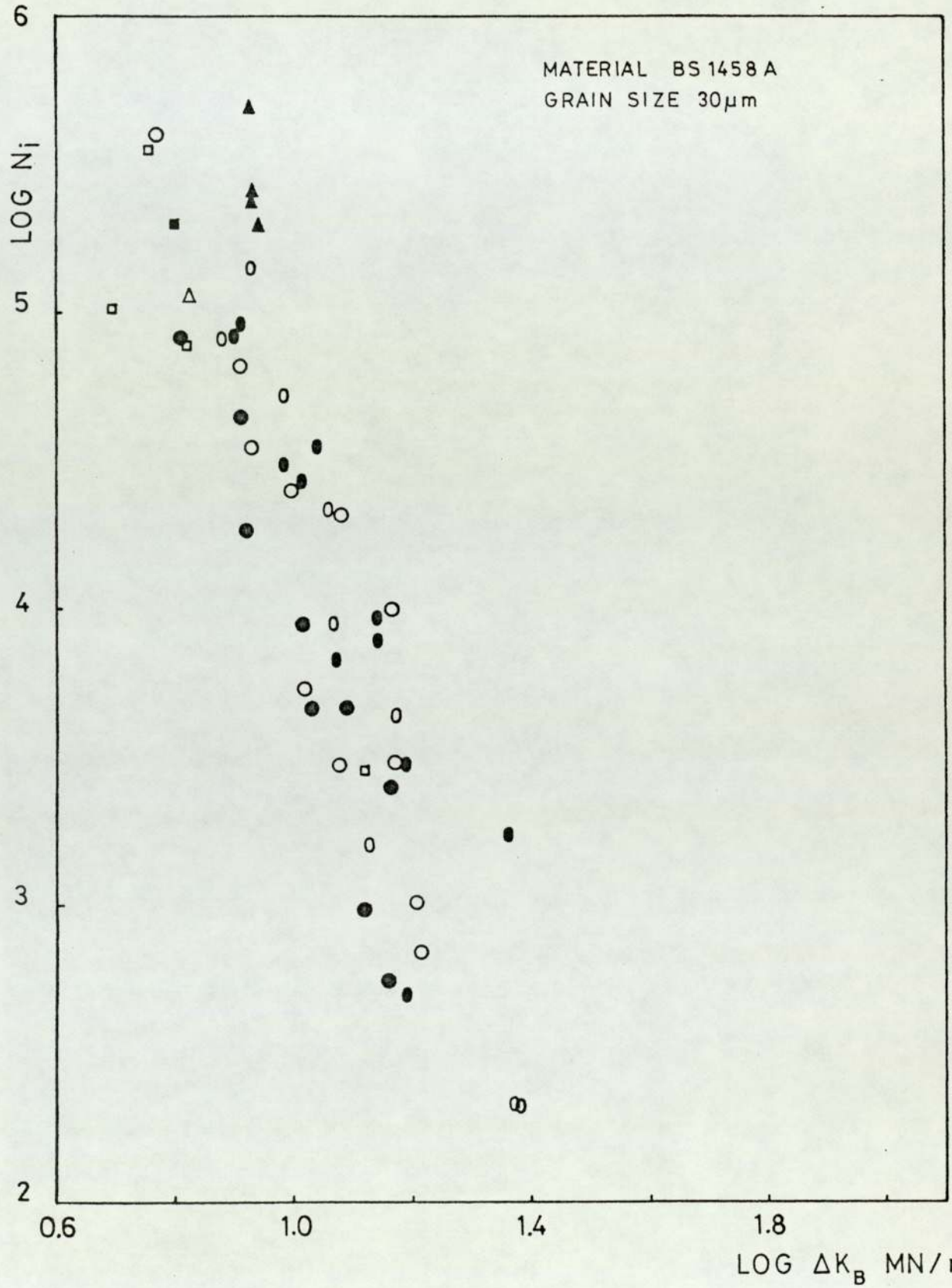

FIGURE 62a Fatigue crack initiation data for BS1458A[35]: parameter ΔK_B

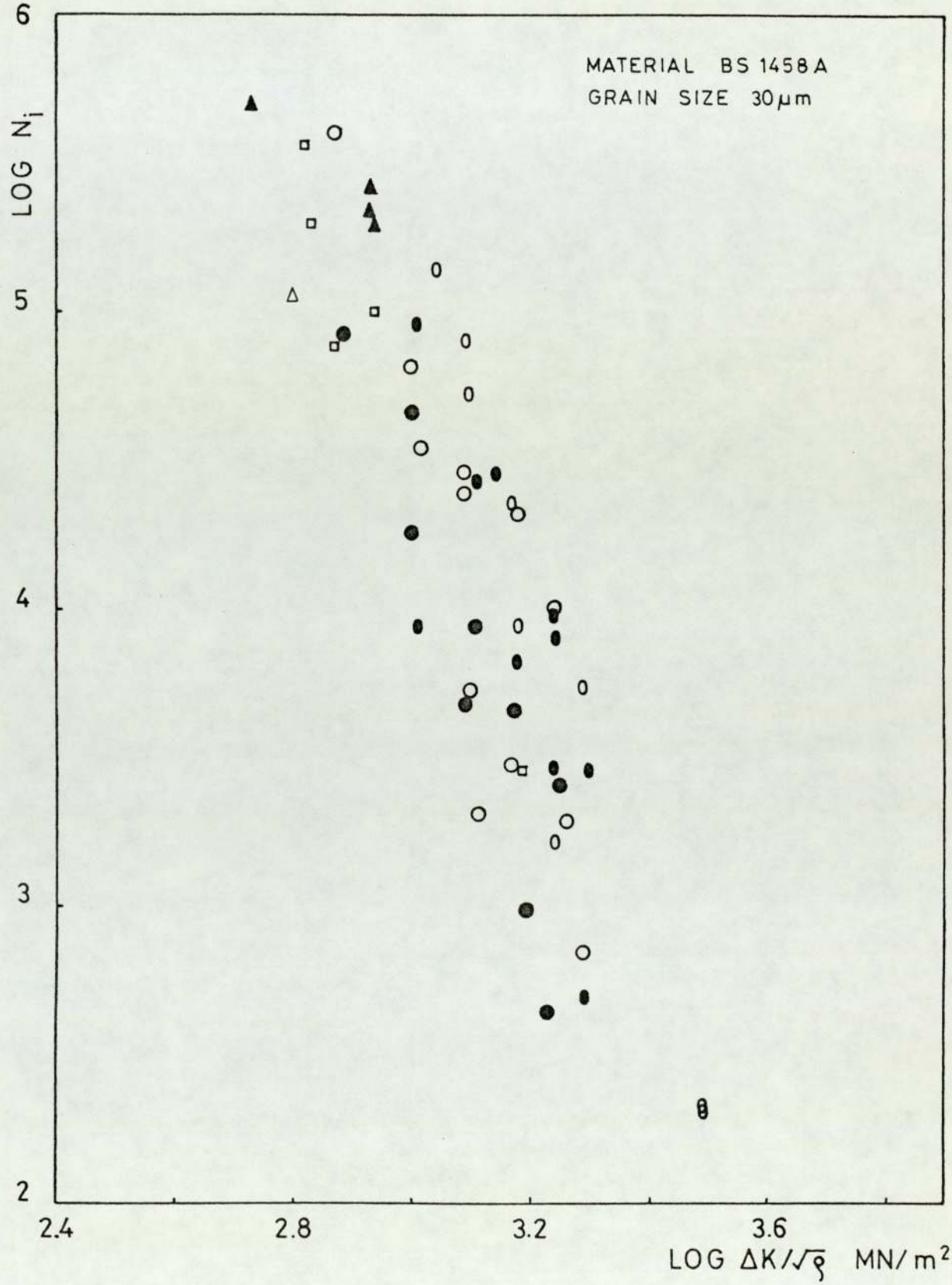

FIGURE 62b Fatigue crack initiation data for BS1458A(35): parameter $\Delta K/\sqrt{\rho}$

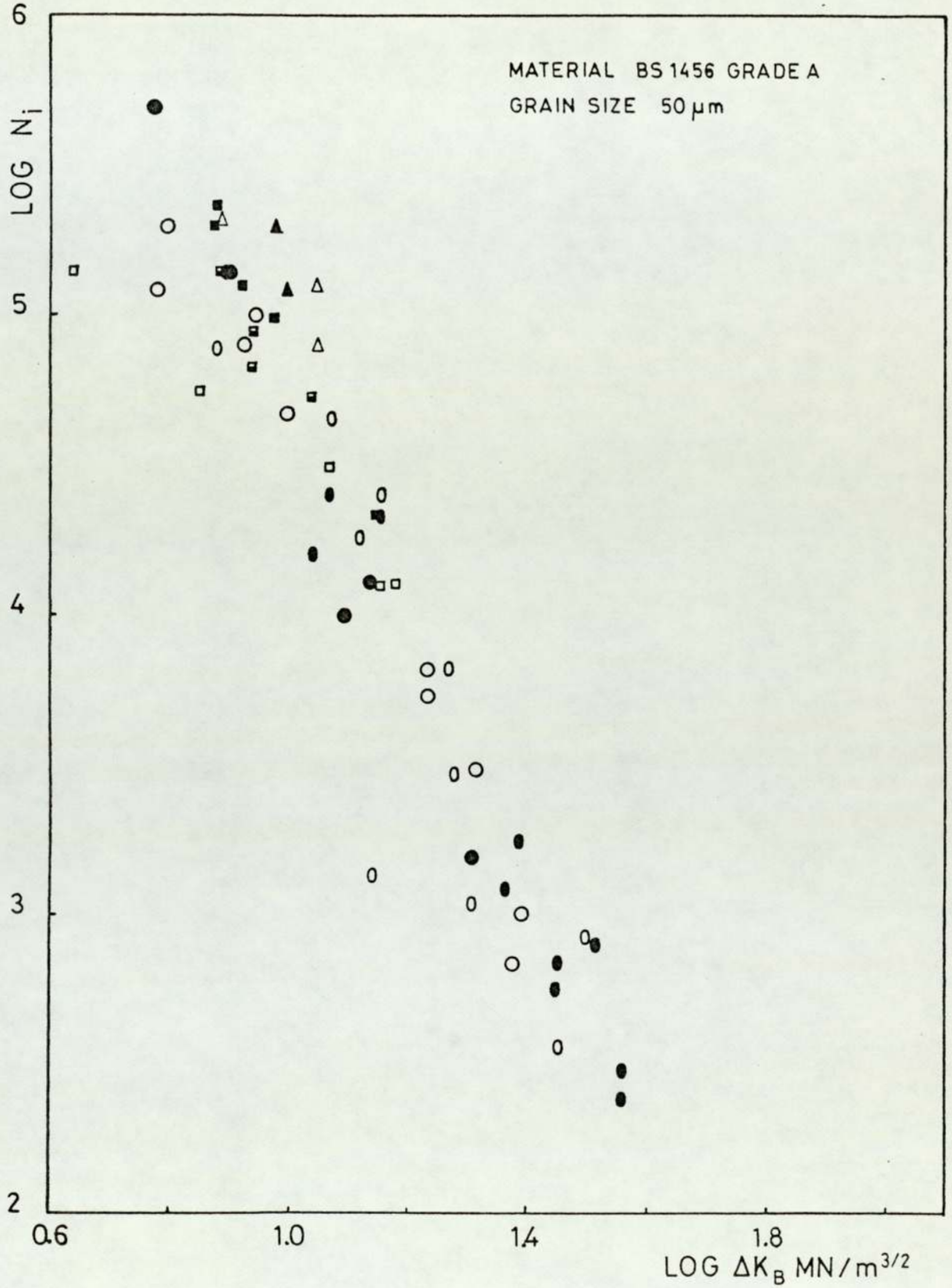

FIGURE 63a Fatigue crack initiation data for BS1456 grade A [35]: parameter ΔK_B

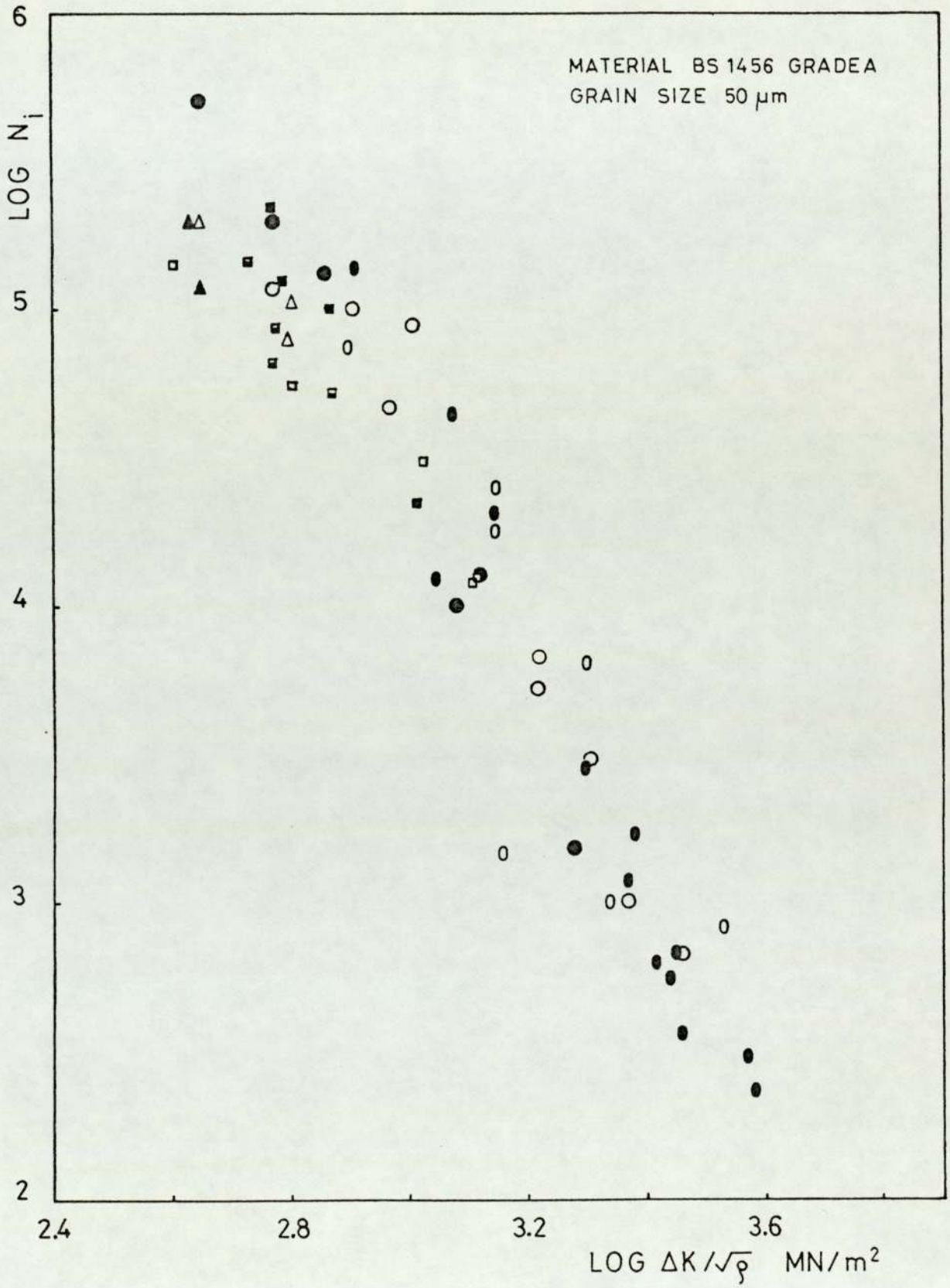

FIGURE 63b Fatigue crack initiation data for BS1456 grade A [35]: parameter $\Delta K/\sqrt{\rho}$

7.3.3. Effect of Case Hardening of Fatigue Crack Initiation

The fatigue crack initiation data for case carburised and carbonitrided samples showed a better correlation between the number of cycles to initiation N_i and the stress intensity factor ΔK_B than other parameters. The stress intensity factor was calculated for the engineering crack as stated in the previous section. These calculations do not take into account the residual stress distribution existing in the sample as a result of case hardening. This may explain the larger data banding observed in the case hardened samples and the correlation may improve if the residual stress distribution could be taken into account. It should be noted that the samples were tempered after case hardening. As stated earlier in section 3, tempering tends to reduce the residual stresses. Thus in the present experiments the effect of residual stresses may not have been fully realised. The results, however, tend to separate into two groups, sharp and short notches exhibiting one type of behaviour and, blunt and deep notches another. This could be attributed to different residual stress distributions present due to different notch geometries. The shorter notches have more ligament length beneath the notch as compared to deep notches. Assuming that the volume changes occuring are the same, the short notches will have a shallower but flatter residual stress distribution, as compared to deep notches. As suggested by Landgraf and Richman [89], such residual stress distributions improve the fatigue strength of case hardened samples. The residual stresses lead to a more complicated shape of

stress distribution than that predicted by the stress intensity factor ΔK_B. The effect of stress gradient may thus influence the fatigue crack initiation. The notch geometry with the stress concentration factor 3.42 seems to be in the transition region. This is clearly seen in that when N_i is plotted against $K_t \Delta s$ or $\frac{\Delta K}{\sqrt{\rho}}$, the data for this notch geometry coincides with the deep notch geometries, whereas when plotted in terms of ΔK_B it coincides with the short notch.

The data plotted is for both carburising and carbonitriding and for both the case depths. The results show that the initiation of a fatigue crack is not affected by changing the case hardening treatment or the case depth. Carburising and carbonitriding are not known to have significantly different effects on fatigue properties, as already discussed in the previous sections (sections 3.2, 3.3). Further, tempering the samples may have reduced the residual stresses by a considerable amount thus nullifying the effect of case depth on residual stresses. Both these effects may contribute towards making the notch geometry the most significant factor when examining fatigue crack initiation in case hardened specimens.

The results of fatigue tests on nitrocarburised material show that the fatigue crack initiation life N_i cannot be correlated to any of the parameters in the range considered. The range being small it is irrelevant to carry out statistical analysis to establish a correlation.

The data plotted for induction hardened 080A47 showed correlation between N_i and different parameters for a particular notch geometry. The notch with the highest K_t showed maximum life for the same value of parameter. This indicates that the residual stresses developed in this geometry may be higher than the others in addition to the effect of higher stress gradient, as normally observed in the sharp notches. The scatter observed, however, made any statistical analysis irrelevant.

7.3.4 Fractography of Fatigue Crack Initiation

Fracture surface examination of case carburised and carbonitrided specimens showed that the fatigue cracks initiated in a transgranular mode. The cusps seen in plates 71 to 75, with a transgranular mode of fracture are surrounded by an area with a mixed mode of fracture, intergranular mode being the predominant mode. The size of these cusps is equivalent to the size of an engineering crack. The change in the mode of fracture was not reflected in the electrical potential versus time plot. The microstructure at the notch roots in carburised and carbonitrided specimens was martensite colonies surrounded by non-martensitic transformation products. The most preferable site for crack nucleation in such a microstructure would be the boundaries between the martensite colonies as these are the preferential sinks for various trap elements which lower the cohesion strength of the boundary. The carbides precipitated at the boundary will also enhance crack form-

ation by particle fracture or void formation at the carbide matrix interface. This however was not apparent from the examination of the fracture surface. The crack seemed to have initiated by fracture of brittle martensite plate. Further, the initiation of a crack in a martensitic matrix is associated with an inclusion or carbide. This also was not observed in any of the fractographic examinations. This suggests that the non-martensitic transformation products present in the microstructure as a result of slack quenching or tempering are not detrimental as regards the fatigue crack initiation is concerned.

The examination of specimens of nitrocarburised 080M15 did not show any indication of crack initiation site. The outer compound layer consisting predominantely of the ε carbonitride phase showed a relatively flat fracture surface. In the absence of evidence of subsurface crack initiation, this would mean the crack initiated by brittle fracture of the compound layer under tensile load, which would then extend into the case by a mixed mode of fracture. The thickness of this case varied between 10 μm to 62 μm. As the electrical potential difference measurement suggests a longer crack length at initiation, a part of the initiated crack would be in the inner case. The outer case though enhances the tribological properties of the surface, the inner case, known as the diffusion zone, is responsible for effective strengthening. The initiation of an engineering crack will therefore depend on the contribution from both the cases, a significant part of the initiation life being spent in the diffusion zone, till the crack reaches a detect-

able size. From the microstructure point of view the compound layer may have the necessary thickness. A thicker layer may not necessarily enhance the fatigue properties.

The examination of notch roots of the induction hardened 080A47 specimen did not indicate subsurface crack initiation. The cusps, as observed in carburised and carbonitrided specimens, were not evident. The examination in scanning electron microscope revealed a mixed mode of fracture, transgranular being the dominant mode. The microstructural variation observed in samples with different notch geometries did not seem to affect the surface topography, transgranular still being the dominant mode of fracture.

Fractographic examination indicated, to some extent, the size of the material parameter C_B. In all the case hardened material it approached the prior austenitic grain size as measured from the microstructure. The areas of notch root fractured in mixed mode and the sizes of units fractured in transgranular mode are closer to the prior austenitic grain size. The sizes of facets in areas fractured in intergranular mode yield the same result. This was not apparent in the fracture surface examination of induction hardened 080A47.

7.4 Fatigue Crack Initiation Threshold

The threshold values of stress concentration parameter $K_t \Delta s$ and fracture mechanics parameter $\frac{\Delta K}{\sqrt{\rho}}$ were higher than the monotonic ultimate tensile strength for untreated 080M15. This is not surprising since the triaxiallity at the notch root and plasticity effects in cyclic loading render the values of engineering mechanical properties irrelevant. The threshold values of the new parameter ΔK_B compares favourably with the crack propagation threshold quoted in literature for 080M15, which is 3 to 6 $MN/m^{3/2}$ depending on R-ratio. Similar observation can also be made regarding untreated 080A47. The microcracks exist at and even below the fatigue limit [2]. The threshold values of the new parameter ΔK_B therefore, could be treated as the crack propagation threshold, i.e. a threshold for growth of a microcrack into a macrocrack. Further, if the threshold values of ΔK_B are substituted in the equation to calculate the number of cycles to initiate an engineering crack the values obtained are in excess of 10^7 for 080M15. Similar results were obtained for 080A47.

The effect of case hardening in improving the fatigue crack initiation threshold can be clearly seen. The results also confirmed the previously reported results that the highest improvement is generally observed for the highest stress concentration factor. The statistical analysis (one way analysis of variance, [107] of the results in terms of different parameters are presented in

tables 18 to 20. The results suggest that the fatigue crack initiation threshold values obtained for two carburised case depths for one particular notch are comparable; except for one notch geometry (notch depth 10 mm, root radius 1.52 mm). For two carbonitrided case depths, however, the threshold values were comparable only in the case of sharpest and the bluntest notch. For other two notch geometries the threshold values showed significant difference. Table 20 presents a comparison of threshold values for carburised and carbonitrided cases, (one way analysis of variance [107]). The results show that the threshold values are significantly different for two notch geometries (K_t = 3.42 and K_t = 2.26), whereas the threshold values are comparable for the remaining two notch geometries. Thus the results are inconclusive as regards the effect of heat treatment or case depth on the fatigue crack initiation threshold on the basis of statistical analysis.

7.5 Fatigue Crack Propagation

Fatigue crack propagation data for case carburised, carbonitrided and nitrocarburised material was presented in terms of the new parameter ΔK_B as defined by equation 33. The data could be represented by the Paris law which is of the form

$$\frac{da}{dN} = C(\Delta K_B)^n$$

TABLE 18

COMPARISON OF FATIGUE CRACK INITIATION THRESHOLD VALUES OF CARBURISED 080M15 FOR DIFFERENT NOTCH GEOMETRIES FOR CASE DEPTHS 0.38 mm AND 0.76 mm (ONE WAY ANALYSIS OF VARIANCE DEGREES OF FREEDOM $\nu_1 = 1$, $\nu_2 = 4$)

Parameter	Notch root radius mm	Variance ratio	Significant at 1% level
$K_t \Delta s$	0.13	1.113	-
	0.76	3.148	-
	1.52	92.42	Yes
	3.17	0.232	-
$\Delta K/\sqrt{\rho}$	0.13	1.119	-
	0.76	3.131	-
	1.52	148.14	Yes
	3.17	0.781	-
ΔK_B	0.13	1.119	-
	0.76	3.031	-
	1.52	157.46	Yes
	3.17	0.817	-

TABLE 19

COMPARISON OF FATIGUE CRACK INITIATION THRESHOLD VALUES OF CARBONITRIDED 080M15 FOR DIFFERENT NOTCH GEOMETRIES FOR CASE DEPTHS 0.38 mm AND 0.76 mm (ONE WAY ANALYSIS OF VARIANCE, DEGREES OF FREEDOM $\nu_1 = 1$, $\nu_2 = 4$)

Parameter	Notch root radius mm	Variance ratio	Significant at 1% level
$K_t \Delta s$	0.13	3.974	-
	0.76	52.840	Yes
	1.52	150.81	Yes
	3.17	0.0081	-
$\Delta K/\sqrt{\rho}$	0.13	3.949	-
	0.76	53.06	Yes
	1.52	137.80	Yes
	3.17	0.191	-
ΔK_B	0.13	3.940	-
	0.76	24.60	Yes
	1.52	120.41	Yes
	3.573	3.573	-

TABLE 20

COMPARISON OF FATIGUE CRACK INITIATION THRESHOLD VALUES OF CARBURISED AND CARBONITRIDED 080M15 FOR DIFFERENT NOTCH GEOMETRIES FOR CASE DEPTHS 0.38 mm AND 0.76 mm (ONE WAY ANALYSIS OF VARIANCE, DEGREES OF FREEDOM $\nu_1 = 3$, $\nu_2 = 8$)

Parameter	Notch root radius mm	Variance ratio	Significant at 1% level
$K_t \Delta s$	0.13	4.28	-
	0.76	17.09	Yes
	1.52	124.14	Yes
	3.17	5.423	-
$\frac{\Delta K}{\sqrt{\rho}}$	0.13	4.283	-
	0.76	17.21	Yes
	1.52	121.31	Yes
	3.17	6.331	-
ΔK_B	0.13	4.32	-
	0.76	14.997	Yes
	1.52	108.32	Yes
	3.17	7.04	-

The damage accumulation theories predict the value of the exponent to be 2, assuming that the damage is controlled by the crack opening displacement. The present data for different heat treatments yielded values of n between 3.5 and 5.6. Such values are generally observed for martensitic microstructures and where static modes of fracture are observed in fatigue due to particular microstructure.

Examination of the fracture surface in most of the carburised and carbonitrided samples showed that the crack front in the case is ahead of the crack front in the core. This could be attributed to the fatigue fracture of the case which exhibits a mixed mode of fracture, intergranular mode being the principal mode. This is generally a static mode of fracture in carburised and carbonitrided steels, which would result in high crack growth rates. The core shows a ductile mode of failure. The high values of n suggest that the higher crack growth rates in the case result in higher overall crack growth rates. A comparison of fatigue crack growth data presented in Figures 34 to 37 shows that the crack growth rates for long cracks are similar and the differences in the constants C and n of the Paris law for different heat treatments result from the crack growth behaviour of short cracks in the region near the notch root.

Crack growth in the core of nitrocarburised 080M15 occurs in a ductile manner. The outer compound layer breaks in a brittle manner and thus may not contribute significantly to the resistance to crack propagation. The diffusion zone

exhibits a mixed mode of fracture. Some grains showing cleavage facets and others showing fatigue striation. Finally the fatigue fracture changes entirely to ductile mode in the core. The fatigue crack growth data in this case is also a combination of crack growth rates of case and core. The exponent n in the Paris law is 3.52, which suggests that the crack growth was dominated by ductile modes of fatigue fractures.

7.6 Application of Results

The results indicated that for adequate design against fatigue failure it is necessary to consider both the initiation and propagation of cracks from crack like defects. Though the results were obtained from notches, use of the stress intensity factor to describe initiation and propagation has made the application more general. The information required for computation are the fatigue crack initiation data, the crack propagation equation, the appropriate stress intensity factor coefficient calibration for the geometry and the grain size.

The number of cycles to initiation can be calculated from

$$N_i = B(\Delta K)^m$$

To determine the duration of fatigue crack propagation Paris law can be integrated

$$\frac{da}{dN} = C(\Delta K)^n$$

$$\int \frac{da}{C(\Delta K)^n} = \int dN$$

The integration limits for the left hand side are

a_i = crack size at initiation

a_f = critical crack size

The critical defect size can be determined from known values of K_{IC}.

$\Delta K = \Delta\sigma * Y * \sqrt{a}$

$\Delta\sigma$ = stress amplitude

Y = appropriate stress intensity factor coefficient

a = crack length

Number of cycles corresponding to a_i is N_i and Number of cycles corresponding to a_f is N_f

$$N_p = N_f - N_i = \int_{N_i}^{N_f} dN$$

$$N_p = \frac{1}{C(\Delta\sigma)^n} \int_{a_i}^{a_f} \frac{da}{(a)^{n/2} * Y^n}$$

The integration can be done numerically reducing the value of Δa to the smallest value possible.

Thus $N_f = N_i + N_p$

The limits of validity of a linear $\frac{da}{dN}$ versus ΔK relationship are very restricted and this must be appreciated before any attempt to use such information. At high crack propagation rates the cyclic stress intensity approaches

the material's cyclic fracture toughness. This is invariably higher than the monotonic fracture toughness due to crack tip blunting. The lower part of the curve is an area in which the relationship between da/dN and ΔK changes rapidly as the crack grows. This leaves a small region at the intermediate levels of ΔK at which the power law relationship may be appropriate.

The stress intensity factor calibrations for a wide variety of component configurations is now available. Equation 32 can be used to estimate the effect of stress concentration on the K calibrations.

Robinson [58], Woodvine [88], and Landgraf and Richman's[89] analysis to determine the optimum case depth is based on cyclic material properties and residual stress distribution. Further, to maximise the fatigue resistance, equal likelihood of failure is assumed in case and core. In the present experiments, the fatigue crack always initiated at the notch root, i.e. at the surface. Moreover, the fatigue crack initiation life N_i showed no effect of case depth. The statistical analysis of threshold values for fatigue crack initiation showed evidence for and against the effect of case depth. This suggests that the above-mentioned analysis (section 3.5) cannot be applied to notched samples. It may be attributed to stress concentration which raises the stress at the notch root to a sufficiently high level, thus making the subsurface crack initiation unlikely.

Fatigue crack initiation and propagation curves cannot be predicted from the uniaxial tensile properties, thus a conservative design needs to be specified. For 080M15 steel, gas carburised or carbonitrided as described in (5.2), the number of cycles to initiation of crack could be calculated from

$$N_i = 8.032 * 10^{13} (\Delta K_B)^{-7.11}$$

However, as shown in Figure 25, the case hardened 080M15 is inferior to untreated 080M15 at short lives, i.e. N_i less than 10^5 cycles. The cross over for case hardened deep notches occurs at low value of stress intensity factory range, whereas for short and sharp notches it occurs at large values of ΔK_B. This suggests a maximum value of ΔK_B to which case hardened 080M15 could be subjected to, so as to yield some degree of improvement.

In this particular case the value of ΔK_B was 23.00 $MN/m^{3/2}$. The above analysis refers to estimation of limited life. To design for long lives, i.e. in excess of one million cycles, the values of fatigue crack initiation threshold will be more appropriate. The average threshold values for each treatment condition for 080M15 are presented in Table 21 in terms of ΔK_B. The average fatigue crack initiation threshold values in terms of parameter ΔK_B for induction hardened 080A47 are also presented in Table 21.

As stated earlier, the value of the stress intensity factor coefficient can be modified using equation 32, to take into account the effect of notch stress field. Due to the scatter

TABLE 21

THRESHOLD VALUES FOR FATIGUE CRACK INITIATION IN TERMS OF ΔK_B $MN/m^{3/2}$, MATERIAL 080M15

Condition	Case depth mm	ΔK_B $MN/m^{3/2}$
Untreated	-	4.3 ± 0.35
Carburised	0.38	7.24 ± 0.62
Carburised	0.76	7.32 ± 0.54
Carbonitrided	0.38	7.10 ± 0.70
Carbonitrided	0.76	6.16 ± 0.37
Nitemper	-	5.74 ± 0.12

MATERIAL 080A47 CASE DEPTH 2.0 mm

Condition	K_t	ΔK_B $MN/m^{3/2}$
Untreated	-	4.6 ± 0.34
Induction hardened	4.65	19.41 ± 0.03
Induction hardened	3.42	15.2 ± 0.04
Induction hardened	2.26	8.09 ± 0.06
Induction hardened	1.69	6.11 ± 0.23

observed in the data (Figures 16-18), a conservative estimate is necessary. The fatigue crack growth data for the sharpest notches, case hardened by different treatments were used to establish the modification necessary to account for the effect of stress concentration on the stress intensity factor coefficient after case hardening. The constants of the Paris law for different case hardening treatments are presented in Table 22. The ratios obtained Y_s/Y_1 for case hardened 080M15 in different treatment conditions are presented in Figures 64 to 68. An estimate for the curve for the data points in all the graphs is given by

$$\frac{Y_s}{Y_L} = \sqrt{\frac{5 \tanh (2.632 * (c+C_B)) + c + C_B}{5 + c}} \quad ..(34)$$

the value of C_o is 0.97 mm.

TABLE 22

CONSTANTS OF PARIS LAW FOR CASE HARDENED 080M15 (NOTCH DEPTH 5 mm, ROOT RADIUS 0.13 mm)

Heat Treatment	Case depth mm	C	n
Carburised	0.38	$1.0583 * 10^{-16}$	7.204
Carburised	0.76	$8.6139 * 10^{-13}$	4.827
Carbonitrided	0.38	$8.4863 * 10^{-14}$	5.459
Carbonitrided	0.76	$4.8184 * 10^{-13}$	5.047
Nitrocarburised	-	$1.2181 * 10^{-9}$	3.126

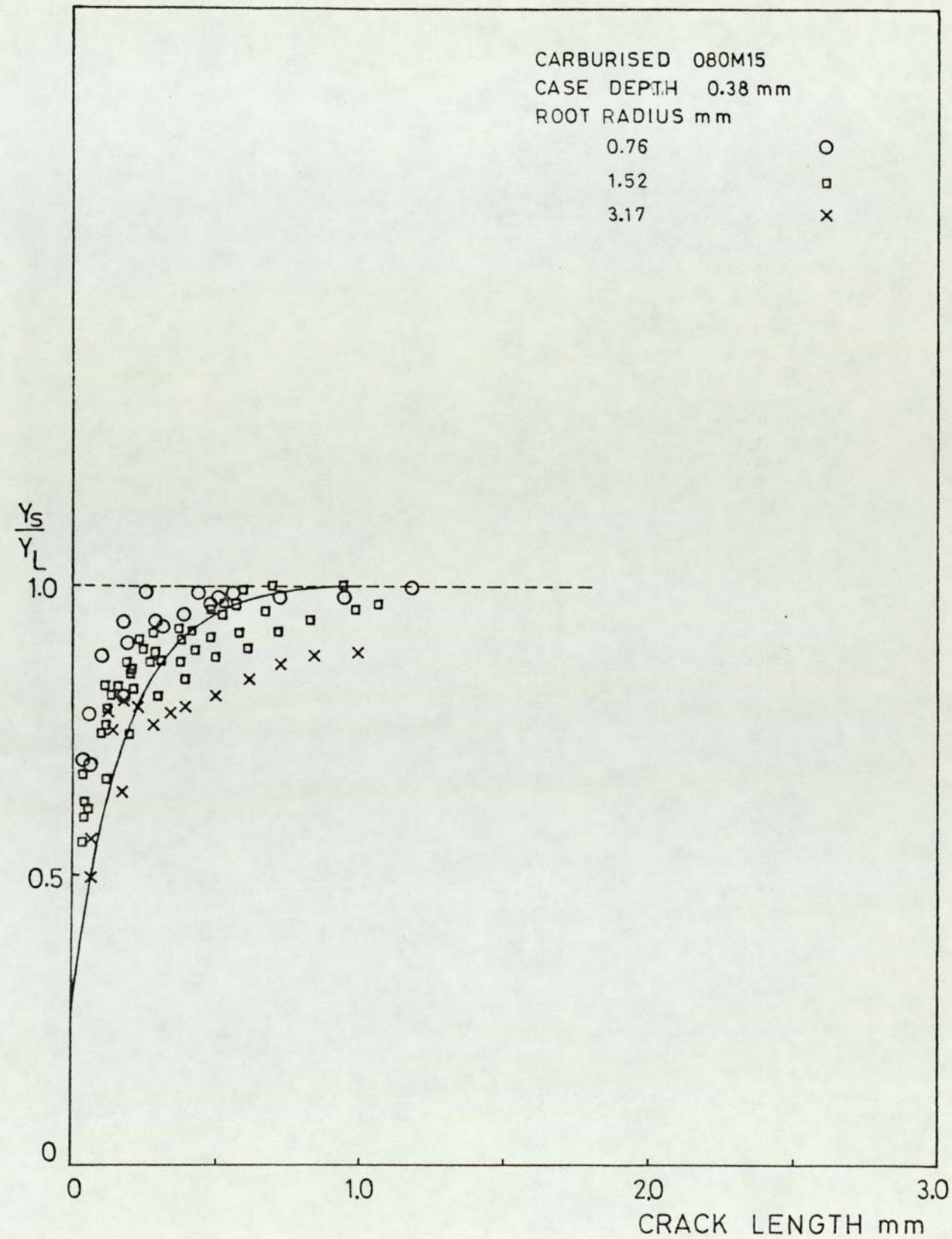

FIGURE 64 Modification function Y_s/Y_1 as a function of crack length, carburised 080M15, case depth 0.38 mm (curve represents equation 34)

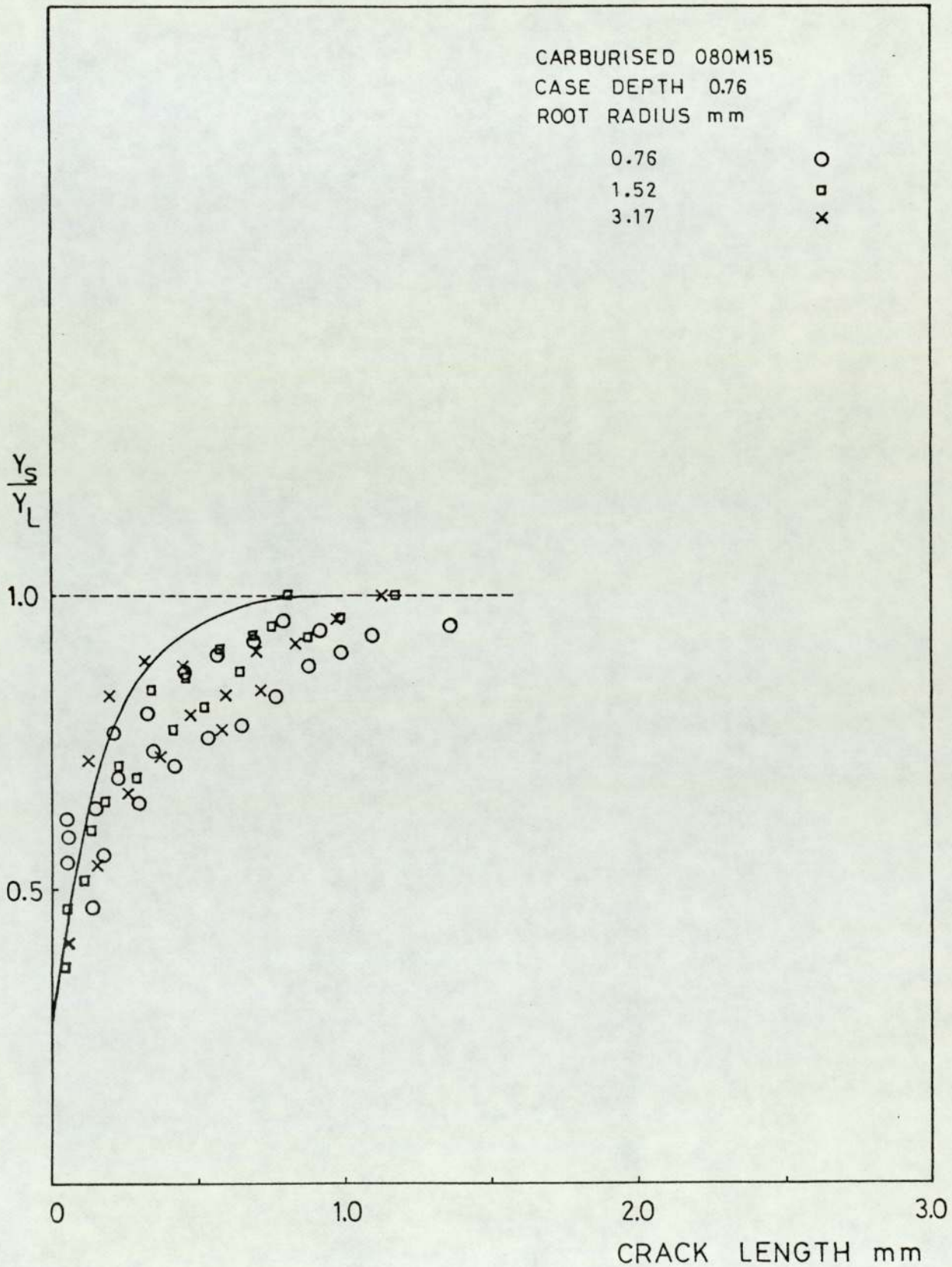

FIGURE 65 Modification function Y_s/Y_1 as a function of crack length, carburised 080M15, case depth 0.76 mm (curve represents equation 34)

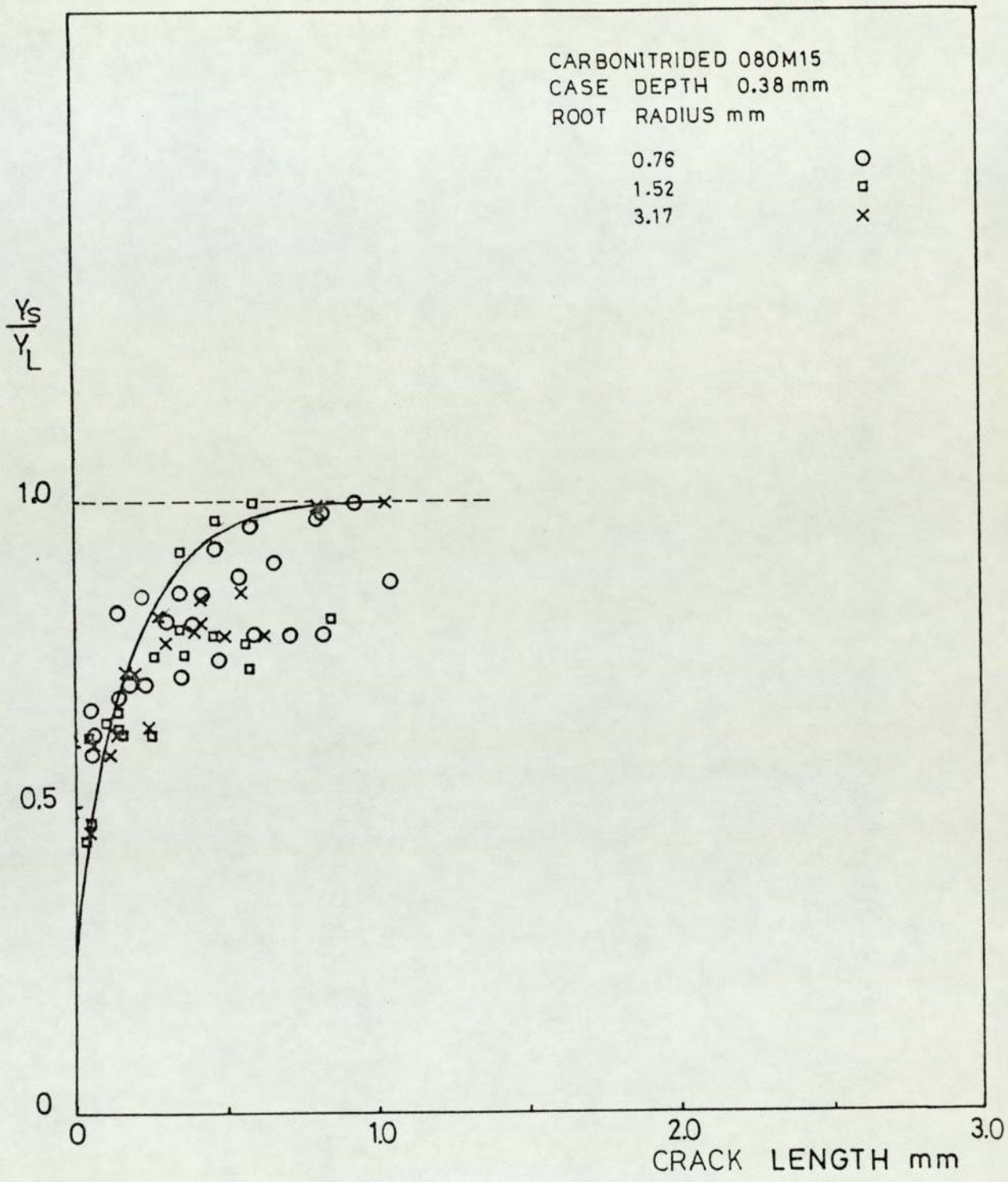

FIGURE 66 Modification function Y_s/Y_1 as a function of crack length, carbonitrided 080M15, case depth 0.38 mm (curve represents equation 34)

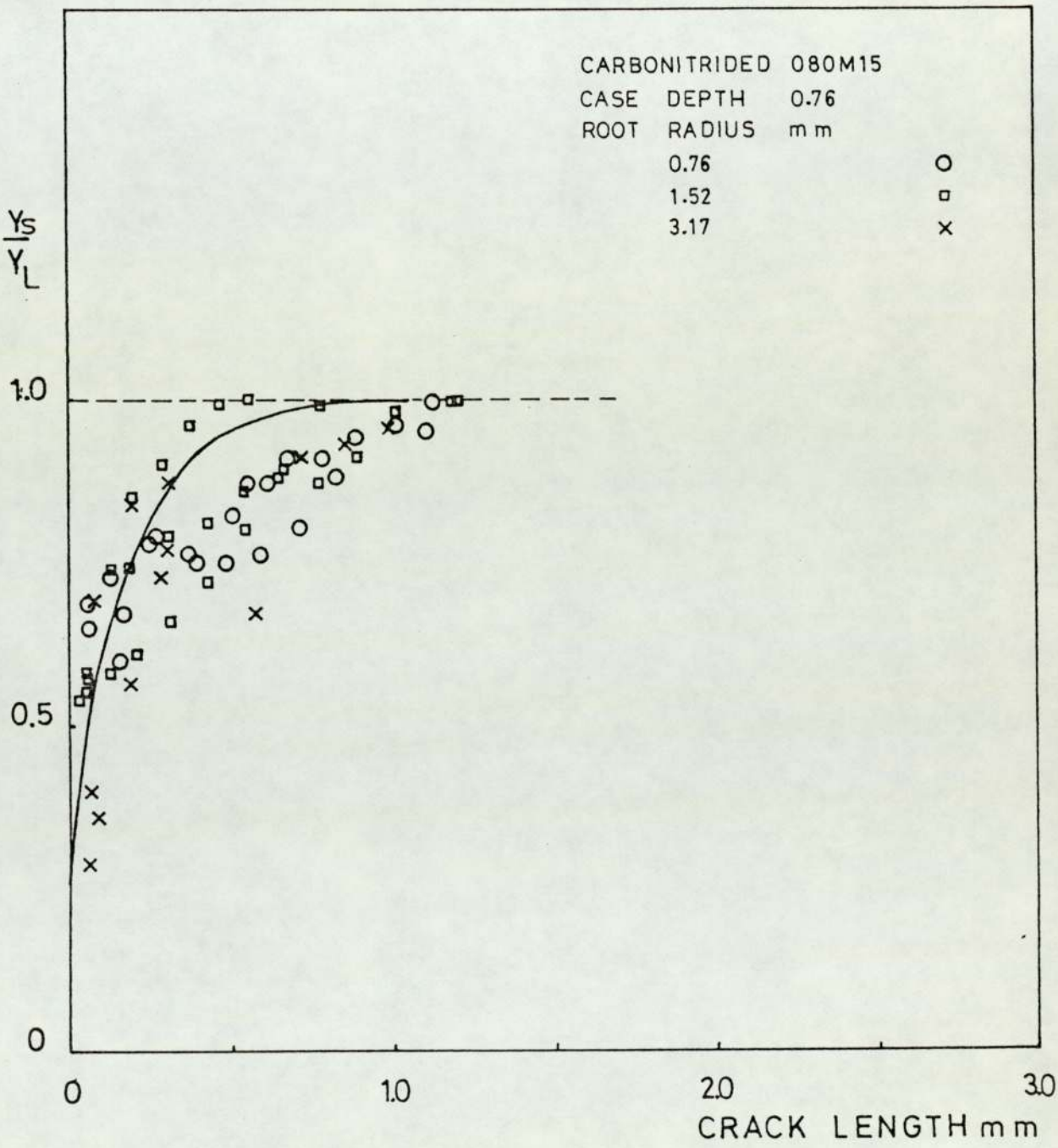

FIGURE 67 Modification function Y_s/Y_1 as a function of crack length, carbonitrided 080M15, case depth 0.76 mm (curve represents equation 34)

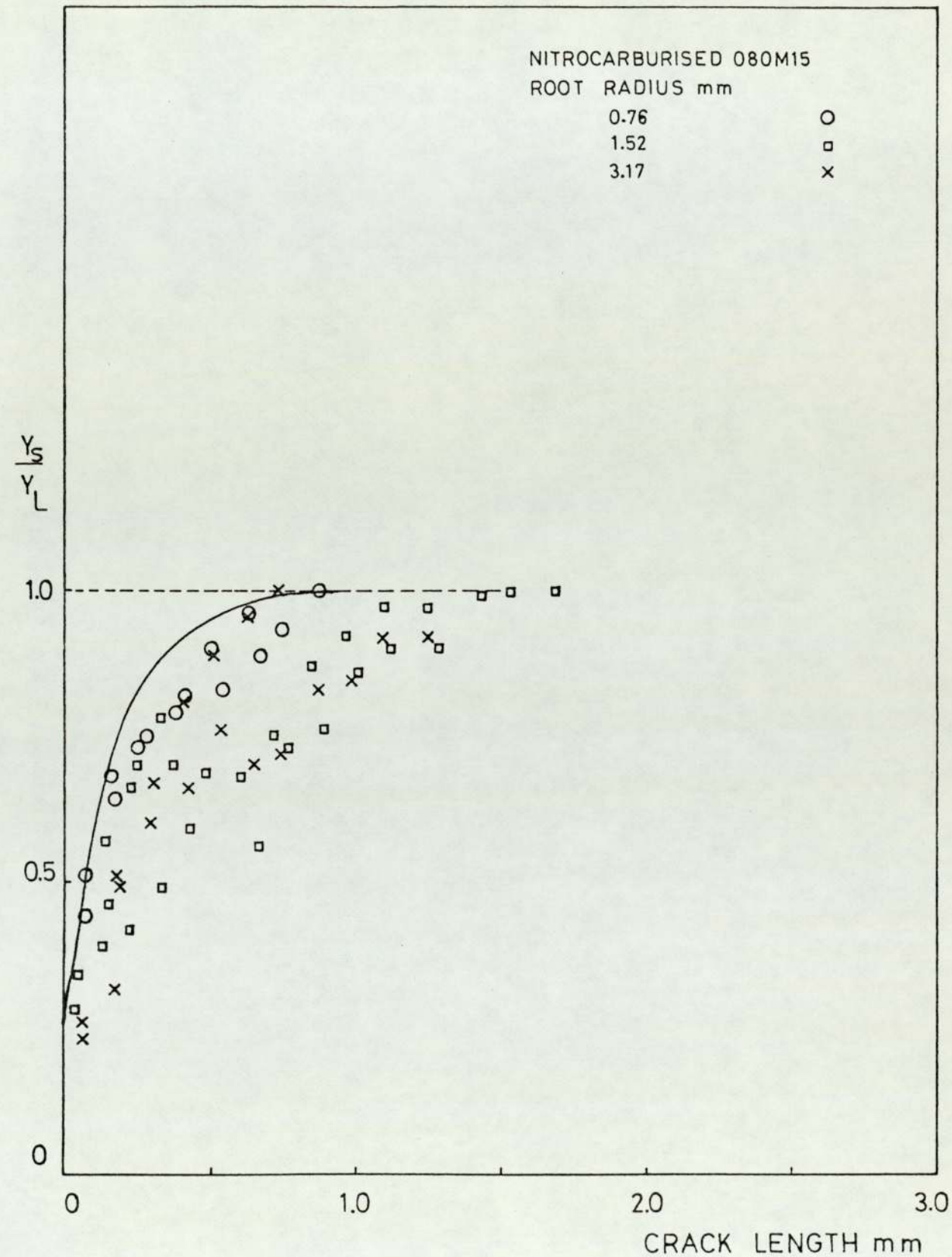

FIGURE 68 Modification function Y_s/Y_1 as a function of crack length, nitrocarburised 080M15 (curve represents equation 34)

8. CONCLUSIONS

1. The electrical potential difference technique was found to be a satisfactory crack detection method to monitor fatigue crack initiation and propagation. The crack length increments of 10 μm could be detected. Maximum error found in estimating the crack length was 0.1 mm.

2. The initiated cracks were found to be cusp shaped, which conformed to the size of an engineering crack (approximately 0.5 mm long and 0.15 mm deep) in carburised and carbonitrided 080M15. In untreated 080M15 and 080A47 the initiated cusps were found to be larger. The fatigue cracks were found to be cusp shaped until the crack length was 1 mm, after which a through thickness crack was formed. During this transition the electrical potential change varied smoothly.

3. The stress intensity factor coefficients for short crack emanating from notches were determined using fatigue crack growth data. Under laboratory conditions this method was found to be a satisfactory technique. The results could be represented by equation:

$$\frac{Y_S}{Y_L} = \sqrt{\frac{a \tanh\left[\frac{2*\sqrt{(1+\frac{a}{\rho})} * (c+C_B)}{\sqrt{a\rho}}\right] + c + C_B}{a + c}}$$

4. The equation determines the value of stress intensity factor coefficient for a notch, which is dependent on the notch geometry and the material parameter C_B. The material parameter correlated very well with the grain size or the mean free path.

5. The values of the stress intensity factor ranges for "blunt" notches calculated using the above equation correlated well with the number of cycles to initiation of an engineering crack in untreated 080M15, 080A47, carburised and carbonitrided 080M15 over the range of notch geometries tested.

6. The stress concentration parameter $K_t \Delta s$ and the fracture mechanics parameter $\frac{\Delta K}{\sqrt{\rho}}$ were also found to correlate reasonably well with the number of cycles to initiation N_i in untreated 080M15, 080A47, carburised and carbonitrided 080M15, over the range of notch geometries tested.

7. Fatigue crack initiation threshold for different case hardening treatments showed improvements over corresponding untreated material for all notch geometries. The improvements ranged from 29% to 170%, maximum improvement realised for a notch geometry with the stress concentration factor of 7.59.

8. Statistical analysis of threshold values of various parameters showed that the case depth has no effect on fatigue crack initiation threshold except for one notch geometry (K_t = 2.26). Statistical analysis of threshold values of fatigue crack initiation for carburising and carbonitriding suggested that there is evidence for and against the effect of case depth. The same notch geometries when nitrocarburised, showed lesser improvements in fatigue crack initiation threshold than those obtained for carburised or carbonitrided samples. Higher improvements in fatigue crack initiation thresholds were obtained in induction hardened 080A47 than case hardened 080M15 for corresponding notch geometries. The improvements ranged from 34% to 282% maximum improvement veing obtained for the notch geometry with highest stress concentration factor (K_t = 4.65).

9. Results of fatigue crack initiation from notches in untreated and case hardened 080M15 were compared. The comparison showed that the carburised and carbonitrided 080M15 is inferior to the untreated 080M15 at initiation lives below 10^5 cycles, for deep and blunt notches. The results indicated that the same observation applies to short and sharp notches.

10. The fatigue crack propagation data for case hardened 080M15 could be correlated with the modified stress intensity factor range and represented by the Paris Law.

11. The examination of fracture surface of untreated and case hardened samples showed that the fatigue crack initiated at the surface, i.e. at the notch root. Subsurface crack initiation was not observed in any of the samples.

9. SUGGESTIONS FOR FURTHER WORK

One of the interesting features of the present work is that the modified stress intensity factor coefficient does not fall to zero at the tip of a blunt notch. The effective stress intensity factor coefficient for blunt notches could be written as a function of notch geometry and microstructural features of steel, viz. grain size. The usefulness of the relationship between the modified stress intensity factor range and the number of cycles to initiation N_i in design has already been mentioned. The range of applicability of the relationship should be explored over a wide range of material. The Bilby and Heald analysis [28] suggests that the relationship should exist between material uniaxial yield strength and constants B and m of the initiation plot mentioned above. Such a relationship will be very useful as it will eliminate an otherwise great expenditure in time and effort, and it is probable that the crack initiation has been neglected, due to these influences.

The electrical potential method of monitoring initiation and growth of fatigue crack is found to be convenient and simple. However, theoretical calibrations cannot be used for specimen geometries which do not conform to those specified in theoretical calibrations. A generalised theoretical calibration needs to be developed. Further, as the electrical and stress fields are analogous the stress intensity factors for crack amanating from notches

could also be determined from the electrical potential fields.

The material parameter C_B is found to be grain size or mean free path. This needs to be confirmed over a large variety of material. Effect of residual stresses has not been accounted for in the present results. The residual stress distribution should be measured and incorporated in the parameter ΔK_B for a complete analysis. Only one type of carburising and carbonitriding treatment has been considered. Similar experiments could be repeated for other treatments.

10. APPENDIX

Notations

a	Notch depth
B	Specimen thickness
B_o, B_1, B_2	Material constants (from fatigue crack initiation equation)
B_m	Modification factor for stress intensity factor coefficient
C	Material constant (from fatigue crack growth equation)
C_o	Value of crack length which indicates extent of notch stress field
C_B	Material constant
c	Crack length
da/dN	Fatigue crack growth rate
d_o	Depth of penetration in induction heating
e	Equivalent crack length of notch
E	Young's modulus
G	Elastic shear modulus
K_t	Theoretical stress concentration factor
K_f	Fatigue strength reduction factor
K_σ	Stress concentration factor
K_ε	Strain concentration factor
K	Stress intensity factor
ΔK	Stress intensity factor range
ΔK_{th}	Fatigue crack initiation threshold in terms of ΔK
ΔK_B	Modified value of ΔK for a notch or short cracks emanating from notch
ℓ	Crack length including notch

m, m_1, m_2	Material constants (exponents from fatigue crack initiation equation)
n	Material constants (Paris law exponent from fatigue crack growth equation)
N	Number of cycles
N_i	Number of cycles to initiation of fatigue crack
N_p	Number of cycles during fatigue crack propagation
N_f	Number of cycles to failure
ΔP	Load range
R	Stress or stress intensity factor ratio
r_y	Plastic zone size
ΔS	Fibre stress range, nominal stress range
t	Induction heating time
V_o	Potential gradient in an uncracked specimen
V_a	Potential difference measured across a crack over a fixed gauge length
W	Specimen width
Y	Stress intensity factor coefficient
Y_s	Stress intensity factor coefficient for short crack emanating from notch
Y_l	Stress intensity factor coefficient for long crack
Δe	Nominal strain range
$\Delta \varepsilon$	Local strain range
ε_f'	Fatigue ductility coefficient

ρ	Notch root radius
ρ_o	Critical notch root radius
σ_f	Fatigue strength
σ_f'	Fatigue strength coefficient
$\Delta\sigma$	Local stress range
σ_{ys}	Yield strength
ϕ	Crack tip displacement
ϕ_c	Cummulative crack tip displacement
ϕ_c^*	Critical cummulative crack tip displacement

11. REFERENCES

1. N. Frost, K. Marsh and L. Pook, Metal Fatigue, Oxford Engineering Science Series, 1974, pp. 143

2. W. Plumbridge and D. Ryder, The Metallography of Fatigue, Metallurgical Reviews, 1969, Vol. 14, 119-142

3. P. Forsyth, The Physical Basis of Metal Fatigue, Blackie and Sons Ltd., 1969,

4. E. Orowan, Theory of Fatigue Failure of Metals, Proc. Royal Soc. of London, 1939, Vol. 1714, 79-106

5. W. Wood, Fine Slip in Fatigue, Bull. Inst. of Metals, 1955, Vol. 3, 5-6

6. H. Gough and D. Hanson, The Behaviour of Metals Subjected to Repeated Stresses, Proc. Royal Soc. of London, 1923, Vol. 140A, 538-565

7. A. Cottrell and D. Hull, Extrusion and Intrusion by Cyclic Slip in Copper, Proc. Royal Soc. of London, 1957, Vol. 242A, 211-215

8. N. Mott, A Theory of Origin of Fatigue Cracks, Acta Metall., 1958, Vol. 6, 195-197

9. P. Forsyth, C. Stubbington and D. Clark, Cleavage Facets Observed on Fatigue Fracture Surface in Aluminium Alloys, J. Inst. of Metal, 1961-1962, Vol. 90, 238-239

10. C. Laird, The Influence of Metallurgical Structure on the Mechanism of Fatigue, ASTM STP 415, ASTM 1967, 131-169

11. T. Duggan and J. Byrne, Fatigue as a Design Criterion, The Macmillan Press Ltd., 1977, pp. 51

12. Airplane Damage Tolerance Design Requirements, Military specification, USAF, MIL-A-83444, (tentative), May 1974

13. S. Pearson, Initiation of Fatigue Cracks in Commercial Aluminium Alloys and Subsequent Propagation of Vary Short Cracks. Engng. Fracture Mech., 1975, Vol. 7, 235-247

14. J. Barson and R. McNicol, Effect of Stress Concentration on Fatigue Crack Initiation in HY-130 steel, ASTM STP 559, ASTM 1974, 183-204

15. H. Fuchs, A Set of Fatigue Failure Criteria, Trans. ASME, series D, 1965, Vol. 87, 333-343

16. R. Landgraf, The Resistance of Metals to Cyclic Deformation, ASTM STP 467, ASTM 1970, 3-36

17. S. Manson, Fatigue a Complex Subject, Some Simple Approximations, Exp. Mech., 1965, Vol. 5, 192-226

18. P. Paris and F. Erdogan, A Critical Analysis of Crack Propagation Laws, Trans. ASME, series D, 1963, Vol. 85, 528-534

19. J. Knott, Fundamentals of Fracture Mechanics, Butterworths, 1976, pp. 246

20. R. Forman, V. Kearney and R. Engle, Numerical Analysis of Crack Propagation in Cyclic Loaded Structures, Trans. ASME, series D, 1967, Vol. 89, 459-464

21. P. Irving and L. McCartney, Prediction of Fatigue Crack Growth Rates, Theory, Mechanism and Experimental Results, Metal Science, 1977, Vol. 11, 351-361

22. H. Neuber, Theory of Stress Concentration for Shear Strained Prismatical Bodies with Arbitrary Non-linear Stress-Strain Law, J. of Appl. Mech., 1961, Vol. 28, 544-550

23. T. Wilshaw, C. Rau and A. Tetelman, A General Model to Predict the Elastic-plastic Stress Distribution and Fracture Strength of Notched Bar in Plane Strain Bending, Engng. Fracture Mech., 1968, Vol. 1, 191-211

24. G. Spinks, P. Worthington and P. Heald, The Effect of Notch Acuity on Fracture Toughness Testing, Materials Science and Engng., 1973, Vol. 11, 113-117

25. I. Milne, G. Chell, and P. Worthington, The Mechanisms of Fracture in Blunt Notched Specimens of Low Alloy Steel and the Effect of Fracture Assessment, CERL report VH266, 1978

26. V. Weiss, Application of Weibull's Statistical Theory of Fracture to Sheet Specimens, ASME paper 62-WA-270, 1962

27. A.Jack and A. Price, The Initiation of Fatigue Crack from Notches in Mild Steel Plates, Int. J. of Fracture Mech., 1970, Vol. 6, 401-409

28. B. Bilby and P. Heald, Crack Growth in Notch Fatigue, Proc. Royal Soc. of London, 1968, Vol. A305, 429-439

29. J. Barnby and R. Holder, Fatigue from Notches in Cast Steels, Metal Science, 1977, Vol. 11, 5-10

30. A. Jack and A. Price, Effects of Thickness on Fatigue Crack Initiation and Growth in Notched Mild Steel Specimens, Acta Metallurgia, 1972, Vol. 20, 857-866

31. Y. Kim, T. Mura and M. Fine, Fatigue Crack Initiation and Microcrack Growth in 4140 Steel, Met. Trans. A., 1978, Vol. 9A, 1679-1683

32. W. Clark, Evaluation of Fatigue Crack Initiation Properties of Type 403 Stainless Steel in Air and Steam Environment, ASTM STP 559, ASTM 1974, 205-224

33. S. Pearson, Fatigue Crack Initiation and Propagation in 12.7 mm thick Specimen of Aluminium Alloy, RAE Tech. report 71109, 1971

34. J. Barnby and K. Dinsdale, Fatigue Crack Initiation from Notches in Two Titanium Alloys, Materials Science and Energy, 1976, Vol. 20, 245-250

35. R. Holder, Fatigue Crack Initiation from Stress Concentration in Cast Steels, Ph.D. Thesis, University of Aston in Birmingham, 1976

36. M. Haddad, K. Smith and T. Topper, Fatigue Crack Propagation of Short Cracks, Trans. A.S.M.E., 1979, Vol. 101, 42-46

37. J. Benthem and W. Koiter, Methods of Analysis and Solutions of Crack Problems, Noordhoff Int. Publishing, 1973, 131-178

38. Y. Yamamoto and K. Ao, Stress Intensity Factors for Cracks in Notch Bend Specimens for Three Point Bending, Int. J. of Fracture, 1976, Vol. 12, 495-499

39. R. Smith and K. Miller, Prediction of Fatigue Regimes in Notches Components, Int. J. of Mech. Sci., 1978, Vol. 20, 201-206

40. J. Newman, An improved method of collocation for the stress analysis of cracked plates with various shape boundaries, NASA-TN-D-6376, Aug. 1972, pp. 46

41. H. Nishitani, Strength and Structure of Solid Materials, Noordhoff Int. Publishing, 1976, 53-69

42. H. Jergeus, A Simple Formula for the Stress Intensity Factors of Cracks in Side Notches, Int. J. of Fracture, 1978, Vol. 14, R113-R116

43. N. Dowling, Notched Member Fatigue Life Predictions Combining Crack Initiation and Propagation, Fatigue of Engineering Materials and Structure, 1979, Vol. 12, 129-138

44. S. Novak and J. Barsom, Brittle Fracture (K_{IC}) Behaviour of Cracks Emanating from Notches, ASTM STP 601, ASTM 1976, 409-447

45. L. James and W. Anderson, A Simple Experimental Procedure for Stress Intentity Factor Calibration, Engng. Fract. Mech., 1969, Vol. 1, 565-567

46. A. Grandt and G. Sinclair, Stress Intensity for Surface Cracks in Bending, ASTM STP 513, ASTM 1972, 37-58

47. W. Seidl, Methods of Experimental Determination of Stress Intensity Factors of Simplified Geometries of Structural Parts, 4th Int. Conf. on Fracture, Waterloo, 1977, Pergamon, 1978, 601-608

48. R. Stephens and G. Glinka, Experimental Determination of K_I for Surface Cracks in Square Tubes Under Torsion, Exp. Mech., 1980, Vol. 20, 24-30

49. M. McGuire, A. Trolino and L. Ebert, Phase Transformation Effects on Bending Stress Distribution in Carburised Steel Components, Trans. ASME, series D, 1971, Vol. 93, 699-707

50. H. Child, Surface Hardening of Steel, Oxford University Press, 1980

51. G. Fomenko, Investigation of the Wear Resistance of Case Hardened 12KhN3A steel, Metal Science and Heat Treatment, 1963, Vol. 1-2, 19-21

52. R. Richman and R. Landgraf, Some Effects of Retained Austenite on Fatigue Resistance of Carburised Steels, Met. Trans. A., May 1975, Vol. 6A, 955-964

53. R. Johnson, The Role of Nickel on Carburising Steel, Metals Eng. Quart., 1975, Vol. 15, No. 3, 1-8

54. C. Apple and G. Krauss, Martensite, Microcracks and Fatigue in 8620 Steel, Proc. 3rd International Conf. on the Strength of Metals and Alloys, Cambridge 1973, The Iron and Steel Institute 1973, 441-445

55. D. Diesburg and E. Eldis, Fracture Resistance of Various Carburised Steels, Met. Trans. A., 1978, Vol. 9A, 1561-1570

56. G. Krauss, The Microstructure and Fracture of a Carburised Steel, Met. Trans. A., 1978, Vol. 9A, 1527-1535

57. G. Parrish, The Influence of Microstructure on the Properties of Case Hardened Components, Part 3, Retained Austenite, Heat Treatment of Metals, 1976, Vol. 4, 101-109

58. G. Robinson, Effect of Surface Conditions on the Fatigue Resistance of Hardened Steel, Fatigue Durability of Carburised Steel, ASM, 1957, 11-47

59. S. Macorski, Total Approach to Reliability of Case Hardened parts, Metal Progress, Sept. 1970, Vol. 98, 96-98

60. D. Koistinen, The Distribution of Residual Stresses in Carburised Cases and their Origin, Trans. ASM, 1958, Vol. 50, 227-241

61. D. Diesburg, High Cycle and Impact Fatigue Behaviour of Carburised Steels, SAE 780771, 1978

62. W. Coleman and M. Simpson, Residual Stresses in Carburised Parts, Fatigue Durability of Carburised Steels, ASM 1957, 47-68

63. L. Ebert, The Role of Residual Stresses in the Mechanical Performance of Case Carburised Steels, Met. Trans. A., 1978, Vol. 9A, 1537-1551

64. R. DePaul, High Cycle and Impact Fatigue Behaviour of some Carburised Gear Steel, Metals Eng. Quart., Nov. 1970, Vol. 10, 25-29

65. T. Aida, H. Fujio, M. Nishikawa and R. Higashi, Influence of Impact Load on Fatigue Bending Strength of Case Hardened Steel, Bull. J.S.M.E., 1972, Vol. 15, 817-833

66. B. Pathiraj and P. Dhar, Influence of Carburised Case Depth on Fatigue and Impact Strength of IS 20MnCr1 - Carburising Steel, 2nd International Conf. on Mechanical Behaviour of Metals, 1976, 835-837

67. R. Mattson and G. Robinson, Case Carburising, A.S.M.E. Handbook, Metals Engineering Design, McGraw-Hill, 1965, 284-290

68. P. Forrest, Fatigue of Metals, Pergamon Press, 1962, 175-204

69. A. Diament, R. Haik, R. Lafont and R. Wyss, Surface Fatigue of Carbonitrided and Carburised Layer, Traitment Termique, Aug-Sept 1974, 87, 87-97

70. A. Diament, R. Haik and R. Wyss, Residual Micro-Deformation Stresses and Crystalline Structures of Carburised and Carbonitrided Layers, Traitment Thermique, Apr. 1978, 124, 68-79

71. T. Ericsson and M. Knuuttila, Fatigue Properties of Carburised and Carbonitrided C-Mn and C-Mn-B Steels, 2nd International Conf. on Mech. Behaviour of Metals, 1976, 823-828

72. L. Kiessling, A Comparison of Wear and Fatigue Characteristics of Carburised, Carbonitrided and Nitrocarburised Low Carbon Steel, Heat Treatment of Metals, 1979, 5, 97-100

73. L. Semenova, V. Teldeko and E. Tesker, The Increase of Fatigue Strength of Tractor Gears with Optional Carbonitriding, Metal Science and Heat Treatment, 1973, 15, 756-758

74. V. Krylov, L. Semenova, B. Slobin and G. Kucheruk, Influence of Carbonitriding Defects on Fatigue Strength of 25KhGT Gear Teeth, Metal Science and Heat Treatment, 1971, 13, 1028-1031

75. B. Alexsandrov and G. Memdlov, The Fatigue Strength of Steel 18Kh2N4VA after Different Heat Treatments and Chemicothermal Treatments, Metal Science and Heat Treatment, 1971, 13, 228-230

76. B. Prenosil, Effect of Retain Austenite in Carbonitrided Case Structure upon Fatigue Strength, Czech. J. Phy., 1969, B19, 397-398

77. T. Bell and D. Thomas, Cyclic Stressing of Gas Nitrocarburised Low Carbon Steel, Met. Trans. A., 1979, 10A, 79-84

78. K. Sachs and D. Clayton, Nitriding and Nitrocarburising in Gaseous Atmospheres, Heat Treatment of Metals, 1979, 5, 29-34

79. C. Dawes, D. Tranter and C. Smith, Reappraisal of Nitrocarburising and Nitriding when applied to Design and Manufacture of Non-alloy Steel Automobile Components, Metals Technology, 1979, 345-353

80. A. Bavaro, M. Franzosi and G. Mengoni, Gaseous Carbonitriding at Low Temperature, Traitment Thermique, 1975, 95, 51-55

81. T. Ito, K. Isokawa, H. Kamiya, T. Watanbe and M. Saito, Application of Gas Nitro-carburising for Gears Operating at Hertz Pressure of Over 180 Kg/mm^2, Heat Treatment '76, Metals Society Book No. 181, 1976, 15-20

82. T. Bell and S. Lee, Gaseous Atmosphere Nitro-carburising, Heat Treatment '73, Metals Society Book No. 163, 1975, 99-107

83. S. Kern, Selecting Steels for Heat Treated Parts, Part II, Case Hardenable Grades, Metal Progress, 1968, 94, 71-81

84. K. Nishioka, Fatigue Strength of Induction Hardened Railway Axles, J. of Materials, 1969, 4, 413-436

85. K. Hayashi, Effect of Cold Working and Induction Hardening on the Fatigue Strength of Carbon Steels, Tech. Report IQ 73-620, Soc. of Manufacturing Eng., 1973

86. K. Yamada, Microstructural Approach of the Fatigue Behaviour of Rapidly Heat Treated Steel, Proc. 2nd International Conf. on Fracture, Brighton, 1969, 630-642

87. F. Krotine, M. McGuire, L. Ebert and A. Troiane, The Influence of Case Properties and Retained Austenite on the Behaviour of Carburised Components, Trans. ASM, 1969, Vol. 62, 829-838

88. J. Woodwine, The Behaviour of Case Hardened Parts under Fatigue Stresses, Carnegie Scholarship Memoirs, Iron and Steel Institute, Vol. XIII, 1924, 197-237

89. R. Landgraf and R. Richman, Fatigue Behaviour of Carburised Steel, Fatigue of Composite Materials, ASTM STP 569, ASTM, 1975, 130-144

90. P. Frith, Crank Shaft Steels, Effect of Nitriding and Composition on Fatigue Properties, Iron and Steel, 1948, Vol. 21, 542-548

91. M. Balter and I. Dukarevich, The Relationship between the Properties of Steels Subjected to Chemicothermal Treatments and Fatigue Limit, Metal Science and Heat Treatment, 1971, Vol. 13, 729-732

92. B. Jones and J. Martin, Fatigue Failure Mechanisms in a Nitrided En41B Steel, Metals Technology, 1978, Vol. 5, 217-221

93. C. Li and R. Wei, Calibrating the Electrical Potential Method for Studying Slow Crack Growth, Material Research and Standards, 1966, Vol. 6, 392-394

94. J. Lowes and G. Fearnhough, The Detection and Slow Crack Growth in Crack Opening Displacement Specimens Using an Electrical Potential Method, Eng. Fracture Mechanics, 1971, Vol. 3, 103-108

95. A. Anctil, I. Kula and E. De Cesare, Electrical Potential Technique for Determining Slow Crack Growth Rate, Proc. ASM, 1963, Vol. 63, 799-808

96. H. Johnson, Calibrating Electrical Potential Method for Studying Slow Crack Growth, Material Research and Standards, 1965, Vol. 5, 442-445

97. D. Gilbey and S. Pearson, Measurement of the Length of a Central or Edge Crack in a Sheet of Metal by an Electrical Resistance Method, RAE Technical Report 66402, 1966

98. R. Cooke and J. Robinson, Some Further Consideration of the Potential Drop Method for Measuring Crack Lengths, Internal Report, University of Birmingham, 1971

99. G. Clark and J. Knott, Measurement of Fatigue Cracks in Notched Specimens by means of Theoretical Electrical Potential Calibrations, J. of Mechanics and Physics of Solids, 1975, Vol. 23, 265-276

100. R. Ritchie, G. Garrett and G. Knott, Crack Growth Monitoring: Optimisation of the Electrical Potential Technique using an Analogue Method, Int. J. of Fracture Mechanics, 1971, Vol. 7, 462-467

101. H. Katagiwa and S. Takahashi, Applicability of Fracture Mechanics to very small Cracks or the Cracks in the Early Stage, 2nd Int. Conf. on Mechanical Behaviour of Metals, 1976, 627-631

102. W. Plumbridge, Problems Associated with Early Stage Fatigue Crack Growth, Metal Science, 1978, Vol. 12, 251-256

103. Standard Method of Test for Plane-Strain Fracture Toughness of Metallic Materials, ASTM Designation E399-4, Part 10, ASTM Annual Standards 1979

104. P. Wood and T. Richards, Stress Concentration Factors for some Blunt Notched Three Point Bend Fracture Specimens, Internal Report, University of Aston, 1977

105. S. Rolfe and J. Barsom, Fracture and Fatigue Control in Structures, Prentice-Hall 1977, 208-232

106. Euronorm Standards 105:1971, Determination and Verification of the Conventional Depth of Case-Hardening of Steels.

107. C. Lipson and N. Seth, Statistical Design and Analysis of Engineering Experiments, McGraw-Hill Inc., 1973